University of Strathclyde

Department of Pure and Applied Chemistry

Developments in photonic systems for Raman spectrometry in microreactors

by

Sergey Mozharov

A thesis submitted to the Department of Pure and Applied Chemistry, University of Strathclyde, Glasgow, in fulfilment of the requirements for the degree of Doctor of Philosophy

2010

This thesis is the result of the author's original research. It has been composed by the author and has not been previously submitted for examination which has led to the award of a degree.

To my mum, dad and Julia

Acknowledgements

On reflecting about the three years that I spent in Glasgow I was astonished to realise how many people were involved in my work, directly and indirectly, and how difficult it would be to mention everyone. Working at Strathclyde was a great and very pleasant experience in my life and it is my pleasure to recognise the importance of the help that I received from other people for the results I am presenting in this thesis.

First of all, I would like to thank my supervisors, David Littlejohn and Alison Nordon, not only for their continuous guidance and invaluable support throughout the years but also for being with me through some difficult times. Their professional and friendly attitude and trust in me ensured my quick integration in the new environment and provided comfortable conditions where I learnt and developed inspiration to do my work.

I spent the first year of my research at the Institute of Photonics where I was introduced to the world of lasers and optics. Being a novice in this field, I received a lot of advice and help from Untzizu Elejalde and John Girkin. John's supervision and inexhaustible cheerfulness were the major sources of my enthusiasm during that time. I want to thank other students and members of staff of the Institute of Photonics, particularly Paul Hynd and Lisa Muir, for their help with manufacturing my Raman probe. Jennifer Mains from SIPBS and Paul Dallin from Clairet Scientific provided microfluidic and spectroscopic equipment at different stages of my research, for which I owe them a great deal of gratitude.

My fellow colleagues from both Department of Pure & Applied Chemistry and the Institute of Photonics are thanked for a very friendly atmosphere, many laughs and informal events. My life at Strathclyde would not be so smooth without Natalie Driscoll who was a great team coordinator and helped me on numerous occasions. Special thanks go to Nichola Townshend and David Wilsdon for their friendship, many cups of Nicci tea and our insightful conversations about the steamed fish, Terminator, Mr Raman and other interesting things. The time when we all were together in R-501 was unforgettable and I am thankful to Melissa, Ally, Peter, Salah,

Bushra, Nicci and David for creating a magical atmosphere in the office. The closer I came to the end of my project the more I realised how incredibly lucky I was to be a member of such a great group where I felt as comfortable as I did at home.

I also express acknowledgements to John Murphy and Isabel Scott for their kind support during the difficult process of my application to the University of Strathclyde and to the ORS award and CPACT that funded my research.

The final stages of my work took place at the University of Hull (UK) and the University of Washington (Seattle, USA). It was not trivial to find money for these trips and I want to take an opportunity to thank those who made decisions to invest in me and my work. The funding was provided by Centre for Process Analytics and Control Technology (CPACT), Mac Robertson Trust (University of Glasgow), University of Strathclyde, University of Washington, University of Hull, Royal Society of Chemistry and the Optical Society of America.

My 5-week stay in Hull was a difficult but very rewarding experience. It would have been impossible to succeed within such a short period of time without the assistance from my colleagues from the University of Hull, Charlotte Wiles and Paul Watts. I am also grateful to my friend Bongkot Ngamsom who was always with me when I needed help. I will never forget her encouraging smile and the amazing Thai food that she cooked for me.

The work in Hull was followed by a 10-week visit to the University of Washington in Seattle where I received a lot of help and guidance from Brian Marquardt and his team. I thank Brian for his excellent supervision, and for our long and entertaining debates about the theoretical feasibility of some of my ideas. I experienced many technical problems in Seattle that were solved thanks to my own efforts, and help from Brian and Wes. Later I realised that those problems were as important for my professional experience as were my achievements.

And finally, I want to thank my parents and my sister Julia for their love and support of my pursuit of knowledge that led me far away from home at the age of 17.

Contents

Abstract

Liquid-phase chemical reactions are very popular in both industry and research labs. In recent years these reactions have been increasingly performed in microfluidic devices that provide high efficiency, throughput, convenience and safety. In many microfluidic applications fast and reliable process analysis is needed. One of the most powerful tools for reaction monitoring is Raman spectrometry. However, its use with microreactors sets a number of technical and methodological challenges that have to be resolved.

In this thesis, development of a fibre-optic Raman probe optimised for the analysis of transparent liquids in microreactors is presented. Increased sensitivity, a more localized collection volume, a simplified construction and reduced instrument cost are demonstrated. With only a 2 s acquisition time, accurate performance of the probe in monitoring an esterification reaction at any point along the 150 μm wide serpentine of a microreactor was achieved. Fast data acquisition reduced the process optimisation time, allowed tracking of the reaction along the serpentine, and demonstrated the high-frequency instabilities that can be introduced by unstable pumping.

The optimised Raman probe was employed to develop a novel method for kinetic studies based on flow rate manipulation and fast data acquisition. By use of a single experiment, the developed procedure reduced the time and the amount of reagents required to obtain the rate constant and order of reaction compared to conventional multi-experiment methodology. Further improvement in the use of non-invasive Raman spectrometry for monitoring of microreactors was achieved through design of a measurement cell, optimised geometrically and optically for better signal-to-background, which could be added to the flow path. The combined results of the research can lead to the development of a universal Raman system for process analysis in microreactors that could be utilised in previously difficult situations where optical access to the channels is restricted.

1. Microreactor technology

1.1. Introduction

The interest in flow chemistry has increased considerably over the last decade[1]. The main reason for this was the emergence of the field of microfluidics that concerns manipulation and analysis of liquids in microfabricated channels. The rapid development of microfluidic technology has been driven simultaneously by many factors. The integrated circuit revolution in the late 20th century has demonstrated the impressive effects of miniaturisation and automation of computer systems that have changed the way we live. It was natural to look for ways to apply these approaches to other research areas[2]. Although the unique behaviour of liquids inside miniaturised channels had been known long before the advent of computers[3], it seems likely that the staggering influence of the computer revolution on society and the global economy played its role in moving microfluidic systems from the subject of scientific curiousity to applied science. The demand for sustainable, more efficient and safer chemical reactions, the interest in reducing associated analysis time and cost, and a desire to increase the throughput of chemical and biochemical assays have all served as powerful incentives to develop microfluidic technology that offers solutions to all these challenges.

A great deal of the recent research activity has been focused on integrating various microfabricated components into microfluidic chips. The ultimate goal of this approach is to develop a completely integrated, fully operational device within a single chip. Such devices of the future are referred to as "lab-on-a-chip" or "micro-total analytical systems" (μTAS)[4]. The term lab-on-a-chip, however, is often used interchangebly with the more general concept of microfluidics.

Today microfluidic devices are ubiquitous. They have been applied in most, if not all, areas where liquid-phase processes are involved. In turn, advances in microfluidic technology have promoted interdisciplinary research involving biology, mechanics, photonics, chemistry and engineering. The wide variety of applications and the increasing number of publications in this field make it difficult to review this subject in a comprehensive way. In fact, reviews of lab-on-a-chip technology are

updated on a regular basis to highlight the thousands of new studies reported each year[1, 5].

The work presented in this thesis concerns microreactors, which are microfluidic devices designed to perform chemical synthesis. Several practical advantages of using microreactors, instead of traditional batch vessels, have been demonstrated for a range of chemical processes[6-8]. These advantages include higher yield and selectivity of reactions, enhanced safety, efficient heat transfer, and scale out to production scale without the need for re-optimisation of process parameters. Recent developments in microreactor technology have created a growing demand for process monitoring and control methods suitable for application in this technically challenging environment. The goal of the present work is to investigate the suitability of Raman spectroscopy for microfluidic applications, identify limitations and so improve the performance of Raman spectroscopy by means of optimisation of the optical interface with the sample, and then use the interface to facilitate the development of new experimental procedures.

Before discussing Raman spectroscopy, an introduction to essential microfluidic physical concepts and a review of the most relevant applications are provided.

1.2. Fluid physics at the micro-scale

The essential physics of a flow system is dictated by a competition between various phenomena. As the channel dimensions decrease, the balance between these phenomena changes very rapidly resulting in the unique fluid behaviour that usually contradicts the day-to-day human experience with liquids. In order to understand the unusual effects emerging in microchannels it is convenient to compare the competing forces governing the fluid motion against each other.

The special properties of microfluidics concern several aspects of fluid behaviour. In this Section, only three aspects that are most important to understand microfluidic physics will be discussed. The areas that will remain untouched include various non-Newtonian effects important for solutions containing polymers or proteins, and

buoyancy. The description and analysis of these phenomena can be found in special texts[2].

The competing forces are best characterised by dimensionless numbers that help compare different microfluidic systems and predict their behaviour.

1.2.1. The Reynolds number: inertial and viscous forces

Motion of the majority of fluids (Newtonian fluids) obeys the Navier-Stokes equation[2]:

$$\rho\left(\frac{\partial \mathbf{v}}{\partial t}+\mathbf{v}\cdot\nabla\mathbf{v}\right)=-\nabla p+\eta\nabla^2\mathbf{v}+\mathbf{f} \qquad (1.1)$$

where ρ is the fluid density, $\mathbf{v}$ – linear flow rate, p – pressure, η - viscosity, $\mathbf{f}$ represents density of forces (per unit volume) applied to the fluid, and ∇ is a vector differential operator $\left(\frac{\partial}{\partial x}+\frac{\partial}{\partial y}+\frac{\partial}{\partial z}\right)$. The bold style of some characters indicates that they are vector variables.

This equation can be derived by applying Newton's second law (conservation of momentum) to a small portion of a fluid. Similar to Newton's law, the left part of equation (1.1) represents acceleration terms or convective effects; $\frac{\partial \mathbf{v}}{\partial t}$ accounts for changes in the velocity amplitude, and $\mathbf{v}\cdot\nabla\mathbf{v}$ for changes in the flow direction. The right part consists of forces that include a normal component (e.g. pressure) and a tangential component (shear stresses).

The Reynolds number (Re) is a measure of the competition between the inertial forces ($f_{in}=\rho\mathbf{v}\cdot\nabla\mathbf{v}$) and the viscous forces ($f_{vis}=\eta\nabla^2\mathbf{v}$). In a situation where the channel makes a sudden turn, the fluid will lose its momentum (ρv) over a travel distance L, which represents a length scale of the flow system (e.g. the channel diameter or the radius of the turn). The velocity gradient over this distance can be replaced by an average value ($\nabla\mathbf{v}\approx\frac{v}{L}$), and the ratio of the inertial and viscous force densities can be written as follows:

$$\mathrm{Re} = \frac{f_{in}}{f_{vis}} \approx \left(\frac{\rho v^2}{L}\right) \Big/ \left(\frac{\eta v}{L^2}\right) = \frac{\rho v L}{\eta} \qquad (1.2)$$

The small channel dimensions (L) and low linear flow rate (v) typical for microfluidic systems correspond to small Reynolds numbers (usually in the range of 10^{-6} - 10), which means that the contribution of inertial effects is negligible and viscous dissipation is the dominant force. In these conditions, liquids flow in a laminar regime characterised by a parabolic flow profile (Figure 1.1a). The flow rate is the greatest near the central axis of the channel and gradually reduces to almost zero when approaching the capillary wall.

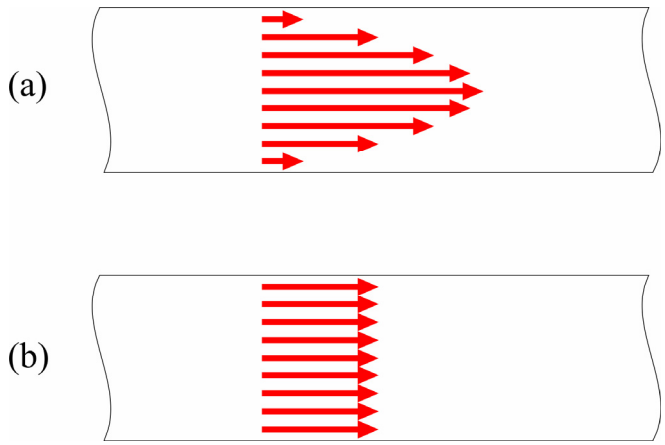

Figure 1.1. Flow rate vectors across the pipe: (a) laminar flow; (b) turbulent flow.

For systems with low Reynolds numbers, the term responsible for convective acceleration in equation (1.1) disapears giving the linear Stokes flow:

$$\rho \frac{\partial \mathbf{v}}{\partial t} = -\nabla p + \eta \nabla^2 \mathbf{v} + \mathbf{f} \qquad (1.3)$$

When the channel dimensions and the flow rate increase, the effect of inertial forces becomes more apparent and can destabilise the parabolic velocity profile. The flow becomes unpredictable when the Reynolds number exceeds 2000-3000[2]. Such flow is called turbulent. It gives a uniform velocity profile across the entire cross section of the channel (Figure 1.1b).

Although the Reynolds number is useful to demonstrate the different flow regimes in micro- and macro-systems it may be the least interesting parameter because almost without exception microfluidic devices operate very far from the conditions where the flow can become turbulent. Nevertheless, it should not be assumed that inertia does not play any role in microfluidics. For example, inertial effects can be noticeable when the flow path makes a series of sudden turns, which can be used to facilitate mixing (see Section 1.3.3).

1.2.2. Diffusion and convection

Consider a thin tracer stripe inside a microchannel of radius r (Figure 1.2a). The laminar flow stretches the tracer into a parabola (Figure 1.2b). It is tempting to assume that as long as the liquid is moving, the parabola will continue to stretch over a large length, with the regions near the wall remaining stationary. However, at this stage of reasoning it is important to remember that matter is made of molecules. In liquids, discreteness of matter manifests itself in the phenomenon of diffusion, which is a direct consequence of chaotic movements of molecules. Molecular diffusion is described by Fick's laws:

$$J = -D\frac{\partial C}{\partial x} \tag{1.4}$$

$$\frac{\partial C}{\partial t} = D\frac{\partial^2 C}{\partial x^2} \tag{1.5}$$

where J is the diffusive flux (the amount of solute flowing through a certain area over a certain time), C is the local solute concentration and D is the diffusion coefficient.

The first Fick law (1.4) shows that the diffusive flux is proportional to the concentration gradient. The second Fick law (1.5) describes how the concentration distribution evolves with time.

Diffusion plays an important role at the micro-scale and cannot be neglected. In the system shown in Figure 1.2, diffusion disperses the slower fluid regions towards the channel centre where the faster flow carries them downstream. Similarly, the fast

fluid layers located near the channel centre are dispersed towards the walls. Therefore, after a sufficient amount of time is allowed, the composition across the channel becomes uniform and the parabola turns into a plug (Figure 1.2c).

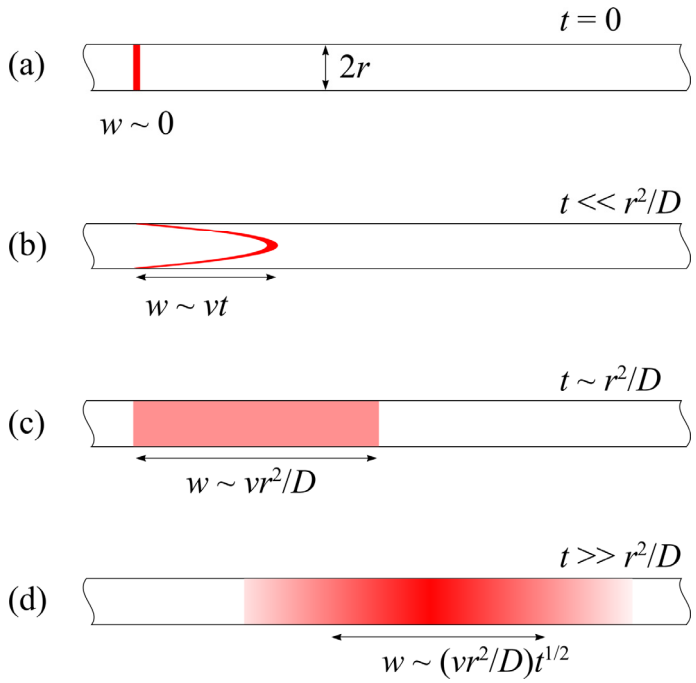

Figure 1.2. Taylor dispersion. (a) A thin tracer stripe is inserted into a laminar flow with a flow rate of *v*. (b) The flow stretches the stripe into a parabola of width $w \sim vt$. (c) After a characteristic time $t \sim r^2/D$ the parabola is smoothed into a homogeneous plug of width $w \sim vr^2/D$. (d) After a sufficiently long time the plug evolves as a Gaussian spreading with a width of $w \sim (vr^2/D)t^{1/2}$ (adapted from [2]).

A mathematical analysis of this problem was provided by Taylor[3]. He derived a characteristic time t_e, after which the radial compositional difference across the channel reduces by a factor of e [9]:

$$t_e = r^2 / 14.4D \qquad (1.6)$$

where r is the radius of the channel and D is the molecular diffusion coefficient of the tracer.

If the flow time is much longer than t_e, the tracer distribution along the channel evolves as a Gaussian band with a width of $w \sim (vr^2/D)/t^{1/2}$ (Figure 1.2d). Therefore,

the convective stretching of a thin stripe is followed by diffusive homogenisation producing a Gaussian plug moving at the mean flow speed. This process is referred to as Taylor dispersion and it plays a key role in transporting fluids in microchannels. Without Taylor dispersion, convection would stretch the initial tracer stripe infinitely with time. Taylor dispersion reduces the rate of such stretching to diffusive growth (proportional to the square root of time).

In some applications, it is desirable to achieve higher compositional resolution along the flow path. To do so, the experiment should be carried out at lower flow rates and, more importantly, in narrower channels.

Molecular diffusion is also important for fluid mixing in microchannels. In contrast to large-scale flow systems, where mixing is greatly facilitated by turbulence, mixing in microchannels usually occurs solely by diffusion. During the characteristic diffusion time as given by equation (1.6) the liquid will have moved a distance of $Z = vr^2/14.4D$. By relating this characteristic travel distance to the channel radius and neglecting the numerical factor, the following equation is obtained[2]:

$$\frac{14.4Z}{r} = \frac{vr}{D} = \mathrm{Pe} \qquad (1.7)$$

Equation (1.7) defines another dimensionless parameter of a microfluidic system, the Péclet number (Pe), which is a measure of the relation between convection and diffusion. The Péclet number shows the approximate number of the channel widths that an inhomogeneous liquid has to travel downstream to become homogeneous. Two conclusions can be made from equation (1.7): (i) the relative importance of diffusion over convection increases as the channel radius and the flow rate decrease; (ii) for a given channel and the flow rate, the diffusion time is inversely proportional to the diffusion coefficient of the solute, which can be a useful rule for the mixing time estimations. For illustration purposes, diffusion coefficients of various species in water are given in Table 1.1.

Table 1.1. Diffusion coefficients for various particles in water at room temperature (adapted from [2]).

Particle	Diffusion coefficient / $\mu m^2\ s^{-1}$)
Solute ion	2000
Small protein	40
Virus	2
Bacterium	0.2
Mammalian cell	0.02

The information in the table demonstrates that the diffusion coefficients can differ by several orders of magnitude depending on the particle's size. This difference is used in several microfluidic separation techniques[2]. However, in most analytical applications, it is important to achieve fast mixing regardless of the solute's nature. In these situations, various micro-mixers can be used (see Section 1.3.3).

1.2.3. Capillary forces and surface effects

Another consequence of the decreased channel size in microfluidics is the greater surface to volume ratio. Apart from the improved efficiency of heat transport through the channel walls, it results in the greater importance of various surface effects that can have a notable influence on the flow dynamics. The nature of this influence can be demonstrated using the example of two immiscible liquids, one flowing into the other inside a microchannel. The boundary between the fluids is characterised by surface tension γ that acts to reduce the interface area. On the other hand, viscous stresses tend to drag the boundary downstream thus extending the interface surface. The competition between these stresses can destabilize the interface and cause droplet formation. It is remarkable that the generated droplets are of the same radius (R) that can be estimated by balancing the Laplace pressure on the droplet surface ($2\gamma / R$) and the viscous stress ($2\eta v / r$) exerted on the interface between the liquids flowing at the linear flow rate v in a channel with the radius r [10]:

$$R \approx \frac{\gamma r}{\eta v} = \frac{r}{\mathrm{Ca}} \tag{1.8}$$

where Ca is the capillary number, a dimensionless parameter that gives a measure of the relative importance of viscous stresses to surface stresses[2]:

$$\mathrm{Ca} = \frac{\eta}{\gamma} v \tag{1.9}$$

For $\mathrm{Ca} << 1$, the capillary forces prevail and the liquids flow side by side without droplet formation, otherwise droplets will form. The controlled formation of monodispersed droplets in microfluidic devices has a number of applications, including emulsification[11], production of special materials[12] and measuring the kinetics of fast reactions[13]. Droplets can also serve as micro-vessels for conducting chemical reactions, which is advantageous in two respects: (i) a much faster mixing can be achieved in micro-droplets than in a homogeneous flow[13]; (ii) convection and diffusion do not disperse a droplet beyond its boundary.

Another area where surface effects play an important role concerns systems where a liquid-gas interface is present, for example, paper-based microfluidic devices, thin layer chromatography or flow systems with gas bubbles. In general, the surface tension on the gas-liquid interface is lower than that on the solid-liquid interface. This difference draws the fluid into wetting the channel. The effect is widely applied as a simple method of flow manipulation. For example, by coating a glass plate with a monolayer of a hydrophobic compound, it is possible to confine the flow of aqueous solutions to the hydrophilic pathways, thus creating a channel with "virtual" walls[14, 15]. Recently, a similar approach has been applied to paper-based microfluidics[16] demonstrating the possibility to make low-cost disposable paper chips for bioassays. The surface tension on the solid-liquid interface can be controlled by other means, such as thermal gradients and electrowetting techniques[2]. Overall, controlling the capillary forces and surface effects presents a useful way to drive and direct the flow in low-cost lab-on-a-chip systems.

1.3. Practical considerations

1.3.1. Microreactor materials

Microreactors are fabricated from various materials such as glass, silicon, ceramics and polymers[17]. Choosing the right material for a particular application is a very important step that determines the device performance because each material is suitable for a limited range of conditions and chemistries. Silicon-based microreactors are attractive due to their high thermal conductivity and resistance to high temperature and pressure. They are fabricated using wet etching, photolithography or deep reactive ion etching (DRIE) methods[17]. The latter method is capable of etching steep-sided structures, which are not achievable with other techniques. The disadvantages of silicon chips are their opacity, relatively high cost and sensitivity to alkali fluids.

Metal microreactors[18] are useful when the reactions are conducted at high temperatures and pressures. In addition, metal has excellent thermal conductivity. Microchannels in metal can be created using mechanical micro-machining and stamping[17].

Ceramics offer high thermal and chemical resistance. This material is a suitable alternative to metals when acidic fluids are used at high temperatures. However, creating micro-structured features in ceramics is costly and time-consuming. Although simpler processing methods have been developed[19], ceramic microreactors are rarely used.

Polydimethylsiloxane (PDMS) is the most popular material amongst polymers. Its main advantages are low cost and variable viscoelastic properties that allow it to be moulded and subsequently cured with heat. However, PDMS cannot withstand high temperatures and is incompatible with some organic solvents (alkylamines, hydrocarbons and others) that cause it to swell[20]. Therefore, PDMS chips have been used with aqueous systems, primarily in biomedical applications. Recently, Lee et al.[21] reported that that the swelling problem can be significantly reduced by modifying the inner surface of the microchannel with poly(urethaneacrylate).

Borosilicate glass and fused silica are two other materials that became very popular for manufacturing microreactors. Similar to PDMS, glass is cheap and relatively easy to process. The microchannel network is usually created on the glass surface using photolithography with subsequent wet etching or powder-blasting[22]. The etched glass plate is then thermally bonded with another plate to produce a chip with the designed channel network inside[23]. An important property of PDMS and glass microreactors that makes them unique among other materials is their transparency. This property makes them compatible with spectroscopic methods of analysis, which are helpful in many applications.

1.3.2. Fluid delivery methods

In order to operate a microreactor properly, it is essential to be able to control the flow rate in a precise and accurate manner. Reagents are delivered via narrow tubings that are tightly connected to the microreactor inlets. The tubings can be made of various materials, usually organic polymers and steel. Polyether ether ketone (PEEK) and teflon tubings are most popular due to their mechanical properties and chemical inertness.

There are two main methods to drive liquids in microchannels, hydrodynamic pumping and electroosmotic flow (EOF)[22]. Hydrodynamic, or pressure-driven fluid delivery, relies on external syringe pumps or pneumatic systems.

Electroosmotic flow is unique in several respects[22]. The equipment for its generation does not involve any moving parts and therefore the flow control unit can be easily miniaturised. In contrast to the hydrodynamic pumping, electroosmotic pumping gives a uniform flow profile across the channel similar to that shown in Figure 1.1b. The linear flow rate of an EOF-driven fluid (v) is determined by the following equation[24]:

$$v = -\frac{E\varepsilon\varepsilon_0\zeta}{\eta} \qquad (1.10)$$

where E is the electric field inside the channel (the applied voltage divided by the distance between the electrodes), ε is the relative dielectric constant of the liquid, ε_0

is the dielectric constant of free space, η is viscosity of the fluid and ζ is the zeta potential of the fluid/channel interface. The zeta potential is formed on the internal channel surface because of the partial ionisation of the immobile surface groups. In a glass channel, the surface usually has a negative charge that attracts cations from the solution to form a mobile diffuse layer surrounding the surface (Figure 1.3). For aqueous solutions in glass channels[24], the zeta potential varies from zero at pH 2 to -100 mV at pH 7. Formation of the diffuse layer enriched with cations creates deficiency of cations outside the diffuse layer. Therefore, when an electric field is applied along the channel, the excess of the anions inside the channels will drive the fluid towards the positively charged electrode. This explains why the flow rate profile in EOF-pumped fluids is uniform resembling that of turbulent fluids. It should be noted that within the thickness of the diffuse layer, the flow rate is not uniform (Figure 1.3). However, due to the small thickness of the diffuse layer (in the order of a few nm) this effect can be neglected.

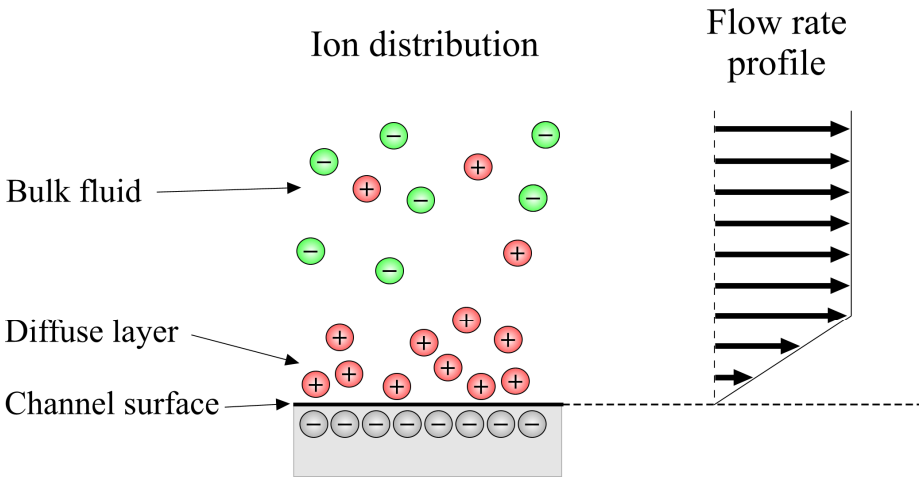

Figure 1.3. Distribution of ions and the flow rate profile across the channel in electroosmotic flow (adapted from [22]).

Electroosmotic pumping is attractive not only due to the simplicity of the flow control equipment, but also because electrokinetic control results in separation of molecules by charge and size, which can be useful for separation methods and chemical analysis[25]. The uniform flow profile reduces dispersion along the channel and therefore improves resolution. However, electroosmotic pumping is restricted to a small range of microreactor materials (glass and some polymers) and solvents that

can generate a zeta potential with the channel surface. In addition, the method is sensitive to the physiochemical properties of the fluid such as pH and ionic strength. Other limitations are the sensitivity to the presence of air bubbles and the inability to achieve high flow rates especially in relatively wide channels. In this respect, hydrodynamic pumping is advantageous and a more universal method.

Apart from hydrodynamic and electroosmotic pumping, it is worth mentioning a number of less popular methods of fluid delivery. Duffy et al.[25] developed a pump based on "centrifugal force" (inertia). They used a rotating circular disc with a series of radial microchannels. Upon disc rotation, the liquids stored near the disc centre are pumped through the channels towards the disc edge. By incorporating valves inside the channels, the authors were able to control the flow and carry out real-time analysis of multiple enzymatic assays in parallel.

A recent trend in fluid delivery methods is the development of microfabricated pumps that can be integrated into the channels. These systems can be actuated and controlled optically or by piezo-electric elements[26]. Optically actuated pumps consist of micro-particles assembled inside the microchannels. The pump action is provided using optical trapping and manipulating the particles with a laser beam. With optically-driven micro-pumps, a flow rate of up to several micrometres per second can be achieved[27].

Another method is based on the utilisation of capillary forces (see Section 1.2.3). This approach is associated with thin-layer chromatography (TLC) where the eluent propagates along the TLC plate due to capillary force. In microfluidic applications, capillary pumping is used in paper-based devices and in fuel cells[28].

1.3.3. Mixing

Due to the low Reynolds numbers in microchannels, mixing is primarily controlled by diffusion. As mentioned in Section 1.2.2, the time required for diffusive mixing depends on the size of the molecules or particles of which the mixing fluids are composed. For large molecules and relatively thick channels, diffusion can take a considerable amount of time compared to the characteristic time of the processes involved in the experiment. This effect presents a problem for synthetic and some

analytical applications of microreactors because slow diffusion prevents direct contact between the reacting molecules thus slowing down the whole process. To estimate the relative effect of diffusion on the reaction under study, the characteristic times of the reaction and diffusion should be compared. Based on this comparison, chemical process in microchannels can be reduced to three categories[29]: chemical, diffusional and mixed regimes.

The *chemical regime* is characterised by a relatively fast diffusive mixing compared to the reaction time. In this regime, the fluid becomes homogeneous before a considerable amount of the product is generated. Therefore, mixing can be assumed to be instantaneous. Examples of reaction-controlled processes include slow chemical reactions and reactions occurring in very narrow channels such that mixing distances are minimal. In the *diffusional regime*, the reaction is much faster than mixing, such that the rate of the whole process is independent on the reaction rate constant and is limited only by diffusion. Diffusion-controlled systems can be used to study mixing efficiency in microchannels by monitoring the product formation[30]. However, they are inefficient for synthetic purposes. The *mixed regime* represents a transitional class of microfluidic processes that exhibit comparable rates of diffusion and chemical reaction.

To maximise the speed and efficiency of microfluidic reactions and reduce the variable effect of diffusion, it is desirable to accelerate mixing, which can be achieved using one of two general strategies: (i) reduction of the channel dimensions to a scale where diffusive mixing is nearly instantaneous (a few micrometres or below); (ii) manipulating the flow in such a way as to maximise the contact area between the mixing fluids and minimise the diffusion distance.

The first approach is disadvantageous due to the lower throughput, increased pressure drop, and difficulties with controlling and analysing fluids on such a small scale. Therefore, the majority of methods to facilitate mixing are based on the second strategy that is realised by using specially designed sections in the flow path called micro-mixers. There are two types of micro-mixers that are based on passive and active mixing[31]. *Active mixers* rely on rotating elements that require external power to be actuated. For example, Lee at al.[32] utilised the controlled stirring of magnetic

micro-particles embedded into the channel. A mixing efficiency of 96% was achieved over a flow path of only 800 μm in less than a second. Development of more sophisticated active micro-mixers is driven by advances in nano-technology and micro-electromechanical systems (MEMS). In this context, it is appropriate to mention a recent study carried out by Al-Fandi et al.[33]. They tethered a living *E. coli* bacterium to the internal surface of a PDMS channel using a single flagellum. The rotation of the bacterium acted to mix the surrounding region, which was visualised by movements of 1 μm polystyrene beads suspended in the solution. This approach can be used in future to develop disposable bio-mixers.

At present, however, active mixing is often considered as a complicated approach. The preference is given to *passive mixers* that are attractive due to their simplicity and flexibility. Passive mixers contain no moving parts and operate by diverting some of the kinetic energy of the fluid into creating vortices and other perturbations in the flow that distort and elongate the interface between the liquids thus increasing its area. The simplest example of passive mixers is a curved capillary where the curvature of the trajectory causes the faster fluid elements in the channel centre to experience a greater centrifugal pull than other layers of the flow. As a result, a secondary flow appears that drives the fluid perpendicular to the main flow direction and therefore facilitates mixing (Figure 1.4).

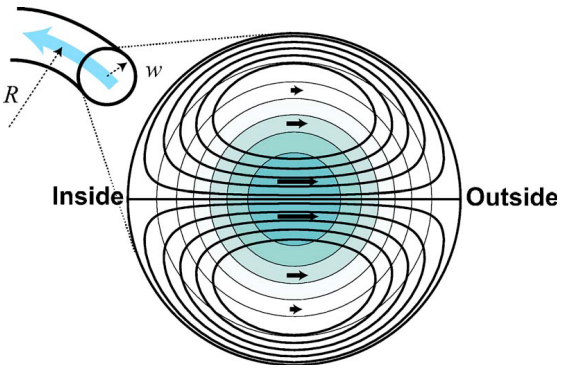

Figure 1.4. A secondary flow in a curved channel caused by the inertial effects (adapted from [2]).

The mixing effect of secondary flows can be enhanced by utilising chaotic advection, a phenomenon responsible for various flow perturbations observed inside microchannels with repeated barriers, grooves, twists and other geometrical features.

The majority of passive mixers available today rely on chaotic advection. For example, Liu et al.[31] developed a passive micro-mixer based on a three-dimensional twisted channel structure. The size of each twist was less than 1 mm. The authors demonstrated that the developed three-dimensional micro-mixer worked significantly better than a similar planar structure or a straight channel for Reynolds numbers from 6 to 70. More recently, Egawa et al.[34] reported the fabrication of a two-dimensional passive micro-mixer that consists of a simple T-junction followed by several alcoves arranged in a zigzag shape. The mixer occupies only 200 μm of the flow path and provides fast mixing of both high and low viscosity fluids.

Another method of passive mixing is based on geometric structures that cause repeated or simultaneous lamination of the flow that does not create significant flow perturbations but effectively increases the contact area between the fluids. This approach is particularly useful in channels with a relatively large diameter[8] (e.g. a few millimetres). A similar approach is used in micromixers based on hydrodynamic focusing[35], which relies on increasing the contact area between the mixing fluids by means of joining several flows in a narrow channel, similar to multi-lamination. The mixing times can be as low as 10 μs.

Microfluidic systems that involve the flow of droplets are unique due to the spatial confinement of the fluid within a droplet. It is important that chaotic mixing in droplets can be easily generated by driving them through twisted channels. The mixing times can be less than 2 ms[13].

An efficient passive micro-mixers was reported by Shastry et al.[36]. It consists of two axial glass capillaries, one inside the other, with a small platinum sphere at the tip of the inner capillary. A narrow gap (10 μm) between the sphere and the outer capillary causes significant acceleration of the flow making it turbulent in the ball proximity. The mixing time was determined to be as low as 15 μs in a channel with a diameter of 250 μm. Thanks to the existence of such mixers, accurate kinetic characterisation of very fast chemical reactions became possible (see Section 6.1.1).

In concluding this Section, it can be summarised that in order to determine whether the micro-mixer is required, the diffusion time should be compared with the reaction

time. All strategies of reducing the mixing time are based on assisting molecular diffusion. In all cases, even in turbulent flows, mixing ultimately occurs by diffusion, with micro-mixers only increasing the interface area and reducing the diffusion time. It is also important to note that integration of various micro-structures inside the channel increases the flow resistance and therefore the pressure required to pump the fluids. This should be taken into consideration when selecting a micro-mixer.

1.4. Overview of applications

Microfluidic devices are used in a wide range of applications including studies of rheology[37], phase transitions[38], surface effects[39], chemical analysis[1] and synthesis[40], to name just a few. For the purposes of this thesis, only the main trends in chemical analysis and chemical synthesis will be reviewed in this Section. The majority of other applications are related to fundamental studies wherein the use of microfluidic chips allows the experiments to be performed in unique or more convenient conditions.

1.4.1. Chemical analysis and medical diagnostics

Analytical chemistry has gained considerable benefits from microfluidic technology such as minimisation of the sample amount, automated sample preparation and analyte separation, significant reduction of the analysis time and cost, extended functionality of the sensors, high-throughput analysis and massive parallelisation due to compactness and integration of various micro-machined components in a single chip. The importance of these benefits is difficult to overestimate because not only they change many traditional practices in analytical chemistry but also they open new opportunities to promote discoveries in biochemical sciences and revolutionise some aspects of public life, particularly health care.

Polymerase chain reaction (PCR) is a method of amplifying DNA prior to analysis in order to improve the detection limit. The amplification of a small number of the DNA copies in a sample is realised by means of thermal cycling, upon which repeated enzymatic replication of the DNA takes place doubling its amount in the sample after each cycle. PCA was among the first analytical techniques to be implemented in microfluidic chips[41]. The use of microfluidics reduces the cycle time

due to the efficient thermal control in microchannels. The process is particularly convenient in continuous flow where instead of repeated heating and cooling of the stationary sample, it flows in a serpentine through regions of different temperatures. Recent developments in microfluidic PCR allowed several samples to be amplified simultaneously[42].

Cell manipulation and analysis. Microfluidics offer a convenient way to transport, manipulate, count and analyse cells, which is a subject of flow cytometry. Using optical trapping allows continuous observation and analysis of individual cells[43]. Various methods have been developed for differentiating and analysing cells in microchannels. Blood analysis is an example of high practical significance. Microfluidic biosensors are capable of sorting different blood cells, detect pathogens such as hepatitis C virus and syphilis[5], and determine other parameters for health monitoring.

Environmental analysis. Rapid monitoring of trace levels of various pollutants in water, food and air using microfluidic technology has been demonstrated by several researchers[1]. Examples include ultratrace monitoring of ammonia for semiconductor manufacture, nitrogen dioxide in air[44], nitrites and pesticides in food products and the environment[45, 46], and selective sensing of lead ions in water[47].

Optofluidics. Optical detection is one of the most powerful and convenient techniques of microfluidic analysis. One of the main challenges is to miniaturise spectroscopic and optical components of the detection system to make the whole sensor more compact and reliable. Several researchers achieved this by integrating some or all optical components on the microfluidic device[26]. The interest in this approach has been steadily increasing over the last few years and resulted in the emergence of a separate class of devices called optofluidics[48, 49]. Optofluidic chips contain integrated optical components such as lenses, waveguides, lasers and detectors. Apart from the compactness intrinsic to optofluidic devices, they offer additional benefits due to a more robust optical interface between the sample and the measurement system improving reproducibility of analyses and minimising sampling-related errors.

Paper-based diagnostic devices. Recently, an increasing interest has been focused on developing diagnostic devices that can be printed on sheets of ordinary paper using standard inkjet printers. The ink in the cartridges can be replaced by wax or other hydrophobic compounds that serve to confine an aqueous sample within pre-defined fluidic paths. The printing process takes a few seconds and costs less than a penny[50]. The reagents (such as antibodies) can be printed in a similar manner offering opportunities for new applications such as disposable test kits for medical diagnostics and quality control[51]. For example, Abe et al.[52] demonstrated an inkjet-printed immunosensing microfluidic device that can detect 10 μg/l of immunoglobulin G in 20 min. In another study, Hossain et al.[53] reported a paper-based sensor for colorimetric detection of organophosphate pesticides that are illegally used in some countries. The achieved detection limits were in the range of a few nM with the analysis time of just 5 min. that allows direct detection of pesticides in food products.

The focus has been on test kits based on colour-change reactions that do not require any equipment to read and interpret the results. However, devices relying on some analytical equipment are also considered. Thus, Dungchai and co-workers[54] fabricated micro-electrodes on a paper-based microfluidic device and utilised chronoamperometry to demonstrate enzymatic detection of glucose, lactate and uric acid in biological samples. Another example is an electrochemical microfluidic sensor for monitoring glucose concentration in blood that is widely used today in diabetes management[55].

1.4.2. Chemical synthesis

Library synthesis. Library synthesis in microreactors has numerous advantages over traditional batch reactors, enabling reduced synthesis times, much lower consumption of chemicals and a significantly higher throughput due to the ease of parallelisation. Integration of such systems with non-contact or in-line sensors and the use of feedback loops can offer a way to create highly automated “smart” microreactors. Recently, Wang et al.[56] made a compact microfluidic device, in which more than 1000 chemical reactions can be performed simultaneously. The device integrates sample preparation, the reaction step and analysis by mass spectrometry. This approach has a potential to revolutionise the process of library synthesis and can

speed up the discovery of new drugs such as enzyme inhibitors for treating various diseases including cancer[57].

Small scale manufacture. Using continuous flow microreactors to perform chemical synthesis at the laboratory scale often leads to improved selectivity and yields. In addition, due to efficient heat and mass transport, the reactions can be carried out faster and under more benign conditions compared with conventional large scale batch reactors[8]. Various homo- and heterogeneous reactions have been successfully performed in the laboratory[58-60], including reactions at super-critical conditions[61] and direct fluorination that is difficult to perform in batch reactors[7]. Catalytic reactions can be performed by immobilising the catalyst on the channel wall or on the surface of packed beads[59]. This approach is popular in biochemistry because enzyme immobilisation helps reduce its consumption and carry out multi-step processes on a single chip[62].

The use of microreactors is advantageous not only in the laboratory but also for small scale production. Roberge et al.[63] analysed reactions in the fine chemical and pharmaceutical industry and concluded that 50% of them would benefit from using a continuous flow process based on microreactor technology. The financial benefits for small scale production companies come mainly from the high speed and low cost of the process development stage that can be achieved by using microreactors. The main problem is that many processes in pharmaceutical and other industries involve solid reagents that cannot be used in microfluidic systems.

Large-scale manufacture. For large scale productions, the main motivations are maximising yield, enhancing safety and reducing scale-up issues[63]. Microreactor technology can meet these requirements. The most interesting question is how the production can be scaled up. In traditional batch synthesis, scaling up is realised by increasing the reactor size that often necessitates an additional time-consuming and expensive optimisation step because the changes in geometry, mixing and heat transfer efficiency often result in different performance than that achieved at the stage of process development. By using microreactors, it is possible to increase the production scale by using several reactors in parallel scaling out production instead of scaling up. With the scale-out approach, process development is carried out on a

single microreactor chip in the laboratory environment. After the process development phase is complete, the desired throughput is achieved by increasing the number of microreactors. In this case, the critical process parameters remain constant and the risk of different performance after scaling out is greatly reduced. The production scale can be controlled according to variations in demand by changing the number of active microreactors. With modern technologies it is possible to achieve throughput of several tonnes per year[64]. A few dozen pilot plants based on microreactors already exist[65], with several large companies such as BASF, Dupont, Merck and Bayer involved in the use of microreactor technology[23]. However, the scale-out approach has several challenges[7]. One of them is the requirement to provide identical flow rates and other conditions in all parallel units. Other problems are the difficulties of controlling the production process at each microreactor unit simultaneously and detecting possible faults in the system.

Multi-step synthesis. Organic synthesis often involves several steps carried out in different conditions between which the products usually need to be separated, purified and transferred to another reaction vessel where the next synthetic step is performed. To save time and minimise cost of the final product, it is desirable to carry out several reaction steps in a single vessel. This strategy is easier to implement using continuous flow processes and microreactor technology. However, sequential synthetic procedures often require solvent change or the use of solid catalysts or chemicals. The necessity to perform these procedures complicates the development of multi-step continuous flow synthesis on a single chip. A significant turning point was the use of reagents and catalysts immobilised on the channel walls or on the surfaces of micro-beds tightly packed in dedicated regions of the flow path.

In one study, Lee et al.[66] synthesised ^{18}F-labeled fluorodeoxyglucose in five sequential steps including pre-concentration, water evaporation, fluorination, solvent exchange and hydrolytic deprotection. More recently, Baxendale et al.[67] reported the multi-step microfluidic synthesis of a natural alkaloid oxomaritidine with a purity of more than 90%. In another study, Tokeshi et al.[68] demonstrated the possibility to perform complicated chemical processing steps including solvent extraction, operation in a multiphase flow network and purification. Although their work

involved analysis of metal ions rather then synthesis, the demonstrated procedures can be useful for multi-stage reactions. These and other examples[69] demonstrated the feasibility of multi-step continuous flow synthesis despite the difficulties associated with the necessity to change the conditions of the reaction.

Process analysis in microreactors. The necessity to develop sensitive detection techniques to analyse and control microfluidic reactions in real time is well understood in the scientific community[70]. However, this area is still at the early stage of development, with off-line detection being the dominant way of extracting analytical information from microreactor channels. It is important to note that the advances in integrated detection systems discussed in Section 1.4.1 have only a little influence on the development of process analysis for microfluidic synthesis. The reason for this is that microfluidic chips for chemical sensing are configured specifically to facilitate detection, whereas the design of microreactors is defined by the process requirements rather than by the needs of an analytical method employed to control or analyse the process. Therefore, the detection methods for process analysis must be optimised so that they are readily compatible with microreactors. This issue makes on-chip process analysis a challenging subject.

In concluding this Chapter, it is noteworthy to mention a recent study reported by McMullen and co-workers[71], in which the benefits of using process control equipment with microreactors is best demonstrated. The authors developed a fully automated self-optimising microreactor system that measures the product yield by HPLC and feeds this information to the optimisation programme that finds the optimal conditions for the reaction in several steps. The performance of this system was demonstrated on a widely used Heck reaction. The optimal conditions were found after 19 automated experiments that took only two days without any manual work.

1.5. Research objectives

Could the performance of the self-optimising system described above be improved further if a real-time non-invasive method was used for rapid collection of analytical information along with, or instead of, HPLC?

The specific goals of this research are:

- Investigate the applicability of Raman spectroscopy for real-time non-invasive analysis of chemical processess in microreactors;
- Develop a dedicated optical interface with the microreactor for maximising the Raman signal obtained;
- Explore opportunities for improving the existing methodology of process optimisation and kinetic studies in microreactors.

The next two Chapters will focus on the theoretical and practical aspects of Raman spectroscopy.

2. Raman Spectroscopy

2.1. Discovery and theory of Raman scattering

2.1.1. The Raman effect

Rayleigh scattering of light is a well-known phenomenon, which is the cause of the blue colour of the sky and reddening of the sun at sunset. Rayleigh scattering is the elastic scattering of light quanta from molecules or small particles, where the particle size is much less than the wavelength. Most of the scattered light consists of the Rayleigh component. It was not known until 1928 that a very small fraction of incident photons undergoes energy exchange with vibrational-rotational states of scattering molecules resulting in scattering at shifted wavelengths. This effect was first reported and explained in 1928 independently by the Indian physicist C.V. Raman with his student K.S. Krishnan and the Russians L.I. Mandelstam and G.S. Landsberg[72]. The theoretical basis for inelastic light scattering was provided in 1923 by an Austrian physicist A. Smekal and further developed by H.A. Kramers and W. Heisenberg[73]. Despite involvement of several scientists, this discovery was officially attributed to C.V. Raman and the effect was named after him. Meanwhile, many Russian, Austrian and German scientists felt that the credit should be shared and did not use the term "Raman scattering" for a long time. Even today it is referred to as "combination scattering" in all Russian textbooks and papers.

The discovery of the Raman effect was of high importance. Raman Spectroscopy became a new way (apart from infrared absorption) to obtain information about the structure and properties of molecules and later turned into a powerful tool for non-invasive chemical analysis. Professor Raman was awarded with the Nobel Prize for Physics in 1930 for his discovery.

In order to resolve the structure of Raman spectra, a very narrow-band excitation light source is needed. Raman and Krishnan used a combination of a mercury lamp and optical filters to select a line from the emission spectrum of mercury. Nowadays lasers are used (see Section 3.3). The schematic diagram explaining the Raman effect is shown in Figure 2.1. Laser light excites a molecule to a "virtual state" that does

not necessarily correspond to any fundamental state of the molecule. Scattered light consists mostly of the Rayleigh component that is shown with thick arrows on the diagram. Raman scattering can occur with either lower frequencies (Stokes scatter) or higher frequencies (anti-Stokes scatter). Since anti-Stokes scattering events require the molecule to be initially in an excited vibrational state, most of which are scarcely populated at room temperature, the intensity of anti-Stokes bands are normally much weaker than that of Stokes bands. However, the intensities of Stokes and anti-Stokes bands in rotational Raman spectra of gases are more similar due to lower energies of the excited rotational states.

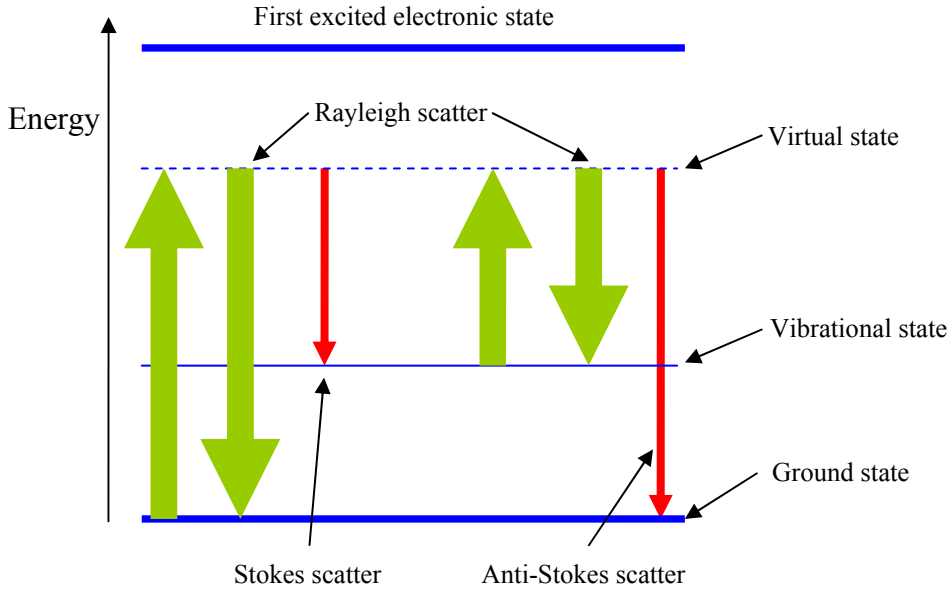

Figure 2.1. Energy diagram for Rayleigh and Raman scattering.

Raman spectra are plotted as the intensity of scattered light versus the Raman shift, which is usually expressed in wavenumbers (inverse centimetres) and is calculated by equation (2.1):

$$RS = \frac{10^7}{\lambda_{exc}} - \frac{10^7}{\lambda_{Raman}} = \frac{\lambda_{Raman} - \lambda_{exc}}{\lambda_{Raman} \cdot \lambda_{exc}} \cdot 10^7 \qquad (2.1)$$

λ_{ex} and λ_{Raman} are the wavelengths of the excitation and scattered light respectively in nanometres and 10^7 is a conversion factor from nm^{-1} to cm^{-1}.

2.1.2. Selection rules and intensity of the Raman signal

Although a quantum-mechanical approach[74-76] is preferable for careful analysis of Raman scattering, a classical treatment is more illustrative for general description of the theory and results in the same basic conclusions[77, 78].

Light induces local periodic fluctuation of the electric field *E*:

$$E = E_0 \cos 2\pi \nu_0 t \tag{2.2}$$

Here E_0 is the amplitude of the electric field, ν_0 is the laser frequency and *t* the time. These fluctuations induce a dipole moment *P* in the molecule:

$$P = \alpha E = \alpha E_0 \cos 2\pi \nu_0 t \tag{2.3}$$

where α is polarizability. In simple words, polarizability can be explained as a tendency to charge redistribution in electronic orbitals. As will be shown below only those molecular vibrations which cause a polarizability change yield Raman scattering. Vibrations are expressed analytically as a periodic nuclear displacement *q* with frequency ν_i:

$$q_i = q_{i0} \cos 2\pi \nu_i t \tag{2.4}$$

Expressing polarizability modulation by vibrations as a Taylor series and assuming that the vibration amplitude is small, the resulting series can be represented by a linear function:

$$\alpha = \alpha_0 + \left(\frac{\partial \alpha}{\partial q_i} \right)_0 q_i \tag{2.5}$$

Combination of equations (2.3) - (2.5) and subsequent trigonometrical transformation result in the following expression:

$$P = \alpha_0 E_0 \cos 2\pi \nu_0 t + \frac{E_0 q_{i0}}{2} \left(\frac{\partial \alpha}{\partial q_i} \right)_0 \cos 2\pi (\nu_0 + \nu_i) t + \frac{E_0 q_{i0}}{2} \left(\frac{\partial \alpha}{\partial q_i} \right)_0 \cos 2\pi (\nu_0 - \nu_i) t \tag{2.6}$$

Electronic oscillation (oscillation of an induced dipole moment *P*) triggers radiation which is actually scattered light. Equation (2.6) illustrates that electrons can oscillate at Stokes $(\nu_0 - \nu_i)$ and Anti-Stokes $(\nu_0 + \nu_i)$ frequencies only if molecular vibrations cause a change in polarizability ($\partial\alpha / \partial q_i \neq 0$). The value of $\partial\alpha / \partial q_i$ defines a fundamental molecular characteristic related to the intensity of the q_i-vibration in its Raman spectrum. This characteristic is called the Raman cross section (σ). The magnitude of σ varies for different classes of substances and types of vibrations.

The Rayleigh theory of scattering states that the intensity of the scattered wave is proportional to the intensity of incident radiation I_{exc} and to the fourth power of its frequency[79]. Since all three components in equation (2.6) – Rayleigh, Stokes and anti-Stokes – are linear with E_0 and are expressed in the same form, it is obvious that the observed intensity of Raman scattering I_R depends on I_{exc} and ν_R in the same fashion as does the intensity of Rayleigh scattered light:

$$I_{\mathrm{R}} = k\sigma I_{\mathrm{exc}} \nu_{\mathrm{R}}^4 \qquad (2.7)$$

where ν_R is the frequency of Raman photons, and k is a parameter reflecting signal collection efficiency and losses. Equation (2.7) shows a strong dependence of the Raman signal intensity on the laser wavelength.

2.1.3. Raman scattering and infrared absorption

Raman spectroscopy is a complementary technique to mid-infrared (MIR) absorption spectroscopy. Both methods probe fundamental molecular vibrations, but the mechanism of obtaining this information differs greatly for the two methods. Quantum mechanics establishes different selection rules for the excitation of molecular vibrations by absorption and scattering. As mentioned above, Raman scattering requires a change in polarizability, whilst infrared absorption can only occur if the vibration causes a change in dipole moment[77]. Therefore, MIR and Raman spectra look different and the two techniques are complementary. However, Raman spectroscopy has a number of advantages over MIR absorption[77, 80]. Firstly,

Raman measurements can be done remotely with a non-contact probe whilst MIR probes require contact with the sample. Secondly, water strongly absorbs in the MIR region and poses a problem for absorption measurements. In contrast, Raman spectroscopy is compatible with water solutions as water is a very poor Raman scatterer. Thirdly, a wide range of wavelengths can be used as an excitation source in Raman measurements, from UV to NIR. This fact makes Raman instruments compatible with cheap, compact and efficient silicon CCD detectors, except for the spectrometers equiped with lasers in the NIR spectral range that require other detectors. Moreover, visible and NIR light is efficiently transmitted by simple silica fibres whereas ATR-probes for MIR absorption require expensive optical elements that transmit in the MIR region. Furthermore, there are a number of sensitive resonance and non-linear Raman techniques such as coherent anti-Stokes Raman spectroscopy[81] or surface-enhanced Raman spectroscopy[82] that play an important role in modern analytical practice.

2.2. Sensitivity, spectral background and noise

2.2.1. Increasing intensity of the Raman signal

Although Raman spectroscopy is a powerful analytical method, the probability of Raman scattering is extremely low. In typical experimental situations, only 1 in 10^{10} incident photons undergo Raman scattering[77]. Therefore, the sensitivity of Raman spectroscopy is relatively low.

According to equation (2.7), there are four ways to enhance the Raman signal:

(i) increase the laser intensity I_{exc};

(ii) reduce the excitation wavelength (increase ν_R);

(iii) improve the throughput and collection efficiency (parameter *k*);

(iv) increase the Raman cross section σ;

Increasing laser power. High power radiation can be suitable for a limited range of samples that do not absorb the excitation light. It might be especially useful for analysis of gases and liquids in flow cells, where absorption effects are minimised

and intracavity illumination can be implemented (see Section 4.1). In other situations, there is a greater risk of sample damage due to the presence of absorbing impurities in the sample. The risk can be reduced by expanding the illuminated spot size, thus decreasing power density on the sample. However, signal collection optics need to be optimised for large laser spot size. Typically, commercial Raman instruments are equipped with laser sources with output powers of 50 - 500 mW or more depending on the wavelength and application.

Reducing laser wavelength. As Raman intensity is proportional to the fourth power of the scattered frequency, reducing the excitation wavelength seems an effective method to improve the Raman signal. However, the extent to which a reduction in the laser wavelength can be useful is limited by the possible occurrence of fluorescence. Short wavelength photons (UV and visible region) often have enough energy to induce electronic excitation in the molecule (see Figure 2.1), which can result in emission of fluorescence photons. Fluorescence has a much higher cross section than Raman scattering and appears as an intense and broad background on the Raman spectrum. It reduces the signal-to-noise ratio and can completely obscure the Raman signal. Even when the analyte does not fluoresce, minor impurities can significantly reduce the spectral quality. Therefore, Raman systems with red or near infra-red lasers tend to be preferred despite the fact that they provide much lower intensity than lasers in the UV or visible wavelength range. However, there are a number of approaches to eliminating fluorescence interference that are discussed in Section 2.2.3.

Improving collection efficiency. Improving throughput and signal collection efficiency has been a subject of research for many years and has led to significant improvements in sampling methodology and design of Raman instrumentation. When a sample is illuminated with the laser beam, scattered photons propagate to all directions posing a challenge to collect them efficiently in a convenient way. The advent of Fourier transform spectrographs and high-throughput multichannel dispersive spectrometers have had an important impact on the development of Raman spectroscopy. Among other achievements in this field are the development of

efficient detectors and fibre-optic probes. Various sampling techniques allowing substantial enhancement of the Raman signal are mentioned in Section 2.3.

Increasing Raman cross section. The Raman intensity can be enhanced under specific conditions where the magnitude of the Raman cross section becomes several orders of magnitude higher compared to analysis under normal conditions. One of the methods where these conditions are realised is called resonance-enhanced Raman spectroscopy[83]. Resonant enhancement occurs when the energy of excitation photons approaches that of an electronic transition. The typical enhancement factor is 10^2 - 10^4. However, the resonant transition is not sharp and a 5 to 10-fold signal increase is observed when the excitation wavelength is a few hundreds of wave numbers below the energy of electronic transition. Relative peak intensities in resonance Raman spectra differ from those in conventional spectra of a sample, with only selected vibrations being amplified.

Another type of enhancement occurs when molecules are absorbed on rough metal surfaces or, more commonly nowadays, metal nanoparticles. The enhancement factor can be very high – up to 10^{13} or greater[84, 85]. Methods based on this technique are surface-enhanced Raman spectroscopy (SERS) and surface-enhanced resonance Raman spectroscopy (SERRS). The latter combines the advantages of surface enhancement and the choice of a resonant excitation wavelength[86]. Thousands of papers devoted to SERS have been published so far and the interest in this field does not go down. The enhancement mechanism is still a matter of debate but two processes have been proposed: electric field enhancement near the rough metal surface (localized surface plasmons) and chemical enhancement, which results from formation of charge-transfer complexes[77]. Due to the complicated nature of enhancement, it is not easily achievable and there is no "universal" type of surface. In addition, reproducible quantitative analysis by SERS is often difficult.

Non-linear Raman spectroscopy is another group of Raman techniques that exhibit increased sensitivity. These methods have different selection rules making up a separate part of spectroscopy and will not be discussed here in detail. The theory of nonlinear scattering is based on third-order nonlinearity in the expression for induced dipole moment (2.3):

$$P = \alpha E + \frac{1}{2}\beta E^2 + \frac{1}{6}\gamma E^3 + \ldots \quad (2.8)$$

The contribution of non-linear components becomes significant only where high-power pulsed lasers are used[87]. Extreme excitation conditions induce a number of specific effects such as the hyper-Raman effect, and stimulated and coherent scattering. These methods are often used for analysis of gases due to their high resolution and sensitivity[88]. Among non-linear Raman methods are coherent anti-Stokes Raman spectroscopy (CARS), hyper-Raman spectroscopy, inverse Raman spectroscopy (IRS), stimulated Raman gain spectroscopy (SRGS) and photoacoustic Raman spectroscopy (PARS)[78, 87].

The main conclusions concerning methods to increase Raman sensitivity are summarized in Table 2.1.

Table 2.1. Methods of increasing the weak Raman signal.

Action	Problems	Results
Increasing laser power	• Sample damage • Compromised safety • Reduced spectral quality of high-power lasers	• Typical power on sample 50-500 mW
Decreasing excitation wavelength	• Fluorescence	• Red and infra-red lasers are preferred
Increasing throughput	• Impossible to collect all Raman photons	• FT-Raman • High-throughput spectrometers • Multiplexing • Efficient fibre-optic probes • Special sampling techniques
Resonance Raman spectroscopy	• Tunable lasers and special optics needed • fluorescence	• Instrumentation is configured for specific analyte
Surface-enhanced Raman spectroscopy	• Invasive • Complicated sample preparation • Low reproducibility	• Sample preparation procedure is designed for each sample type
Non-linear methods	• Expensive • Bulky and complex instrumentation • Limited range of samples	• Used in a limited number of applications

2.2.2. Noise in Raman spectroscopy

In Raman spectroscopy as well as in all other physical methods of analysis, the analytical signal is corrupted by noise that limits the reproducibility of measurements and the detection limit. The level of noise is usually compared with the analytical signal in the form of the signal-to-noise ratio (SNR)[77]:

$$SNR = \frac{I_R}{s} \tag{2.9}$$

where I_R is the intensity of the Raman peak and s is the standard deviation of the peak intensity. The detection limit is defined as the minimal signal that can be clearly distinguished on a noisy background. It is generally accepted that the detection limit corresponds to $\mathrm{SNR} = 3$.

Sometimes SNR is calculated using the standard deviation of the background intensity instead of that of the peak intensity. This method is simpler because background noise is independent of the analyte content and can be determined without taking many consecutive measurements of the sample. However, the standard deviation of the peak is usually greater than that of the background (because of shot noise). Therefore, using background noise for estimation of the SNR is generally incorrect and causes overestimated results. This method can only be useful for detection limit calculations when the signal intensity is low or at least comparable to the background intensity.

Generally, there are two types of noise: random and fixed-pattern. While random noise can be reduced by increasing the overall acquisition time, fixed-pattern noise cannot. Fixed-pattern noise is usually caused by incorrect instrument calibration or an offset on the response function. It is of interest for later discussion to review the major sources of random noise in spectroscopy.

Shot noise is a fundamental source of noise in spectroscopy. It is a direct consequence of the statistical nature of light. The greater the number of photons in a beam the greater the uncertainty of its accurate detection. Mathematically, it is regarded as counting random events. This process is governed by Poisson statistics

where the standard deviation of the number of counted random events is equal to the square root of the number of the events. Thus, provided that sensitivity of a spectrometer is shot noise limited, the standard deviation of the Raman signal can not be less than $\sqrt{I_R}$:

$$SNR \leq \frac{I_R}{\sigma} = \frac{I_R}{\sqrt{I_R}} = \sqrt{I_R} \qquad (2.10)$$

As I_R is proportional to the signal acquisition time (t), the SNR is proportional to the square root of t. Shot noise is the main reason why any high background on the spectra (for example from fluorescence) is detrimental for Raman spectroscopy. While the background can be subtracted from spectra, its noise cannot[80].

Dark noise is caused by a signal spontaneously generated by the detector due to thermal processes such as spontaneous photoemission or charge/electron generation. These effects are effectively reduced by cooling the detector. For example, for CCD detectors the dark current halves for every 7 - 8°C decrease in temperature.

Readout noise originates in electronics that process the primary signal from a detector and converts it to a readable form – a digital or analogue value. Readout noise is independent on the signal value or integration time. For instruments with high readout noise, it is advantageous to split the experiment time into several equal spans and then average the collected spectra. In this case, the readout noise is reduced by the factor of the square root of the number of averaged spectra[89]. The readout noise of modern detectors such as CCD arrays is negligible so this procedure is of little benefit (it neither increases nor decreases SNR).

Other sources of noise in Raman spectroscopy include flicker noise, which is attributed to laser power fluctuation, and the noise caused by variations in sample position relative to the Raman probe. Modern lasers can be very stable, and flicker noise is usually negligibly low. However, variations in the sample position can cause substantial changes in the Raman spectra obtained.

2.2.3. Methods of fluorescence rejection

As mentioned above, fluorescence is a fundamental problem that deteriorates the quality of Raman spectra by causing a broadband background thus reducing the signal-to-noise ratio. Fluorescence can come not only from the analyte but also from trace-level contaminants. There are a number of ways to reduce or eliminate the effect of fluorescence. One method is based on using lasers with longer wavelengths (in the red and near-infrared regions). The energy of near-infrared photons is not sufficient to cause electronic excitation of most substances. Therefore, fluorescence does not occur. However, there are two problems associated with this approach. The first one is fundamental – the probability of scattering decreases with higher wavelengths (i.e. lower frequency) according to equation (2.7). The second problem is technical and is related to the necessity of using detectors that need to be cooled to reduce the dark current signal. In addition, using longer wavelengths results in reduced spatial resolution due to the fundamental resolution limit defined by the diffraction of light.

The interference between fluorescence and Raman photons can be eliminated by shifting the excitation wavelength to the deep ultraviolet. Although UV photons cause many substances to fluoresce, most emission occurs at wavelengths of 260 nm or longer[90]. In other words, 260 nm corresponds to the photon energy that is sufficiently high to excite nearly all molecules to their higher electronic states. At 260 nm, the region of useful Raman shifts is about 20 nm wide. Therefore, using lasers operating at 240 nm and below is an excellent way to obtain fluorescence-free Raman spectra. Fluorescence will be present but will not interfere with the Raman spectra. Suitable detectors for this wavelength range already exist[89], and the Raman cross section is much higher in the UV region compared to NIR. Unfortunately, the use of this method is hampered by the high cost and complexity of UV lasers.

An alternative to changing the excitation wavelength is the use of time discrimination between scattering and fluorescence events in a pulsed excitation mode. While scattering is an almost instantaneous event, fluorescence occurs after a few nanoseconds[91, 92]. To take advantage of this difference, pulsed picosecond lasers and gated detection equipment are needed so that light is allowed to hit the detector

only within a short time window after the pulse. Such gated systems can operate at the frequencies of several MHz providing efficient signal collection. Time-resolved Raman spectroscopy is also limited by the high cost and complexity of the equipment.

These are the main methods to address fluorescence interference. Among others is the use of anti-Stokes Raman spectra that are free from fluorescence. Anti-Stokes bands are probed by non-linear Raman methods such as CARS[78]. Fluorescence can also be suppressed to some extent by means of specific sampling or signal collection techniques that are described below.

2.3. Sampling and signal collection

2.3.1. Sampling geometry

Since scattering is a two-photon process, various optical geometries for illumination and signal collection are possible. In general, these possibilities are divided into three groups according to the relative position of the excitation and collection beams: back-scattering, transmission and 90° configurations (Figure 2.2). The latter two configurations are less common and were not used in the project, and so will be discussed here only briefly.

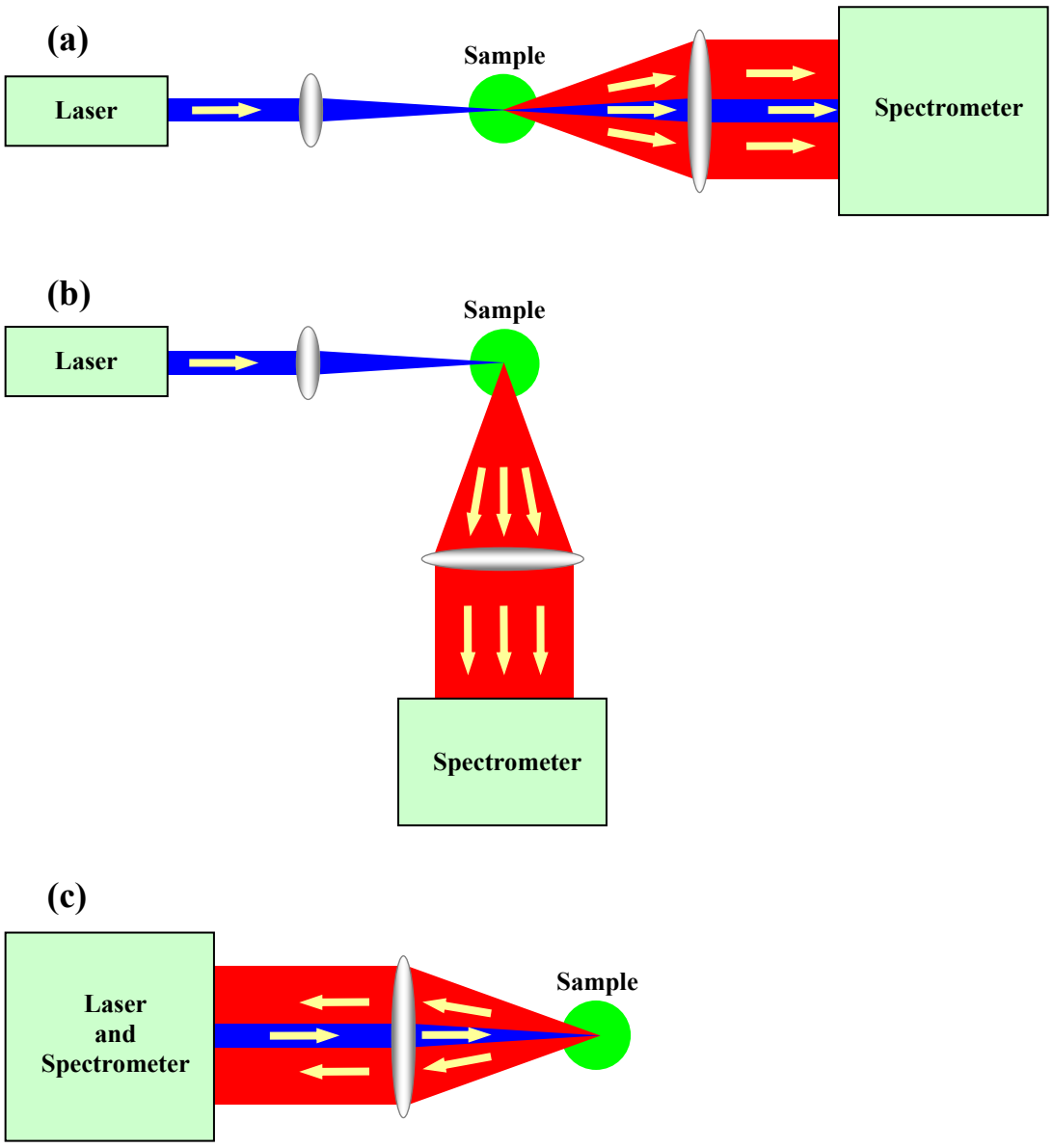

Figure 2.2. Sampling configurations in Raman spectroscopy: (a) – transmission; (b) – 90° configuration; (c) – back-scattering.

In the transmission geometry, a sample is illuminated from one side and the Raman signal is collected from the other. In the case of highly transmitting samples a problem arises from the necessity of filtering the extremely strong laser light which passes through the sample and hits the detector together with the Raman scattered photons. If a sample strongly absorbs the laser light, signal collection is inefficient or impossible. The only situation where the transmission geometry can be successfully applied is analysis of diffusely scattering samples: colloids, tablets, biological

samples etc. For biological samples transmission Raman microscopes are very common. Application of transmission Raman spectroscopy for analysis of diffusely scattering media is discussed below in this Section.

The 90° collection geometry is probably the simplest way to organize a Raman experiment. The collection and excitation optics are spatially separated which is convenient in terms of instrument simplicity. Therefore, historically, this layout was common[77]. However, the 90° configuration has two disadvantages that make it uncompetitive compared to back-scattering instruments. The first disadvantage is the low flexibility and high sensitivity to the refractive index of the analysed sample. For optimum performance, the excitation and collection beams must be crossed in their focal points inside a sample. Once aligned for one sample the instrument will not have the same efficiency for another sample of a different type because the crossing condition is disturbed by refractive index variations. This fact makes the 90° configuration applicable only for analysis of gases. Another disadvantage is the generally poor collection efficiency.

Most modern Raman instruments are based on the back-scattering configuration where the illumination and collection optics are shared and the two beams are combined. A great number of methods have been devised to combine the two beams[77, 93]; the main procedures will be described later in this Section.

2.3.2. Fibre-optic probes

Optical fibres have played a crucial role in the development of analytical spectroscopic techniques[94] and Raman spectroscopy is no exception. At present, most if not all Raman instruments use fibres to deliver the excitation beam to a sample as well as to collect the signal. Fibre coupling allows the sampling compartment to be spatially separated from the spectrometer, which significantly simplifies the analysis, and increases instrument flexibility and throughput. Both *in situ* and remote analysis without sample preparation have become possible. Before discussing different fibre-optic sampling techniques, a brief description of optical fibres is necessary.

An optical fibre consists of a long glass cylinder (core) with refractive index n_1 and surrounding cladding with refractive index n_2. The materials are chosen to suit the condition $n_1 > n_2$. Light entering the fibre at incident angle α is refracted and travels further along the fibre core at angle β defined by the equation for the law of refraction:

$$\sin\beta = \frac{\sin\alpha}{n_1} \qquad (2.11)$$

If the condition for total reflection at the core-cladding interface is met (equation 2.12) the beam will be transmitted through the fibre by means of multiple total reflections.

$$\cos\beta \geq \frac{n_2}{n_1} \qquad (2.12)$$

Transmission losses may only be caused by absorption or scattering processes, which are negligible in case of visible/NIR light and silica fibres. In Figure 2.3 a cross section of the described optical fibre is shown.

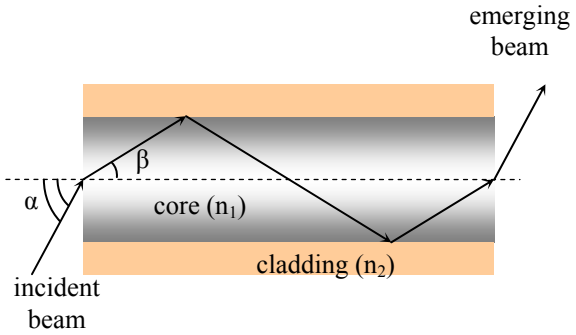

Figure 2.3. A schematic cross section of a step-index optical fibre.

Many types of fibre-optic Raman probes have been reported[95]. They are different in their design, sensitivity, probing distance, and size. All of them are optimal for a particular application. A good comparative analysis of different fibre-optic probes was published in 1996[96, 97]. Raman probes can be divided into two major groups: filtered and unfiltered probes. The latter group is more plentiful and comprises various designs (Figure 2.4).

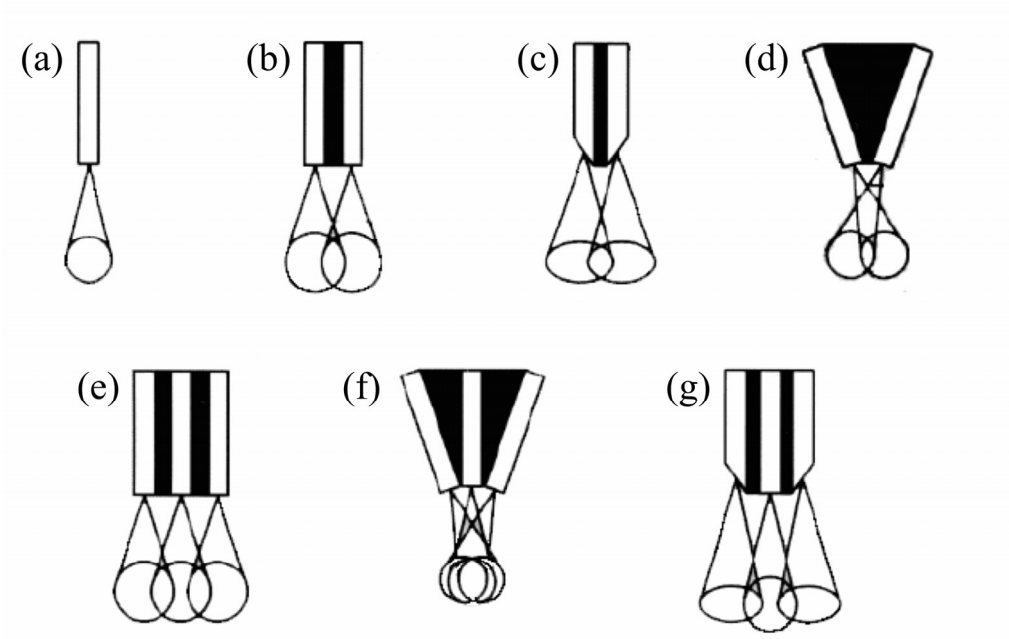

Figure 2.4. Unfiltered Raman probes (adapted from [95]). (a) unfocused bi-directional probe; (b) 1-in/1-out traditional design; (c) 1-in/1-out McLachlan design; (d) q-in/1-out chisel-tip design; (e) 6-around-1 traditional probe; (f) 6-around-1 McLachlan design; (g) 6-around-1 chisel-tip design.

Most unfiltered probes have one excitation fibre and several collection fibres around it ("*n* around one" probe). In order to collect a spectrum, a sample should be located close to the probe tip. No additional optics are needed, which makes these probes incredibly compact, simple and cheap. However, the quality of Raman spectra is degraded by background generated inside the silica fibres. Unlike crystalline quartz, fused silica has a broadband Raman spectrum[87] (Figure 2.5) that appears as a high background signal and significantly reduces the signal-to-noise ratio as well as spectral quality.

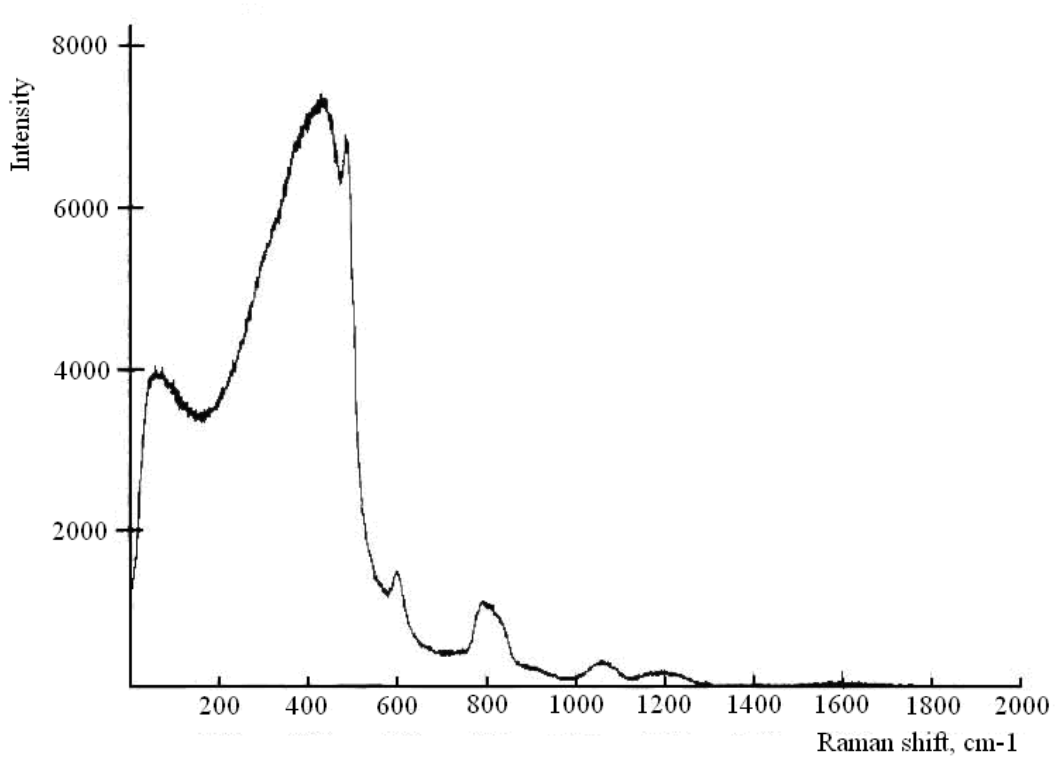

Figure 2.5. Raman spectrum of fused silica (adapted from [95]).

Although silica glass is a very weak Raman scatterer, the high laser power density in the fibre core and its long fibre length make silica bands strong enough to cause interference problems. The silica Raman background appears according to two different mechanisms:

1) Silica Raman bands are generated inside the excitation fibre and transmitted towards the sample together with laser light; these photons are elastically scattered (secondary scattering) or reflected from the sample creating the background spectrum.

2) If a fraction of the excitation laser radiation is reflected from the sample, cuvette, packaging, optic elements or any other reflecting surface, the intensity of this light can be high enough to cause strong Raman scattering from silica in the collection fibre. This background appears even when the excitation laser is free from any background.

A number of approaches have been attempted to overcome this problem: from the use of special materials and probe designs[95, 98, 99] to hollow-fibre probes[100, 101].

However, for best results double filtration must be performed: for excitation (before illuminating the sample) and collection of light (before it enters the collection fibre). This double filtration is realised in all modern Raman probes available on the market. There are three main types of filtered Raman probes (Figure 2.6). All of them are based on the same idea, but differ in the filtering method. In the design of Carraba and Rauh which was patented in 1992[102], band-pass and long-pass dielectric filters refine the excitation and collection beams, respectively, while a dielectric beamsplitter combines the two beams coaxially. The two other designs were introduced a year later. They utilize a holographic beam combiner rather than a dielectric one. The Kaiser Mark II probe has a unique laser filtration system – a combination of a holographic transmission grating with a spatial filter (Figure 2.6c).

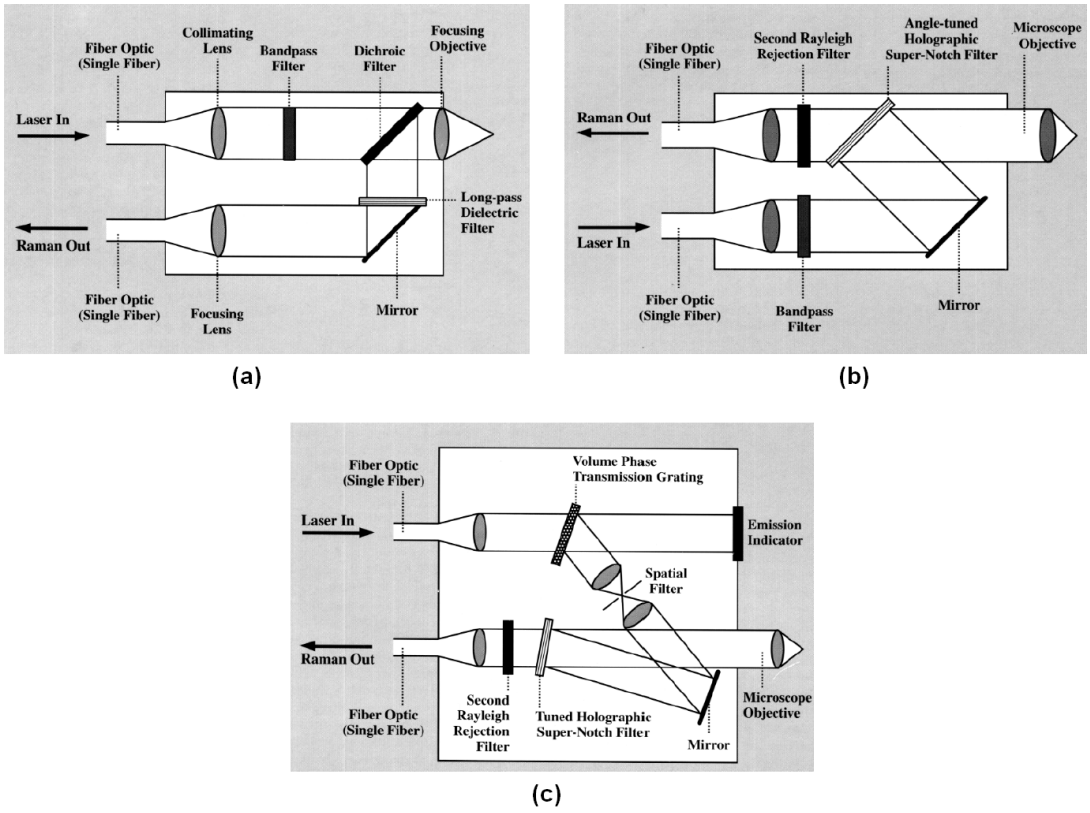

Figure 2.6. Filtered Raman probes: (a) the design of Carraba and Rauh; (b) Dilor's Super-Head design; (c) Kaiser Mark II probe [95].

Later on J. Slater patented his Raman probe[103] which is analogous to Dilor's Super-Head with the only difference that holographic filters were substituted by dielectric ones. At that time, holographic filters performed much better than dielectric filters

and the Mark II was the probe of choice. However, recent advancements in thin-film deposition technology made it possible to produce dielectric filters with excellent characteristics[104], and led to new dielectric Raman probes. Another advantage of dielectric-filtered probes is their compactness, as illustrated by the comparison of the dielectric probe (Carraba and Rauh design) and Mark II probe with holographic-spatial filtering in Figures 2.7-2.8.

Figure 2.7. NIST probe with immersion sleeve based on the design of Carraba and Rauh (InPhotonics, USA)[105].

Figure 2.8. Mark II Probe with standard optic head (Kaiser Optical systems, USA)[106].

Filtered fibre-optic Raman probes are very convenient due to their flexibility. They can be used with various optics such as: immersion sleeves for in-line process control; microscope objectives for spatially resolved micro-analysis; and temperature- or pressure-resistant heads. Optic heads can be easily interchanged

making a single probe with a set of optic tips a perfect tool suitable for various applications.

Recently, another filtered Raman probe was introduced and patented by Kaiser Optical Systems in 2005[107-109]. This probe is known as the PhAT probe and is designed primarily for solid samples. The key features of the PhAT probe are an increased illumination/collection area and multiplexed collection by a fibre bundle rather than a single fibre. The PhAT probe is very good for analysis of solids such as pharmaceutical tablets or powders. Because of possible non-uniformity of active ingredients distribution in tablets, wide area illumination gives much more reproducible results[110]. Discussion of the Raman analysis of solids will be continued in the next Section.

2.3.3. Diffusely scattering samples

Unclear liquids and solids require a different approach. Raman photons generated in turbid media propagate along random (not straightforward) routes. This process is referred to as Raman photon migration. A recent study of this phenomenon showed that in diffusely scattering media, Raman photons propagate with much slower attenuation than the elastically scattered photons[111]. This study initiated development of new methods for probing deep layers of turbid media including transmission Raman spectroscopy, time-resolved Raman spectroscopy and spatially offset Raman spectroscopy.

The transmission collection geometry can be used to probe tablets and colloids. The laser beam is incident on one side of the sample whilst the Raman signal is collected from the opposite side. Raman photons are uniformly collected from all layers of the sample, thus the spectrum obtained represents the bulk composition of the probed sample. The transmission geometry is not as efficient as back-scattering and had been largely neglected until it was shown that it had very good performance when probing turbid media with highly fluorescing surface layers such as, for example, pharmaceutical capsules with coloured shells[112, 113]. In that case, the advantage of transmission geometry compared to conventional back-scattering Raman is that the fluorescence background from shells is efficiently reduced resulting in enhancement of the signal-to-noise ratio. Another important advantage of transmission Raman

spectroscopy is that it collects compositional information from the whole sample volume rather than only from the top layers as realised in the back-scattering geometry. Instrumentation for transmission Raman spectrometry is available commercially[114]. Using a high-power laser and a proprietary optical configuration, pharmaceutical tablets can be analysed in less than a second depending on the analyte concentration.

Another method for probing turbid media is spatially offset Raman spectroscopy (SORS)[115]. This technique is based on the results obtained from studying the photon migration process in diffusely scattering media[111]. The main feature of this method lies in collecting Raman photons from regions offset from the illumination point. These offset regions typically form concentric circles surrounding the illumination point and are measured by means of a circular fibre bundle. Raman spectra obtained from different offset distances contain different contributions from sample layers located at different depths because lateral diffusion is growing with greater depths[92, 111]. That is why SORS is capable of discerning an analytical signal from different layers of a probed sample, unlike the transmission collection geometry[115]. This important feature of SORS has easily found applications where spatially resolved non-invasive analysis is needed. One interesting example is *in vivo* transcutaneous Raman spectrometry of bones[116, 117]. Active research is being carried out to develop a non-invasive diagnostic method of osteoporosis based on SORS.

There is one more important practical advantage of SORS, which also stems from its depth-selective nature. When Raman spectra are collected from samples covered with diffusely scattering or coloured packaging this method exhibits substantially higher sensitivity than the conventional Raman technique, mostly because the fluorescence background from the package is efficiently reduced. This fact underlines the sampling simplicity that is achieved by SORS. Thus, SORS has been reported to be effective in detection of explosives concealed in various containers which can be useful for security control in airports[118].

2.3.4. Other sampling techniques

Apart from traditional non-invasive analysis by fibre-optic Raman probes, there are a number of other less utilised sampling techniques. One of them provides

enhancement of the Raman signal collected from transparent liquid samples. The measurements are taken from a thin capillary filled with the liquid sample. Provided that the refractive index of the liquid is less than that of the capillary material, light entering the fibre within a certain angle range is trapped by total internal reflection within the waveguide, resulting in very high pathlengths through a very small volume of liquid. Every point inside the capillary efficiently contributes to the Raman signal*. Such waveguides are referred to as liquid core optical fibres (LCOFs). The first report of this technique appeared in the early 1970s[119]. Quartz capillaries of 75 μm in diameter and 10 - 25 metres long provided 10^2 - 10^3 times more intense spectra compared to traditional sampling in a cuvette. However, the refractive index of the liquids that can be studied by this sampling method must exceed that of quartz (1.46). Nowadays, low refractive index Teflon®-AF fibres are used allowing water solutions to be analysed[120, 121]. Another advantage of LCOF-sampling is that the fluorescence background superimposed on Raman spectra can be reduced owing to photobleaching induced by the high laser radiation density within the capillary[120].

If the refractive index of a sample is not sufficient to provide total internal reflection, then the internal surface of a silica capillary can be coated with metal (usually silver). Although silver reflectance is not 100% efficient, as total internal reflection and multiple reflection events will lead to light loss, the use of these capillaries still gives significant signal gain. It proved to be useful for analysis of gases where total internal reflection cannot be implemented[122].

In spite of the fact that Raman spectra obtained by single-fibre probes had proved to be severely contaminated with silica Raman bands, it is worthwhile to mention an early work of Kyle et[123] al.[123]. The authors of this work observed *evanescent Raman scattering*. A bare fibre was dipped into a liquid sample and imaged lengthwise on to the entrance slit of a spectrometer. If the sample's refractive index was less than that of the fibre, the requirement for total internal reflection in the fibre was met and no light except for the evanescent field penetrated into the sample. In this setup, Raman

* A similar situation occurs in a glass optical fibre: although glass is a poor Raman scatterer, the actual Raman signal from fibre output is unusually high.

peaks of the surrounding liquid could be detected, which proved that evanescent field fibre-optic Raman spectroscopy is an observable phenomenon. Initially, this work was only of theoretical interest and evanescent Raman sampling was not expected to find application owing to its very poor efficiency. But 11 years after the appearance of Kyle's paper, Chinese chemists reported successful results from evanescent SERS experiments[124]. Their setup is shown in Figure 2.9.

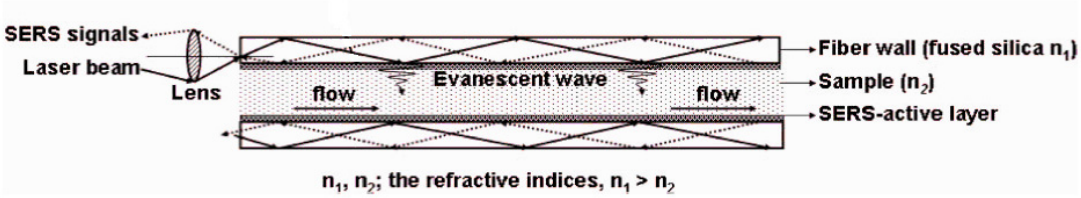

Figure 2.9. Evanescent SERS setup[124].

A layer of silver nanoparticles was deposited on the inner surface of a glass capillary with liquid sample flowing in its core. The laser beam was focused to a tiny point of glass at the end of the capillary and back-scattered photons were collected and analysed with a Raman spectrometer. The solvent was chosen to have a lower refractive index than glass, so that only the evanescent wave could penetrate the glass-sample boundary. The detection limit for a phenylene derivative was found to be as low as 10^{-9} mol/L. Since the capillary was only 3 cm long, the silica Raman background was negligible. This approach has a potential to become a more convenient way of analysis by SERS compared to the traditional sampling with nanoparticle colloids.

3. Raman instrumentation

3.1. Raman spectrometers

Spectroscopic methods of analysis based on electromagnetic radiation rely on spectrometers, instruments that collect and analyse light. All spectrometers are based on the same principles, but each analytical method has its unique requirements concerning sensitivity, wavelength range, throughput, resolution, speed, or frequency of data acquisition. These requirements define the optimal layout and components of a spectrometer designed for a particular application.

In order to be suitable for detecting feeble Raman scattering, a spectrometer must first of all have a sensitive low-noise detector. Detectors for Raman spectrometers are discussed in Section 3.2. The requirements concerning the spectral range are determined by the laser wavelength. Assuming that in conventional Raman spectroscopy only Stokes bands are used, in the case of the most common 785 nm laser, the spectral coverage should be 785 - 1080 nm to allow Raman shifts up to 3500 cm^{-1} to be recorded. In contrast, resolution requirements are rather strict because Raman bands (especially for gaseous samples) are very narrow and should be well resolved for many applications. However, gases are not often analysed by conventional Raman spectroscopy. The peaks from condensed-phase samples are much wider, so a resolution of a few cm^{-1} is enough to resolve most peaks.

Generally, there are two types of spectrometers: dispersive and non-dispersive. *Dispersive* spectrometers spatially split the light according to wavelength and analyse each wavelength separately either with a single detector by means of sequential scanning over the whole wavelength range or simultaneously with a detector array. *Non-dispersive* spectrometers operate in a completely different way: the light is not split but modulated with an interferometer such that all wavelengths have different modulation frequencies. The detector records an interferogram, which is then mathematically processed and converted to a spectrum. In this Section, the two types of spectrometers will be discussed in turn and then a summarized comparison will be made.

3.1.1. Dispersive spectrometers

As mentioned above, dispersive spectrometers split incoming light according to wavelength. This can be achieved by either prisms or diffraction gratings. Glass prisms were the first practically useful dispersive elements known to humanity. Their operating principle is based on the refraction of light: photons of different wavelengths travel at different speed in a medium. In modern systems, prisms are virtually completely replaced by gratings that are lighter, more compact and have greater efficiency. Therefore, it is worthwhile to discuss grating-based spectrometers in some more detail.

A diffraction grating is an optical component that diffracts incident light such that different wavelengths travel in a different direction. It consists of a regular pattern of grooves created mechanically (ruled gratings) or holographically. There are two main types of gratings: reflection and transmission gratings. Reflection gratings are easier to make and were initially more widely used.

For both types of gratings, the grating equation applies [125]:

$$d(\sin\alpha + \sin\beta) = m\lambda \qquad (3.1)$$

where λ is wavelength of light, d is the distance between successive grooves, α and β are the angles of incident and diffracted beams respectively, and m is diffraction order (Figure 3.1).

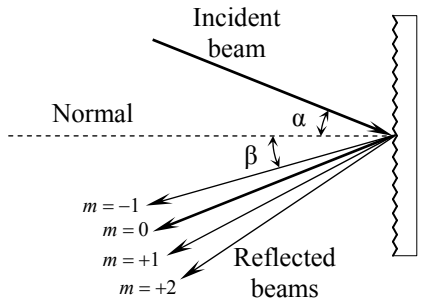

Figure 3.1. Transmission diffraction grating.

The first Raman spectrometers were based on scanning monochromators. Various types of scanning spectrographs are known[126]. The most common monochromators were based on the Czerney-Turner design (Figure 3.2a). They operate on the following principle: an image of a light source is focused on a narrow entrance slit; a concave mirror collimates the beam, which is then diffracted by the grating; another concave mirror focuses the resulting beam on the focal plane where wavelength-dependent shifts of the source image appear. The exit slit selects one of the images, which is measured by a detector. By tilting the grating or moving the slit, the whole spectrum can be recorded. Resolution in such instruments is defined by both the grating's properties and the dimensions of the slits. The narrower the slit the better the resolution. A trade-off lies in the fact that narrow slits limit throughput allowing only a small fraction of incident photons to come through. This is a fundamental disadvantage of all dispersive spectrometers.

Single-grating Czerny-Turner spectrographs produce a significant amount of stray light inherent to all ruled gratings. Stray light is diffuse reflectance from grating defects. It causes some fraction of light to be reflected diffusely to all directions, rather than obey the diffraction law. In early years, there were no efficient wavelength-selective filters that would reject the intense Rayleigh scatter from the collected beam. Therefore, stray light was a particularly important issue in Raman spectroscopy and had to be addressed.

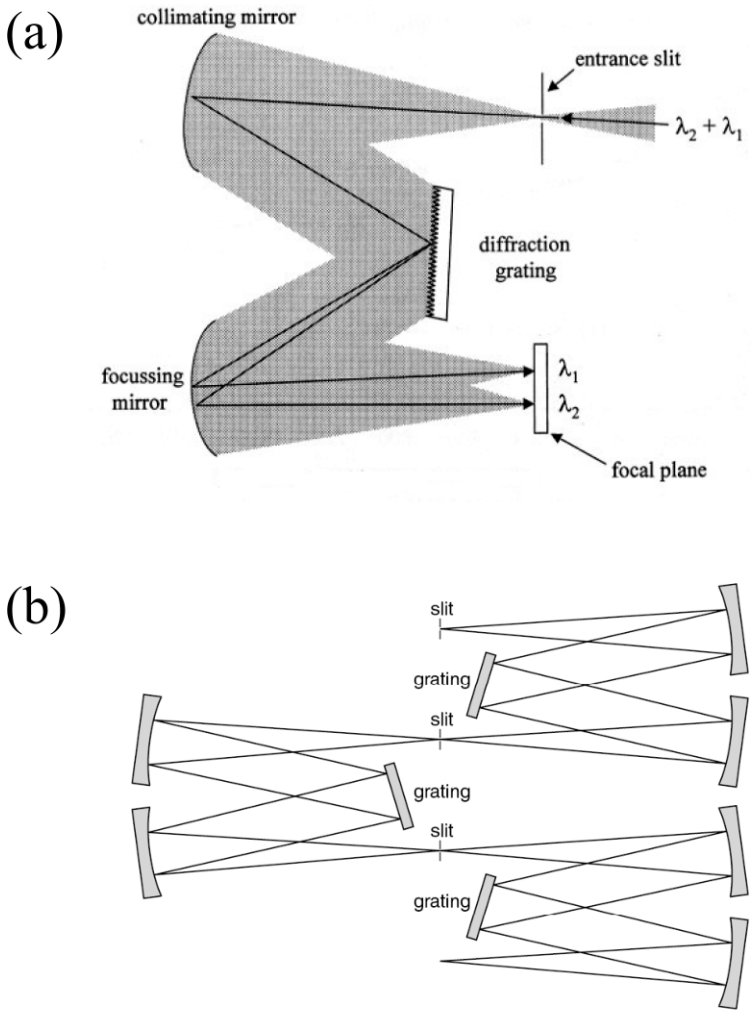

Figure 3.2. Schematics of Czerny-Turner monochromators with a single (a) and triple grating (b)[77, 93].

The problem was solved by using double and triple grating spectrographs (Figure 3.2b). Stray light from the first grating is very efficiently reduced by the second and third gratings. Double-grating monochromators have a stray light level of about 10^{-11} permitting highly scattering samples to be analysed[77]. In addition, multiple-grating systems provide high diffraction efficiency and therefore resolution. They allow high resolution to be achieved with wider slits. However, all these advantages are accompanied with several negative properties. Firstly, much more time is needed to scan over the whole spectrum. Secondly, a great fraction of signal is lost due to multiple diffraction events that are not 100% efficient. Thirdly, the increased number of optical elements, especially concave mirrors, resulted in a high level of aberrations

that restricted the resolution advantage. Strong aberrations are peculiar to all Czerny-Turner spectrographs.

A breakthrough in spectroscopy occurred in 1966 when the first holographically recorded gratings were produced[126]. The benefit of using holographic gratings instead of ruled ones is that they almost completely eliminate stray light owing to the high quality of the groove pattern.

Many modern spectrometers use volume phase holographic (VPH) transmission gratings[127] as a dispersive element. VPH gratings are produced by recording a hologram on a photosensitive emulsion deposited between two glass plates. A standing wave creates local refraction index changes in the emulsion that work like a periodic pattern of grooves, causing light to be diffracted at the angle of approximately 90° as shown in Figure 3.3.

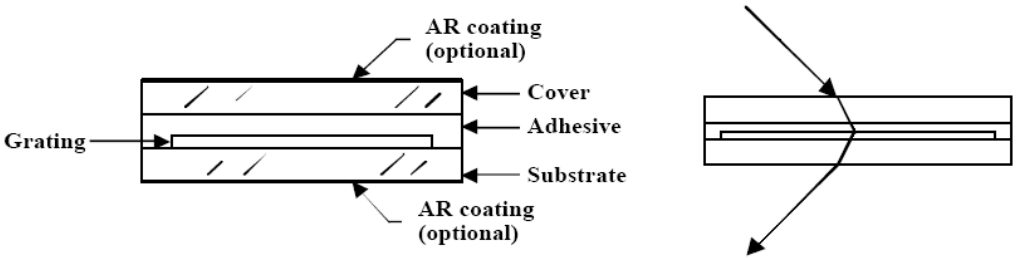

Figure 3.3. Configuration and light pathway in a VPH transmission grating (adapted from [127]).

Development of holographic technology also brought the introduction of efficient notch filters. Both these developments along with the use of multichannel detectors formed the basis of the next generation Raman spectrometers[128]. A schematic of the state-of-the-art high throughput Raman spectrometer developed by Kaiser Optical Systems is shown in Figure 3.4. The high precision, high numerical aperture optics and on-axis design of the spectrometer significantly reduce aberrations and enhance resolution.

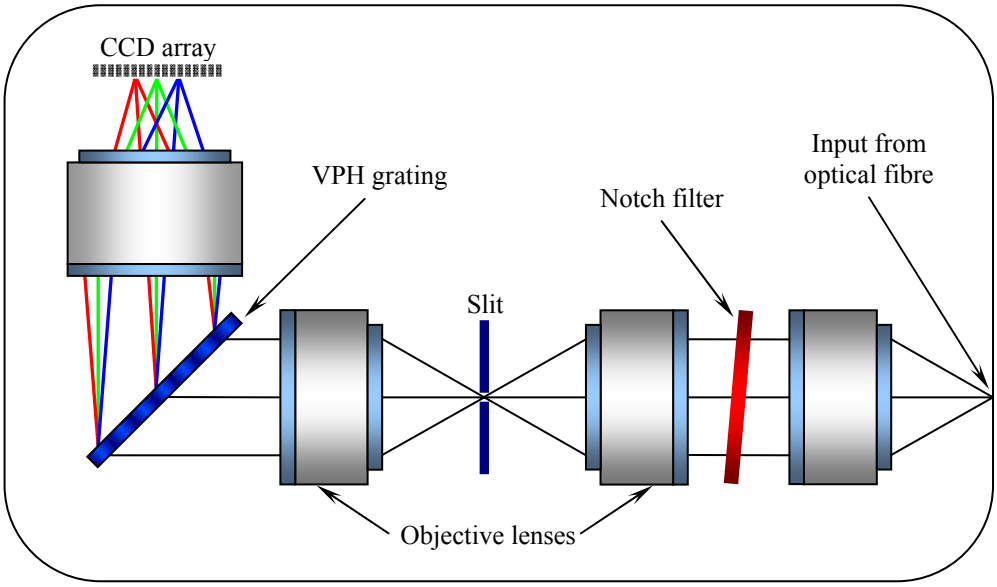

Figure 3.4. Layout of an on-axis Raman spectrometer (adapted from[77, 129]).

Multichannel detectors (see Section 3.2.3) reduce analysis time by the factor of N, which is the number of resolution elements of the detector. The corresponding signal enhancement is $\sqrt{N}$ according to Poisson statistics. This is known as the "multichannel advantage". In general, modern dispersive spectrometers are very efficient instruments that outperform non-dispersive spectrometers in signal-to-noise ratio. The only significant limitation is their relatively low throughput that is limited by slit size. However, with modern 2-dimensional CCDs this problem is reduced, as it is possible to record several spectra simultaneously. For example, instead of a single collection fibre, a bundle of fibres can be used to collect the signal. The fibres are then reallocated lengthwise and their image is projected on a CCD. This approach is realized in Kaiser's PhAT probe[107]. One dimension of the CCD is used for recording spectra while the other dimension – for collecting multiple spectra. Summation of these spectra results in higher SNR due to increased throughput.

An alternative approach to eliminating the throughput disadvantage is the use of coded apertures instead of slits[130, 131]. A coded aperture is a tiny film with an engraved mask consisting of alternating black and transparent spots (Figure 3.5).

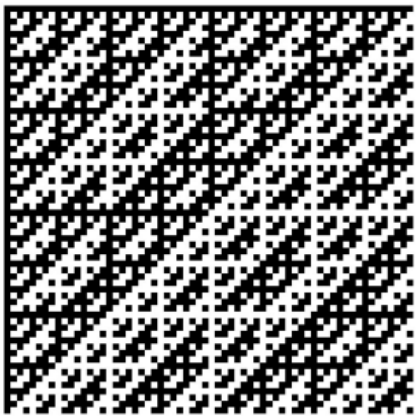

Figure 3.5. Coded aperture mask based on Hadamard matrix[130].

The pattern is usually defined by the Hadamard code based on Hadamard matrices[130]. This mask is used instead of a slit. The image on a CCD is then decoded, and the Raman spectrum is reconstructed. Because Hadamard masks have equal numbers of black and white spots, the throughput increase should be as high as $\frac{S}{2d}$, where S is the area of the mask exposed to light and d is slit size in an alternative instrument.

3.1.2. Fourier transform spectrometers

Fourier transform (FT) is the most common type of non-dispersive Raman spectroscopy. The first paper describing FT Raman spectroscopy appeared in 1964[132] but did not attract the attention of the scientific community[133]. The interest in this technique revived only in the 1980s[134] when many technical difficulties accompanying the pioneering work made 20 years previously were overcome. People realised the potential of interferometric spectrometers for detecting Raman scattering particularly with regards to the Nd-YAG excitation laser operated at 1064 nm[87, 133, 135]. NIR Raman excitation is advantageous for many organic substances that could not be analysed with UV/visible lasers because of fluorescence interference. At that time detectors were very noisy in the NIR region and scanning dispersive spectrometers were not able to provide sufficient signal-to-noise ratio. FT-spectrometers effectively reduced this problem by the multiplex advantage (see below). Therefore, the advent of FT-Raman spectrometers boosted the use of NIR lasers in the field. The popularity of FT Raman equipment grew significantly.

However, rapid technological developments have also brought significant improvements in dispersive Raman instrumentation. The rest of this Section is devoted to an up-to-date comparison of FT and dispersive Raman spectrometers, which is useful to help understand the advantages and limitations of the two methods.

The key part of a classic FT-spectrometer is the Michelson interferometer shown in Figure 3.6.

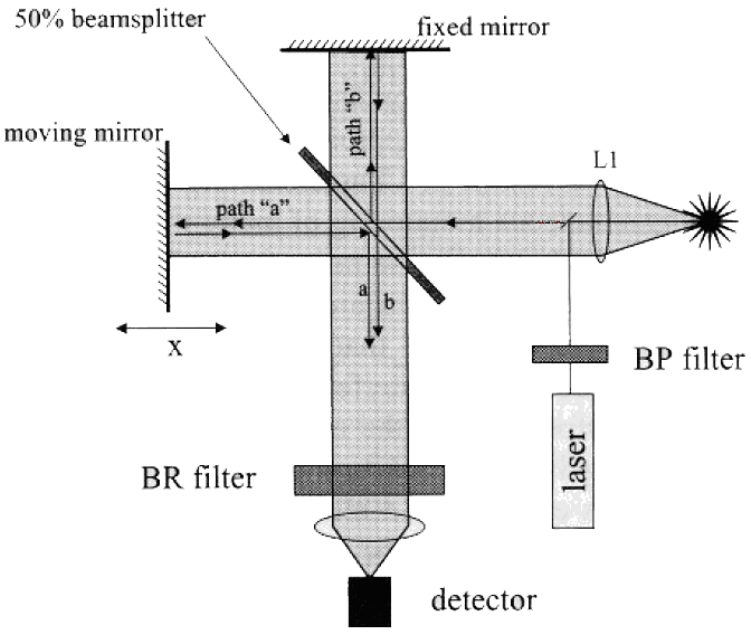

Figure 3.6. Schematic of FT-Raman spectrometer based on a Michelson interferometer[77].

The beamsplitter is 50% reflective and located at 45° incidence. The two paths of incident light (transmitted and reflected) are reflected from the mirrors one of which is fixed and the other one is moving. The beams are then recombined by the beamsplitter and interfere with each other. Depending on the relative mirror displacement, the interference can be destructive or constructive for various wavelengths so that the overall intensity recorded by a single detector is the function of the displacement and spectral characteristics of the incident light. The dependence of the overall intensity on the mirror displacement is called an interferogram (Figure 3.7).

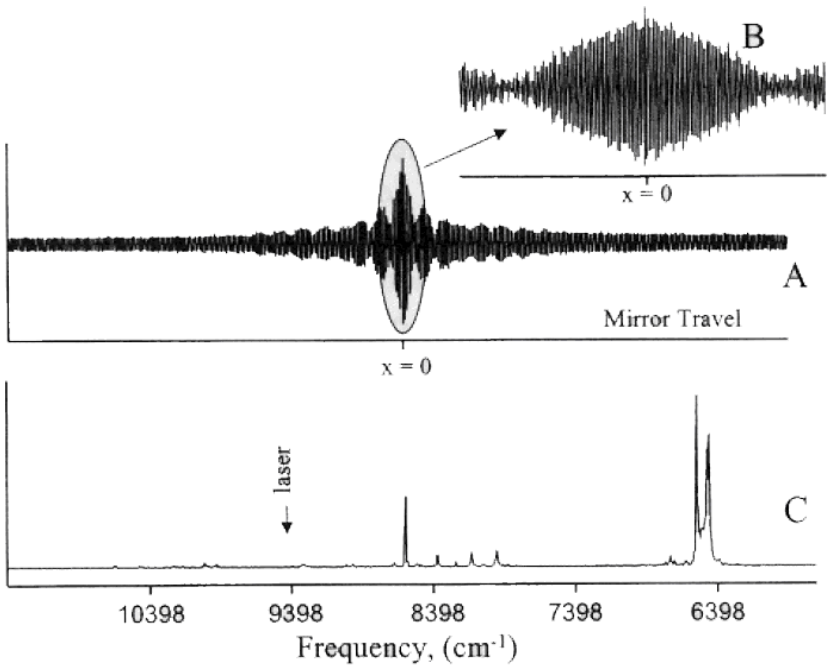

Figure 3.7. Interferogram (spectrum A) obtained from cyclohexane and reconstructed Raman spectrum (spectrum B) after Fourier transformation[77]. The spectrum is plotted against absolute wavenumber rather than Raman shift.

Fourier transformation of an interferogram converts it from the time domain to the frequency domain, and a conventional Raman spectrum is obtained. The mathematics of Fourier transformation is available in textbooks[136].

Not all FT-spectrometers are based on the Michelson interferometer. Another relevant technology is the lamellar grating interferometer. A lamellar grating consists of a set of equidistant grooves. The depth between the grooves is variable and can be mechanically tuned in a linear fashion. This interferometer does not need a beamsplitter because it splits the beam at the grating. This technology was initially used for the far-infrared region[137], but with the development of micro-electromechanical systems (MEMS) lamellar gratings could be made very compact and applied to the visible-NIR region[138] (Figure 3.8).

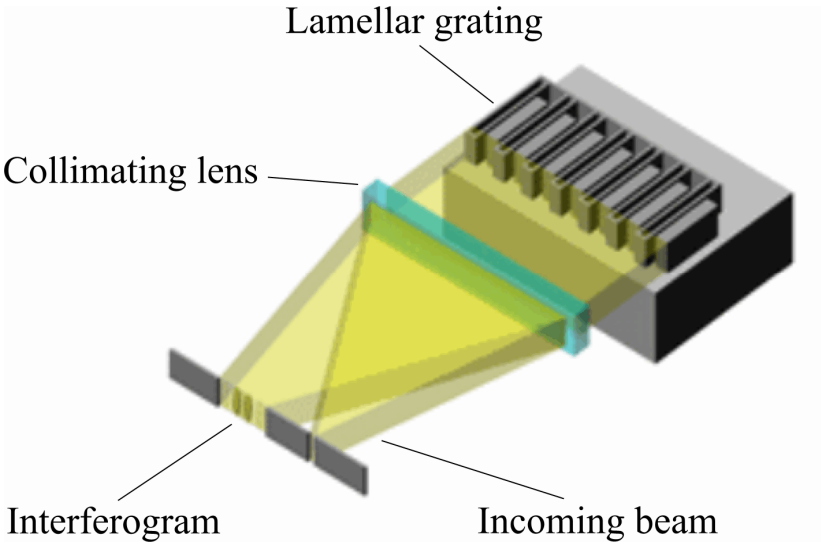

Figure 3.8. Schematic of lamellar grating interferometer manufactured by ARCoptix S.A., Switzerland (adapted from [138]).

Key characteristics of FT-Raman spectrometers. The resolution of FT-spectrometers depends on the maximum displacement between the interferometric elements (mirrors or grating grooves): the higher the displacement, the higher the resolution. This fact makes FT-spectrometers very different from dispersive systems and defines the main feature of FT-spectrometers – *luminosity or the Jacquinot advantage* – the throughput advantage over dispersive spectrometers[†]. As stated before, dispersive spectrometers have the trade-off between throughput and resolution. FT-spectrometers do not exhibit this trade-off and do not require narrow slits to achieve high resolution.

However, the resolution of FT spectra and the light source dimensions are not completely independent, because for accurate operation of an interferometer a collimated light beam is needed, which ideally can be achieved only from point light sources. Larger entrance apertures decrease the resolution although this effect can be less pronounced in interferometers compared to dispersive spectrometers.

Another useful property of FT-spectrometers is the very accurate frequencies in spectra. This is known as the *Connes advantage*. Accurate calibration of FT-

[†] It should be noted that the Jacquinot advantage also refers to dispersive spectrometers with coded apertures and multiple-fibre collection sampling.

spectrometers is achieved by using a HeNe laser beam as an internal wavelength standard[87]. This additional laser beam is irradiated collinearly with the light under study and causes unique fringes on the interferogram that are tracked to control mirror displacement. The wavelength of the HeNe laser is precisely known and the described procedure allows FT spectra to be accurately calibrated.

Multiplex advantage. The multiplex advantage (also known as Fellgett's advantage) is an improvement of the signal-to-noise ratio if an interferometer is used instead of a scanning monochromator in detector noise-limited conditions. This improvement stems from the fact that while scanning monochromators absorb all photons except for those that pass through a narrow slit, interferometers transmit all photons to detector at any time. This reduces the time needed to collect the entire spectrum and increases the Raman signal by the factor of $\sqrt{N}$, where N is the number of resolution elements in a single-channel scanning system[77, 87]. This enhancement is the same as that observed for multichannel systems, but has a fundamentally different origin. The multiplex advantage is equal to $\sqrt{N}$ only if detector noise is a lot greater than shot noise. This was the case 20 years ago, but today high quality NIR detectors operating near the shot noise limit are available. In this case (shot noise limited operation) the multiplex advantage is relevant only if the spectrum consists of a single narrow line. For more complex spectra, the signal enhancement is reduced and completely lost for flat spectra or spectra with a very high background. This occurs because shot noise is summed up from the entire spectrum and is recorded by one detector that does not know which wavelengths contribute to the noise. As a result, the noise of each peak in a reconstructed spectrum will have contribution from all other wavelengths. Therefore, if the overall signal intensity is much higher than the intensity of a particular peak, the recorded shot noise will be higher than it actually is, and the signal-to-noise ratio will be low as if the spectrum was collected by a scanning monochromator.

It should also be remembered that the multiplex advantage is relevant only when a FT-spectrometer is compared with a scanning dispersive spectrometer rarely used today. Therefore, the term "multiplex advantage" has little practical importance today and can be confusing. In fact, multi-channel spectrometers can be comparable

or better in this respect than FT-spectrometers. In contrast to the multiplex advantage, the multichannel advantage does not depend on spectral complexity and remains constant because each CCD pixel monitors only one wavelength and its SNR is not related to other wavelengths. Except for a single ideal case, multiplex spectrometers give lower SNR than modern dispersive spectrometers. Although it is partially compensated by the luminosity advantage of FT-spectrometers, the resulting SNR is still lower than for dispersive spectrometers especially when the latter comprise multiple collection fibres or coded apertures.

Multichannel FT-Spectrometers. Multichannel FT spectrometers (MCFT) combine the properties of dispersive and non-dispersive systems. They are based on interferometers with no moving parts. The incident beam is stretched by spherical or cylindrical lenses, and then passes through an interferometer that provides a variable pathlength difference across its aperture. On the output, the beam is modulated in the same way as in the case of traditional interferometers, but the interferogram is created in the spatial domain (not in the time domain). In order to read spatial interferograms, a position sensitive detector is needed, i.e. a CCD array.

There are several types of interferometers with stationary components. One of them known as a common-path or Sagnac interferometer is shown in Figure 3.9. It is similar to a Michelson interferometer, with the path difference being created by tilted mirrors instead of moving mirrors.

Another type of stationary interferometer is based on a Wollaston prism[139, 140] or Wollaston prism array[141]. A Wollaston prism is made from birefringent material that separates unpolarized light into two orthogonally polarized beams. Two cross-polarizers located at each side of the prism select only those fractions of the two beams that are identically polarized and can interfere with each other. An imaging lens is used to focus the interference pattern on to a CCD. A typical layout of such a spectrometer is presented in Figure 3.10. MCFT spectrometers with Wollaston prisms are more compact compared to traditional FT spectrometers.

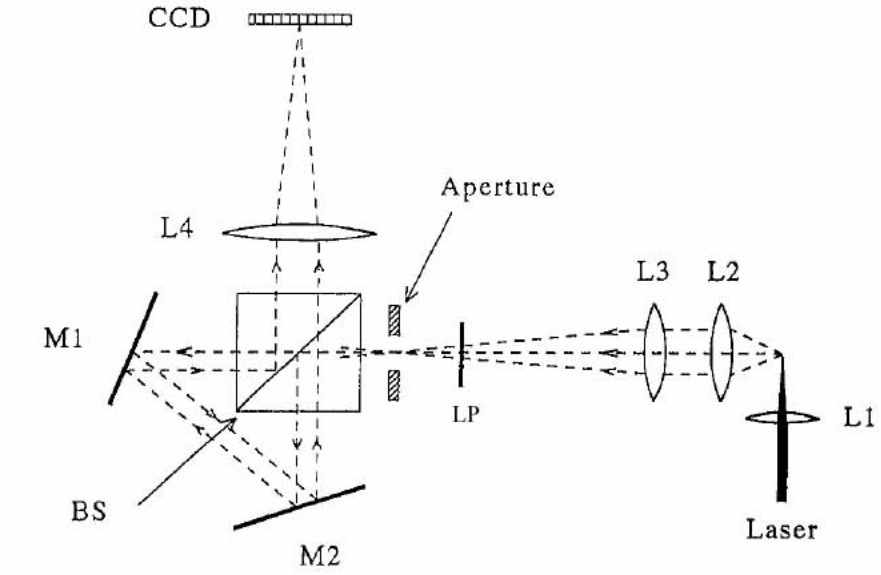

Figure 3.9. Common-path (Sagnac) multichannel FT interferometer (adapted from [142]). L1-L4 – lenses, LP – long pass filter, BS – beamsplitter, M1-2 – interferometric mirrors.

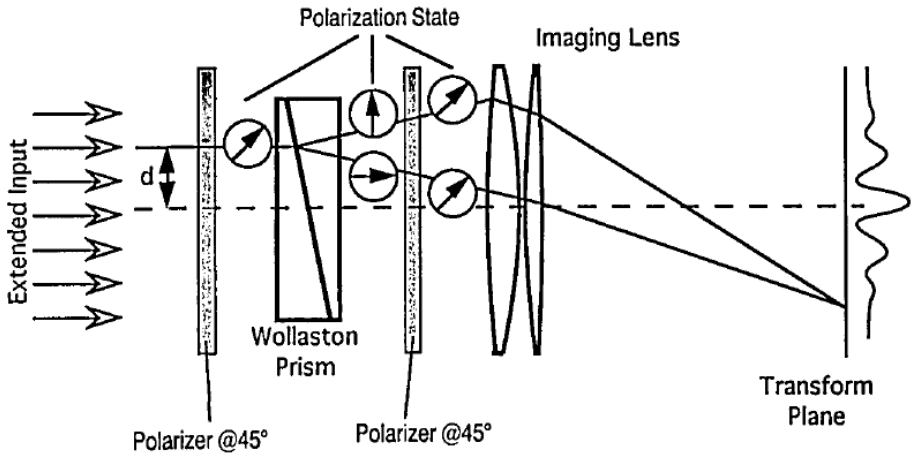

Figure 3.10. Multichannel FT spectrometer based on Wollaston prism[139].

Recently, an interferometer based on a micro-machined lamellar grating with variable groove depth along its length was introduced[143]. A simpler technology reported by Andersson at al.[144, 145] is based on a wedge Fabry-Perot interferometer. A Fabry-Perot interferometer is a thin film with semi-transparent edges. It has been used in many photonics applications but is not yet firmly recognized as a key element for non-dispersive spectrometers. However, the simplicity and compactness of a Fabry-Perot interferometer has great potential for miniaturized and cost-effective

FT and MCFT spectrometers. The design reported by Andersson at al. (Figure 3.11) does not need many lenses or other bulky components and can be potentially made in micro-scale.

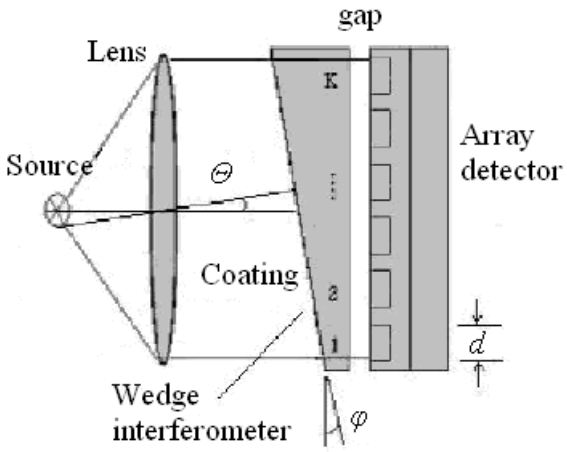

Figure 3.11. Wedge Fabry-Perot interferometer with array detector[145].

MCFT spectrometers retain some advantages and disadvantages of both dispersive and non-dispersive systems. New features are compactness and mechanical stability. However, since a detector array is used, the resolution depends not only on the maximum pathlength difference, but also on the number of pixels on the CCD. Generally, there is a complicated dependence between pathlength difference, resolution, and frequency precision. Currently, MCFT devices have lower resolution and much lower SNR compared to dispersive spectrometers. The SNR disadvantage is inherited from non-dispersive spectrometers. In addition, MCFTs are less flexible than classic FT spectrometers.

The rapid growth of MEMS technology and microfabrication techniques may soon allow extremely compact micro-FT and MCFT spectrometers to be produced. They can be integrated into micro-analysers that are attracting increasing interest of the scientific community[146].

A summary of the main features of all three types of spectrometers is presented in Table 3.1. Properties that are advantageous in one technique and disadvantageous in the other are not duplicated to simplify the picture. Since the luminosity (Jacquinot) advantage is relevant for all three types it is not included in the advantages row (in

dispersive spectrometers, the Jacquinot advantage is achieved by using coded apertures).

Table 3.1. Comparison of dispersive, FT and MCFT Raman spectrometers.

	Dispersive/CCD spectrometers	FT spectrometers	Multichannel FT spectrometers
advantages	👍 Higher SNR 👍 Constant multichannel advantage 👍 No moving parts 👍 Wide range of wavelengths	👍 Excellent frequency precision 👍 Good for NIR excitation 👍 Generally more compact	👍 Good frequency precision 👍 Good for NIR excitation 👍 Low-noise CCD detectors 👍 No moving parts, excellent stability 👍 Extreme compactness
disadvantages	👎 Trade-off between throughput and resolution (it is overcome in coded aperture spectrometers)	👎 Not available for UV or visible region 👎 Distributed noise 👎 High-precision mirror-scanning mechanisms are required 👎 Analysis time is limited by scanning speed 👎 Delicate design	👎 Not available for UV or visible region 👎 Distributed noise 👎 Generally low resolution 👎 Less flexible (resolution and noise cannot be adjusted)

It can be concluded from the table that modern dispersive spectrometers have no significant disadvantages over FT instruments. The merit of FT Raman spectroscopy is that it brought enthusiasm and excitement to the field at the end of the 20th century[135]. Subsequent development of dispersive Raman instrumentation left many of the benefits of FT Raman behind. Supposedly, further development of Fourier transform Raman analysis will be directed towards miniaturization up to micro-scale, while dispersive spectrometers will continue to have "scientific grade" status.

3.2. Detectors for Raman spectroscopy

Advancements in light detecting technology were important for the development of Raman spectroscopy because the feeble Raman signal requires high-quality detectors that were unavailable until the end of the 20th century. The first Raman experiments were carried out with photographic films placed at the focal plane of a spectrograph. Although photographic films are "multichannel" detectors, they are not convenient to use or calibrate and are not suitable for quantitative analysis.

3.2.1. Photomultiplier tubes

The first electronic detector, the *photomultiplier tube* (PMT), was developed in 1939[126]. It had been the detector of choice for Raman spectroscopy for a long time owing to its high sensitivity and linear response. The operation of PMTs is based on the photoelectric effect – electron emission from matter initiated by photon absorption. A PMT is a vacuumized tube containing a photosensitive cathode and collection anode, which are separated by a series of other electrodes (dynodes). Dynodes serve for signal multiplication. Each dynode is held at a more positive voltage than a previous one, so that the initial electron beam is accelerated when traveling from one dynode to another and knocks out more and more electrons each time. The multiplication factor can be as high as 10^8 providing very high sensitivity[87]. The final electron beam reaches the anode and the resulting current is measured.

The PMT is a single-channel detector because it has only one sensitive area. As PMTs are bulky, it was impossible to arrange arrays from them, so these detectors could be used only in scanning spectrometers. Indeed, scanning monochromators

with PMTs had been the most common spectrometers for Raman measurements during the period from 1960 to 1990. The use of PMTs with FT-spectrometers was impossible as these detectors were either absolutely insensitive in the near-infrared region or had very high dark current[133]. Among the disadvantages of PMTs are low quantum efficiency, large dimensions, insensitivity to wavelengths above 900 nm, low dynamic range, susceptibility to intense light which can damage the electrodes, and sensitivity to external stray magnetic fields[147]. The only advantage of PMTs that remains important today is high gain that allows them to be used for single photon detection. With a few exceptions[148] PMTs have virtually been replaced by other detectors.

3.2.2. Photodiodes

The next generation detectors were based on *photodiodes* made of silicon[87]. Silicon photodiodes held at reverse bias absorb light in the p-n junction (see Section 3.3.1). As a result, an electron-hole pair is created causing the change in potential across the p-n junction. This change is measured as a signal. Although silicon photodiodes are less sensitive than PMTs, they are simpler and much more compact (25 - 50 μm). Their small size made it easy to construct array detectors to be used in non-scanning multichannel dispersive spectrometers.

Photodiode arrays (PDAs) contain up to 4000 pixels and therefore provide high resolution for dispersive spectrometers. Silicon PDAs are optimal for operation in the visible spectral range: the maximum quantum efficiency is about 70% (at 550 nm) and drops to 20% at 200 and 900 nm. Therefore, silicon is unsuitable for NIR light detection. The wide popularity of 785 nm lasers in Raman spectroscopy is partially caused by silicon's photoresponse. The red sensitivity edge of silicon – 1100 nm – corresponds to a Raman shift of 3648 cm^{-1}, which is approximately the upper value of analytically useful Raman shifts. For longer excitation wavelengths silicon detectors will not be able to detect the whole Raman spectrum and other detectors are needed. There are two other limitations of PDAs. The first is a high dark current that can be reduced by cooling. Thus, at -20°C PDAs typically have a dark current of 40 electrons per second[89]. The second limitation is very high readout noise of a few thousands of electrons per pixel. Such high readout noise is unacceptable for the

sensitivity requirements of Raman spectroscopy. To overcome this problem, avalanche photodiodes were designed.

The construction of *avalanche photodiodes* (APDs) is very similar to that of conventional photodiodes. An important difference is that a much higher bias voltage is applied to the p-n junction so that the created photoelectrons exhibit acceleration in this internal field and produce secondary electrons due to impact ionization. A typical multiplication factor of the order of 300 is not as high as in photomultipliers but provides an important advantage over simple photodiodes. As multiplication is performed prior to reading, the readout noise is reduced by approximately the same factor (300). APDs can be manufactured in the form of arrays (APDA) or as a single detector with large area up to 20 mm in diameter (LAAPD)[147]. The latter can be useful for FT Raman spectroscopy.

Another type of modified detectors is the intensified photodiode array (IPDA)[77, 87]. It has an image intensifier deposited on the front facet of the detector that amplifies the signal by a factor of approximately 3000. This amplification efficiently reduces readout noise. IPDAs were the main type of detectors before the appearance of CCDs and their main disadvantage is high dark current, which is inherent in their design.

3.2.3. Charge-coupled devices

Charge-coupled devices (CCD) were invented in 1969, became commercially available in 1973 but were not widely used until the early 1990s[87, 89]. CCDs are now the main multichannel detectors for UV-visible light and should be considered in some more detail. In a CCD there is a photosensitive silicon epitaxy layer deposited on a semiconductor wafer (substrate). The top side of the epitaxy layer is covered by an array of thin electrodes (gates). Gate electrodes constitute an array of pixels. Each pixel contains only a few electrodes (usually 3 or 4); one of them is held at a positive potential to attract and trap electrons (charge) in the region just below that electrode. This trap is called a potential well. An incident photon creates an electron-hole pair in the substrate layer. The electric field from the gate electrode repulses holes and collects electrons. The number of trapped electrons is proportional to the number of incident photons. In order to read the accumulated charge in each pixel, the whole pattern is transferred (shifted) along the array towards the charge amplifiers located

on the chip edges that convert the charge to voltage. By means of such consecutive shifts, the whole array can be read and digitized. Charge transfer between pixels is controlled by other gate electrodes. The efficiency of this process is very high – more than 99.9%. Therefore, although the reading process is complicated it is very reliable. A schematic of a CCD is shown in Figure 3.12.

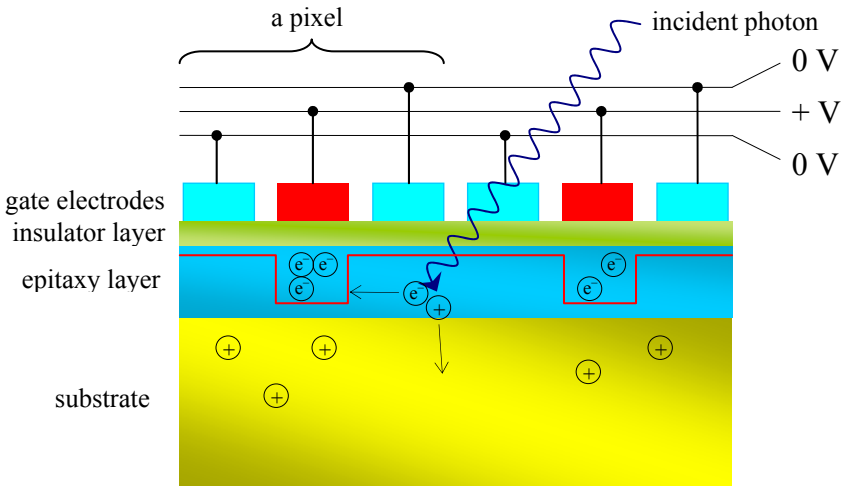

Figure 3.12. Layout of a three-phase front-illuminated CCD.

As the photoactive layer is made of silicon, the wavelength response of CCDs is similar to that of silicon photodiodes. However, the specific architecture of CCDs makes them slightly different. The problem is that photons of different wavelengths have different penetration depths in silicon. UV photons are more likely to be absorbed and only a few of them can pass through the layers of electrodes and insulator to reach the epitaxy layer and create an electron-hole pair. In contrast, the penetration depth of infrared light is very high and many photons pass through the epitaxy layer undetected.

The sensitivity of a CCD to red and near-infrared light can be increased by thickening the epitaxy layer. To enhance quantum efficiency in the UV range, the majority of the substrate is etched off and the CCD is illuminated from the other (back) side. This method turned out to be very effective, but etching is costly and leaves the device in a very fragile state. In addition to higher sensitivity in UV range, the flat surface of back-illuminated CCDs (free from electrodes) makes it possible to apply an anti-reflection coating and thus improve the overall quantum efficiency.

An alternative approach to back-illumination is to coat the front side of the chip with a phosphor layer that absorbs UV photons and fluoresces at longer wavelengths that are easily detected by CCD. A disadvantage of this design is a low quantum efficiency not exceeding 50% because fluorescence is isotropic and half of the photons are emitted away from the epitaxy layer. The quantum efficiencies of various CCDs are shown in Figure 3.13.

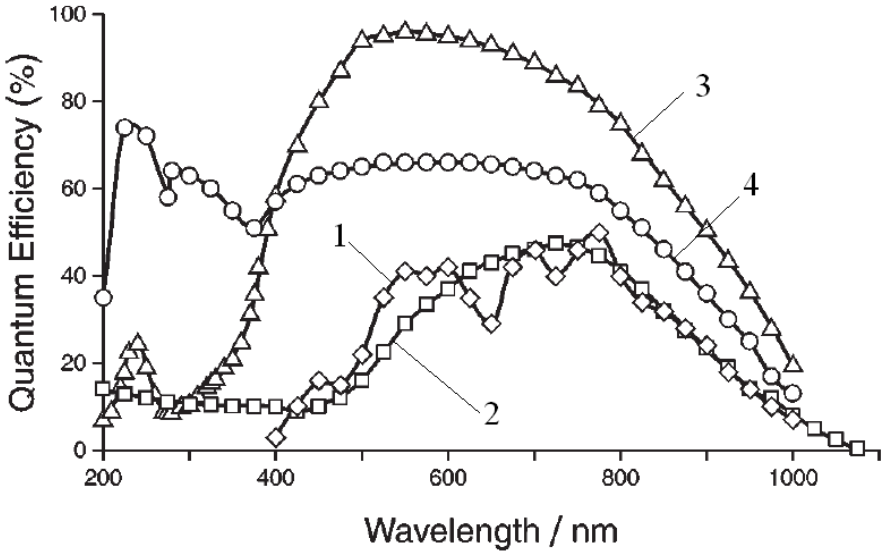

Figure 3.13. Quantum efficiency of different CCDs[89]: 1 – normal front-illuminated CCD; 2 – front-illuminated CCD with a phosphor coating; 3 – AR-coated back illuminated CCD optimized for the visible; 4 – AR-coated back-illuminated CCD optimized for the ultraviolet.

Recently, multiplier CCDs were invented. They have on-chip charge multiplication electronics that provide substantial signal enhancement before readout. All these and other advancements are described in special texts[89].

Currently, the CCD is the most commonly used multichannel detector for the UV-visible range. It has lower dark and readout noise, and higher dynamic range and quantum efficiency. The main disadvantage of CCDs is so called “blooming”. Each pixel can accumulate only a limited amount of charge. If an incident light intensity generates more electrons than a pixel can hold then an excess of electrons is transferred to adjacent pixels. Very intense light can swamp the entire array and

make the analysis impossible. This is one of the reasons that necessitate removal of the intense Rayleigh signal to a value below the full well capacity of CCD pixels[‡].

3.2.4. Non-silicon detectors

Non-silicon are used when samples are excited with NIR lasers. At the beginning of the FT Raman era (1980s) germanium-based photodiodes were employed[134]. Germanium photodiodes are sensitive in the range from 800 to 1600 nm and must be cooled (with liquid nitrogen) to reduce dark noise. Similarly, to traditional silicon photodiodes, germanium detectors have very high readout noise. InGaAs photodiodes have better characteristics compared to Ge analogues: lower dark current, wider wavelength range (800 - 2600 nm) and higher quantum efficiency (average 80%)[89, 149]. However, the readout noise is still significant. It remains the main disadvantage of photodiodes and photodiode arrays compared to CCDs. By analogy with silicon detectors, avalanche InGaAs photodiodes (InGaAs APD) have been studied[150, 151]. Several Raman instruments based on InGaAs detectors are available commercially.

There are many other materials for making photodiode detectors for the NIR range. They are based on platinum silicide (PtSi), palladium silicide[152], mercury cadmium telluride (MCT or HgCdTe)[89], indium antimonide (InSb)[149] and other substances. HgCdTe detectors are promising for infrared Raman spectroscopy having 60% quantum efficiency, a wavelength range of 800 - 2500 nm, negligible dark current and a readout noise of under 10 electrons per pixel. This technology is not commercialized yet for Raman spectroscopy.

Hybrid detectors with a Si photodiode mounted over an InGaAs photodiode have become available[153]. They are sensitive to photons in a wavelength range from about 250 to 1700 nm.

To conclude, there are three main types of detectors that are applicable for Raman spectroscopy today: CCD arrays, photodiodes and photodiode arrays. CCDs are currently based only on silicon. They outperform all other detectors for the UV-

[‡] In FT Raman spectroscopy the necessity to filter the Rayleigh signal is defined by another reason – the multiplex disadvantage: any intense peak increases the overall noise and therefore should be removed.

visible range. Photodiodes are used in FT Raman instrumentation. PDAs for the near-infrared region are mainly made of InGaAs. These detectors are used in NIR dispersive Raman systems and multichannel FT spectrometers. Commercially available photodiode arrays have substantially higher readout noise compared to CCDs.

3.3. Semiconductor lasers for Raman Spectrometry

A perfect laser for Raman spectroscopy would have very narrow bandwidth, high power, and excellent wavelength- and power-stability. Preferably, it should also be compact, power- and cost-efficient. Combining all these characteristics in one device is very challenging. Gas-ion lasers (Ar^+ or Kr^+) used for Raman spectroscopy in the past are inefficient in terms of energy conversion and frequently require water cooling. Moreover, they are bulky and expensive. HeNe lasers emitting at 632.8 nm turned out to be more applicable in practice: their excellent frequency stability, low-diverging output and higher efficiency ensured their wide use over a long period of time[77, 126]. A disadvantage of HeNe lasers is their low power: usually less than 50 mW.

In the 1990s solid-state lasers, especially Nd:YAG (1064 nm) and frequency-doubled Nd:YAG (532 nm), became very popular in Raman spectroscopy. To some extent their use was driven by the increasing interest in FT Raman instrumentation[135]. These lasers are relatively small ($\sim 2 \times 2 \times 12$ in.), capable of output powers exceeding 10 W, and do not require water cooling.

Although solid-state lasers are still actively used today in Raman spectroscopy, most commercial systems utilize semiconductor lasers[154]. The advent of semiconductor lasers revolutionized many aspects of our life: data storage devices (CD/DVD), telecommunications, surgical systems, barcode scanners, printing and many others. The main benefits of semiconductor lasers that enabled all these technical advancements are their compactness, low cost, wide spectral range and excellent power efficiency.

Nowadays the main trends in the development of analytical instrumentation are in the reduction of size and cost while maintaining similar or even higher efficiency. Therefore, there are no doubts that semiconductor lasers will continue to be an important class of excitation sources for Raman spectroscopy.

3.3.1. Basic physics of semiconductor lasers

The theory of semiconductor lasers is well documented[155-157]. In this Section, only the most important aspects relevant to Raman spectroscopy will be presented. The majority of semiconductor lasers are specially designed semiconductor diodes. Laser diodes have high energy conversion efficiencies, often exceeding 70%[158, 159], because they are pumped electrically and produce light directly in response to electric current. In fact, the active region of diode lasers is a part of the electric circuit and this makes them unique among all other laser types.

Before discussing the principles underlying the operation of diode lasers, some basics of semiconductor electronics should be considered. A semiconductor is a solid crystal material that has conductivity in between that of a conductor (metal) and an insulator (e.g. resin). Most electrons are bound in a crystal lattice by adjacent atoms. These electrons are fixed in the *valence band* and cannot conduct electricity. However, a very small fraction of electrons has sufficient thermal energy to escape from these lattice bonds and find themselves in the *conduction band*. This energy can also be acquired by absorbing a photon. Once this transition occurs an uncompensated positive charge is formed in the lattice, which is called a "*hole*". Along with conduction electrons, this charge can travel in the crystal and therefore contribute to conductivity. Hole conductivity is performed by means of multiple "jumps" of adjacent valence electrons.

Although the conductivity of pure semiconductors (such as silicon) is very low at room temperature, it can be significantly increased by doping a crystal with very small concentrations of impurities. The atoms of a doping element replace host atoms in the lattice and if their electronic structures are different, this process creates an excess, or lack, of electrons in the crystal. For example, a silicon atom has 4 valent electrons; if it is replaced by arsenic that has 5 valence electrons, the fifth electron will be superfluous in the silicon crystal lattice. In contrast, doping silicon with boron

results in electron deficit or, in other words, excessive positive charges (holes) in the silicon lattice. However, it should be remembered that in both cases these charges are excessive only in terms of the crystal lattice, while electro-neutrality of the doped material is maintained. In other words, "excessive" carriers (electrons and holes) have increased energy and can be more easily transmitted to the conduction band that results in the higher conductivity of doped semiconductors. Impurities that create excessive electrons or holes are called n- and p-dopants, respectively. In n-doped semiconductors, electrical current is carried by electrons, while in p-doped semiconductors – by holes.

The most important and interesting events occur when n- and p-doped regions are in direct contact with each other. Electrons from the n-region diffuse to the p-region and recombine (annihilate) with holes. Similarly, holes diffuse from the p- to the n-part of the crystal and recombine with electrons. This process results in two effects:

(i) the concentrations of both electrons and holes in p-n junction are remarkably reduced – therefore, the p-n junction is also called the *depletion region*;

(ii) although electrons and holes are annihilated in the p-n junction, this is not a "true" annihilation because the lattice does not compensate excessive charges that came by diffusion and the neutrality condition is broken – as a result, an internal electrical field is established across the depletion zone that prevents further carrier diffusion.

The *p-n junction* is the key element of many semiconductor electronic devices. It operates as a diode by the following mechanism (Figure 3.14). If an external voltage V is applied at the same polarity as the internal potential E_{int} (reverse bias), the depletion region becomes larger and the p-n junction acts as an insulator. It can also act as a photodetector because electron-hole pairs created in the p-n junction by absorbing a photon are separated by an internal field and create electric current. In contrast, if the external voltage V has opposite polarity to E_{int}, the depletion zone is reduced and when $V > E_{\text{int}}$ electric current will flow across the p-n junction.

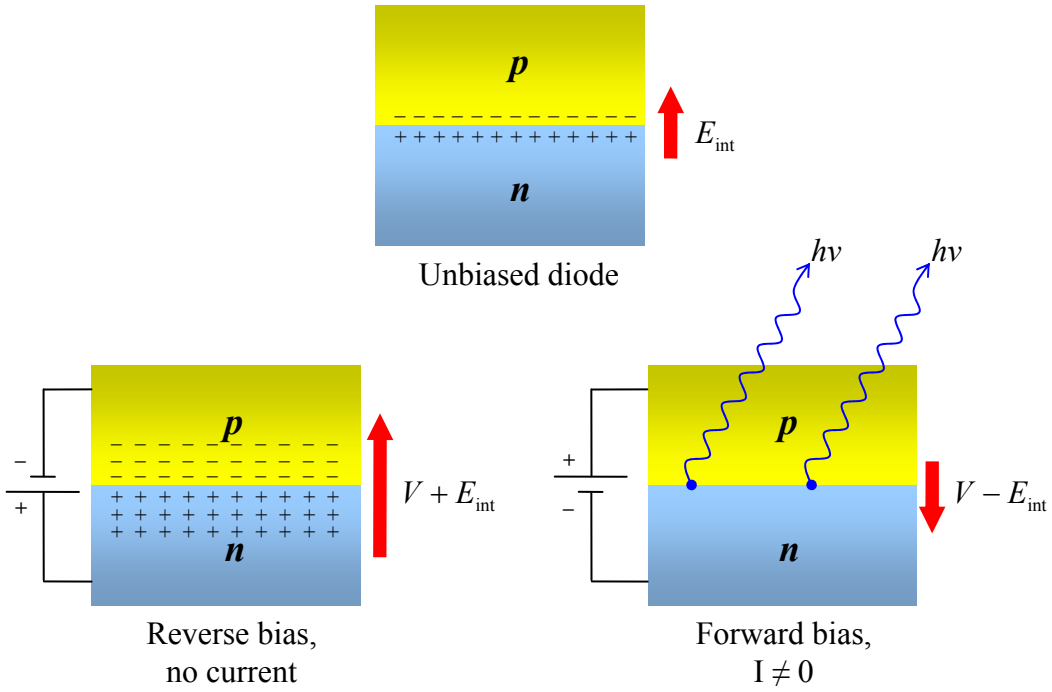

Figure 3.14. Schematic drawings of a semiconductor diode at different bias voltages.

The electric current causes recombination between electrons and holes that can be accompanied by release of a photon. This is the principle of operation of light-emitting diodes (LED). Diode lasers work according to a similar principle except for a few design considerations that must be met to ensure satisfaction of the two conditions applicable for all lasers: (1) population inversion, and (2) stimulated emission energy loss exceeding all other loss mechanisms. The first condition is met by higher dopant levels and higher current densities, while the second condition is satisfied by a special design allowing efficient feedback and light confinement within a resonant cavity.

Laser diodes can be manufactured relatively inexpensively by means of well established techniques: photolithography and vapour deposition. P- and n-doped layers are progressively deposited on the semiconductor substrate surface (usually Ga(Al)As) to form a p-n junction. A resonant cavity in the simplest form is created by polishing the diode facets; the high refractive index of GaAs provides relatively high reflectivity – about 30%. Alternatively, dielectric coatings may be deposited on the facets to increase or decrease reflectivity. Light emitted in the direction

perpendicular to the polished facets is amplified by stimulated emission. When stimulated emission becomes higher than all other optical losses in the cavity, the device starts lasing. It occurs at a certain current value called the *threshold current*. The scheme of a simplest laser diode and typical current-power characteristics for diode lasers are shown in Figures 3.15 and 3.16.

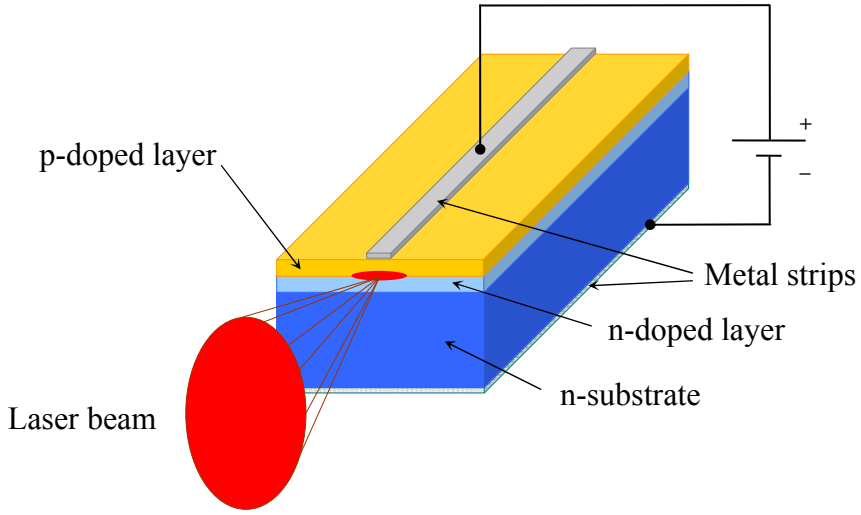

Figure 3.15. A homostructure laser diode.

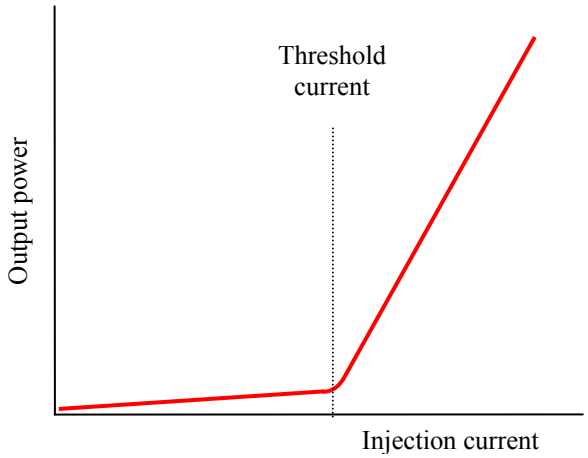

Figure 3.16. Typical current-power characteristics of a diode laser.

The laser diode shown in Figure 3.15 has only two different layers and is referred to as a homostructure laser. These lasers are not used today because they have high threshold currents and operate only at very low temperatures. Much more efficient devices are made from several composition materials and called heterostructure lasers. The most common type consists of an active layer of p-GaAs sandwiched

between p-GaAlAs and n-GaAlAs[154]. Heterostructure lasers operate in exactly the same way as homostructure lasers, but due to discontinuities of physical parameters at the boundaries between the different composition materials, the active region can be made much smaller. For example, in *index-guided* lasers the material surrounding the active region has a lower refraction index such that light is confined by total internal reflection. *Gain-guided* diodes use restricted electrode contacts (as shown in Figure 3.15) to confine the current and therefore improve laser emission. In both cases light propagates through a very narrow "tube" with thickness of the order of 0.4-5 μm and length 1-5 mm[154, 158, 159]. Such tight spatial confinement (comparable to the wavelengths of light) and the high refractive index of crystals cause diffraction and refraction on the end facet, so the output beam divergence is very high: about 30° vertically and 10° laterally. It is, however, easy to collimate the output beam.

At a given temperature the operating wavelength depends on the design and composition of a semiconductor material and can vary widely from 370 nm[160] to more than 2000 nm[161] covering all excitation wavelengths used in Raman spectroscopy (except for UV). Each laser can emit in a maximum range of a few tens of nanometres. Tuning can be accomplished by temperature or controlled external optical feedback (see Section 3.3.2).

The gain curve is determined by the population inversion achievable by the material at different wavelengths. In addition, since the two polished ends of the semiconductor crystals form a Fabry-Perot interferometer, wavelength tuning is not continuous but discrete corresponding to Fabry-Perot maxima. This is illustrated in Figure 3.17.

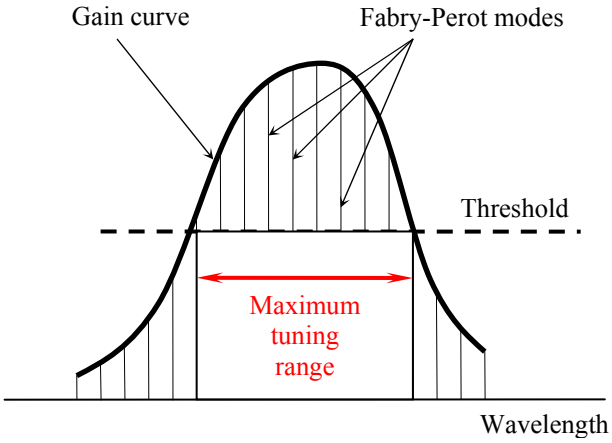

Figure 3.17. The gain curve and mode structure of a laser diode.

As already mentioned above, the majority of diode lasers used in Raman spectroscopy is made from AlGaAs/GaAs/InGaAs heterostructures. This composition provides lasing in the range of 640-1080 nm[154, 159] covering the most popular excitation wavelengths in Raman spectroscopy. Although there are many other semiconductor materials, only semiconductors of the *direct bandgap* type can satisfy the threshold condition for laser emission. The rate of stimulated emission is too slow in indirect bandgap semiconductors regardless of population inversion. For example, silicon has an indirect bandgap and cannot be used in laser diodes.

3.3.2. Stability, spectral control and external feedback

Figure 3.17 shows that several Fabry-Perot modes lie within the gain curve above the threshold, and this allows diode lasers to emit at several wavelengths simultaneously. These lasers are called multimode lasers and they are not suitable for Raman spectroscopy. Specially designed *single-mode laser*s emit only one wavelength at a time, but the lasing wavelength is usually unstable unless measures are implemented to stabilize the wavelength. A common phenomenon is *mode hopping*[162] induced by changes in injection current, temperature or undesirable external optical feedback. Electric current changes the temperature and sometimes the refractive index of the active medium, both causing alterations of the effective length of the Fabry-Perot cavity and/or shift of the gain curve.

External photons entering the cavity can be amplified by stimulated emission and cause the diode to lase at another wavelength. Eliminating these effects is not an easy

task. Moreover, once the wavelength has been suddenly changed it is impossible to restore it quickly. It may seem to be not a big issue as, firstly, the hops are insignificant – not more than 1 nm for 785 nm diodes – not enough to compromise the performance of notch filters, beamcombiners, etc; and, secondly, changes in wavelengths are not accompanied by changes in power and do not deteriorate Raman spectra. As long as mode hops do not occur during spectrum acquisition the whole spectrum is uniformly shifted along the wavenumber axis, which can be monitored with an internal standard and corrected by software. However, when the laser wavelength changes in the process of acquiring a Raman spectrum, the spectrum will be distorted, with bands widened or doubled. These spectra cannot be used for accurate analysis. Therefore, it is preferable and generally accepted to adapt diode lasers to stable single-frequency operation.

Following the discussion provided above it is clear that three measures must be taken to ensure wavelength and power stability: (1) power control; (2) temperature control; (3) eliminating unwanted effects of optical feedback. The first condition is realized by using precision current drivers that provide very stable output, sufficient to achieve shot-noise limited operation. Temperature is controlled by mounting the diode into a metal housing that serves as a heat sink. The heat sink is connected to a thermoelectric cooler and thermocouple providing a feedback loop. In modern devises, the laser active region lies within a few microns from the heat sink surface that ensures constant temperature operation and reduces the probability of mode hops[163]. The third measure, eliminating unwanted optical feedback, is hardly achievable. A way to deal with it is to deliberately create such feedback that will stabilize operation and make the diode insensitive to any other light. The effect of optical feedback on diode lasers has been explicitly studied in many works[89, 164-167]. It was shown that depending on its strength the feedback could either stabilize or destabilize lasers. Strong narrow-band feedback from reflective diffraction gratings not only can stabilize single-mode operation but also improve the beam quality: reduce linewidth and suppress side modes. Many arrangements are suggested to achieve this goal[168-174], the most popular being Littman[175] and Littrow[176] configurations. All grating-stabilized diode lasers are called External (or Extended) Cavity Diode Lasers (ECDL).

In the Littrow configuration (Figure 3.18), a grating reflects the first-order diffraction beam back to the diode while the zero-order beam becomes an output. Wavelength tuning is achieved by tilting the grating. This setup is very efficient because the grating can be blazed for a particular wavelength and provide relatively high diffraction efficiency in the first order – up to 80%. A drawback of Littrow ECDLs is that when the grating is tilted, the output beam changes its direction. Nevertheless, it can be corrected by various technical tricks. For example, with chirped gratings wavelength selection can be done by translating the grating along its plane without any need to rotate it[173]. Another method of keeping the beam direction during the wavelength tuning is to direct the output beam to a mirror fixed parallel to the rotating grating[170]. In this case the mirror compensates the angular displacement of the beam caused by the grating rotation.

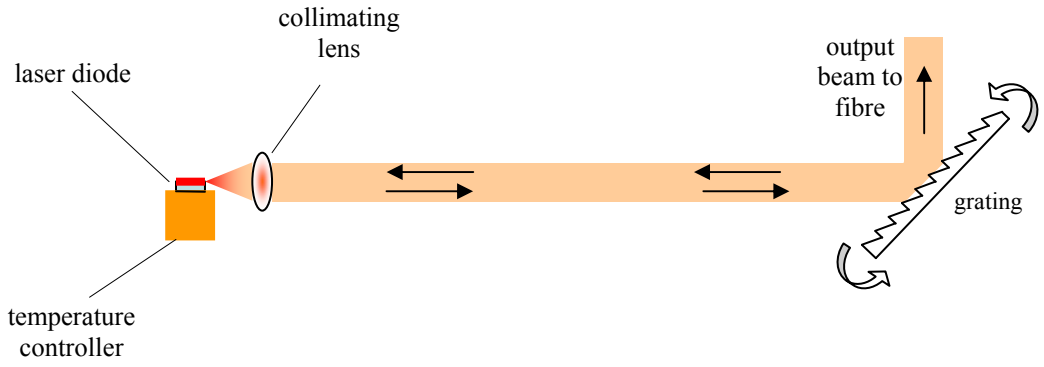

Figure 3.18. ECDL in Littrow configuration.

The Littman configuration is another well known arrangement for ECDLs. It is schematically shown in Figure 3.19. As in the Littrow layout, the laser output is formed by zero-order reflection from the grating. The difference is in the grating being located at grazing incidence so that the first-diffraction order beam is reflected in another direction – away from the diode. An external mirror then reflects this beam back to the grating, and the grating "rediffracts" it to the diode. By tilting the mirror, the laser can be tuned. Since the grating is fixed, directional stability of the output beam is very high. Another advantage is much purer feedback due to double diffraction. However, the efficiency is lower than in a Littrow-ECDL because the 0^{th} order diffraction beam from secondary diffraction is lost. The Littman arrangement is

often used in applications where laser tunability is very important. However, in Raman spectroscopy it is not and Littrow ECDLs are preferred.

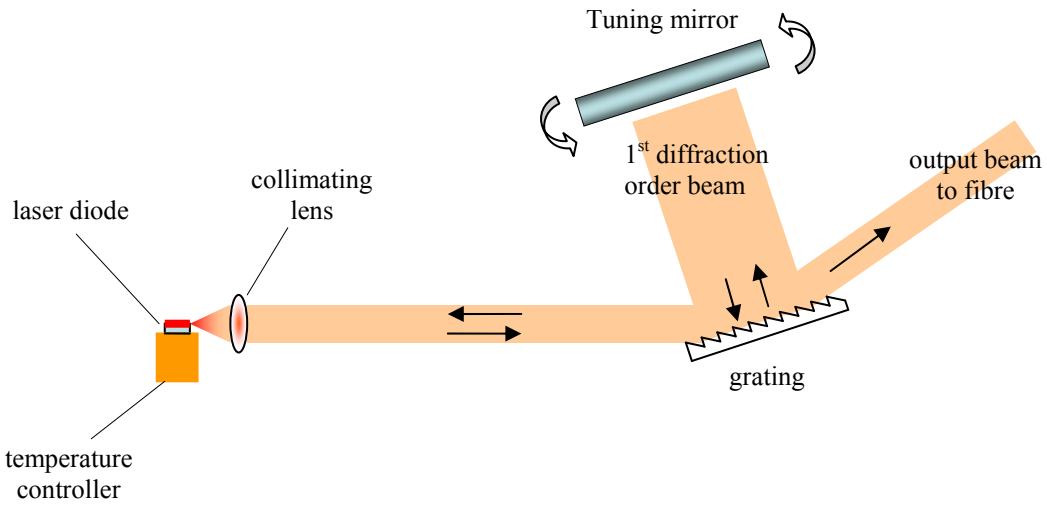

Figure 3.19. ECDL in Littman configuration.

Two more general remarks should be made in regard to external-cavity diode lasers. The first is the necessity of preparation of the laser diode to external-cavity operation. An external grating acts as a coupling mirror and therefore creates another cavity, which "competes" with the internal diode cavity. This competition makes it difficult to stabilize the laser and often results in significantly less stable output than that of a single laser diode. To eliminate this effect an anti-reflection (AR) coating is deposited on the front facet of the diode. This prevents the front facet from acting as a mirror and, hence, eliminates mode competition. Because of the tiny dimensions of laser diodes this procedure is costly but worth doing. For even better efficiency, the rear facet can be covered with a high-reflectivity (HR) coating.

The second remark concerns an important property of ECDLs. Since an external cavity is much longer (2-20 cm) than a single laser diode, the spacing between the Fabry-Perot modes in the extended cavity is a lot narrower resulting in a nearly continuous tuning capability.

Although ECDL technology allows reliable single-mode operation, which is so important in Raman spectroscopy, it also involves some issues related to increased probability of permanent damage of the active medium and particularly the front

facets of laser diodes. Degradation of the laser diode facets occur due to generation of surface defects and oxidation of aluminium-containing semiconductor material[163]. The defected regions distort light refraction paths and cause an increase of threshold current and decrease of slope efficiency[177]. Apart from gradual degradation there is also danger of instantaneous catastrophic damage, which can be caused by high currents[178]. This is why for example, laser diodes are very sensitive to static discharges. Another cause of catastrophic optical damage is very high photon density when strong optical feedback is provided[179, 180]: it can cause local melting of the front facet and damage the laser permanently.

Because of power density limitations, high-power ECDLs for Raman spectroscopy are most often made from *broad-area laser diodes* (BAL)[181, 182]. Their emitting region on the front facet has the shape of a long stripe – typically 1×100 μm. Due to this asymmetry, such diodes have poorer spatial beam quality, but it can be corrected to some extent by proper collimation and fibre-coupling. Fibre-coupled BAL ECDLs in the Littrow configuration became one of the most popular types of lasers for routine Raman measurements. They have high power (up to 1-2 watts), excellent stability, narrow linewidths as well as long lifetime (several tens of thousands of hours). However, extended cavity, collimating optics and control electronics all make them big and heavy, with weight often exceeding 1 kg[93].

An alternative way to stabilize diode lasers is to integrate the grating into the diode itself. One type of these devices is the *distributed feedback laser* (DFB)[183], where the active medium is structured as a diffraction grating. This integrated grating acts as a distributed reflector and provides wavelength-selective feedback for single-mode operation. In DFB diodes, facet reflectivity is not necessary and anti-reflection coatings are often used.

Distributed Bragg Reflector lasers (DBR) have one or two integrated Bragg reflectors separated from the active region. Essentially, DBR is a Bragg mirror, i.e. a periodic structure providing efficient reflection in a narrow wavelength range. Bragg mirrors consist of an alternating sequence of layers of two different materials. To ensure the high reflectivity, the refractive indices of these materials should be highly different. The thickness of each layer corresponds to one quarter of the wavelength

for which the DBR is designed. This structure provides constructive interference of the reflected beams and, therefore, high reflectivity at certain wavelengths. Both DFB and DBR lasers are less sensitive to temperature variations than traditional single-mode diodes. Temperature changes cause smooth alteration of the effective grating spacing, allowing tunability over a range of several nanometres without mode hopping.

3.3.3. Vertical-cavity surface emitting lasers

A type of DBR lasers are *vertical-cavity surface emitting lasers* (VCSEL)[157]. Although these are regarded as a separate class of diode lasers, their structure is very similar to that of DBR diodes. The only essential difference is that light propagates in the direction perpendicular to the semiconductor wafer surface. The cavity length is therefore very small that results in a number of special properties of VCSELs such as better beam quality and excellent heat dissipation. Electrically-pumped VCSELs are increasingly useful in modern optical communications and as part of miniature chemical sensors[146]. However, their output power is limited only to a few milliwatts.

The upper power limit for stable single-mode operation in VCSELs is dictated by the uniformity of free carrier concentration and, therefore, uniformity of current injection across the lasing area. At present, it is possible to achieve stable operation only for beams diameters up to 10 μm[184]. Scaling to higher power requires larger surface areas, with diameters of tens to hundreds of micrometres. A solution to the problem of uniform creation of free carriers in the laser cavity is optical pumping where the lasing area is illuminated by another laser beam. To realize this, the laser cavity is extended and the gain medium is illuminated by a pump laser as shown in Figure 3.20. These lasers are known as *vertical-external-cavity surface emitting lasers* (VECSEL) or optically pumped semiconductor lasers (OPSL), and they are a separate class of semiconductor lasers, contrasting laser diodes. VECSELs are capable of generating high quality diffraction-limited output with stable wavelength and power of up to several watts. The good beam quality can be maintained over a wide power range of up to 4 orders of magnitude. Therefore, VECSELs can become potentially an excellent excitation source for Raman spectroscopy. At present, however, the main excitation sources in benchtop Raman systems are ECDLs, while

DBR and DFB lasers proved promising for compact devices. Optically pumped semiconductor lasers can be suitable in applications where high-power high-quality laser beams are required, e.g. in Raman analysis of gases, clear liquids or in Raman microscopy. Fast development of semiconductor laser physics does not allow a more detailed conclusion as many new types of lasers emerging from photonics laboratories have not yet been tested for compatibility with Raman spectroscopy.

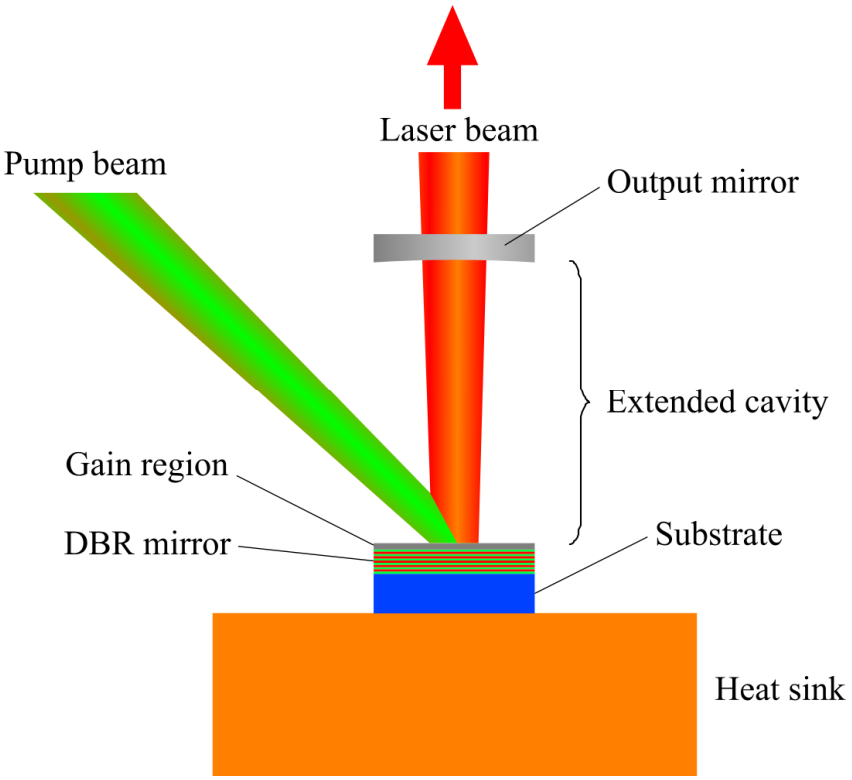

Figure 3.20. Schematic of a VECSEL (adapted from [184]).

4. Development of a Raman probe for analysis of liquids

4.1. Intracavity Raman spectrometry

There are increasing numbers of applications where instead of versatile and expensive instruments people need cheaper, smaller and low power systems that are optimised for a certain application. This approach led to the development of two signal collection techniques suitable for a particular application: Kaiser's PhAT probe, designed for focus-free analysis of solids, and spatially offset Raman spectroscopy intended for analysis of turbid media (see Section 2.3.3). Liquids are usually analysed with back-scattering Raman probes (see Section 2.3.2) that are attractive due to their compactness and the ability to be used with various optic heads (e.g. immersion probes or microscope objectives). This flexibility makes back-scattering Raman probes suitable for many applications. However, there is a potential to improve performance of the probe when it is used for a particular application at the expence of losing some flexibility. An example of such an application is analysis of transparent liquids in flow cells. In this case the Raman probe does not need to be flexible and can be configured for safe operation with a high-power excitation laser to improve the signal-to-noise ratio. In addition, optical components of the Raman probe can be optimised for more efficient signal collection with the particular optic head.

Lasers with extended cavities such as ECDLs and VECSELs allow samples to be put inside the cavity. For analytical spectroscopy two advantages can be gained from this sampling approach. The first advantage stems from the fact that laser emission is very sensitive to extinction inside the resonator. If a sample absorbs laser emission, it can be detected with high sensitivity when placed inside the cavity. This phenomenon is employed in intracavity laser absorption spectroscopy (ICLAS)[185] – a technique that became popular in gas analysis.

Beneficial for Raman spectroscopy is another advantage that comes from increased laser power. If resonator losses are low or, in other words, the laser has a high Q-factor, intracavity power can be significantly higher compared to output power. As

the probability of scattering is low, it will not make a significant contribution to intracavity losses. Therefore, clear non-absorbing samples must produce increased Raman signal in the case of intracavity excitation. This idea was first implemented by Weber et al.[186] only a few years after the first laser-excited Raman experiments. In their work the intracavity device was made from a HeNe laser and was used to observe rotational Raman bands of gases. Since then intracavity Raman spectrometry for gas analysis has become quite common, with a few more works having been published in the 1970-1980s[187-189].

In 1972 Neely et al.[187] presented a way to modify a commercial Ar-ion laser for intracavity Raman experiments at a relatively low cost. A power gain factor of 20 was achieved for the modified laser. A year later Hickman and Liang[188] improved suppression of the side modes of the Ar-ion laser and achieved a 30-fold intracavity enhancement of the Raman signal. Finally, Hercher with co-workers reported an intracavity power of 160 W with an Ar-ion laser whose nominal output power was 1 W[189], giving a corresponding enhancement of the Raman signal.

An example of an industrial application of intracavity illumination in Raman spectroscopy is a gas analyser developed by Atmosphere Recovery, Inc. The analyser is capable of monitoring 8 species in the gas phase[190]. It consists of a gas flow chamber located inside the laser cavity and is equipped with 8 optical windows that transmit the Raman scattered light to the individual sensors. Each sensor has a coating that transmits only a specific wavelength equivalent to a certain Raman band of a certain molecule.

In all these examples 90°-signal collection geometry was employed, probably because it is the simplest way to arrange collection of Raman scattered photons. Intracavity illumination makes it particularly difficult to organise on-axis signal collection. No back-scattering configuration (which is very popular today) is possible because laser light travels backwards and forwards in the cavity. As 90° geometry is very inconvenient for analysis of liquids, it is not surprising that no attempts to apply the intracavity scheme for analysis of liquids were reported in 1970-1980s. However, it is surprising that the subsequent appearance of dielectric beamsplitters allowing efficient on-axis signal collection as well as analysis of liquids did not revive interest

in this field. To the best of our knowledge, no work on the intracavity enhancement of the Raman spectrometry of liquid samples has been published since that time.

The first stage of the present research was to design a Raman probe optimal for sampling transparent liquids. The work described in this Chapter was carried out in two parallel tracks. The first direction concerns intracavity Raman spectrometry when the sample is placed inside the laser cavity where the light intensity is higher and the Raman signal is increased without additional power consumption. The second direction is related to conventional Raman spectrometry and devoted to finding a more efficient optical layout for signal collection from liquids. The development of the latter resulted in a substantial signal improvement, with signal-to-noise ratio values being competitive with the existing commercial systems.

4.2. Experimental

4.2.1. Commercial equipment

Spectroscopic equipment. The instrumentation described in this Section is manufactured by Kaiser Optical Systems Inc., USA. Raman spectra were recorded with a modified "Holoprobe 532" spectrometer adapted to operation with 785 nm excitation wavelength. The schematic of the spectrometer is shown in Figure 3.4.

All optics inside the spectrometer have the aperture ratio f/1.8 with a focal length of 85 mm. The slit size is 50 μm and the average spectral resolution is 5 cm^{-1}. A holographic notch filter with optical density of 6 at the laser wavelength provides rejection of the Rayleigh scattered laser light. The VPH transmission grating is optimised for excitation at 785 nm. The detector is a charge-coupled device, with an 1024×256 array of 26 μm square pixels. The CCD-camera is thermoelectrically cooled and operated at -40°C to reduce the dark current. The readout noise is 1-1.2 counts. Full well capacity of a single pixel is 400,000 electrons. The AD converter is 16 bit.

A "MultiRxn Probe-830" was used for 90°-signal collection experiments. It is designed for an 830 nm laser and equipped with a non-contact optic head (70 mm

focal length and 25 mm aperture). The probe was mounted in XYZ-translation stage for precision alignment and fibre-coupled with the spectrometer.

Cuvettes. For the 90º-signal collection configuration, a 1 cm quartz cuvette (Commack, UK) with four clear windows and without AR coating was used. The back-scattering and intracavity Raman experiments were carried out using a 1 cm AR-coated cuvette with 2 clear windows (Hellma, UK).

In order to prevent resonator stability disturbance by laser reflection from the cuvette walls, the cuvette was slightly tilted in all experiments.

Laser system and controlling electronics. For intracavity experiments in the 90° configuration a temperature-stabilised ridge-waveguide laser diode (model LD-0850-0050-AR-4, Toptica Photonics AG, Graefelfing, Germany) with maximum output power 80 mW was used as an excitation source. It had an AR-coating on the front facet and was tunable from 815 to 855 nm. The operation wavelength was chosen to be 830 nm. For temperature control, the diode was mounted in a cylindrical copper tube connected to the Peltier element and the temperature controller (model 350, Newport Inc, Irvine, California, USA). Laser output power stability was maintained by a precision current driver (model LDC402B, Profile GmbH, Munich, Germany); the diode operated at the fixed current of 170 mA at all times. Output light was collimated by a lens with 0.49 numerical aperture (Olympus Inc., Melvile, New York) and 4.5 mm focal length (*L-4*).

For the back-scattering experiments, the same components were used except for the laser diode which was a 785 nm uncoated edge-emitter (Sanyo DL7140-201S) with index-guided structure and maximal optical output of 70 mW.

Collection optics. In the back-scattering experiments the Raman photons were collected with a graded index glass fibre (Model GIF 625, ThorLabs Inc., USA), with the core diameter 62.5 μm and numerical aperture 0.275. The fibre position was controlled by the XYZ-translation stage. The optics used to focus Raman photons to the fibre tip are described below.

4.2.2. Custom optical arrangements

90° intracavity experiments with a 830 nm laser. Apart from the commercial Raman probes described above, a number of self-made optical arrangements for signal collection were built. These are schematically drawn below. The detailed description and the reasons for switching from one configuration to another will be provided in the subsequent Sections with the references made to the schematics.

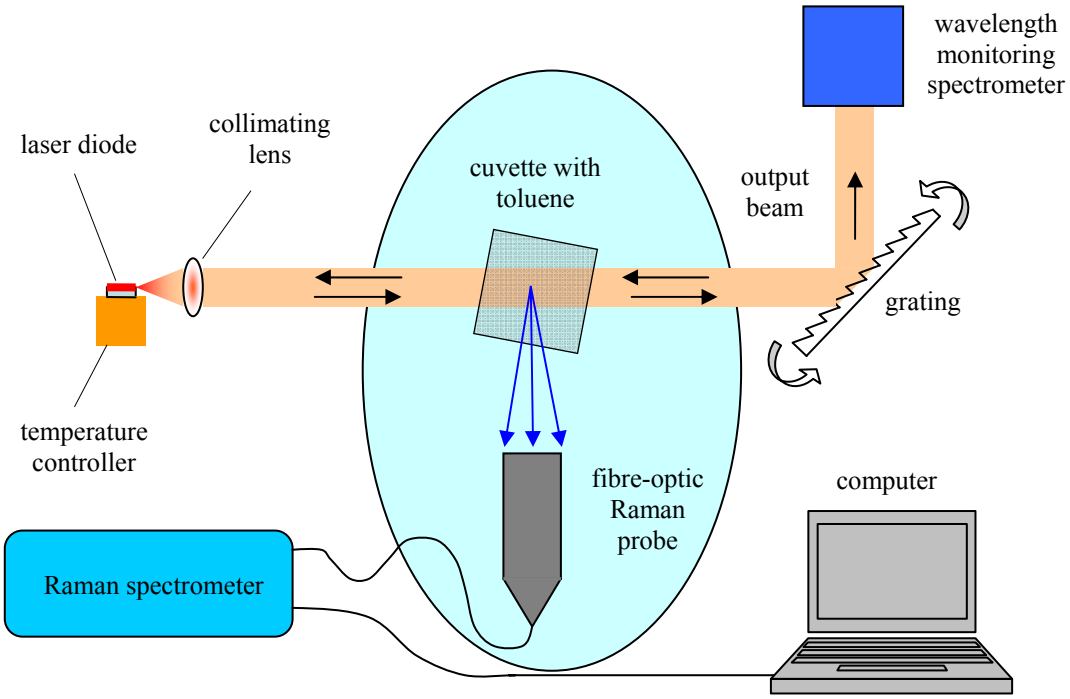

Figure 4.1. A schematic drawing of the 90° collection setup.

The general experimental setup for 90° Raman measurements is shown in Figure 4.1. Components where modifications were made have been highlighted and the details are given in Figure 4.2.

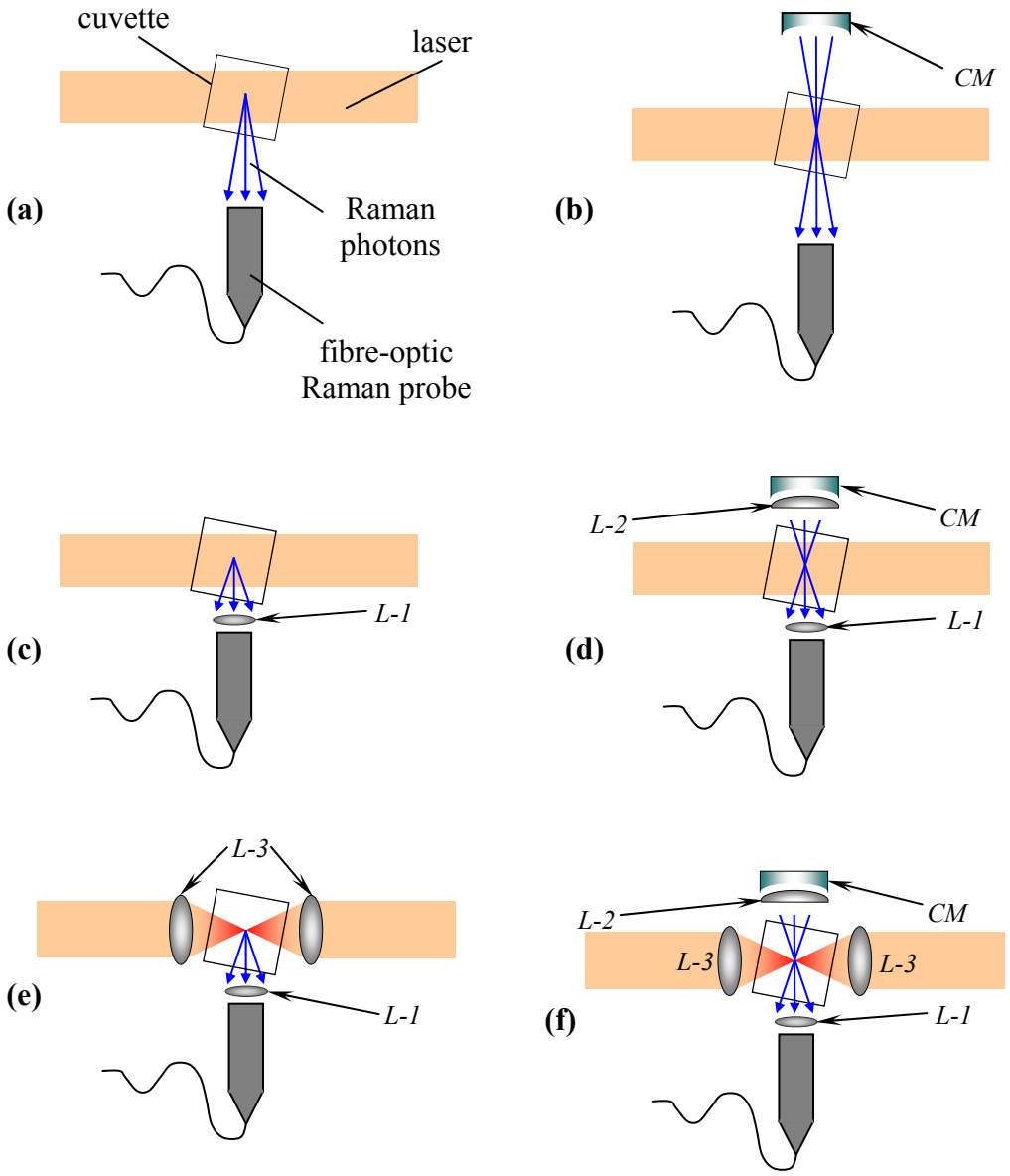

Figure 4.2. Part of the setup from Figure 4.1 showing evolution of the signal collection layout for 90° Raman measurements. *CM* stands for the concave mirror; *L* is a lens. (a) initial setup; (b) *CM* is added to reflect and collect the Raman photon scattered to the opposite side of the probe; (c) *CM* is removed and an additional lens is attached to the probe optic head to increase numerical aperture; (d) *CM* and *L-2* are added; (e) *CM* is removed and two lenses are installed in the cavity with the cuvette between them; (f) *CM* and L-2 are added.

The concave mirror (Comar) (*CM* in Figure 4.2) has a focal length of 40 mm. The ruled gold grating has 1800 grooves per millimetre. It was mounted in the XY-mechanical actuator to form the Littrow configuration of the ECDL. By rotating the actuator's screws, the wavelength could be changed. The zero order diffraction beam

was directed to the fibre-optic spectrometer (model AVS-SD2000, Avantes Inc., USA) to monitor the laser wavelength.

The optical components used to construct the Raman systems are described in Table 4.1.

Table 4.1. Lenses used in the experiments (see Figure 4.5).

Lens	Focal length /mm	Aperture /mm	Type	Manufacturer and model
L-1	25	25	spherical, biconvex, AR-coated	Comar, 25 VB 25
L-2	62.9	25	spherical, plano-convex	Newport, KPX085
L-3	25	8	Aspheric multielement lens, AR-coated at 810 nm	Melles Griot
L-4	4.5	4.5 (NA=0.49)	aspheric multielement lens	Olympus

Backscattering experiments with a 785 nm laser. The general diagram of the back-scattering Raman experiments is provided in Figure 4.3.

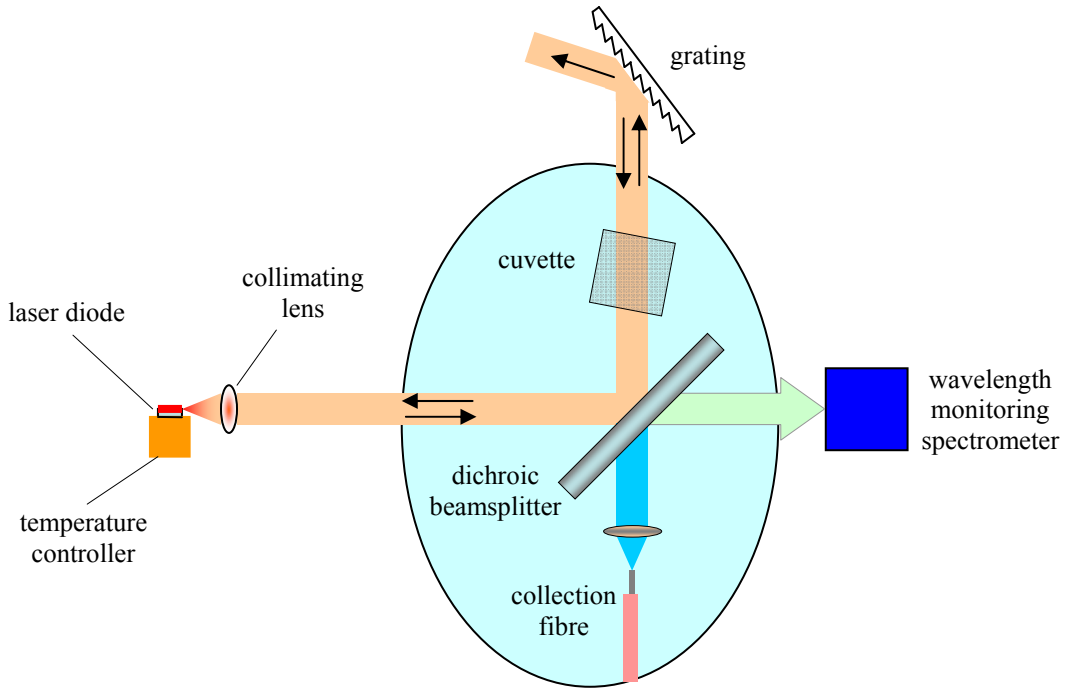

Figure 4.3. A schematic drawing of the back-scattering collection setup.

These experiments were conducted in either intracavity (with grating) or traditional non-intracavity configurations (without the feedback from grating). The key component of the back-scattering setup is the dichroic long-pass beamsplitter (Laser 2000, model LPD01-785RU-25). It combines the excitation and collection beams reflecting the laser light and transmitting the Raman photons. It has a measured transmittance of about 1% at 785 nm and 98% average at Stokes-shifted wavelengths (Figure 4.4).

The details of various modifications of the back-scattering setup are provided below in Figure 4.5. Further details and results for each setup will be given in Section 4.3.2.

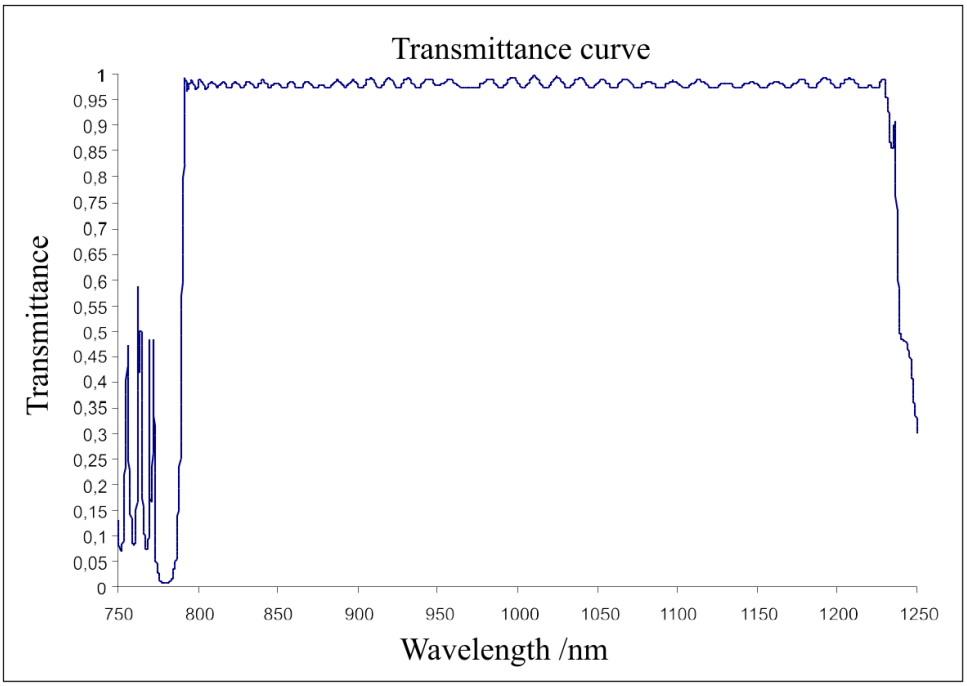

Figure 4.4. Transmission curve for the dichroic beamsplitter.

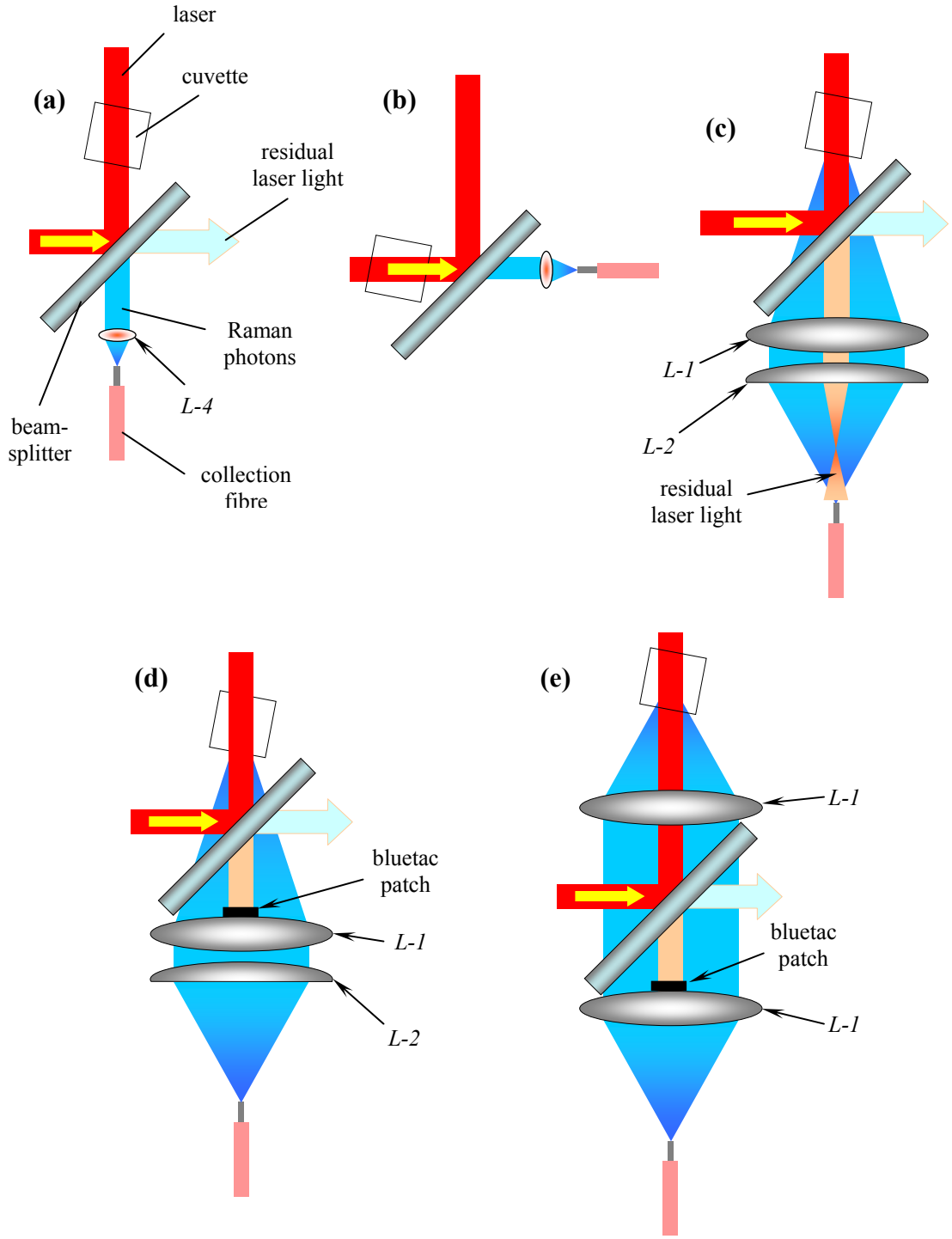

Figure 4.5. Evolution of the signal collection layout for 180° Raman measurements. The red lines denote the laser beam and the yellow arrows show the beam direction. The blue beam corresponds to the collected Raman photons.

The details of lenses denoted in Figure 4.5 were given in Table 4.1.

4.3. Results and discussion

4.3.1. 90° collection configuration

Although 830 nm is not a perfect excitation wavelength for detecting Raman photons with a silicon detector (due to its low quantum efficiency in the near infrared range), this fact was not a serious issue with regard to the main goal of the first set of experiments, which was to estimate the applicability of an intracavity illumination scheme for the Raman analysis of liquids.

Pure toluene was chosen as a sample compound because it is known to have a high Raman cross section and well resolved peaks (Figure 4.6).

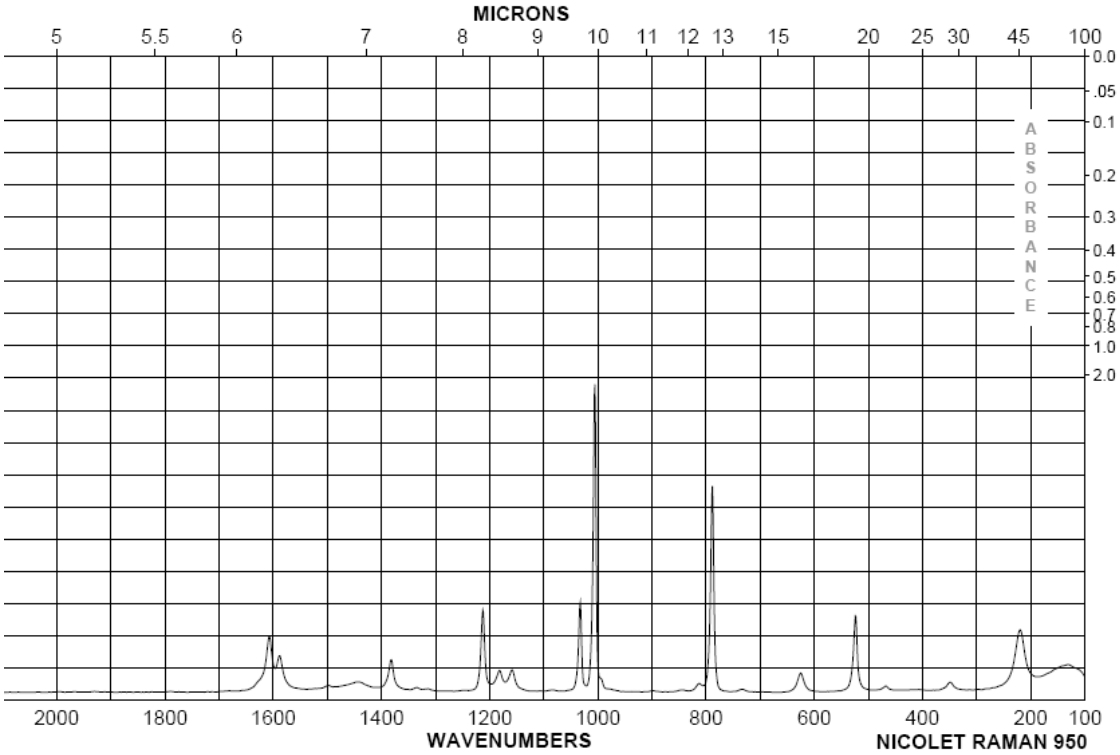

Figure 4.6. FT-Raman spectrum of toluene (the bands above 2000 cm^{-1} are not shown)[191].

Aligning procedure. The laser beam was not perfectly collimated. Therefore, in order to maximize feedback, the grating was placed roughly at the laser focal length (50 cm). The best position of the probe was estimated visually using a white light source coupled to the collection fibre of the probe. For the Raman signal to be efficiently collected, the laser beam must cross the collection beam at its focal point. The two

beams are relatively easy to match. However, when the cuvette with a liquid was inserted in the beam crossing region, the collection beam was significantly refracted. Therefore, it was only possible to estimate the right position of the probe. The only method of fine tuning was to follow the intensities of toluene Raman bands on the spectra continuously collected whilst turning the screws of the translation stage in which the probe was mounted. The best position of the probe corresponded to the most intense Raman signal. To discern the signal changes caused by the probe movements from noise, a good signal-to-noise ratio of Raman peaks must be achieved which was only possible provided that (i) the probe had already been close to the optimal position and (ii) long acquisition times of several seconds were used. Because of these difficulties and strong sensitivity of the signal obtained to the probe position it was not trivial to align the system.

A Raman spectrum of toluene collected at this stage (setup ***a*** in Figure 4.2) is shown in Figure 4.7. Despite the high spectral acquisition time of 120 s the spectrum in the Figure is noisy. In addition, it contains a broad background at low wavenumbers. The background shape is different from the typical silica Raman spectrum (Figure 2.5). It is likely that without the notch filter the background intensity would be very high in the region from 0 to 150 cm^{-1}. It suggests that the background could emerge from the laser's incoherent radiation elastically scattered from the sample.

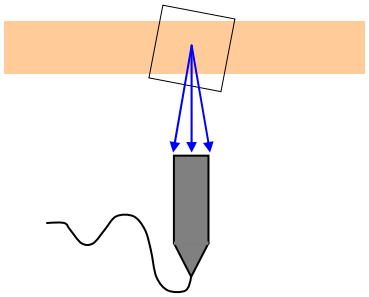

Figure 4.2a

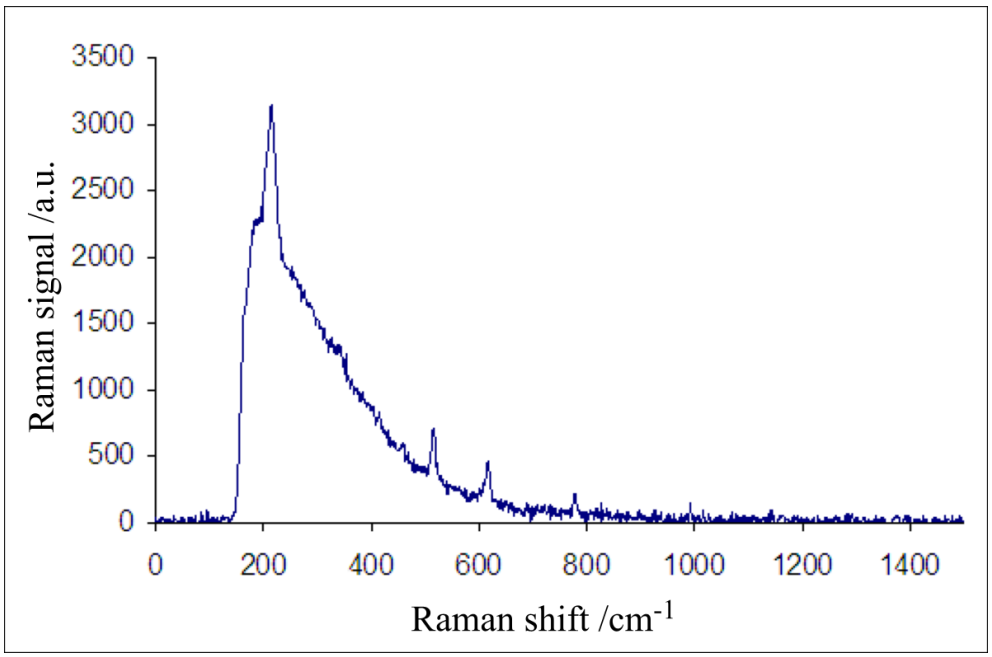

Figure 4.7. A Raman spectrum of toluene collected in configuration *a* (Figure 4.2). 120 s exposure time.

Optical modifications. Several setup modifications were attempted to enhance the Raman signal. Firstly, the concave mirror was placed behind the cuvette, which enabled Raman photons scattered to the direction opposite the probe to be collected (Figure 4.2b). Ideally, the signal should be doubled if the radius of curvature of the concave mirror coincides with collection beam focal length. However, these parameters were different (F_{mirror} = 40 mm against F_{probe} = 70 mm) and the enhancement factor was measured to be approximately 1.7.

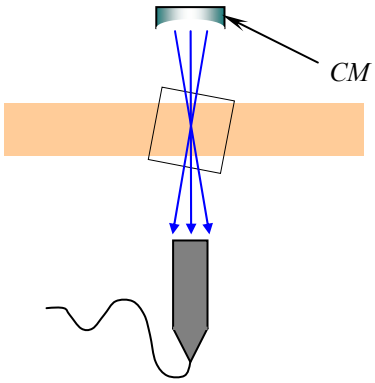

Figure 4.2b

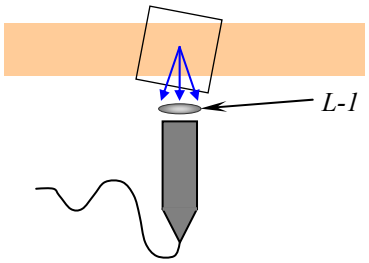

Figure 4.2c

The next step was decreasing the focal length of the collection optics to collect Raman photons from a greater solid angle (Figure 4.2c). This was realised by clamping lens 1 to the entrance aperture of the probe head. The focal length was thus reduced and the probe was brought closer to the cuvette. To take advantage of the concave mirror, its focal length was increased by attaching lens 2 (Figure 4.2d). However, installing the concave mirror did not result in notable signal enhancement as it was in the case of configuration b.

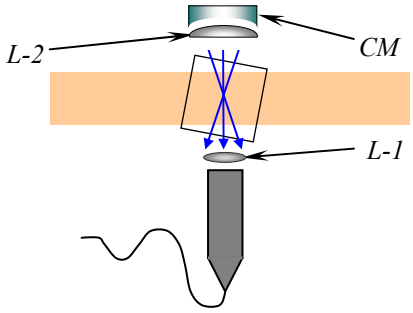

Figure 4.2 ***d***

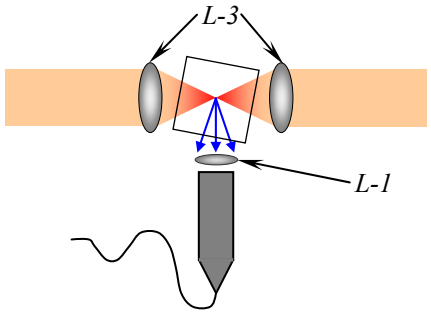

Figure 4.2 ***e***

It was found that the size of the laser beam was greater than that of the collection beam at the point of their crossing. In order to illuminate the sample more efficiently, additional lenses were installed inside the cavity on both sides of the cuvette, such that they focused the laser beam to the very point from which the scattered photons were collected (Figure 4.2e). This resulted in an increase of the laser power density and corresponding signal enhancement. Again, installing the concave mirror (Figure 4.2f) did not improve the signal considerably.

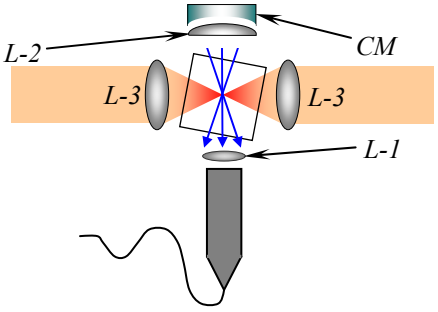

Figure 4.2 ***f***

The best Raman spectrum of toluene that was achieved in the 90° configuration is shown in Figure 4.8.

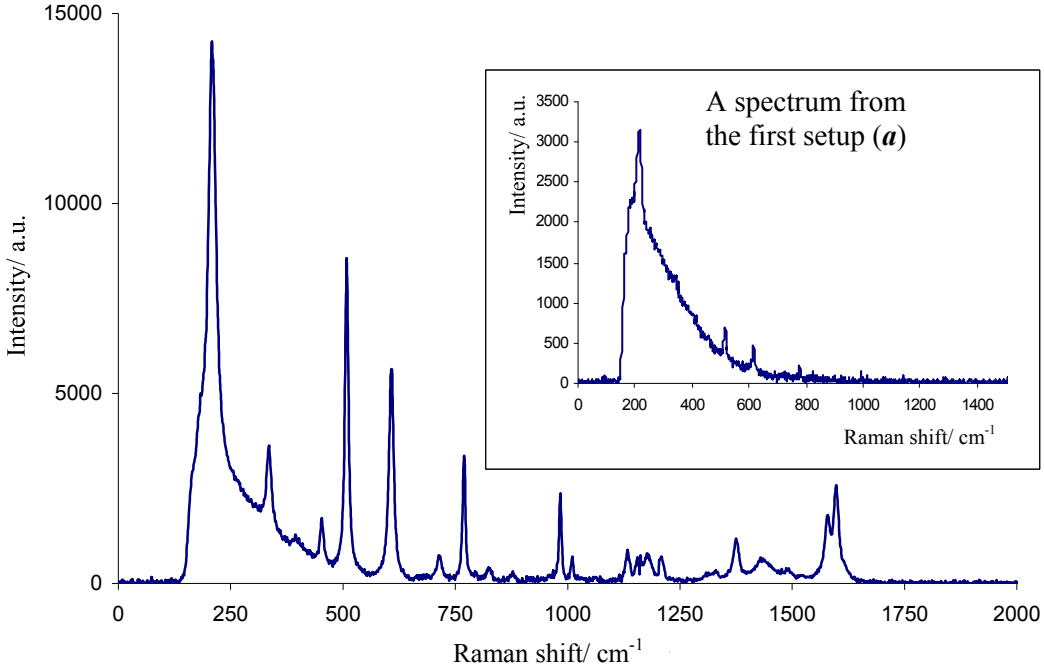

Figure 4.8. The final spectrum for 90° configuration (*f* in Figure 4.2) in comparison with the first spectrum (copied from Figure 4.7 for convenience). Exposure time – 120 s.

The signal-to-noise ratio (noise is calculated from the background as the standard deviation of the base line on the flat regions of spectra) achieved in these experiments was 45 for the 520 cm^{-1} toluene peak when a 2 s exposure time was employed, a notable improvement compared to the value of 13 obtained with configuration ***a***. Compared to the first spectrum obtained with setup in Figure 4.2a, the improvements are clear. However, unfortunately, there was nothing to compare these results with. Because of the poor sensitivity of silicon detectors in the near-infrared, 830 nm is rarely used with CCDs, and relative Raman peak heights obtained in this work are very different from those obtained with other excitation wavelengths. The next step of the research was to build a setup that would be more similar to existing Raman systems. To do so, it was decided to switch to 785 nm excitation and back-scattering signal collection.

4.3.2. 180° collection configuration

General considerations. In all the experiments the laser diode was operated at constant current (100 mA) and the temperature (20.4°C). The laser power at the

sample was measured to be 45 mW at these conditions, and the wavelength was 781 nm. The output wavelength was tunable from 778 to 784 nm by changing the temperature or grating position. The beamsplitter position was slightly tilted from 45° in order to ensure the maximum reflectance of the 781 nm laser beam. The distance between the beamsplitter and the laser diode was 130 mm such that the sample was in the focus of the laser beam. The laser spot size in the focus seemed substantially less than 1 mm. During the experiments the positions of the optical components were optimised by maximizing the non-intracavity Raman signal (setup without the grating).

Laser diode properties. Laser power stability was tested at different drive currents with a power meter. Power fluctuations were monitored for 12 minutes for each current value. The measured power instability was found to be 0.1% (Table 4.2) which is well below the relative shot noise values of all measured Raman signals.

Table 4.2. Output power stability of the 785 nm edge-emitting diode laser.

Current /mAmp	Measured power range /μW	Relative instability /%
60	266.4-266.7	0.11
80	722.2-723.0	0.11
100	1170-1171	0.09

Current-power characteristics at different temperatures were measured with a power meter. The results are plotted in Figure 4.9. In order to prevent catastrophic damage of the diode the current was not increased above the recommended operating value of 100 mA. For the same reasons the operating temperature was chosen to be reasonably low, i.e. 20.4°C.

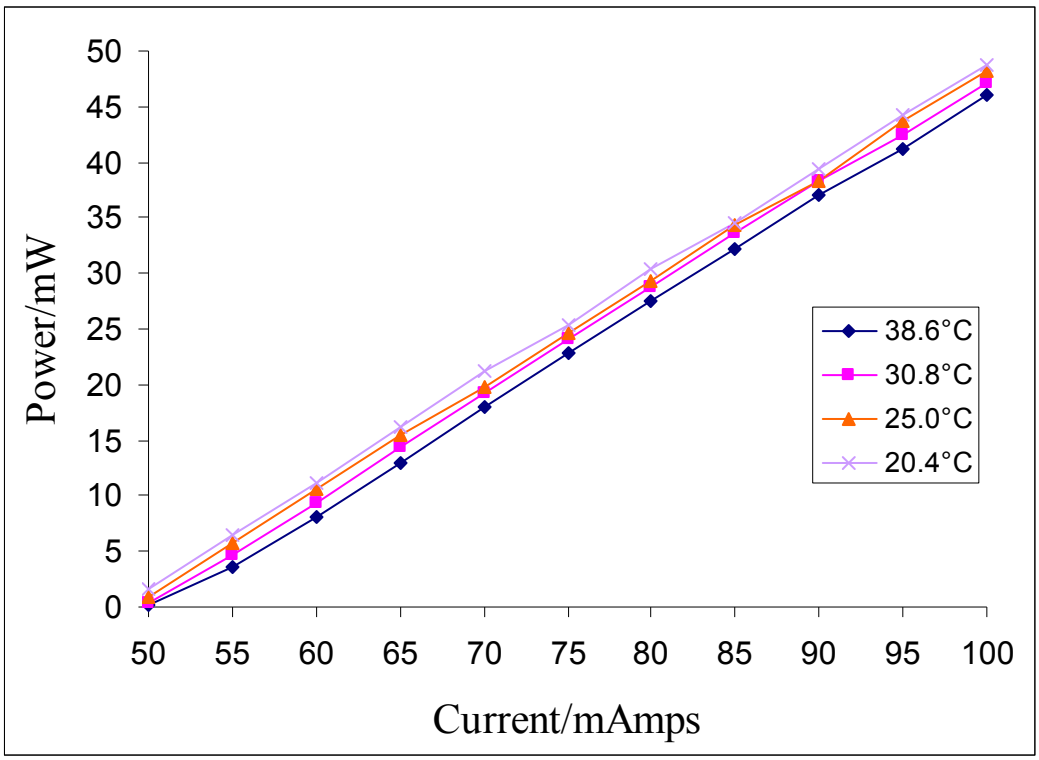

Figure 4.9. Power-current characteristics of the 785 nm diode laser at different temperatures.

The first 180° intracavity configuration. The first modifications of the back-scattering setup (Figures 4.5a and 4.5b) were built on the hypothesis that Raman photons propagating in the same direction as the laser beam might be amplified within the semiconductor gain medium, then come back to the extended cavity and finally reach the detector. To test this conjecture only a front-scattering configuration might be used as shown in Figure 4.5b because back-scattering collection would mean that the amplified Raman photons would be lost by transmission through the dielectric beamsplitter. However, it was decided to try the back-scattering configuration shown in Figure 4.5a first. The collected toluene spectrum without external feedback from the grating is shown in Figure 4.10.

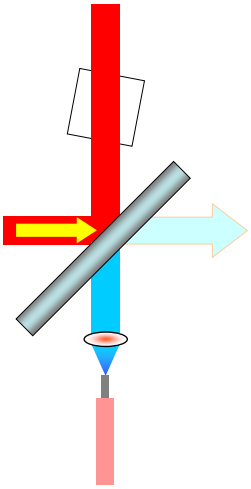

Figure 4.5a

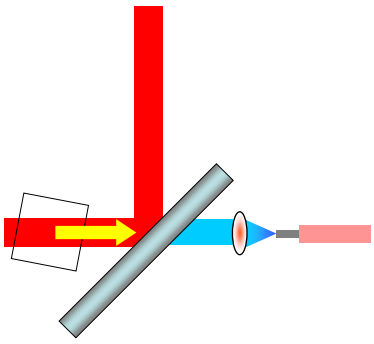

Figure 4.5b

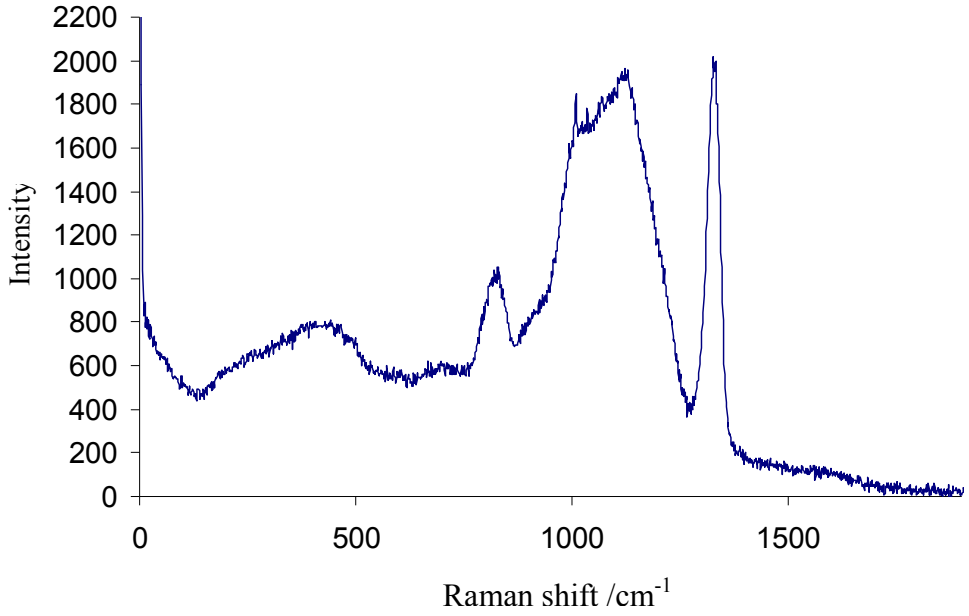

Figure 4.10. The spectrum recorded from configuration *a* in Figure 4.5 (without grating). 10 s acquisition time.

It is clear that this configuration does not give satisfactory results, with only one toluene peak (at 1007 cm^{-1}) being found on the high background. The background has an unusual shape with a high and wide peak at 1300 cm^{-1}, which might be caused by external light, side modes of the laser diode or emanate from the beamsplitter coating.

When the spectra were acquired in the intracavity regime (with grating), the background was so high that only a few milliseconds were enough to overfill the detector, and no Raman signal could be detected. The results obtained with configuration ***b*** in Figure 4.5 did not differ from those obtained with configuration ***a***. These experiments proved the inefficiency of the collinear signal collection. The Raman signal could not be separated from the background in the case of configuration ***b***. No enhancement of the Raman signal inside the laser diode could be detected.

The failure to obtain satisfactory Raman spectra in the intracavity configuration can be explained. Whilst conventional back-scattering Raman experiments require filtration of the Rayleigh photons only, which can be accomplished with modern dielectric or holographic filters, the intracavity configuration poses a more difficult

task – to eliminate the laser light itself which is orders of magnitude more intense than the scattered light.

It is not difficult to estimate how much it is stronger than the most intense toluene Raman peak at 1007 cm^{-1} in terms of photon flux. The best toluene spectrum obtained in this chapter has 10,400 counts per second or 41,600 photoelectrons/second (the spectrometer's gain is 4 electrons/count). Assuming that the quantum efficiency of the CCD at 848 nm (1007 cm^{-1} relative to the laser wavelength 781 nm) is 50%, this corresponds to a flux of $8.32 \cdot 10^4$ photons/second. The laser power on the sample is 45 mW, which is the same as 45 mJ/s. Each laser photon carries the energy of $\frac{hc}{\lambda} = \frac{6.63 \cdot 10^{-34}(J \cdot s) \times 3 \cdot 10^8 (m/s)}{781 \cdot 10^{-9}(m)} = 2.5 \cdot 10^{-19}(J)$. Consequently, the laser photon flux on the sample is equal to $\frac{45 \cdot 10^{-3}}{2.5 \cdot 10^{-19}} = 1.8 \cdot 10^{17}$ photons/second. Supposing that the reflection losses from the cuvette sides and the grating provide only 30% of overall feedback efficiency, the laser photons flux is still $\frac{1.8 \cdot 10^{17} \times 0.3}{8.32 \cdot 10^4} \approx 10^{12}$ times higher than that of the toluene Raman peak at $1007\,cm^{-1}$. The edgepass filter blocks only 2% of the laser light (optical density ~2). The best notch filter available in the market has optical density of 6. This means that one would need to use an edgepass filter with at least 2 notch filters before the signal enters the collection fibre to reduce the background from the fibre core. Stacks of several filters are costly, block considerable amount of useful light and reduce throughput. Moreover, these calculations are relevant for an ideal case as pure toluene was used, which has a Raman cross section much higher than most other Raman-active substances.

It should also be kept in mind that apart from the laser line the excitation beam can contain the background of spontaneous emission from the laser diode. This emission covers the wavelength range corresponding to the diode gain and can exceed the notch filter blocking range. Therefore, when the intracavity layout is employed spontaneous emission can penetrate the collection fibre virtually without attenuation, especially in setup configuration ***b*** in Figure 4.5 where the residual laser light

emanates directly from the laser diode. Although in grating-stabilized laser diodes with coated facets spontaneous emission is suppressed very well[181], the performance of the uncoated diodes is less predictable. Even when the intensity of spontaneous emission is a million times lower than that of the laser line, the former can be comparable to the detected Raman signal.

Therefore, it can be concluded that conventional techniques of laser line removal would be ineffective or awkward when the intracavity configuration is used in a way described here. Other approaches are needed.

Focused collection. It was suggested that one possible way to prevent a good fraction of laser light from hitting the collection fibre is to create different optical profiles for the excitation and collection beams and then spatially separate them. This idea was realised in the setup shown in Figure 4.5c. The biconvex lens (*L-1*) was positioned just behind the beamsplitter, with the collection fibre being located at the distance slightly exceeding the lens focal length. The fibre position is chosen in such a way as to collect the scattered photons from the certain spot on the other side of the lens. This spot is crossed by the laser beam, and therefore both excitation and collection beams remain coaxial but not collinear. By varying the distance from the fibre tip to the lens, one could change the distance from the lens to the collection point according to the lens equation $\frac{1}{F} = \frac{1}{f_1} + \frac{1}{f_2}$. To increase the overall focal power and the collection angle, another lens (*L-2*) was installed.

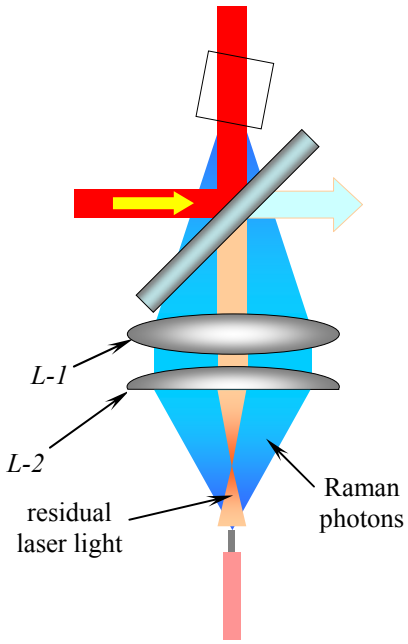

Figure 4.5c

It is shown in Figure 4.5c that the collection and laser beams are focused at different points under the filter. While the fibre position is optimised for efficient collection of the scattered photons, most of the residual laser light left after passing through the beamsplitter does not enter the fibre because on this plane it has a greater beam

diameter than the width of the fibre core. The more divergent the optical beam, the better the spatial filtering.

This configuration proved to be much more efficient than configurations ***a*** and ***b*** (Figure 4.5) in both the intracavity and non-intracavity modes. The collected spectra are shown in Figure 4.11.

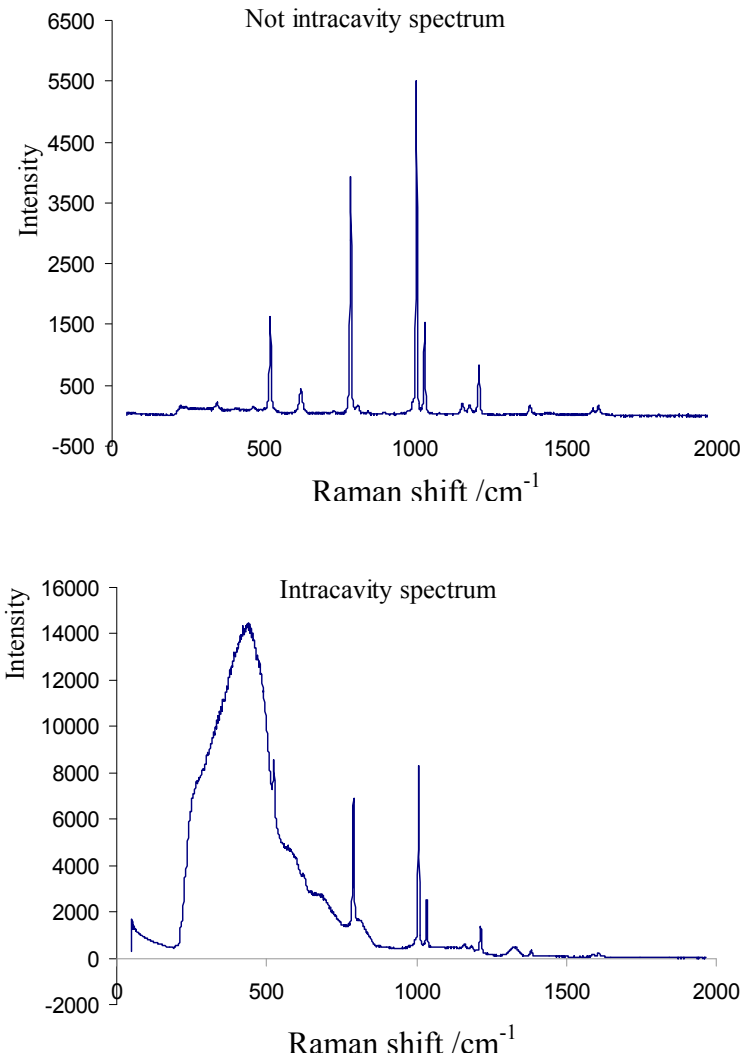

Figure 4.11. The intracavity (bottom) and non-intracavity (top) Raman spectra of toluene collected with configuration *c* in Figure 4.5. Acquisition time – 2 s.

Bluetac patch. Although in the intracavity mode the background was essentially reduced compared to the previous setup, improvements could still be made. The background from the intracavity spectra was completely eliminated by a tiny bluetac patch attached to the very centre of lens 1 as shown in Figure 4.5d. The diameter of

this patch was as low as 1 mm compared to the lens aperture of 25 mm. The narrow laser beam was fully blocked on this patch and did not propagate further to the collection fibre. In order to ensure that the patch dimensions are well below those of the collection beam cross section, the collection beam profile was visualised by means of transmitting the laser beam to the collection fibre in the reverse direction. The overall beam diameter appeared to be 10-11 times less than that of the dark spot in the centre coming from the patch. It was experimentally found that this patch reduced the Raman signal by only 4.6% while giving a significant improvement in background reduction. The intracavity spectra collected with and without the patch are shown together in Figure 4.12.

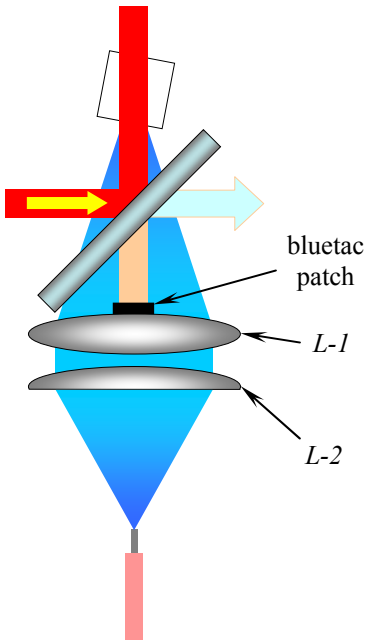

Figure 4.5d

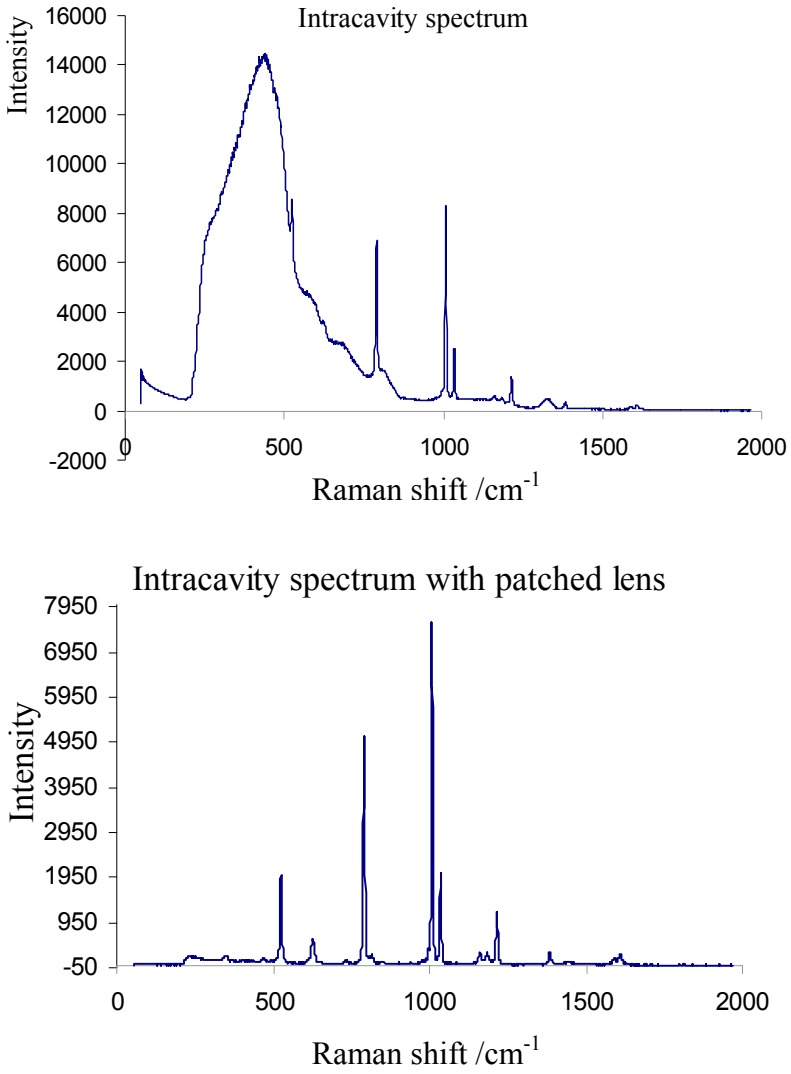

Figure 4.12. The effect of the bluetac patch on the toluene intracavity spectrum background. Top spectrum is collected with setup *c* and bottom spectrum – with setup *d* in Figure 4.5. Acquisition time – 2 s.

Intracavity effect. The signal intensity in the intracavity Raman spectrum (Figure 4.12) and the non-intracavity Raman spectrum shown in Figure 4.11 are different, with the intracavity spectrum having a higher signal.

Before discussing the results related to investigation of the intracavity effect, it is important to note that the laser used in this work is not designed for intracavity operation. The laser diode does not have a high reflectivity (HR) coating on the rear facet and a great amount of laser power (70%) leaks from the cavity. Additionally, the absence of an AR coating on the front facet makes it difficult to stabilise the laser

diode. In addition, with the grating efficiency as low as 80% it is impossible to achieve a substantial intracavity enhancement. Therefore, the results obtained in this work demonstrate viability of the devised optical setup for intracavity operation, although they do not show the intracavity enhancement. Coated laser diodes as well as gas or solid-state lasers would be preferable to obtain a notable intracavity enhancement.

In order to estimate the efficiency of intracavity enhancement of the Raman signal in relation to intracavity laser power enhancement, the two characteristics were measured and compared. The choice of excitation wavelength was defined by maximizing the power enhancement factor over the lasing range (776-784 nm) at the same current. The highest intracavity power was obtained at 780.3 nm. This wavelength was chosen for further experiments.

To measure the laser power in both configurations, a glass beamsplitter was inserted in front of the laser diode, the incidence angle was 45°. The beamsplitter's reflectance was as low as 5% and the two beams (one from grating, the other from diode) reflected from each side were the indicators of the intracavity power and feedback level. The result of summation of the two beam powers was an estimation of the overall intracavity power inside the external cavity. This was measured at different current values from 50 mA (the threshold) to 100 mA. Simultaneously, Raman spectra were acquired in both the intracavity and non-intracavity configurations. The intensity of the highest toluene Raman peak at 1007 cm^{-1} was used as an indicator of the system sensitivity and the results are plotted in Figure 4.13.

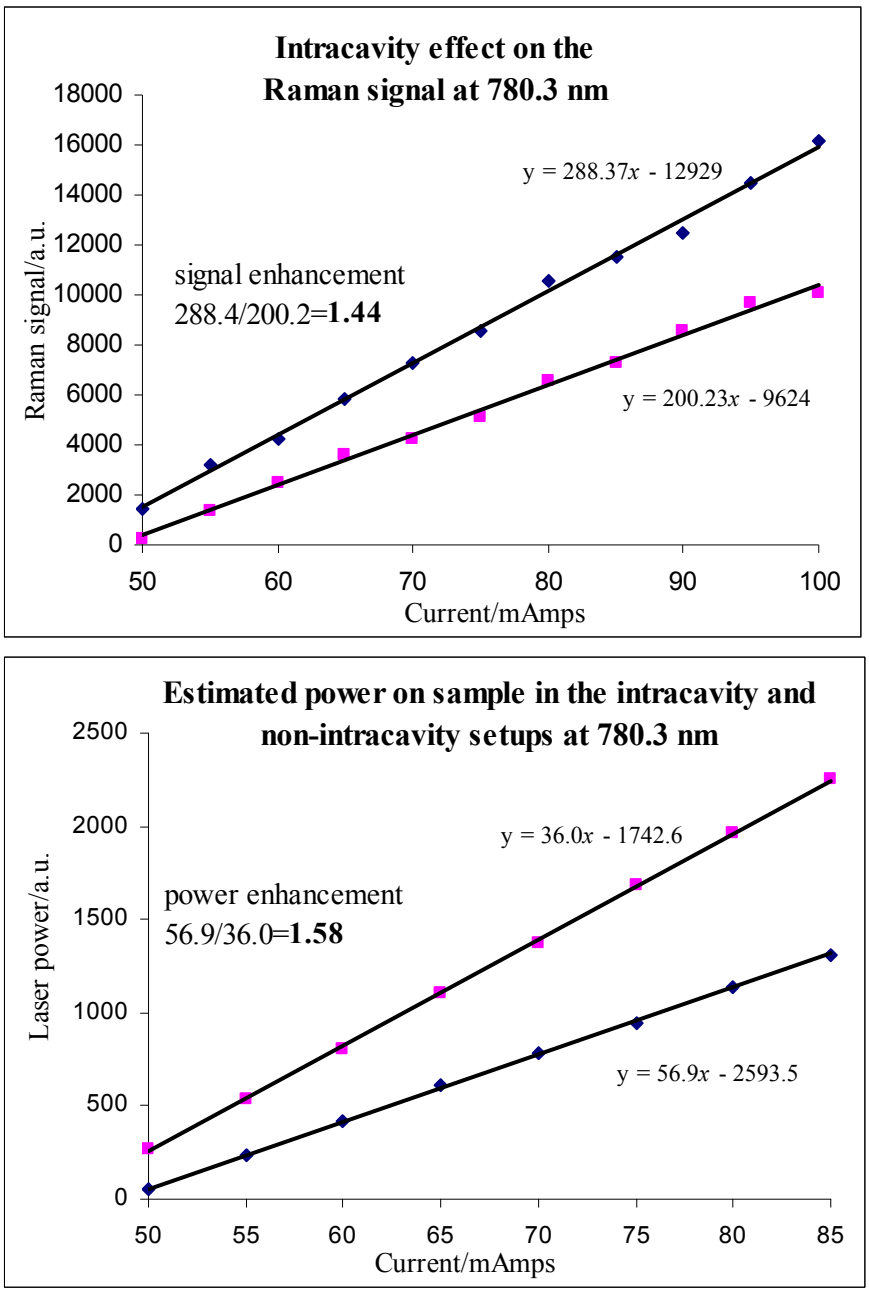

Figure 4.13. Intracavity enhancement of the Raman signal and of the laser power.

The linear least squares regression method was used to fit the experimental data with linear functions. The measured enhancement factor was calculated by comparing the slopes of the two graphs. The value of 1.44 obtained from the Raman measurements was reasonably similar to the power enhancement factor of 1.58. This result confirmed that intracavity laser power enhancement could be used to enhance the Raman signal from the sample located inside the laser cavity. The discrepancy between the intracavity Raman and power enhancement factors can be caused by

imperfect collimation of the laser beam. Power measurements represented the overall power of the beam, while Raman measurements – the power density.

Further improvements. Apart from intracavity experiments, it was important to continue development of the devised setup in the conventional back-scattering configuration because its performance could potentially compete with existing commercial Raman probes.

Lack of flexibility is a disadvantage of the setup described above. It has fixed lenses that cannot be changed as easily as it can be done in the commercial Raman probes. Both excitation and collection beams coming out of a commercial probe are collimated allowing any custom optics to be installed to the probe aperture providing convenience and wider applicability.

Another problem comes from the presence of the beamsplitter between the lens and the sample. This limits the range of distances between the lens and sample and makes it impossible to use higher-NA optics, and therefore, higher collection efficiencies.

The third disadvantage of the current setup is that the beam of scattered photons collected from the sample is highly divergent when passing through the beamsplitter. Dielectric interference optics are very sensitive to the changes of the incident angle and work properly only with collimated beams. An uncollimated beam can be filtered improperly, blocking a fraction of useful light and allowing Rayleigh photons to pass through.

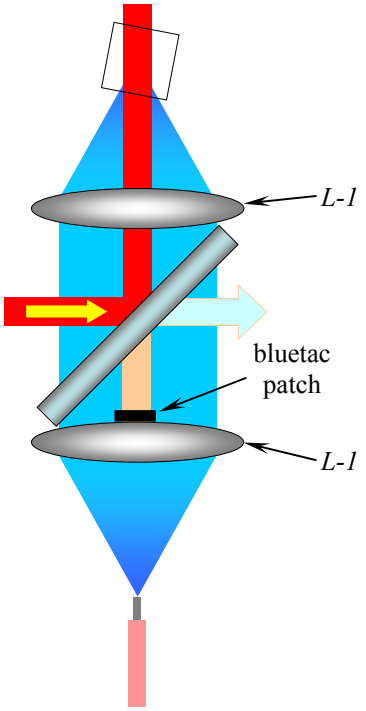

Figure 4.5e

To address these difficulties the setup was modified in the following way (Figure 4.5e). Lens 2 was removed and the fibre tip was shifted closer to lens 1 until the light propagating through the beamsplitter became collimated. The 785 nm laser from the Kaiser spectrometer was used for accurate alignment.

Another lens 1 was installed between the cuvette and the beamsplitter to focus the collection beam to a sample. Because the laser beam diameter is about 100 times less than the lens diameter and its focal length, only insignificant refraction could be observed in the lens proximity. The widening of the laser beam was only notable from afar.

The optimal focal length of the collection beam (the distance from lens 1 to the sample) was 23.5 mm (measured in air). Taking optical refraction inside the cuvette into account this value is in good agreement with the nominal focal length of lens 1 (25 mm).

Several attempts to increase the Raman signal further by modifying the setup optics were made. The best results were achieved with the setup comprising *L-3* as the lens on the collection fibre side and *L-4* as the lens on the sample side.

The detailed description and performance of this setup and its comparison with a commercial Raman probe will be discussed in the next Chapter.

4.4. Conclusions

An extensive study has been carried out to find the optimal optical configuration of a Raman probe for efficient signal collection from transparent liquid samples in a cuvette. Various ways of illuminating and collecting Raman photons from the sample have been described and analysed. The effect of optical modifications on the Raman intensity has been investigated. By means of gradual improvements, significant enhancement of Raman signal was observed in both 90° and back-scattering configurations compared to the initial setups. In addition, appropriate understanding and experience in working with optics and Raman instrumentation have been acquired during this study. This experience played a crucial role in the subsequent work.

Although the 90° layout of the Raman probe is known to be less efficient than the back-scattering layout, its performance was tested in the intracavity configuration. The results suggest that considerable improvements in the signal intensity can be

achieved by means of tight focusing and the use of a concave mirror to collect the photons scattered in the opposite direction.

The first on-axis intracavity Raman setup has been developed. Using low-cost components (spherical lenses, cheap laser source, unoptimised collection fibre, bluetac) this setup demonstrated the ability to record background-free Raman spectra without the necessity to use a notch filter in the probe. Filtration of the residual laser light was achieved by employing spatial filtering that relies on the collection beam having larger cross section than the excitation beam. The designed intracavity setup provided signal enhancement with a magnitude similar to the power enhancement factor in the laser cavity. This result suggests that the use of this setup in higher Q-factor cavities could lead to notable increase in the Raman intensity comparable to the intracavity power enhancement factor. This setup can be used in flow systems where composition of a transparent liquid is monitored in a fixed flow cell. A disadvantage of the intracavity method is that it is very sensitive to laser absorption in the sample, especially when the enhancement factor is very high.

The 180° collection layout experiments were carried out using a low cost 785 nm laser diode that was not designed to sustain optical feedback or to demonstrate superb wavelength stability. As expected, this laser diode was subject to occasional mode hops. This disadvantage prevents the use of such lasers in applications that require high wavelength stability. However, its low cost can justify its use in Raman systems intended for less demanding applications such as demonstration of the Raman effect in teaching laboratories.

The 180° intracavity setup was optimised for use without external optical feedback in the traditional back-scattering configuration. The best combination of lenses was chosen to maximise the intensity of the Raman signal.

5. Non-invasive analysis in microreactors using Raman spectrometry with a specially designed probe

The aims of this Chapter are:

1) compare the back-scattering Raman probe described in the previous Chapter with the commercial analogues;

2) investigate the influence of optical components of the probe on its performance in analysing samples in microreactors and optimise all parameters of the probe for this application;

3) demonstrate advantages of Raman spectrometry in process analysis of an esterification reaction;

4) study potential problems of using Raman spectrometry in microreactors.

5.1. Application of Raman spectrometry to process analysis in microreactors

5.1.1. Methods for non-invasive analysis of microfluidic processes

With the rapid development of microreactor technology there has emerged a demand for detection systems capable of performing rapid and reliable in-line/on-line analysis during process development and reaction optimisation, and for process monitoring[192]. These systems will not totally replace off-line analysis by mass spectrometry or high performance liquid chromatography (HPLC), but real-time and preferably non-invasive analysis will make process optimisation easier and faster, and facilitate development of multi-stage chemical syntheses on a single chip. This approach has been demonstrated by Ferstl et al.[193] who used different optical techniques for off-chip in-line measurements within enlarged millimetre-scale cells. The challenge that needs to be met is to implement real-time measurements on-chip or within much smaller microreactor channels (typically 20-200 μm) to allow more

versatile analysis and avoid broadening of the flow patterns in larger diameter measurement cells.

Although the integration of various optical and electrochemical probes into the microchip structure is possible[26, 146, 194, 195] this approach is not as flexible nor as powerful as non-contact sensing. Two methods that have been used on-chip for non-invasive characterisation of liquids flowing in microchannels are laser-induced fluorescence[146, 195-199] and Raman spectrometry[30, 61, 200-206]. Fluorescence is considered to be the most popular technique for on-chip analysis[197]. However, many of the reported cases relate to various biochemical procedures rather than to the analysis of synthetic chemical processes. Fluorescence is a very sensitive and convenient method, but it cannot be universally applied to process monitoring because few molecules naturally fluoresce. Moreover, fluorescence spectra have wide overlapping bands and carry little or no structural information. Raman spectrometry is free from these limitations and has a number of advantages for in-depth characterisation of reactions in microchannels. For many years Raman spectrometry has been used successfully for monitoring batch chemical reactions[87]. However, in the field of microfluidics, the majority of papers concerning Raman scattering report experiments that are based on surface enhanced (resonance) Raman spectrometry (SERS and SERRS). These methods have proved to be useful for many applications within the μ-TAS concept[207, 208]. Process analysis, however, cannot benefit from surface enhancement due to the poor signal stability of SERS, and the necessity of continuous introduction of stable colloids of nanoparticles, that disturb the system. Conventional Raman spectrometry, although being much less sensitive than fluorescence and SERS, can be more suitable for process analysis applications. Nevertheless, given the practical convenience of Raman measurements and the information that can be extracted from microchannels, the technique remains surprisingly underutilised in this field. It is considered as an unconventional, less common or even esoteric detection method[209], or not mentioned at all in the relevant reviews[210]. Only few researchers have demonstrated the usefulness of conventional Raman spectrometry for the analysis and monitoring of various chemical processes in microreactors. In this Section, the main trends found in these works will be overviewed.

5.1.2. Confocal Raman spectrometry

In conventional Raman spectrometry, illumination and signal collection occur over the entire field of view of the optical system. The volume and shape of the signal collection zone depend on the wavelength and optics used. In many applications, minimizing the collection volume to only a few micrometers is crucial. This minimization is realized by using confocal signal collection. In confocal Raman spectrometry (microscopy), the flux of Raman photons is spatially filtered by a narrow slit at the back image plane of the collection optical lens (Figure 5.1). The narrower the slit the smaller the effective signal collection volume and therefore the higher the spatial resolution. However, the improved resolution is gained at the expense of reduced signal intensity, as the slit blocks a significant portion of Raman photons.

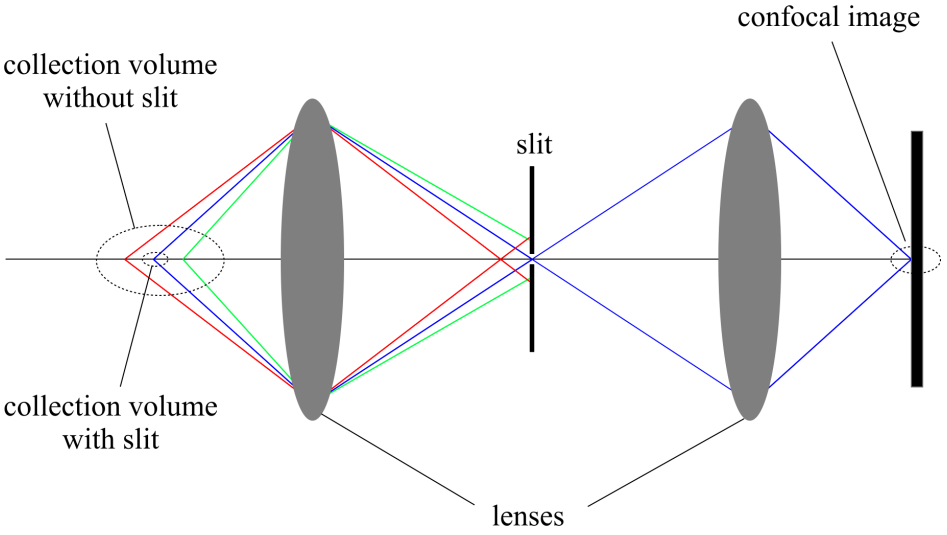

Figure 5.1. Schematics of confocal imaging.

Theoretically, it is possible to achieve diffraction-limited resolution with the dimensions of the signal collection volume comparable to the wavelength of light. In practice however, the resolution turns out to be much lower due to optical aberrations and other artefacts. Optical resolution in Raman spectrometry is often hard to determine accurately without using complex modelling because resolution criteria that are adequate for imaging are not sufficient for confocal spectrometry. In recent reviews[211, 212], Everall outlined several problems that Raman microscopists should be aware of when selecting optics and analysing the data. He pointed out that despite the

wide use of the method and its developed theory, many researchers neglect the technical limitations and tend to misinterpret their results.

5.1.3. Analysis of inter-diffusion profiles

Probing samples flowing inside microchannels is one of the many applications where high spatial resolution is necessary. The requirements are particularly strict when information about inter-diffusion profiles of the mixing streams is obtained. Raman spectrometry offers advantages over other confocal measurement methods such as fluorescence. These advantages include label-free detection, a greater range of samples that can be analysed, and the possibility to monitor chemical reactions within the mixing zones. In addition, non-linear Raman spectrometry, such as coherent anti-Stokes Raman spectrometry (CARS), provides a higher level of sensitivity, much greater spatial resolution and can be a powerful tool for three-dimensional mapping. Thus, Scharfer et al. used CARS microscopy to map the mass transport in a microfluidic device and the chemical reaction profile with sub-micron spatial resolution and an acquisition time of only 100 ms per point[213, 214]. Examples of the mixing and reaction profiles in the mixing zone is given in Figure 5.2, which shows that the data obtained with CARS microscopy agree with the simulation results.

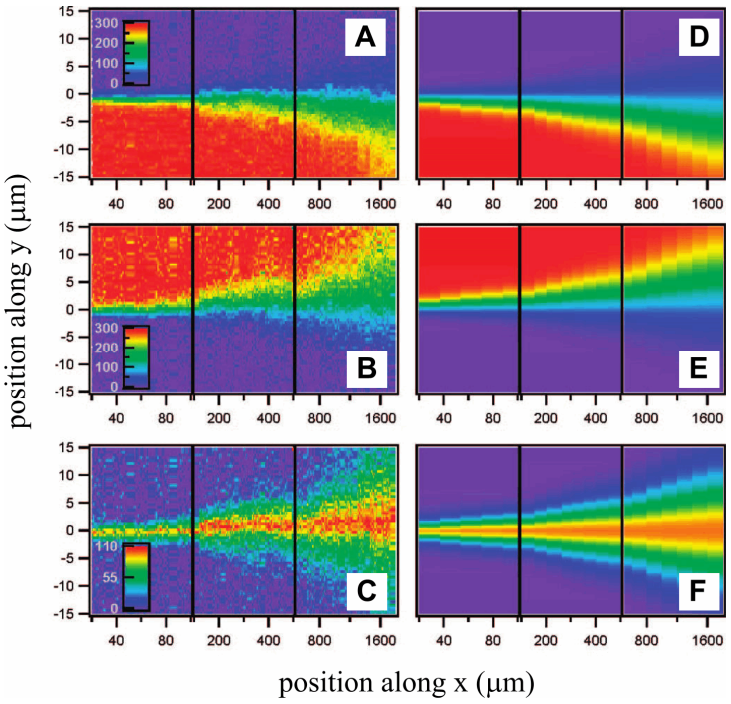

Figure 5.2. Concentration profiles of pyrrolidine (A), acetic acid (B), and the reaction product (salt) (C) within the microfluidic device. Panels (D), (E), and (F) provide the corresponding results of the numerical simulations (adapted from [214]).

Data that can be obtained from confocal Raman measurements are important to validate inter-diffusion models built to understand and predict fluid behaviour inside the microchannels. These models are complex and depend on many parameters such as the channel dimensions and geometry, the nature of reagents and products, the rate of the chemical reaction and associated thermal effects. Therefore, the ability of confocal Raman spectroscopy to map inter-diffusion zones with high spatial resolution is crucial in understanding the processes involved.

Dambrine with co-workers published a comprehensive study on the inter-diffusion of water and glycerol[215]. Using confocal Raman imaging they experimentally validated the numerical model built for this process and revealed displacement of the inter-diffusion layer from the channel centre caused by competition between hydrodynamic processes and mixing. With a 514 nm Ar-ion excitation laser the acquisition time was in the range of 1 - 2 s.

Park et al.[216] applied confocal Raman and fluorescence spectroscopies to evaluate the mixing of ethanol and isopropanol in different passive mixing devices. Using the

confocal configuration of the Raman spectrometer and an acquisition time of 30 s per spectrum the authors eliminated the interfering signal emanating from the microreactor material and concluded that Raman spectroscopy is highly suitable for monitoring mixing processes in microreactors. In another study, Salmon et al.[203] investigated inter-diffusion of chloroform and methylene chloride. The acquisition time was only 1 s per spectrum. However, in order to obtain a steady-state image, spectra were obtained over the 50×50 grid of measurement points, which took almost 1 h. The collected data were sufficient to estimate diffusion coefficients of the pure liquids.

Sarrazin and Salmon[30] studied isotope exchange in the H_2O/D_2O system. Because the reaction is diffusion-controlled, mixing efficiency could be characterized by monitoring spectral features of the product, HOD, without the necessity to take multiple measurements across the channel. The authors observed that in the droplet flow regime, mixing was completed in about 20 ms. Using a 5 s measurement time, 1 hour was required to obtain an image of the mixing zone, a similar time requirement to that reported by Salmon et al.[203].

5.1.4. Time-resolved Raman microchip spectroscopy

Accurate analysis of inter-diffusion profiles would not be possible without employing steady-state analysis (see Section 6.1.3). Temporal invariability of the local reaction profiles allows long spectral acquisition times to be used in order to compensate for the poor sensitivity of confocal Raman spectrometry. Using steady-state analysis in conjunction with Raman spectrometry is equivalent to "freezing" the process at any critical stage and allowing as much time as needed for the detailed non-invasive study of that "snapshot".

One of the most prominent examples of this advantage is time-resolved resonance Raman microchip spectroscopy developed by Pan et al.[217] for accurate Raman measurements of the kinetics of photochemical reactions. The method is based on Raman spectrometry and steady-state analysis with microfluidic sample delivery. The sample molecules are excited with a tightly focused laser beam that triggers a photochemical reaction. The Raman probing beam is displaced from the excitation beam by a small distance along the fluid travel direction. By controlling the

displacement distance between the beams and the flow rate, the reaction profile was probed at different times after the excitation event with high temporal resolution (up to a few hundred nanoseconds). The authors demonstrated the usefulness of time-resolved Raman microchip spectroscopy for getting detailed structural and kinetic information about short-lived transient species and the mechanism of photochemical reaction involving rhodopsin. Because the measurements are taken in the steady state, the Raman acquisition time is independent of the achieved temporal resolution. Using spectra obtained from ten exposures of 1 min. each Pan et al. achieved a time resolution of 250 ns.

5.1.5. Phase transitions in microchannels

Yin with co-workers[38] studied biomineralisation in a microfluidic device. Mimicking a natural system, the authors studied the influence of extrapallial proteins on polymorph formation during $CaCO_3$ crystallization inside a microfluidic channel. Raman spectrometry was shown to be an excellent tool for rapid characterisation of biomineralisation processes at a wide range of experimental conditions. With Raman spectrometry, it was possible to distinguish between polymorphs formed in real time and to carry out quantitative process analysis.

Another example of phase transition studies was presented by Araki et al.[218] who used an inverted Raman microscope with high-NA objective lens to investigate temperature-dependent disappearance of the phase boundary between two liquids, perfluorohexane and n-heptane. Lateral and axial spatial resolutions of the optical system were reported to be 0.25 and 4.8 μm, respectively with acquisition time of 2 - 5 min. per spectrum. With this system, the authors determined whether the fluid was homogeneous or non-homogeneous. Their results demonstrated advantages of using spatially resolved Raman spectrometry on a microfluidic chip for studies of mixing and separation processes.

5.1.6. Fibre-optic Raman spectrometry and reaction monitoring

Coupling Raman instrumentation with microscopes is an excellent way to achieve high spatial resolution of Raman measurements by taking advantage of high-numerical aperture (NA) and immersion microscope objectives, aberration-corrected optics and controlled slit sizes. However, as noted earlier in this text, confocal

imaging is associated with a significant drop in the recorded Raman signal that necessitates the use of longer acquisition times and therefore increased analysis time. Taking into account the fact that low sensitivity is the main limitation of conventional Raman spectrometry, regardless of the signal collection method, it is reasonable to consider the possibility of using larger slits, at least in some applications. These applications include situations where the information obtained from the channels does not have to be spatially resolved between several locations across the channel or, put in other words, a much poorer lateral resolution across the channel would suffice. This is the case with homogeneous solutions flowing in channels. The typical diameter of microfluidic channels is in the range of 20 - 500 μm, which is 1 - 2 orders of magnitude higher than the diffraction-limited resolution in the optical spectral range. Therefore, when only the average fluid composition across the channel cross section is of interest, a significant increase in sensitivity can potentially be obtained by increasing the slit size in the Raman microscope.

When the slit size needs to be in the range of tens to hundreds of micrometres, it is reasonable to use a fibre-optic Raman probe instead of a microscope. A fibre core aperture serves as a slit and can provide the desired level of confocality. Fibre-optics offer several practical benefits through their compactness, lower cost and flexibility. However, in the majority of published papers concerning the use of Raman spectrometry for reaction monitoring in microreactors, Raman microscopes were used. To illustrate the current state of development in this field, several examples of available reports will be given with a distinction made between research based on Raman microscopes and fibre-optic Raman probes.

Reaction monitoring using Raman microscopes. Lee et al.[201] studied imine formation from benzaldehyde and aniline in a glass microchip (depth - 20 μm, thickness of the top glass layer – 2 mm) using steady-state analysis at different locations. The Raman system was equipped with a 20 mW Ar-ion laser operating at 514.5 nm. With a double slit confocal microscope and low-NA 10x objective, the total measurement time was as high as 100 s.

A much faster analysis with only 5 s of acquisition time was reported by Fletcher et al. [202] who used an inverted Raman microscope with a 10x objective and a 780 nm

laser (power not reported) for monitoring the formation of ethyl acetate from ethanol and acetic acid. The channel diameter and the top glass layer thickness were 73 μm and 0.5 mm, respectively.

Leung and co-workers[205] monitored the catalytic oxidation of isopropyl alcohol to acetone using a microreactor with a capillary diameter of 50 μm. The Raman spectra were collected with a Raman microscope with various objectives. The HeNe laser used to illuminate the sample had a power of 17 mW and operated at 633 nm. The acquisition time was in the range of 1 - 60 s.

Reaction monitoring using fibre-optic Raman probes. Barnes et al.[204] studied a polymerisation reaction in droplets flowing in a channel with an internal diameter of 500 μm. Little details were provided about the fibre-optic Raman probe that was used in this study. It is only known that it had a focal length was 5 mm and a spot size of 200 μm. The laser wavelength was 785 nm (laser power not known). The authors concluded that the long acquisition time (180 s) that they had to use to achieve an acceptable signal-to-noise ratio was the main limitation in their work.

Shende et al.[206] monitored esterification of methanol with benzoic acid in a 1 mm glass capillary using a Raman system comprising a 325 mW 785 nm laser, FT spectrometer and a fibre-optic probe, with diameters of the excitation and collection fibres of 200 and 400 μm, respectively. The acquisition time was 30 s per spectrum. The low signal-to-noise ratio was largely attributed to the strong background emanating from the capillary material.

An interesting study was reported by Urakawa and co-workers[61] in which catalytic cyclohexene hydrogenation was monitored by Raman spectrometry in supercritical conditions using CO_2 as a solvent. The pressure in the microreactor was more than 10 MPa. The channel diameter in the microreactor was 390 μm. Satisfactory spectra were obtained with only 10 s of acquisition time per spectrum using a 785 nm excitation source (laser power unknown). The relatively good sensitivity is likely to be attributed to the high Raman cross section of cyclohexane. Details of the fibre-optic Raman probe were not provided.

From analysis of the quoted examples, several conclusions can be made. Firstly, there has been no attempt to optimise the optics of the Raman systems used for measurements in microchannels. It is surprising that in the two examples related to Raman microscopy[201, 202], low-NA objectives were chosen for collecting Raman spectra from rather narrow channels (20 and 73 μm i.d.). The thick top layer of the microreactor possibly prevented use of objectives with higher magnification. However, long working distance objectives can solve this problem and these optics are usually available in microscopy laboratories. Secondly, the importance of reporting the details of the probe's optical configuration and the laser power is often underestimated. With the lack of information, it is difficult to make any conclusion about the relative efficiency of the Raman systems employed in the quoted reports. Thirdly, after a more detailed analysis of the papers, it becomes clear that the application of Raman spectrometry to process analysis in microreactors is in the early stage of development, with authors concentrating on demonstrating the potential of Raman spectrometry rather than investigating the limitations and attempting to improve performance by optimisation of the optical configuration of the instruments. In this situation, it is easy to understand why the benefits of using fibre-optic Raman probes instead of bulky and expensive microscopes in certain applications has not been demonstrated yet.

In this Chapter, the importance of various optical components that constitute a Raman probe on the Raman signal obtained from a microreactor will be discussed, with emphasis on optimisation of the probe configuration, maximizing sensitivity of the Raman measurements and the spatial resolution required for analysis of liquids in microreactor channels.

Based upon these considerations an efficient Raman probe was designed and built that is optimised for operation with 150 μm-deep channels. The analytical characteristics of the probe were characterised and compared with a traditional commercial system. The satisfactory performance of the new Raman probe was illustrated for the monitoring of an esterification reaction in a microreactor. In addition, the potential problems that can arise during the analysis were identified and summarised.

5.2. Experimental

The optical Raman system is based upon a conventional back-scattering design [102] utilising separate optical fibres to deliver the excitation light and collect the signal for subsequent analysis with a commercial Raman spectrometer (Holoprobe, Kaiser Optical Systems Inc). The full configuration is shown in Figure 5.3.

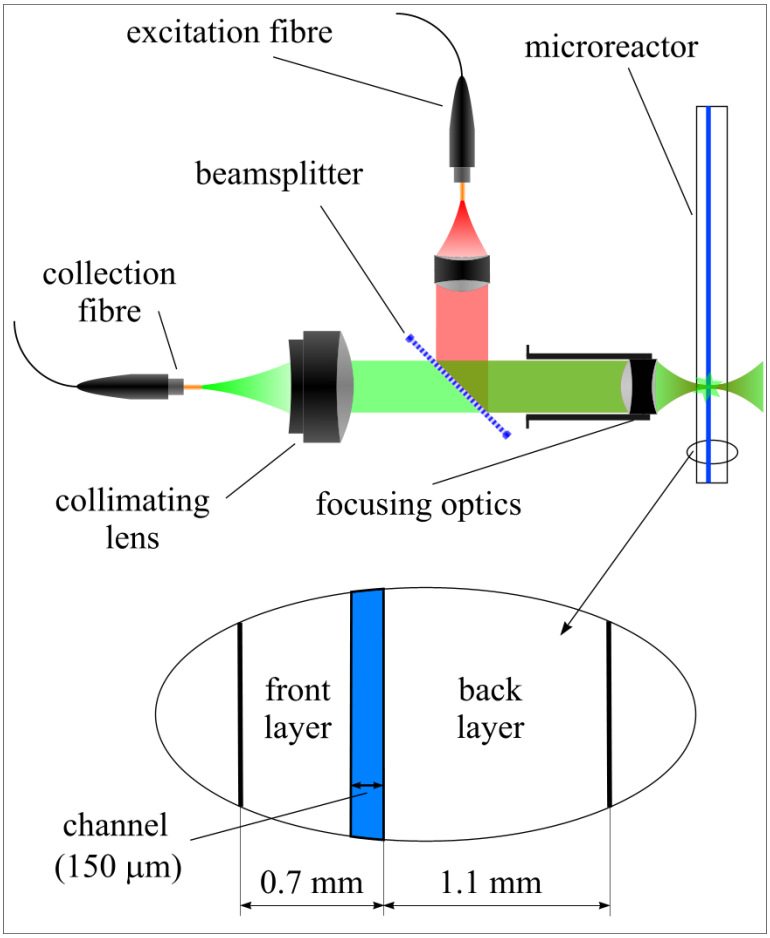

Figure 5.3. Raman optical setup and microreactor cross section schematic.

A 330 mW, 785 nm laser diode (Invictus 785, Kaiser Optical Systems Inc) was coupled into a 62.5 µm 0.28 NA graded index fibre without the use of any laser notch filters. The output was then collimated using a commercial fibre collimator (CF-2-B, Thorlabs) in combination with a multi-element lens (effective focal length (EFL) – 8 mm, 0.28 NA, Melles Griot Inc) resulting in a beam with a diameter of 2 mm. This beam was then directed onto a dichroic beamsplitter before being focussed into the microreactor using various lenses described below, resulting in laser powers

on the target varying from 190 to 240 mW. The returned signal passed through the dichroic filter and was focused into a range of multi-mode graded index fibres (Thorlabs and Kaiser) with a core of 15, 50, 62.5 or 100 μm, using a multi-element lens (EFL 8 mm, 0.28 NA, Melles Griot Inc). The sensitivity of this setup was compared to that of the commercial MR Raman probe (Kaiser). The excitation and collection fibre diameters in the commercial probe are 50 and 100 μm, respectively. The fibres are of graded-index type with numerical aperture 0.29.

Several laser focusing lenses were compared to maximise the Raman signal detected, including an aspheric lens (EFL 4.5 mm, 0.49 NA, working distance 2.4 mm; Olympus, Japan) and microscope objectives with magnification of 10x, 20x, 40x or 60x, and the best setup was selected for detailed study. Careful consideration was given to the selection of this lens as it affects the volume being probed within the channel and also the size of the returned signal (the larger the volume, the larger the signal, but the less localised the measurement). The choice of lens also had an effect on the unwanted background signal seen from Raman features found to be emanating from the glass channels. The focusing lens in combination with the fibre collection lens and fibre diameter provided some level of confocal discrimination, but at the expense of loss of the desired Raman signal. Where applicable, the laser power on the sample was measured to compensate for the varied optical losses induced by the different fibres and lenses used.

The microreactor chip (FC_R150.676.2, Micronit Microfluidics) consisted of 2 thermally bonded plates of borosilicate glass (1.1 mm thickness), and fused silica (0.7 mm). It contained a single serpentine parabolic-shaped reactor channel with two inlets and one outlet (Figure 5.4). The depth and width of the channel were 150 μm and internal volume of the serpentine was 13 μl. The channels were manufactured using powderblasting. The chip was fixed vertically in a XY-translation stage for precise control of its position relative to the optical probe. For the optical optimisation experiments, the microchannel was filled with toluene; comparative Raman measurements were obtained for toluene in a 1 cm diameter silica glass cuvette.

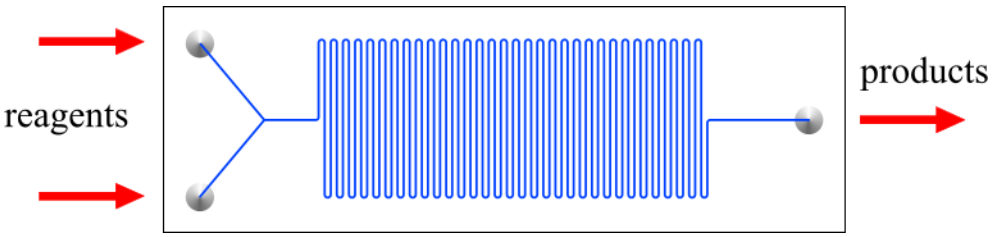

Figure 5.4. A schematic of the microreactor.

The acid-catalyzed esterification of butanol with acetic anhydride was chosen as a model reaction to demonstrate the performance of the new Raman probe.

$$C_4H_9OH + (CH_3CO)_2O = CH_3COOC_4H_9 + CH_3COOH$$

All the reagents were used as supplied by Sigma-Aldrich and contained at least 99.5% of the main component, except for sulphuric acid which was 95% pure. The reaction was carried out at room temperature (~21 °C). Sulphuric acid was added to acetic anhydride immediately prior to the experiments to give a concentration of 3% v/v. The solutions were pumped into the reaction vessel using one of the two pumping systems: a dual syringe pump (CMA 102, CMA/Microanalysis) or an Aladdin NE-1002X (New Era Pump Systems Inc). By varying the flow rate range, the extent to which the reaction was completed could be varied across the microreactor.

The spectral acquisition times were 0.5, 1 or 2 s. To reduce the time between consecutively collected spectra, a cosmic ray filter was not used, and any spectra contaminated with cosmic rays were manually discarded. Selection of the spectral acquisition time was based on the necessity to achieve sufficient signal to noise ratio and at the same time a high sampling frequency to reveal possible short timescale instabilities in the flow system and study the feasibility of high-speed process analysis with Raman spectrometry.

5.3. Results and discussion

5.3.1. Optimisation of probe optics

Figure 5.5 shows typical Raman spectra of toluene, collected with the Kaiser MR probe from a 1 cm diameter silica glass cuvette (a) and the microreactor (b) using a

10x microscope objective. The position of the Raman probe relative to the sample was optimised for the maximum Raman signal. In addition to the narrow toluene Raman lines there are two broad bands at 400 and 1300 cm^{-1} in the spectrum obtained from the microreactor. These signals arise from the glass surrounding the microchannels and could not be fully suppressed. A small portion of the signal around 400 cm^{-1} was generated in the fibres. The intensity of the glass band at 1300 cm^{-1} was used to assess attempts to minimize the contribution to the background from the microreactor material when varying parameters.

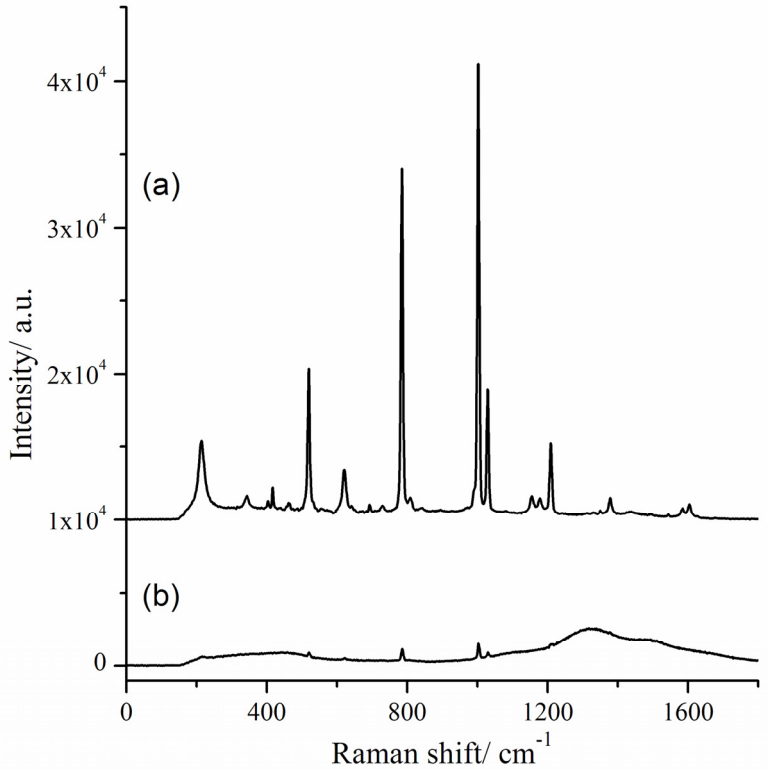

Figure 5.5. Raman spectra of toluene obtained with a Kaiser MR probe and 10x objective from (a) a 1 cm silica glass cuvette and (b) the microreactor. Spectra are plotted on the same scale; 0.5 s acquisition time.

Table 5.1 gives the intensities and signal-to-background values obtained for measurement of the toluene spectrum in the cuvette and the microreactor when different optical elements were used to focus the probing beam onto the sample. Only two microscope objectives (10x and 20x) could be used in this experiment as the working distances of the other objectives (40x and 60x) were too small and the focal point did not reach the microchannel even behind the thin (0.7 mm) glass layer. In contrast, the compact aspheric lens has a working distance of 2.4 mm in air which

is increased to almost 4 mm in glass due to optical refraction. The problem of low working distance could be overcome by polishing the front glass layer of the microreactor. However, it is not always possible if the design of microfluidic connections relying on the integrity of the original chip thickness. It is of interest to investigate the usefulness of Raman spectrometry in this application without anysignificant modification of commercially available microreactors.

Table 5.1. Performance of different focusing optics used with the Kaiser MR Raman probe. An acquisition time of 500 ms was employed, and the diameters of the excitation and collection fibres were 50 and 100 µm, respectively.

Optics	Raman intensity/a.u.			Signal-to-background ratio (micro-reactor)
	Toluene (cuvette), peak at 1004 cm^{-1}	Toluene (micro-reactor), peak at 1004 cm^{-1}	Glass (micro-reactor), peak at 1314 cm^{-1}	
10x objective NA = 0.25	31400	1240	2590	0.48
20x objective NA = 0.50	42600	7640	6640	1.15
Aspheric lens NA = 0.49	48000	17710	4930	3.6

Compared to the objective with the same numerical aperture (NA=0.5, magnification 20x), the aspheric lens produced 2.3 times higher signal and 3.1 times higher signal-to-background ratio when spectra are taken from the microreactor. These results show that significant practical benefits can be gained by using a suitable high-NA aspheric lens instead of microscope objectives. The reduced signal obtained with the microscope objective may be partially due to the optical coating on the lens, which can lower transmission above 850 nm[219]. In contrast, the aspheric lens was originally designed for use with compact disc (CD) laser diodes that operate around 800 nm.

The other important factor defining the quality of spectra is the core diameter of the collection and excitation fibres: these should be small to provide confocality of the probe to confine the signal collection volume within the microchannel boundaries, but a lower intensity is collected with a narrower collection fibre. Therefore, a compromise between these two factors should be sought. Moreover, when the probe is coupled with a dispersive spectrometer it is also important to match the collection fibre diameter with the entrance slit size. The spectrometer used in this study had a 50 μm slit and was designed for operation with a 100 μm collection fibre and a 50 μm excitation fibre. As the microreactor is significantly smaller than conventional systems, and the goal was to minimize the background signal from the reactor channel, two other combinations of fibre diameters were also investigated, as indicated in Table 5.2. All spectra were collected with the compact aspheric lens.

Table 5.2. Influence of the core diameter of the optical fibres on the quality of Raman spectra of toluene collected from a 1 cm silica glass cuvette and the microreactor using the new probe and a Kaiser MR probe. An acquisition time of 250 ms was employed. The values given in brackets for the 50 µm excitation fibre are corrected intensities that account for the reduced coupling efficiency obtained with a 50 µm diameter excitation fibre compared to a 62.5 µm fibre.

Probe	Fibre core diameter/µm		Raman intensity/a.u.			Signal-to-background ratio (micro-reactor)
	Excitation	Collection	Toluene (cuvette) peak at 1004 cm^{-1}	Toluene (micro-reactor), peak at 1004 cm^{-1}	Glass (micro-reactor), peak at 1314 cm^{-1}	
New	62.5	62.5	27500	13270	1250	10.6
	62.5	100	46500	16000	2900	5.5
	50	100	36200 (43100)	13740 (16300)	2140 (2549)	6.4
Kaiser MR	50	100	26300 (29590)	8860 (9970)	2470 (2780)	3.6

Using a larger diameter collection fibre resulted in a substantial increase in the toluene signal intensity from the cuvette. However, the Raman signal from toluene in the microchannel did not change significantly, whereas the glass background became more prominent, and the system was less confocal. Ideally, the probed volume should not exceed the dimensions of the microreactor channels, in which case no background signal from the microreactor material would be recorded. In practice, however, this can hardly be achieved without using very narrow fibres and short focal length lenses that significantly decrease the overall sensitivity. The results presented in Table 5.2 demonstrate that for the three combinations investigated, the signal-to-background ratio was highest when the diameter of both the excitation and collection lenses was 62.5 μm. The data in Table 5.2 also allow comparison of the developed and commercial probes when the same optical fibre combination was used (excitation and collection diameters of 50 and 100 μm, respectively), revealing significant improvement in the signal-to-background ratio for measurements in the microreactor with the new probe (6.4 versus 3.6). A comparison of the toluene spectra obtained from the microreactor when different combinations of lenses and fibres were used is given in Figure 5.6. In addition to higher sensitivity and reduced glass background achieved with the developed probe, the absence of the Rayleigh band and relatively low background around 400 cm^{-1} justify the lack of additional optical filters in the probe.

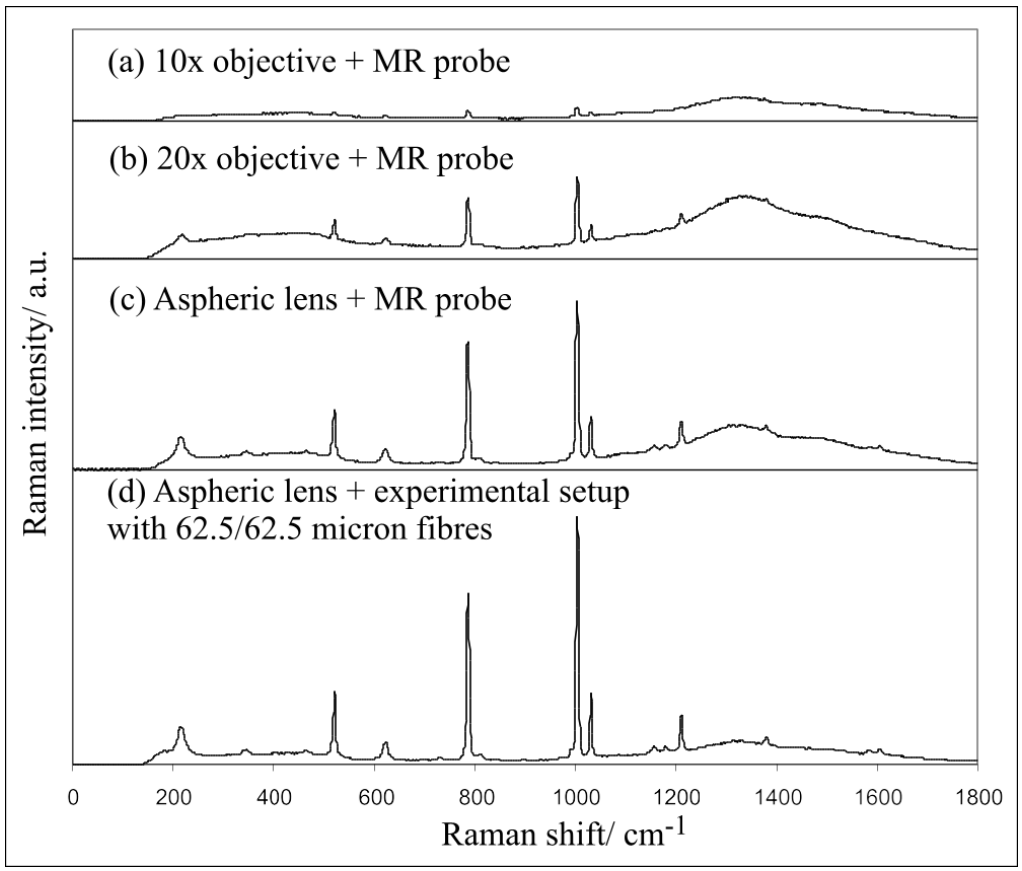

Figure 5.6. Raman spectra of toluene taken from the microreactor using various experimental arrangements. The spectra are shown in the same scale to demonstrate differences in sensitivity and background level. (Acquisition time – 500 ms; for (a) – (c) the excitation/collection fibre diameters are 50/100 μm).

5.3.2. Signal collection volume

To estimate the axial beam resolution achieved with the optimal configuration (62.5 μm excitation and collection fibres and the aspheric lens) a variation of the method for measuring the axial resolution of a confocal microscope was used[220]. The intensity of the residual laser radiation reflected from the glass-air interface was measured as the microreactor was moved axially from the probe. The resulting intensity profile is shown in Figure 5.7 giving an axial resolution of 150 μm in air (obtained from the full width at half height of the peak) or 230 μm in the microfluidic channel when the refractive index is considered.

The beam width was found in a similar experiment where the flat glass surface with a straight sharp end was translated laterally in the focal plane of the probing beam (Figure 5.8). This revealed that the lateral resolution was 25 μm (obtained from the

change over the range 310-335 μm), which equates to an effective width of 40 μm in the channels.

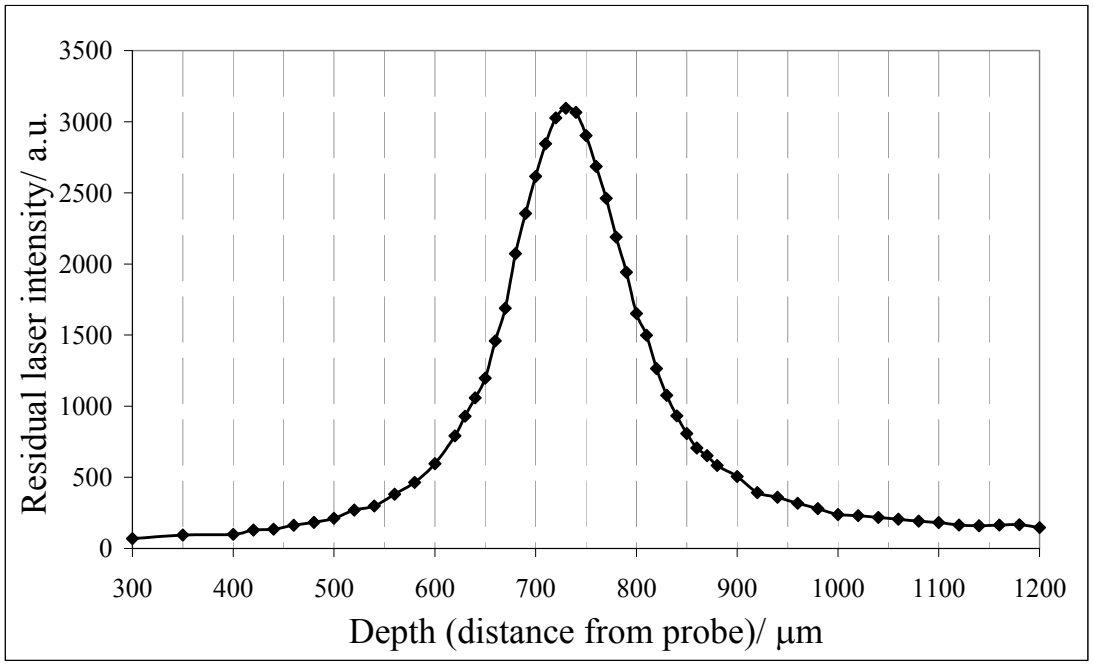

Figure 5.7. Axial beam resolution measured on the glass-air interface by recording intensity of the residual laser light.

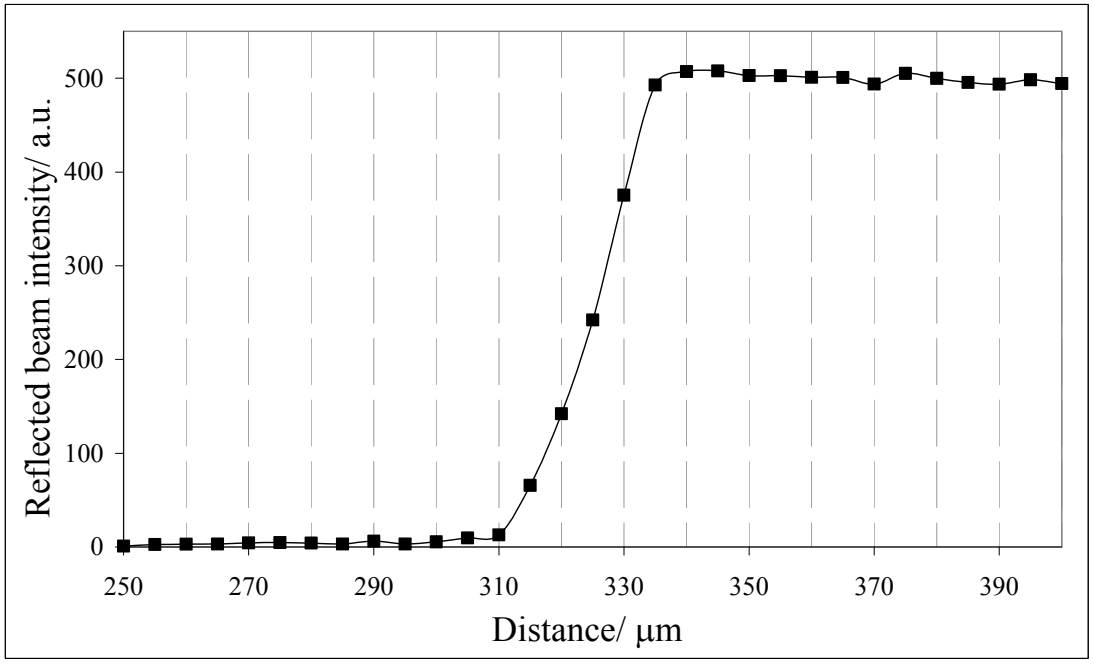

Figure 5.8. Transverse beam resolution measured on glass-air interface by recording intensity of the residual laser light.

The dimensions of the collection volume are comparable with the microchannel size (Figure 5.9) ensuring relatively high quality of the Raman spectra. However, for shallower channels the sensitivity and signal to background ratio will be decreased. In this case, optics with higher numerical aperture and/or narrower fibres will be required.

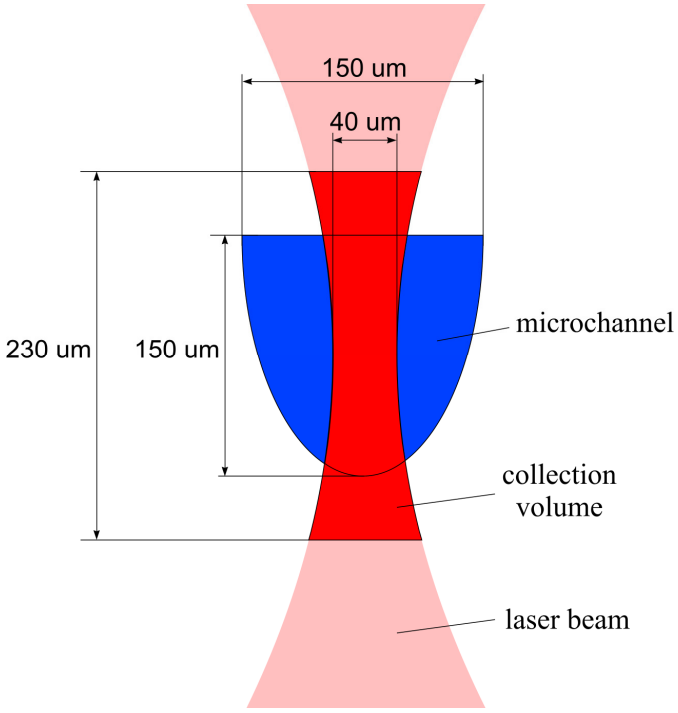

Figure 5.9. Schematic of the channel cross section and signal collection volume, shape and dimensions.

5.3.3. Reaction monitoring

Example Raman and 1st derivative Raman spectra of the pure compounds associated with the model esterification reaction are given in Figures 5.10 and 5.11, respectively. Analysis of these spectra suggested that the acetic anhydride band at 670 cm^{-1} and its negative branch in the derivative spectrum can be used to characterise the reaction in a simple univariate model. This band is sufficiently intense and does not overlap with the bands of the other compounds. Among the Raman features of the products, the butyl acetate peaks at 308 and 635 cm^{-1}, and acetic acid peak at 901 cm^{-1} could be used for monitoring purposes. However, the latter was shown to be unsuitable due to peak shifts caused by the changing chemical environment during the reaction. The butyl acetate peak at 635 cm^{-1} overlaps with

two other spectral features to some extent, but this interference was not prominent as the reaction approaches completion at high yields.

Typical Raman and derivative Raman spectra of the reaction mixture in the microreactor are shown in Figures 5.12 and 5.13. The curved background shape in Figure 5.12, particularly around 1300 cm^{-1} is due to the Raman signal from the microreactor material (borosilicate glass). This background cannot be fully suppressed and the use of derivative spectra was beneficial when the background intensity was variable.

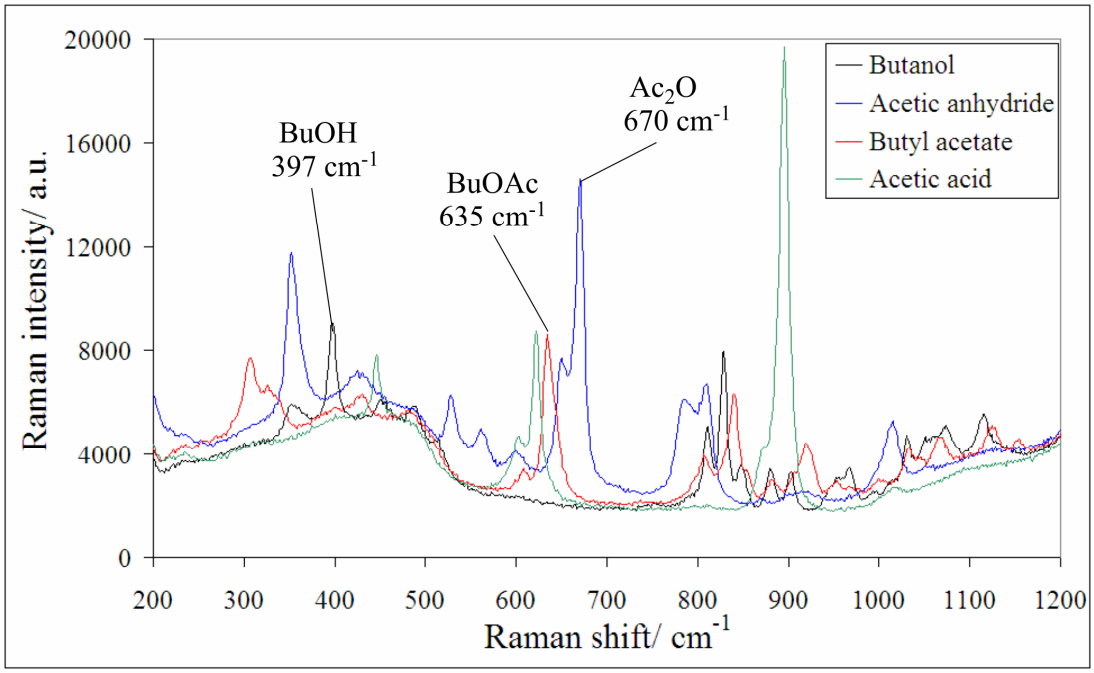

Figure 5.10. An overlay of individual Raman spectra of the pure reagents and products of the esterification reaction collected from the microreactor.

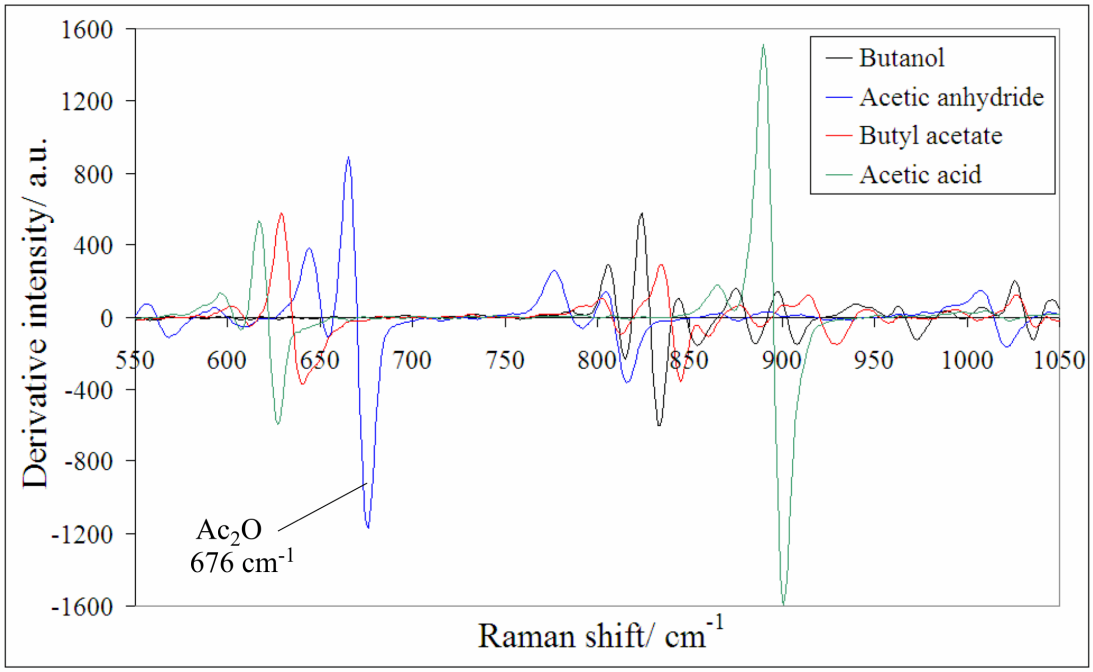

Figure 5.11. An overlay of individual derivative spectra of the pure reaction components plotted in the 550-1050 cm^{-1} region.

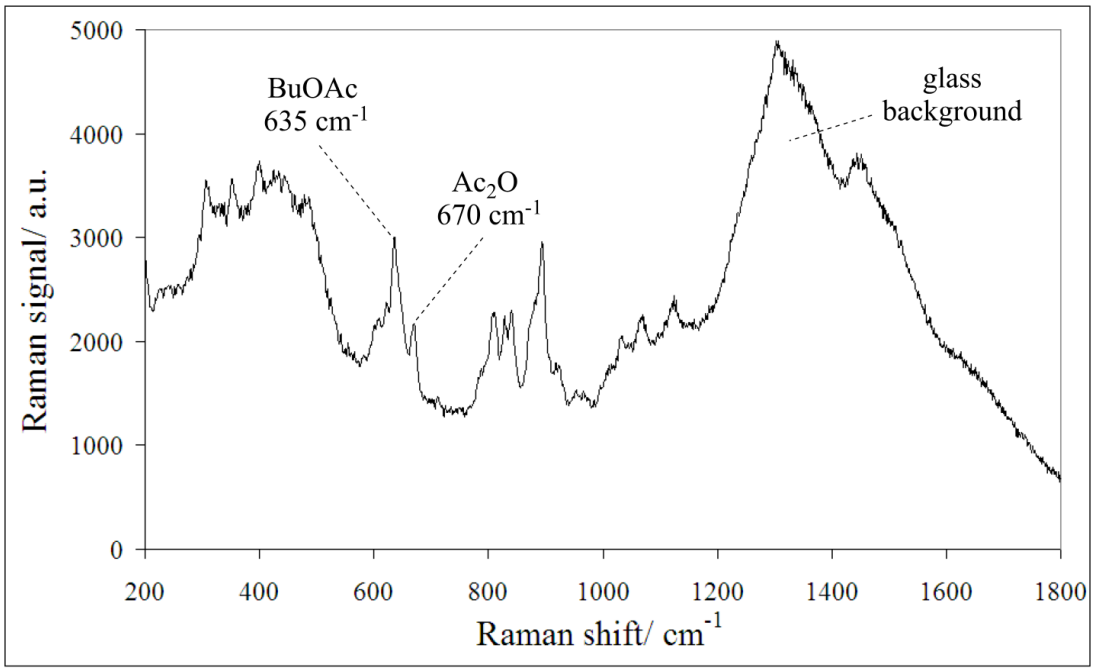

Figure 5.12. Example Raman spectrum of the reaction mixture in the microreactor.

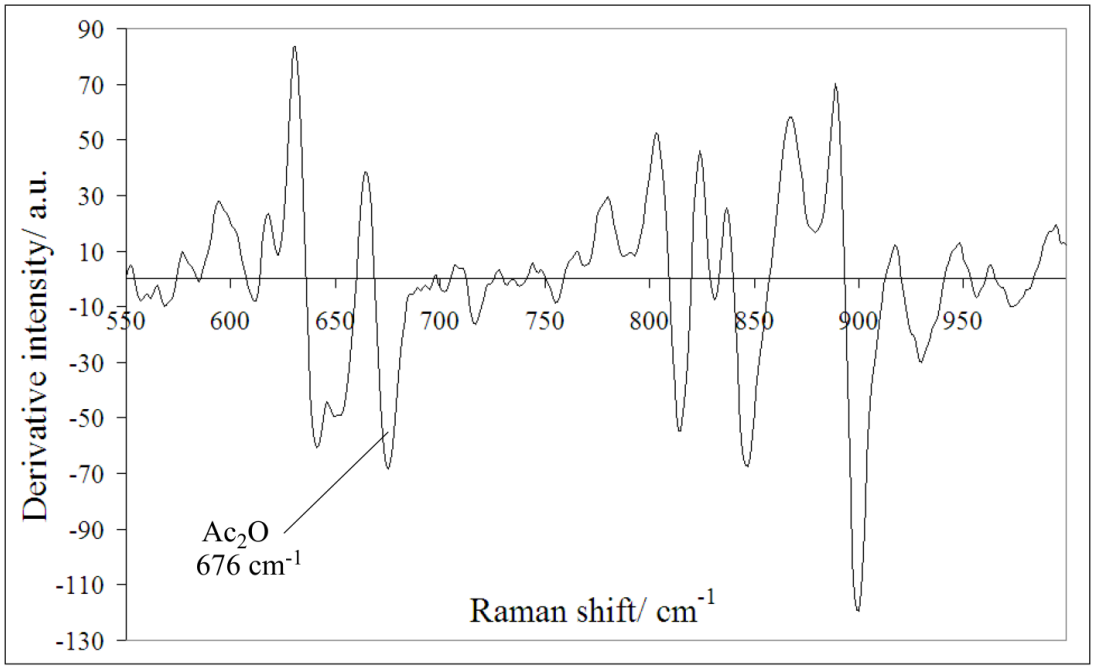

Figure 5.13. Example 1st derivative Raman spectrum of the reaction mixture.

Estimating mixing efficiency. The butanol peak at 397 cm^{-1} was used along with the peak of acetic anhydride (670 cm^{-1}) to evaluate the mixing efficiency of the reagents at the start of the microreactor serpentine. The diffusion profiles obtained when acetic anhydride and butanol were each flowing at 20 or 5 $\mu l \cdot min^{-1}$ are plotted in Figure 5.14. Raman spectra were collected from several lines across the microreactor serpentine at increasing distance from the mixing point. Measurements were made at 10 μm intervals across each line in the serpentine. It was not necessary to use derivative spectra as the background was stable and the two Raman bands selected for analysis (397 and 670 cm^{-1}, Figure 5.15) do not overlap with other peaks. As expected, the results confirmed that with lower flow rates the reagents have to travel a shorter distance to mix. Matching of the peak centres on X-axis is the indication of good mixing. The drop in intensity observed from line 1 to 9 on both figures is caused by diffusive dilution and the chemical reaction. However, it should be noted that due to the relatively large laser spot size (40 μm) and the parabolic shape of the channel (see Figure 5.9), the Raman intensities obtained do not accurately describe the distribution of a substance across the microchannel, but can only be used for rapid estimation of mixing efficiency, which is often hard to calculate in the presence of chemical reactions and related heat and mass transfer effects across the channel.

This information is important for selecting flow rate regimes and deciding whether a micro-mixer is required for the process under investigation. According to Figure 5.14, for the reaction described in the present work, mixing is sufficiently fast at 5 µl min^{-1} and no extra measures are needed to facilitate mixing.

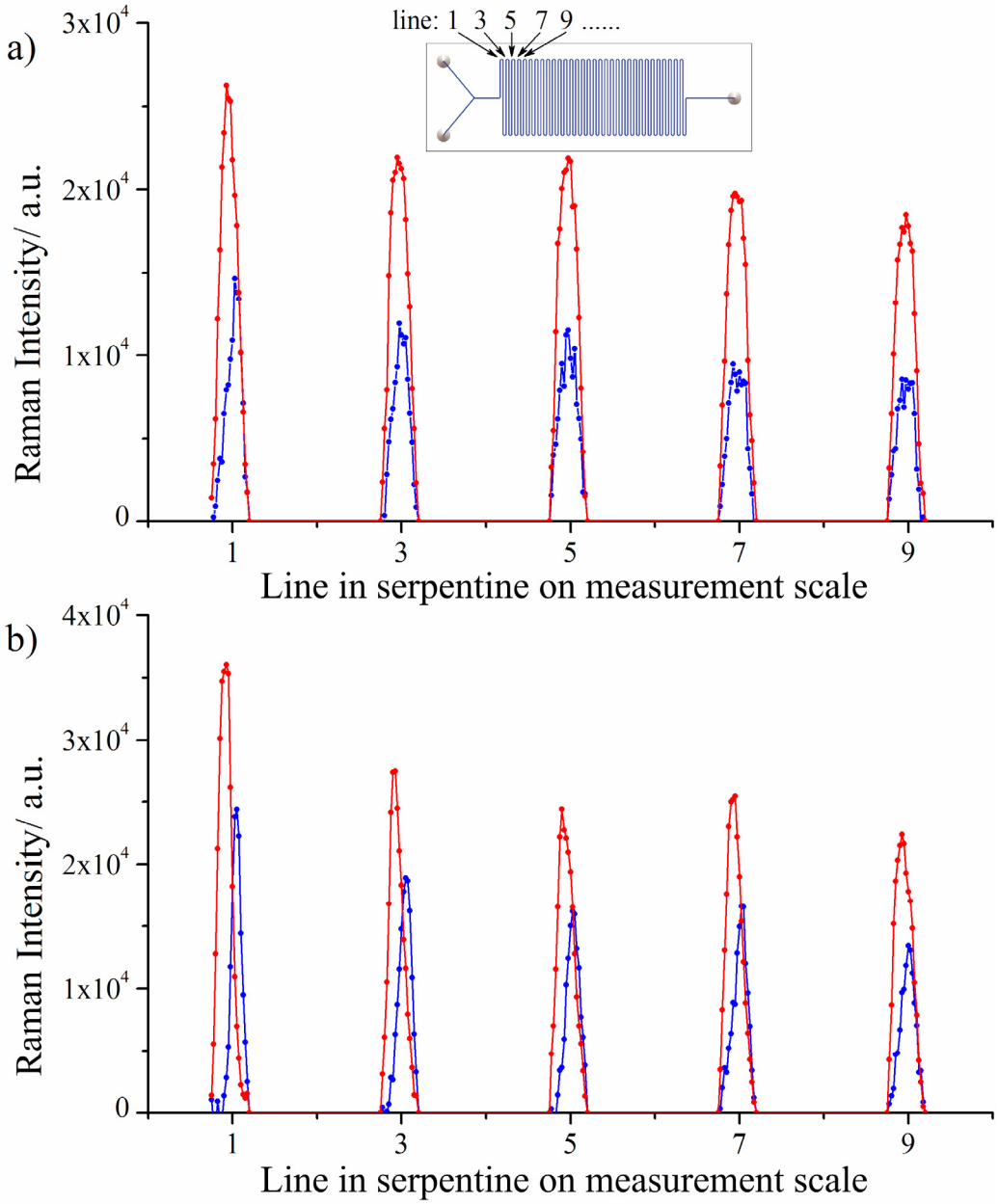

Figure 5.14. Estimation of inter-diffusion profiles within microchannels for butanol (blue line, 397 cm^{-1}) and acetic anhydride containing 3% v/v sulphuric acid (red line, 670 cm^{-1}) at flow rates of (a) 5 µl min^{-1} and (b) 20 µl min^{-1} for each reagent. Each set of measurements represents one line in the serpentine; 2 s acquisition time.

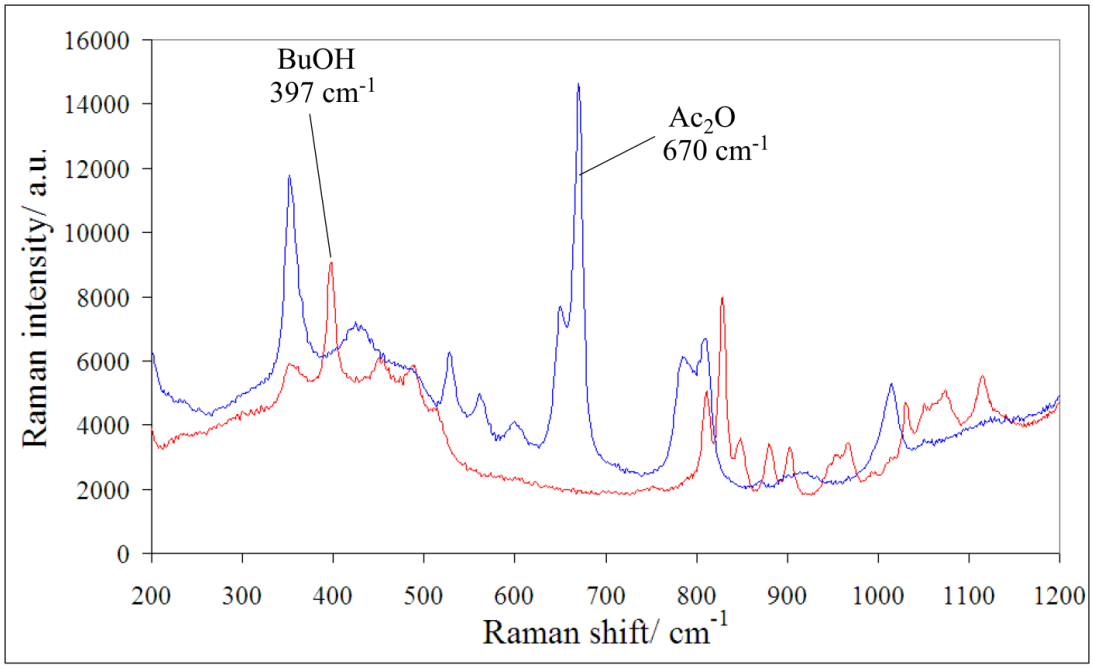

Figure 5.15. Overlaid Raman spectra of pure BuOH and Ac_2O. The peaks used for analysis are indicated.

Analysis at a fixed position in the serpentine. When a multi-stage synthesis is performed in a single chip, the effect of flow rate on the fluid composition at a particular point must be characterized to optimise the process. Raman spectra were recorded at a fixed point in the serpentine (line 33 – in the middle of the microreactor) to investigate the effect of reagent flow rate on the extent of the reaction. Butanol and acetic anhydride were pumped at different rates: 15 and 16; 9 and 9.6; 6 and 6.4; 3 and 3.2; 1.5 and 1.6 µl min^{-1}, respectively. The progression of the reaction was monitored by measuring the change in the intensity of the signal for acetic anhydride at 670 cm^{-1} and butyl acetate at 635 cm^{-1}. The overlap between the butyl acetate and acetic acid peaks at 635 and 622 cm^{-1}, respectively (Figure 5.10), did not pose a problem as both substances are 1:1 products of the reaction, and no side reactions were revealed. It was noted that for this study, use of 1st derivative spectral measurements was unhelpful as the negative part of the acetic acid signal overlapped the positive part of the butyl acetate signal (Figure 5.11). The results for the different flow rate combinations are shown in Figure 5.16 and are based on 50 consecutive spectra with a time interval of 7.53 s between each spectrum. Figure 5.16 indicates the influence of flow rate on the extent of the reaction at the measurement point. The anti-correlating periodic fluctuations of the spectral

responses are much greater than the measurement noise and were found to be caused by unstable fluid pumping (CMA dual syringe pump). When a single pump (Aladdin) was used to drive both syringes, improved flow stability, with no periodic fluctuations in response, was observed. For example, the relative standard deviation (RSD) of the butyl acetate signal in Figure 5.16 was 4.2 %. This compares to a RSD of 1.1 % when a single pump was used to drive the two syringes (each at a flow rate of 10 μL min^{-1}). Rapid data acquisition is essential to detect and track short time-scale instabilities (in comparison to the typical measurement time achieved with off-line methods of analysis) of this type that disturb the steady state of microfluidic reactions. The short measurement time used in this study was adequate to reveal the effects and demonstrates the usefulness of Raman spectrometry for process investigation and optimisation in microreactor methodology.

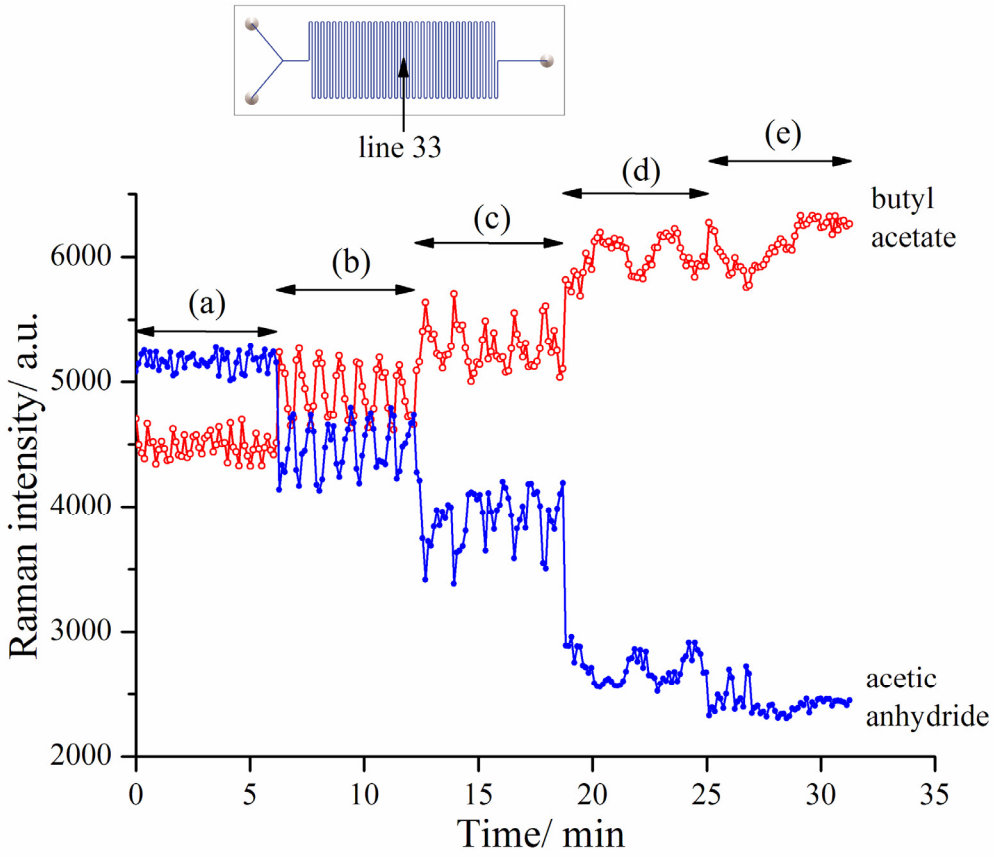

Figure 5.16. Raman signals from a reagent (acetic anhydride; 670 cm^{-1}) and a product (butyl acetate; 635 cm^{-1}) recorded at a fixed location (line 33) in the middle of the microchannel serpentine with butanol and acetic anhydride flow rates of (a) 15 and 16, (b) 9 and 9.6, (c) 6 and 6.4, (d) 3 and 3.2 and (e) 1.5 and 1.6 μl min^{-1}, respectively; spectral acquisition time, 2 s.

Steady-state analysis at different locations across the chip. The usefulness of the developed Raman probe to track the progress of the reaction across the serpentine at a fixed flow rate of the reagents is illustrated in Figure 5.17. First derivative spectra were calculated to remove the small variation in background signal observed over time. To achieve better pumping stability, this experiment was conducted with both syringes attached to a single pump (Aladdin). With flow rates of 10 μl min^{-1} for butanol and acetic anhydride, the reaction was found to be completed by line 62. When the Raman response for both acetic anhydride and butyl acetate was calibrated, the concentrations at line 62 were 1.4 ± 1.5 and 50.8 ± 5.3 % mol/mol, respectively, corresponding to a conversion of 97.0 ± 3.2 and 107.7 ± 11.1 %, respectively. This experiment demonstrates the ability of Raman spectrometry to facilitate process optimisation by extracting information from any point on the glass microreactor. Instead of carrying out several experiments at different flow rates as shown in Figure 5.16, steady-state analysis is faster and more efficient, although it requires accurate positioning of the probe across the chip and optical access to the whole chip surface. It can also be useful in kinetic studies and when designing multi-element microreactors.

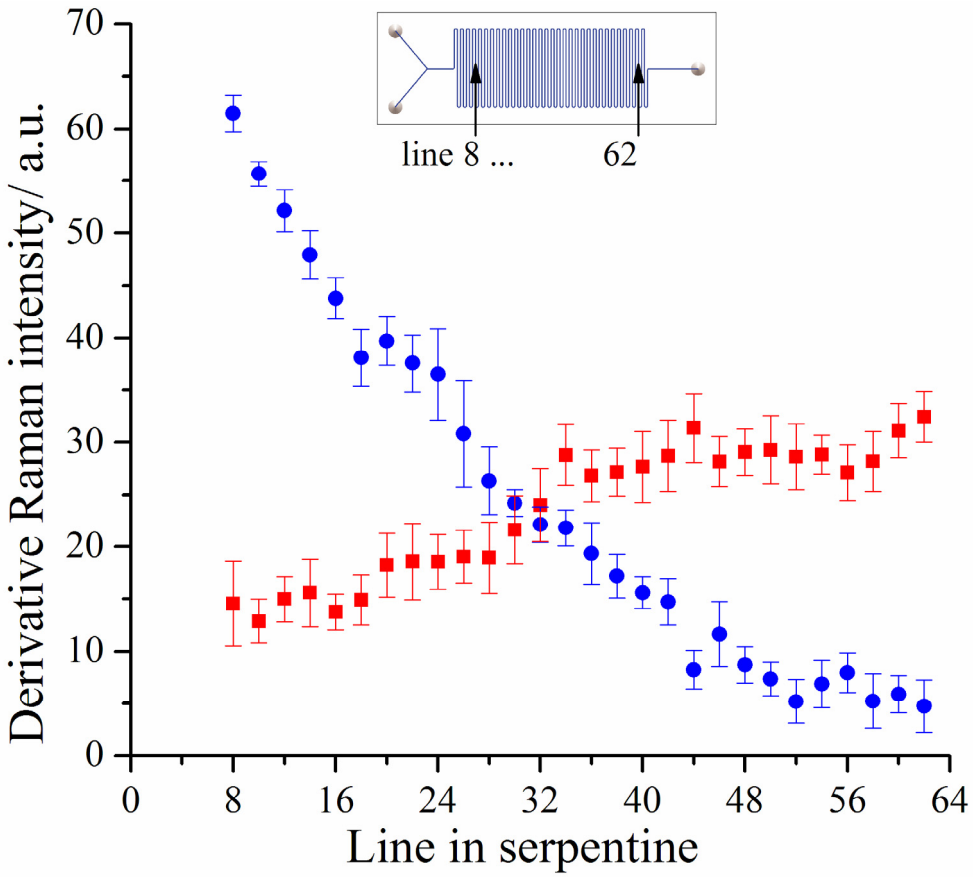

Figure 5.17. Derivative Raman signal from acetic anhydride (blue line, 675 cm^{-1}) and butyl acetate (red line, 300 cm^{-1}) measured at different positions (lines 8 to 62 at 2 line intervals) along the microchannel serpentine. Spectral acquisition time is 500 ms. Flow rate of each reagent is 10 µl min^{-1}. The error bars show ±one standard deviation (n=10).

5.3.4. Challenges

Although Raman spectrometry has considerable potential for reaction monitoring in microreactors, some undesirable effects were noted during the experiments. Although these problems are manageable, it is important to be aware of them when planning to apply Raman spectrometry to microfluidics. Generic issues typical of Raman spectrometry such as fluorescence or peak distortion caused by a changing molecular environment and/or temperature are not discussed here as these issues are well discussed in textbooks[75, 77].

High power density. To overcome the intrinsically low sensitivity of Raman spectrometry, high-power lasers are typically used. It is important to ensure that the sample components do not absorb at the laser wavelength, as the sample can otherwise be damaged as well as causing localised heating for the reaction. Even

provided that none of the reaction components absorb the laser radiation, it can be absorbed by impurities, intermediates or the products of side-reactions which may develop unpredictably. The implications of these effects may be insignificant when a large continuously mixed liquid sample is illuminated, but in the case of narrow microchannels the effects can be clearly visible, particularly when high-numerical aperture optics are used to tightly confine the beam within the microchannel. With the equipment used in this study (238 mW of laser power and 40 μm spot diameter) the power density at the focal point is around 20 kW/cm^2. It is not surprising therefore, that cavitation (bubble formation) and thermal-lensing have been observed during the experiments, probably due to the presence of impurities. Both effects cause local refraction which was observed by the dimming of the transmitted beam projected on a white surface behind the chip. In the case of cavitation, the shape and movement of a bubble can be seen either directly or with the use of a low cost CCD camera. Importantly, the refraction results in distortion of the Raman spectrum (as illustrated for ethanol in Figure 5.18), particularly affecting the intensity of the glass background, which is notably reduced due to the beam expansion behind the channel.

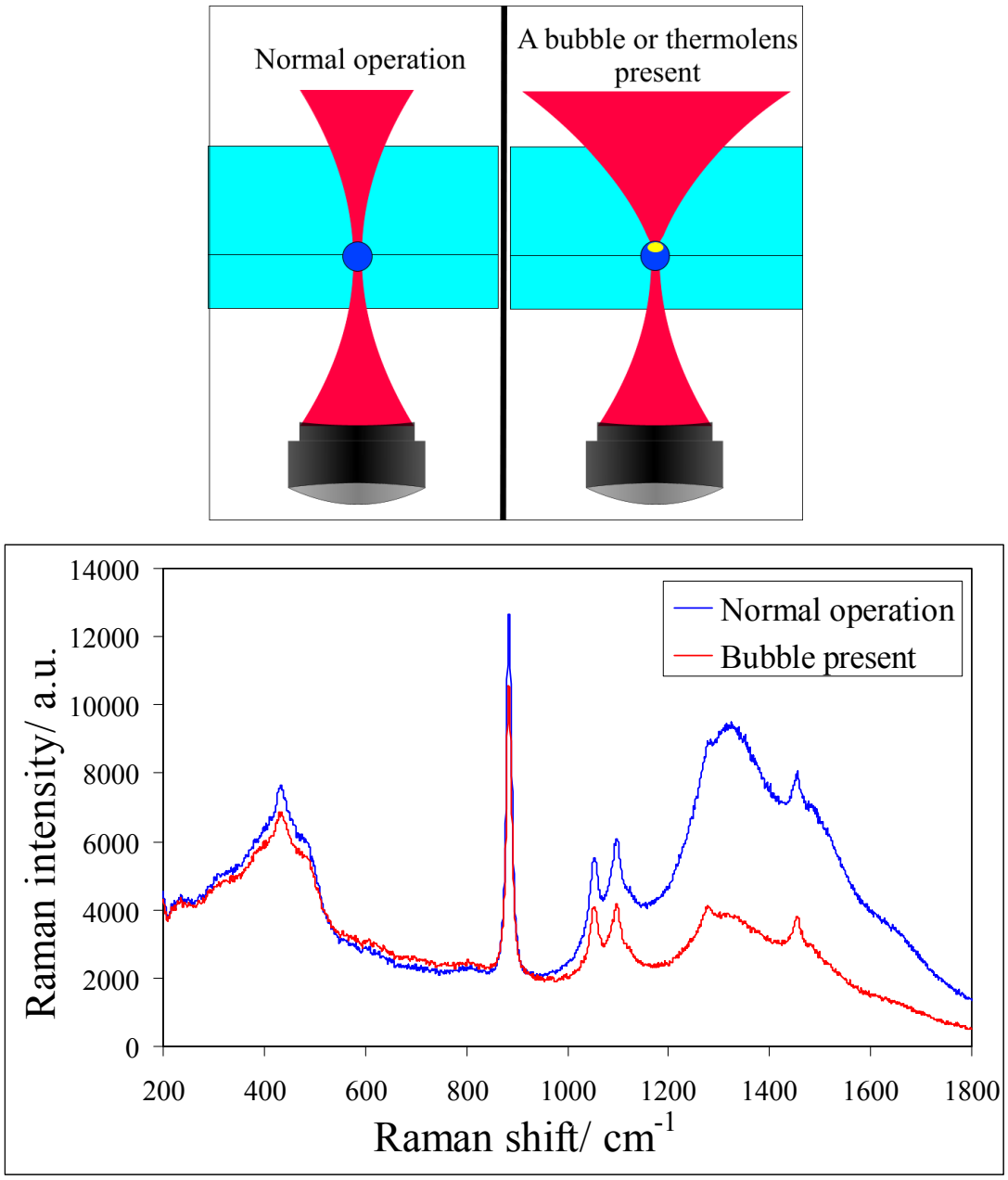

Figure 5.18. Refraction of the laser beam by a bubble or thermal lens and related change in the Raman spectrum of ethanol.

Once a bubble is formed at a certain location, it may be difficult to wash its nucleus off the channel wall. Therefore, they should be prevented from happening by avoiding abrupt drops of the flow rate while the laser is on. Thermal-lensing is only noticeable under static conditions and does not appear when the liquid is flowing, at least at the flow rates used in our experimental investigations. The extent of these effects can be reduced by using lower laser power, but with a concomitant loss of sensitivity. Nevertheless, by using clean reagents, and shuttering the laser beam

when the flow is stopped, or changes are applied, it is possible to completely avoid cavitation.

Background from microreactor material and channel geometry. With appropriate optics and the confocal optical arrangement realised in modern Raman probes it is possible to confine the signal collection volume within the microchannel dimensions and minimise spectral background from the microreactor material. Unfortunately, the signal to background ratio is very sensitive to the channel geometry, rapidly decreasing with reduced depth (due to increased contribution of the Raman signal from the glass channels), and there is no consistency in the shape and size of the microreactor channels as well as in the material from which microreactor chips are made. Moreover, as illustrated in Table 5.3, that even when the same microreactor type is manufactured from different batches of the same glass, the silica background can be significantly different. Raman spectra plotted in Figure 5.19a were collected from toluene in four different microreactors, with channel depth 50, 100 and 150 μm. Figure 5.19b shows the same spectra, but normalised to the background-corrected intensity of the Raman band at 1004 cm^{-1}. Plotting figures in the way shown in Figure 5.19b helps visualise the contribution of the silica glass background. The Figure shows that not only the background intensities, but also their shapes are different. The values of the toluene Raman signal, the intensity of the background at its highest point, and the signal to background ratios obtained from the four microreactors are summarised in Table 5.3.

Table 5.3. Influence of the microreactor type on the quality of Raman spectra of toluene collected from the microchannels.

Microreactor	Raman intensity/ a.u.		Toluene : glass
	Toluene	Glass	
50 μm (Micronit 2006)	2680	1460	1.83
100 μm (University of Hull)	6380	10060	0.63
150 μm (Micronit 2009)	21780	930	23.4
150 μm (Micronit 2006)	26430	2490	10.6

Figure 5.19b and Table 5.3 demonstrate the differences between the two microreactors of the same type manufactured with a 3 year interval. The intensity of the glass background around 450 cm^{-1} remains the same, while the signal at 1300 cm^{-1} is 4 times lower in the newer chip. In e-mail correspondence, Micronit representatives claimed that the glass type used for these two chips were the same. If this is true, the observed differences can only be explained by batch-to batch variations in glass. The difference between the Raman intensities of toluene measured in these two chips was almost 20 %, which is a rather high variation between microreactors of the same design. As sufficient care was taken to focus the laser beam properly, this difference is likely due to either differences in channel size or shape or due to the variations in the signal collection efficiency developed over a few days between the experiments. In any case, it is clear that collecting spectral information from microchannels in a reproducible way is difficult. Calibration is needed prior to a new experiment or when the microreactor is changed.

In terms of background reduction, it is advantageous to use deep and narrow channels, whereas typical microreactors are made with shallow and wide ones. These facts pose a challenge to Raman instrumentation – is it possible to design a probe with which high-quality spectra can be obtained from a wide range of microreactors? Or should a researcher optimise the optics for each particular channel geometry to achieve best results?

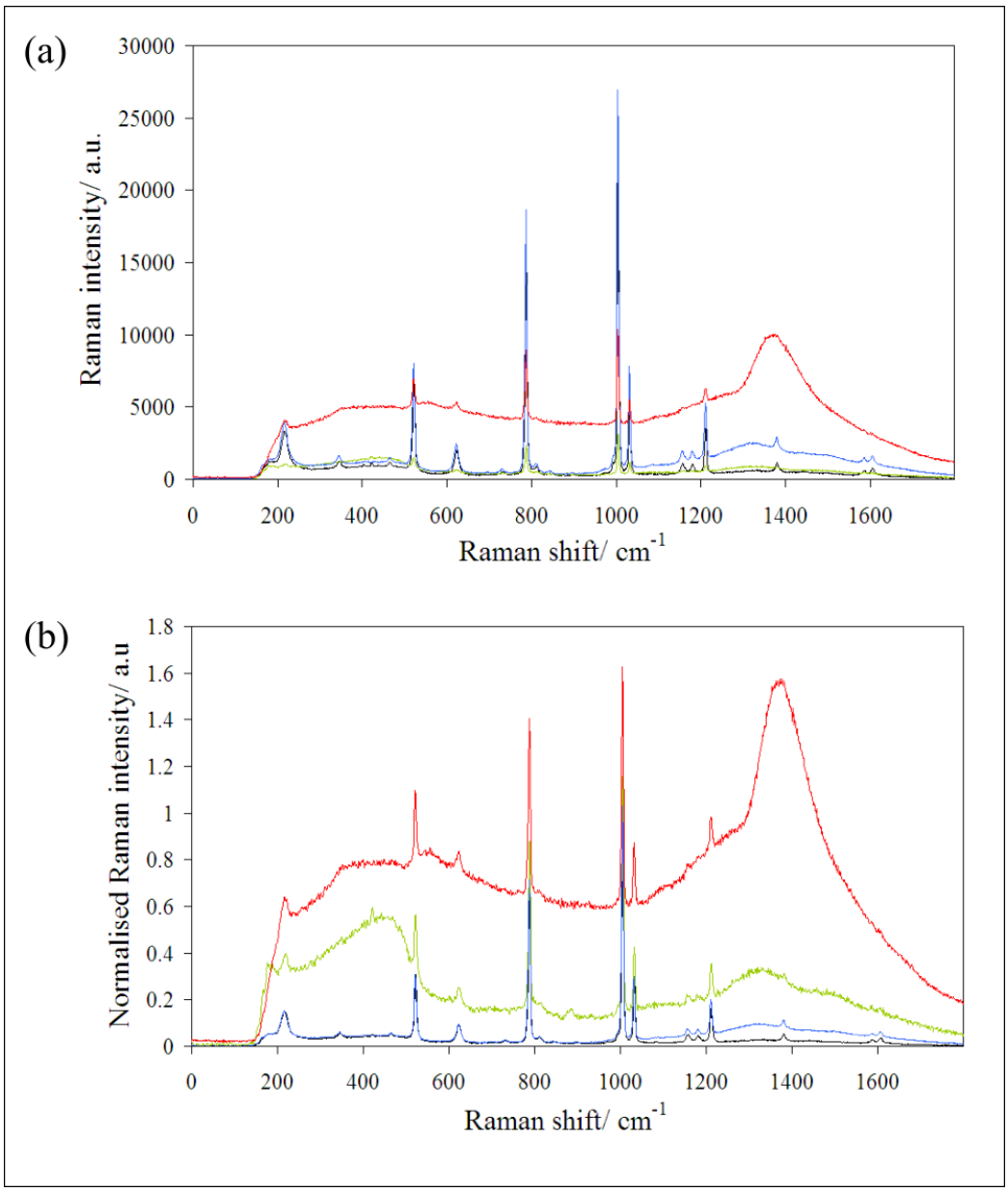

Figure 5.19. Raman intensities (a) and Raman intensities normalised on the magnitude of background-corrected Raman band of toluene at 1004 cm^{-1} (b). Spectra from four microreactors chips are shown, the chip from University of Hull (red line, 100 µm channel), Micronit chip FC_R50.676.2 (green line, 50 µm channel, purchased in 2009), Micronit chip FC_R150.676.2 (blue line, 150 µm channel, purchased in 2006) and Micronit chip FC_R150.676.2 (black line, 150 µm channel, purchased in 2009).

Uniformity of Raman spectra obtained from different locations on the chip. Steady-state analysis across the microreactor serpentine (Figure 5.17) relied on the assumption that all measurement points were identical. If they are not, then the obtained results would have to be corrected. To assess the uniformity of the

microchannel across the measurement points, the microreactor was filled with pure toluene and 10 Raman spectra were collected at several measurement points across the serpentine and compared with each other. The Raman intensities at 1004 cm^{-1} corresponding to the strongest toluene band are plotted for two microreactors in Figure 5.20. The mean values and standard deviations calculated for the data obtained from every channel separately were compared. The t-test revealed only a few measurement points (line numbers) across the 50 μm channel that yield statistically different Raman spectra (e.g. lines 7 and 8 or 11 and 12), whereas the microreactor with 150 μm channels demonstrated more pronounced point-to-point variations. The relative standard deviations of the signal averaged over the whole data set in each of the two microreactors were 0.7% and 1.1% for 50 μm and 150 channel diameters, respectively. This result suggests that for the two microreactors tested the narrower channel is more uniform. The extent of point-to-point variation was lower than the error obtained for the measured reaction conversion in Figure 5.17.

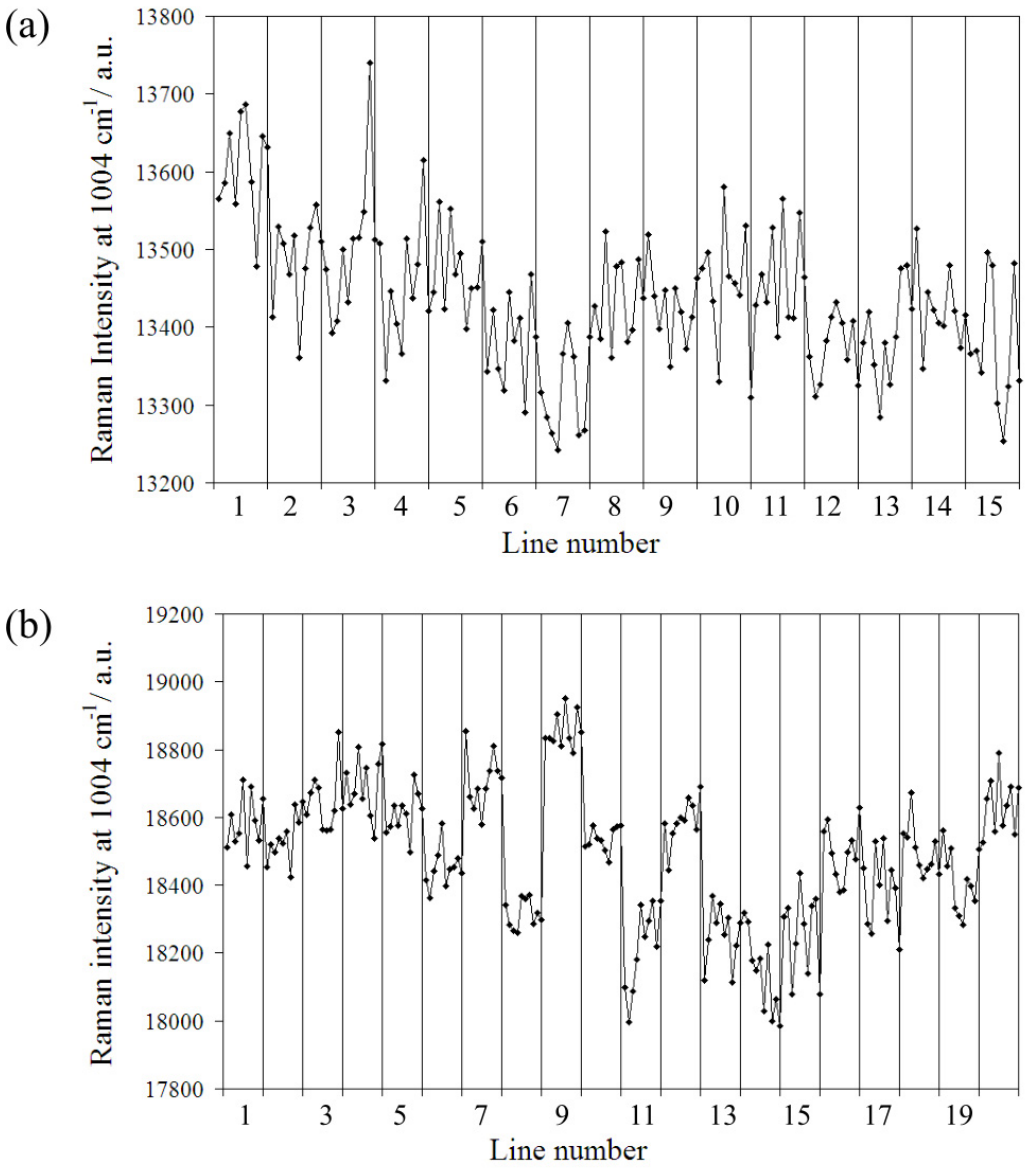

Figure 5.20. Variability of the Raman intensities recorded at different locations across the microreactor serpentine in two different microreactor chips, (a) Micronit chip FC_R50.676.2 (50 µm channel, purchased in 2009), (b) Micronit chip FC_R150.676.2 (150 µm channel, purchased in 2009).

Representativeness. The representativeness of a sample used in any analysis is a critical issue in analytical practice. It takes a rather unusual form when applied to non-invasive analysis within microchannels. Generally it should not be a problem in a continuous flow system where no sample is taken away and it is not difficult to collect spectra from the whole channel cross section ensuring high representativeness of the signal collection volume. However, the problem is with the rheology that is

peculiar to microchannels[2]. Given that the flow is always laminar at such a small dimension, the parabolic flow profile causes different layers of the fluid to move at different speeds, and hence may have different composition as a reaction proceeds. In this case, the average local composition across the channel cross section recorded by Raman spectrometry may be different from the actual average composition of the flowing stream. Although molecular diffusion across the channel combats the inhomogeneity, the speed of this process can be insufficient to make the stream homogeneous across the whole reactor. The situation is severely complicated by the presence of a chemical reaction and related density and temperature gradients, and will be worse at higher flow rates. Moreover, imperfections on the glass surface can nucleate location-specific phenomena at the microchannel walls and also reduce the representativeness of the Raman measurements at that point.

Thus, during the experiments performed in this study, the appearance of fluorescence in the Raman spectra was occasionally observed, which was much stronger at the channel edges. The fluorescing substance underwent rapid photo bleaching and very slow recovery when the spot was not illuminated by the laser. The spectra taken from the collected liquid did not contain the fluorescence background. These observations suggested that due to a side reaction that took place at the liquid-glass interface, an unknown fluorescing product accumulated at the rough internal glass surface and could not be washed away by the flow.

This issue makes it necessary to perform rheological assessment of the processes in microreactors and verify Raman data by other methods. Comparison of the spectra taken from the microreactor and from the collected product can help understand the process and reveal hidden surface phenomena. It is correct to say that the problem with representativeness is not a unique feature of Raman measurements and is equally relevant to any optical method applied to microreactors, especially if high power sources are used.

5.4. Conclusions

The results reported in this Chapter highlight the importance of careful optimisation of the optics of a Raman probe to obtain high quality spectra from microreactor

channels. A fibre-optic probe has been designed to permit real-time monitoring of the content of liquids in microfluidic channels by non-contact Raman spectrometry. The main parameters affecting sensitivity and signal to background ratio were discussed. Firstly, the core diameter of the probe fibres was shown to play one of the key roles; of the combinations investigated, 62.5/62.5 μm for excitation/collection was found to be optimal for 150 μm-deep microchannels, with 62.5/100 μm preferred for bulk liquid samples. Secondly, the optics that focus the probing beam onto a sample were analysed. With both a cuvette and microreactor the miniature aspheric lens performed much better than conventional microscope objectives as well as offering practical advantages through its compactness and relatively low cost. Microscope objectives with high numerical aperture were found to be inconvenient for operation in microreactors due to their low working distance and large size. Although more advanced microscope objectives with a high working distance and high numerical aperture are available in the market, they are not yet compact and are very expensive. The discussion about optimisation of instrumental parameters presented in this Chapter can also be relevant for analysis of the control of microfluidic channels by laser-induced fluorescence.

The fabricated probe has been demonstrated to be suitable for rapid real-time monitoring of the liquid content in microfluidic channels. The potential of Raman spectrometry for this purpose has been demonstrated by characterising the esterification of butanol with acetic anhydride. The rapid data acquisition that became possible owing to careful optimisation of the probe optics has shown unique opportunities for fast process optimisation and efficient reaction monitoring. Although the use of Raman spectrometry with microreactors is associated with a number of challenges that have to be addressed, many of these issues are manageable and are unlikely to prevent this new application of Raman spectrometry from further development and wide use.

6. New "flushed steady-state" methodology for process analysis and kinetic studies in microreactors

In this Chapter, a new procedure will be described that is suitable for the rapid acquisition of location-specific information about the reaction profile along a microreactor channel that involves analysis of the liquid as it exits the reactor. The procedure is based on flow manipulation and the use of rapid and frequent analytical measurements to generate a steady-state profile of the reaction within the reactor under selected temperature conditions. This approach allows much faster generation of kinetic data, such as reaction rate constants, than would be possible with conventional multiple-experiment procedures that use information derived only at a single point in the reaction profile. In this Chapter, the new method is applied to study the kinetics of a Knoevenagel condensation reaction and involves the use of non-invasive Raman spectrometry with a fibre-optic probe described in the previous Chapter. Before discussing the developed method a brief theoretical introduction is necessary to explain the necessity to develop a new approach to analysing microfluidic reactions.

6.1. Kinetic studies on the microfluidic platform

6.1.1. Advantages of using microreactors for kinetic studies

Microfluidic devices have proven to be an exceptionally useful platform for a wide range of chemical applications[1, 5] including the study of reaction kinetics, offering advantages over conventional batch experiments. Due to the efficient heat exchange in microchannels, highly endothermic or exothermic reactions can be studied in virtually isothermal conditions. For example, Cao et al. used a microreactor system to evaluate the performance of a Pd/ZnO catalyst for fuel cell applications and measured the kinetics of the reaction[221]. The authors noted that isothermal conditions were important for the correct determination of the kinetic parameters.

It has been reported that the use of microreactors to study kinetic isotope effects provides better accuracy than alternative methods[9, 222, 223]. Another application of microreactors is kinetic studies of fast reactions. Such studies are difficult or impossible to perform in flasks due to complications that arise from the lack of

homogeneity and relatively slow mixing that typify batch processes. In microchannels of special geometry, mixing can be as fast as 15 μs[36] (see Section 1.3.3), which is essential for studies of extremely fast processes such as formation of intermediates and conformational changes during protein folding[224, 225].

A useful method for studying short-lived intermediates of biochemical reactions with high temporal resolution is time-resolved electrospray ionisation mass spectrometry (ESI-MS)[226-228]. In this method, an electrospray ionisation needle is directly coupled to a continuous-flow mixing capillary. The reaction time is varied by fine-tuning of the capillary volume.

Various enzymatic assays[229] including kinetic characterisation of enzymes[230, 231] are among the most popular applications of microreactors. The use of microreactors can reduce the analysis time and consumption of chemicals by 4 orders of magnitude compared to conventional assays[232]. A strong trend is characterisation of enzymes immobilised on the internal channel walls[62, 233] or packed beds[234, 235]. Immobilisation allows rapid screening of substrates and more effective use of enzymes for synthetic purposes. In addition, by using sequential sections of the capillary with different immobilised enzymes it is possible to perform multi-step reactions[62, 233].

Another advantage of microreactors is the low consumption of chemicals, which is useful for rapid cost-effective catalyst screening[221]. De Bellefon et al.[236] developed a method for high-throughput screening of homogeneous and heterogeneous reactions based on dynamic sequential procedures involving pulsed injection and fast mixing in a microreactor. When rhodium-containing hydrogenation catalysts were assessed[237], only 14 μg of rhodium was required for each test, a 50-fold reduction compared to the analogous batch experiments. With this methodology, libraries of compounds can be assessed with high speed.

The throughput of catalyst screening and kinetic analysis of large amounts of similar reactions can be substantially increased by carrying out the reactions in parallel. Such multiplexing is easier and cheaper to realise with microfluidic technology. Bula et al.[238] used 4 parallel channels to investigate the kinetics of a Knoevenagel condensation and reported considerable reduction of cost and experimental effort.

Duffy and others[25] demonstrated simultaneous analysis of 48 enzymatic assays to determine the yield and the Michaelis constants of enzymes. They used at-line spectrophotometric detection on a specially designed instrument.

An interesting method of parallelisation was reported by Mao an co-workers[62]. They combined two streams of reagents in a Y-junction, which diffused into each other flowing side by side. After a distance of 2 cm, the channel was split into several smaller channels as shown in Figure 6.1. The distance from the Y-junction to the splitting point was calculated such that mixing of the reagents was incomplete and the distribution of chemicals across the channel had a characteristic steady-state inter-diffusion profile. In this geometry, each independent sub-channel containing portions of liquid with a variable proportion of reagents proceeded downstream to the next section where an immobilised enzyme initiated the reaction. The reaction conversion was monitored with fluorescence spectrometry from 12 channels simultaneously.

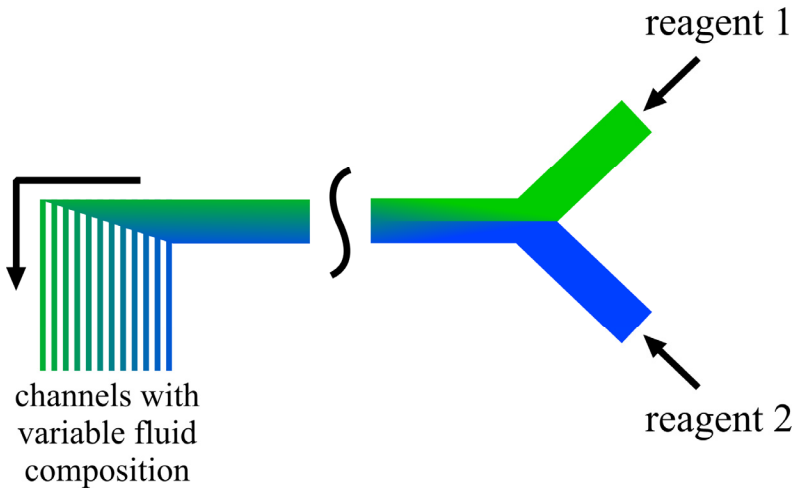

Figure 6.1. Schematic of a diffusion-based microfluidic diluter (adapted from [62]).

6.1.2. Sampling methods

Obtaining relevant and timely analytical information from microreactors can be challenging due to their small size and difficulties associated with interfacing the analytical instruments with microchannels. Depending on the type of the microfluidic device, the complexity of the experiment and the amount of information needed, three categories of sampling methods are generally used based on extractive, in-line or non-invasive analysis.

For extractive procedures, a small portion of the fluid is removed from the microreactor and transported to a detector for analysis. This approach is generally applied to such methods as GC[221], LC-MS[239], or HPLC[240]. Although these methods are destructive, they are very sensitive and can provide useful information about the reaction that cannot be obtained with other techniques.

In-line analysis is performed with an integrated probe and requires no sample removal. The probe can be based on a refractive index sensor[241], electrochemical detection such as amperometry[242, 243], or an attenuated total reflection (ATR) crystal for near-infrared[244] or mid-infrared[245] absorption measurements. The use of mid-infrared absorption is particularly promising because of its high spatial resolution and inherent high throughput achieved by using a combination of an ATR-objective and a detector array that allows simultaneous acquisition of spectra by the array pixels. Wensink et al.[246] carried out NMR analysis on a microfluidic chip using an integrated micro-coil. Despite the rich information about the reaction that can be obtained with NMR, the necessity to insert the microreactor into a large magnet and difficulties with generating a uniform magnetic field inside the microchannel limit applicability of this method. In-line analysis can also be carried out using an analyser module directly attached to the microreactor for UV-visible spectrometry[223, 238, 247] or time-resolved ESI-MS[227].

Non-contact analysis, where no physical contact with the sample is required, offers a unique opportunity to extract analytical information from different locations on the microreactor. This ability can be particularly useful when processes in complex microfluidic devices need to be analysed. So far only confocal optical techniques such as Raman spectrometry[204, 205] and fluorescence spectrometry[248, 249] have been applied successfully. The advantages of using Raman spectrometry were discussed in Chapter 5.

6.1.3. Methodology of analysis

The type of flow manipulation[9] used in microreactors often influences the preferred format of chemical analysis and the selection of an analytical method. The *stopped flow* approach[62, 206, 247, 250] involves initial pumping of the reagents into the microreactor at a fixed flow rate with subsequent cessation of the flow. After the

flow is stopped, the reaction continues in the stationary mixture, and the reaction progress is monitored continuously with an in-line or a non-invasive sensor. This method can be considered as a variety of the traditional analysis of batch reactions. The difference is that the reaction vessel volume and the amount of reagents are very small. There are several reasons that make stopped flow analysis more convenient than the traditional batch analysis of liquid-phase reactions. Firstly, fluid delivery to the measurement point is easy to control. Secondly, the many advantages of microreactors (enhanced safety, reduced consumption of chemicals, efficient heat dissipation, ease of temperature control and automation, and no contact with air) are applicable to stopped flow analysis. Thirdly, stopped flow experiments can be replicated very rapidly without spending much time and effort on cleaning the reaction vessel and on other preparation procedures.

With *quenched flow*, the reaction is terminated by introducing a quenching chemical to the fluidic path[238, 251] or by using immobilised catalysts, where the reaction stops automatically upon leaving the catalytic zone[239], prior to extractive or in-line analysis. In some situations, the quenched flow approach is very convenient. After the reaction is terminated, there is no urgency with the subsequent analysis. Therefore, it is a preferred method for extractive analytical methods.

Continuous flow analysis is performed *in situ*, usually at the end of the microreactor flow path with an in-line or a non-invasive sensor[232, 234], or at many different locations along the reactor by using a non-invasive probe[204, 248, 249, 252]. This is the least disruptive method in respect to the analysed process. The flow does not need to be stopped and the sample is not extracted. This approach can be used to study reactions in real time.

When continuous flow analysis is performed at a fixed flow rate, the fluid composition is constant over time at any location along the microchannel. When analysis is carried out in these conditions, it is sometimes referred to as *steady-state analysis*. It allows the opportunity to make measurements over longer periods to improve the signal-to-noise ratio when less sensitive methods of analysis, such as Raman spectrometry, are used.

6.1.4. The need for a new approach

The use of non-invasive spectroscopic analysis at different locations along a microreactor (steady-state analysis) is extremely useful in obtaining kinetic information about the reaction, optimising reaction conditions in real time, and assisting with the rapid design of multi-stage microreactor assemblies. However, the results described in Chapter 5 suggest that the quality of Raman spectra obtained directly from microchannels depends not only on the optics in the probe, but also on the channel geometry and microreactor material. Moreover, some microreactors are made of non-transparent materials such as silicon or metal, making it impossible to apply optical methods of analysis in these situations. Possible non-uniformity of the channel shape and size along the serpentine is another issue that complicates Raman measurements in different locations. This compatibility issue makes it difficult to develop a universal optical system suitable for analysis in different microreactors. It is a significant limitation to the applicability of steady-state methodology in the field. The diversity of microreactor types on the market is primarily defined by the necessities to minimise their cost and suit certain requirements dictated by the chemistries carried out in these devices. Therefore, adapting microreactor production process to the requirements of analytical instrumentation would be too expensive and unpractical. It is more reasonable to modify the methodology of steady-state analysis in order to make it less demanding.

6.2. Method

6.2.1. Model microfluidic system

The model microreactor is schematically shown in Figure 6.2. The microfluidic pathway is presented as a tube with cross section *s*, length *L*, and total volume $V = sL$. The two liquid reagents are pumped into the microreactor with the same volumetric flow rate. The term 'flow rate' will refer to the combined volumetric flow rate (*F*) which is twice as high as the pump-set value. The streams converge and mix in the microreactor junction ($x = 0$). The mixing zone is negligibly small compared to the total length of the line. Similarly, the mixing time is considered small compared to the reaction time and can be neglected in the analysis.

A non-invasive Raman probe collects data directly from the end of the microfluidic path ($x = L$). The analysis time is minimal and the frequency of measurements is high. The channel cross section of the measurement zone must not be notably greater than that in the rest of the system to prevent dispersion and the accompanying loss in compositional resolution that would result in an enlarged measurement cell.

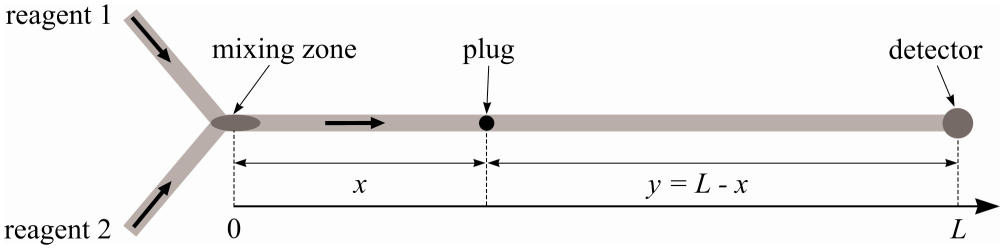

Figure 6.2. Schematic of the model microfluidic system.

6.2.2. Concept

The reaction is initially stabilised at a low flow rate (F_1) such that the reaction is complete or nearly complete by the end of the flow path in the reactor. With some reactors, analytical measurements can be made at various positions along the microreactor capillary, to allow production of a reaction profile from which kinetic information can be derived. However, this convention is not always possible owing to the design of reactor and materials of construction. In the new method, only one measurement position is required at the end of the reactor. After a sufficient period at low flow rate F_1 the flow is increased by an order of magnitude to F_2. The high flow rate pushes the profile of reactants and products that has developed along the reactor capillary to the detector where many short-time interval measurements are made. Knowing the magnitude of F_2, the time when it was applied, the dimensions of the flow path and the times of all analytical measurements, it is possible to recreate the reaction profile that existed along the microreactor capillary when the flow rate was set at F_1.

However, there are two important issues that need to be considered. Firstly, the chemical reaction continues as the profile of reactants and products established at the lower flow rate is moved to the measurement zone at the higher flow rate. The extra reaction time will be least for the material right at the end of the reactor and greatest

for the material at the start of the reactor. The variable extra reaction time has to be calculated and taken into account when trying to derive a true reaction profile corresponding to F_1. Secondly, the step increase in flow rate is never perfect. The system always needs some time to speed up to the higher flow rate. In addition, there is no guarantee that the flow system will respond to an abrupt increase in flow rate in the same way every time the procedure is repeated. The mathematical analysis provided below considers these issues and shows how to account for them theoretically as well as in a semi-empirical way.

6.2.3. Mathematical model

It is convenient to consider the flow line as a series of small liquid plugs moving one after another and each having the length $\Delta x << L$. In the initial state created at F_1, every location in the line can be defined by the reaction time (t_1), proportional to the travel distance (x):

$$t_1 = sx / F_1 \qquad (6.1)$$

At a certain moment in time, $\tau = \tau_0$, the higher flow rate F_2 is applied to the system. Figures 6.3a and 6.3b illustrate the subsequent changes in flow rate and product concentration recorded by the detector, respectively. If τ_0 is considered the zero point for changes to the system, three characteristic events will follow one another after the flow rate change: (i) after τ_1 seconds of speeding up the flow, the system stabilises at the target flow rate F_2; the exact function $F(t)$ during this transitional period is uncertain; (ii) by τ_2 seconds, the earliest plug of the reaction profile established at flow rate F_1 (corresponding to position $x = 0$ in Figure 6.2, at time τ_0) reaches the detector; (iii) by τ_3 seconds, the new end-of-line concentration of product achieved at flow rate F_2 is established at the detector site. At this moment the detector is exposed to the first plug that entered the line at τ_1 when the flow rate stabilised at F_2.

The region from τ_2 to τ_3 in Figure 6.3b corresponds to the period of flow rate increase (from τ_0 to τ_1 in Figure 6.3a). If the flow rate changed instantaneously, the parameters τ_2 and τ_3 would converge to a single point.

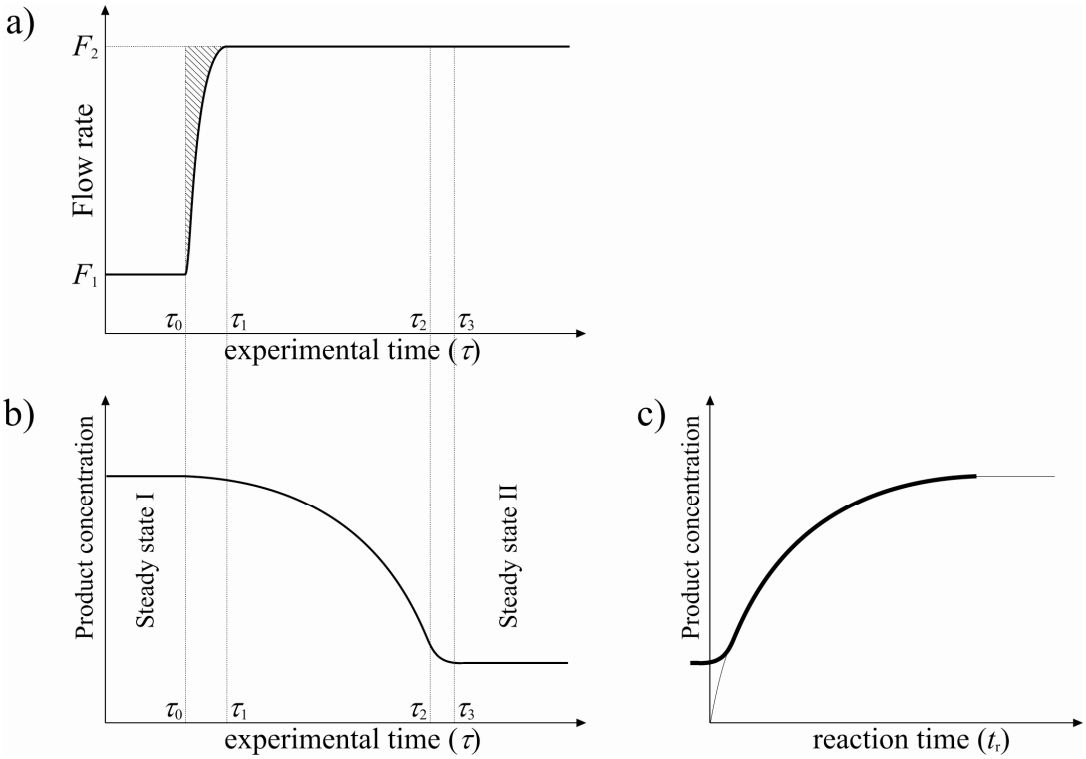

Figure 6.3. Changes in flow rate (a) and the detected product concentration (b) occurring during the proposed procedure, and the calculated kinetic curve (c).

The detector frequently analyses the fluid as it passes through. The absolute time of each analysis (τ) is recorded and after subtracting τ_0 becomes equivalent to the travel time that was required for a plug to reach the detector since the moment of flow rate change:

$$t_2 = \tau - \tau_0 \qquad (6.2)$$

The sum of t_1 and t_2 is the actual reaction time at the moment of detection:

$$t_r = t_1 + t_2 \qquad (6.3)$$

To derive t_r both components in (6.3) need to be found; t_2 is known from the experiment and t_1 can be derived from equation (6.1):

$$t_1 = \frac{sx}{F_1} = \frac{s(L-y)}{F_1} = \frac{V - sy}{F_1} \tag{6.4}$$

The problem comes down to determination of *y,* which is the distance at time τ_0 that needs to be covered by the plug to reach the detector (Figure 6.2). It can be calculated by integrating the flow rate function over time (from τ_0 to τ). For all experimental points obtained within $\tau_1 \le \tau \le \tau_2$ the following equation is true:

$$y(\tau) = \int_{\tau_0}^{\tau} \frac{F(\tau)}{s} d\tau = \frac{1}{s}\int_{\tau_0}^{\tau_1} F(\tau) d\tau + \frac{1}{s}\int_{\tau_1}^{\tau} F_2 d\tau = M + \frac{F_2}{s}(\tau - \tau_1) \tag{6.5}$$

The integral (6.5) has been split into two terms in order to separate out the unknown part, labelled as *M*. After grouping the unknown parameters the following equation is derived:

$$y = \frac{F_2 \tau}{s} - N \tag{6.6}$$

where $N = \frac{F_2 \tau_1}{s} - M$ (6.7)

Parameter *N* denotes the additional distance that the fluid would have travelled over the same time period if the flow rate change was instantaneous. In Figure 6.3a it is represented by the area of the shaded zone.

Using equation (6.6) to substitute *y* in (6.4) yields the solution for t_1:

$$t_1 = \frac{V - F_2 \tau + sN}{F_1} \tag{6.8}$$

The solution for reaction time t_r is obtained from (6.3) and (6.8):

$$t_r = -\frac{F_2 - F_1}{F_1}\tau + \frac{V + sN}{F_1} \tag{6.9}$$

With this equation, the reaction time can be calculated for every experimental point, which allows generation of the kinetic curve of the reaction (Figure 6.3c).

Equation (6.9) suggests that the uncertainty of the system's response to the flow rate change does not affect the shape of the kinetic curve that is obtained within the

boundaries in which equation (6.5) is correct ($\tau_1 \le \tau \le \tau_2$). Therefore, this uncertainty does not compromise the reliability of kinetic studies based on this strategy; it will only cause the recovered kinetic curve to shift along the time axis by $\Delta t = sN / F_1$. Although not essential for kinetic studies, knowing the magnitude of this shift can be useful for process optimisation purposes.

6.2.4. Empirical determination of uncertain parameters

Equation (6.9) does not hold for two regions of the original curve in Figure 6.3b: from τ_0 to τ_1 and from τ_2 to τ_3. Therefore, it is important to determine parameters τ_1, τ_2 and τ_3 in order to estimate the boundaries of these two uncertain zones. τ_2 can be estimated as a point where the change in product concentration starts to decrease (Figure 6.3b), and τ_3 marks the first point where the concentration levels off. τ_1 cannot be directly derived from the curve shape, but it is possible to estimate it via other parameters as shown below.

Mathematically, τ_2 can be derived from equation (6.6) by substituting *L* for *y*:

$$\tau_2 = \frac{V + sN}{F_2} \tag{6.10}$$

This equation provides an empirical solution for the uncertain parameter *N*:

$$N = \frac{F_2\tau_2 - V}{s} \tag{6.11}$$

With this solution equation (6.9) can be rewritten as follows:

$$t_r = -\frac{F_2 - F_1}{F_1}\tau + \frac{F_2}{F_1}\tau_2 \tag{6.12}$$

Determination of τ_1 is based on the following analysis. During the time period from τ_2 to τ_3 the detector is exposed to the plugs of liquid that initially entered the system when the flow rate was uncertain (from τ_0 to τ_1). Consequently, the lengths of these 2 zones in the reactor capillary (corresponding to τ_0 to τ_1 and τ_2 to τ_3) are the same and equal to *M* (see equation 6.5). By time τ_2, the system has already been flowing

at a stable higher flow rate F_2. Therefore, the period from τ_2 to τ_3 can be found from the definition of the volumetric flow rate, from which parameter *M* can be found as well:

$$\tau_3 - \tau_2 = \frac{Ms}{F_2} \tag{6.13}$$

$$M = \frac{(\tau_3 - \tau_2)F_2}{s} \tag{6.14}$$

A combination of (6.7), (6.10) and (6.13) yields an empirical expression for τ_1:

$$\tau_1 = \tau_3 - \frac{V}{F_2} \tag{6.15}$$

6.2.5. Effect of thermal expansion

Equation (6.12), the main result of the present analysis, does not account for the effects of fluid expansion or contraction caused by a chemical reaction or temperature changes. Thermal expansion is likely to have a considerable effect. In fact, organic liquids are known to have especially high thermal expansion coefficients, with the volume changing by up to several percent for every 10°C of temperature change. Microreactors are often kept at elevated or reduced temperatures during syntheses, whereas the temperature of the vials (syringes) from which reagents are delivered to the microreactor can be significantly different. However, the fluid temperature reaches the target value almost immediately upon entry into the microreactor owing to the extremely efficient heat transfer intrinsic to microfluidic systems. For the same reason any heat liberated or absorbed during the chemical reaction is rapidly dissipated so that the temperature remains stable throughout the whole flow line. At higher temperatures the liquid in the microreactor expands occupying more space and, therefore, flows faster than it would at a lower temperature. Thermal expansion is quantified by the volumetric coefficient of thermal expansion α_V [253]. In a flow system, the effect can be accounted for by introducing the effective flow rate F_{eff}, which depends on α_V and the temperature difference ΔT:

$$F_{eff} = (1 + \alpha_V \Delta T) F \qquad (6.16)$$

Replacing the original flow rates F_1 and F_2 by the effective flow rates does not change equation (6.12), therefore thermal expansion does not change the kinetic curve shape. But it does change equation (6.10) that defines τ_2:

$$\tau_2 = \frac{V + sN}{(1 + \alpha_V \Delta T) F_2} \qquad (6.17)$$

If the thermal expansion coefficient for the reacting mixture is unknown, the effect of temperature can be considered as part of the total error contained in expression (6.17). With the latter approach it is sufficient to determine τ_2 from experimental data and enter the value obtained into equation (6.12).

6.3. Experimental

6.3.1. Reaction

The Knoevenagel condensation between ethyl cyanoacetate and benzaldehyde was selected as the model reaction:

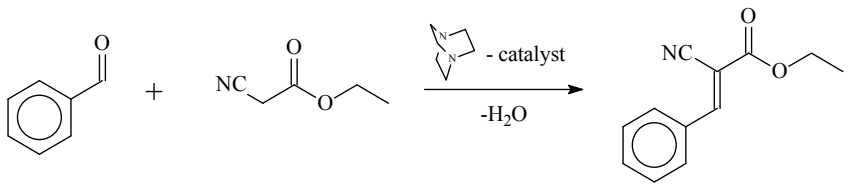

It was demonstrated experimentally that 100% conversion can be achieved at both temperatures used in the study. The absence of any notable side reactions was confirmed with GC-MS.

Solutions of the reagents were prepared according to the following procedure: Solution 1: 639.3 mg (6.02 mmol) of benzaldehyde (99+% m/m, Sigma Aldrich, Dorset, UK) and 67.4 mg (0.60 mmol) of 1,4-diazabicyclo[2.2.2]octane (DABCO; 97+% m/m, Alfa Aesar, Heysham, UK) were diluted to 2 ml with methanol. Solution 2: 814.1 mg (7.20 mmol) of ethyl cyanoacetate (98+% m/m, Sigma Aldrich, Dorset, UK) was diluted with methanol to a total volume of 2 ml.

6.3.2. Microreactor setup

The microreactor setup is shown schematically in Figure 6.4. The microreactor was designed to have a longer than normal path length and consisted of 2 glass microfluidic chips manufactured using wet-etching technology (University of Hull). The internal volumes of the chips were 8.6 and 14.6 µl, with average channel diameters of 125 and 160 µm, respectively. The chips were connected with a 50 cm long piece of PEEK tubing (ID 150 µm, part number 1572, Upchurch Scientific, USA) that was coiled and "sandwiched" between the chips as shown in Figure 6.4.

These arrangements were necessary to increase the total path length of the microfluidic channel in order to account for the deficiency of the pump that performs better at higher flow rates. If the pump had a better stability, a single microreactor chip could be used. The higher path length is also beneficial in reducing the contribution of the mixing time relative to the total reaction time. In the present work, the typical mixing time is estimated to constitute only around 1% of the total residence time. Incorporation of a micro-mixer should be considered when the reaction takes place in larger channels, at higher flow rates or when large organic molecules are involved in the process.

Thermopaste (silicon free heat sink grease; ITW Contamination Control, Denmark) was abundantly applied between the glass microreactors to ensure efficient heat exchange. The microreactor was glued to a Peltier element connected to a temperature controller (model 350, Newport Inc, USA). The aluminium heat sink was secured on an XY translation stage for precise positioning of the microreactor relative to the Raman probe. Reagents were delivered to the microreactor with a syringe pump (Kd Scientific) and 1 ml glass syringes (Gastight 1001, Hamilton, Switzerland).

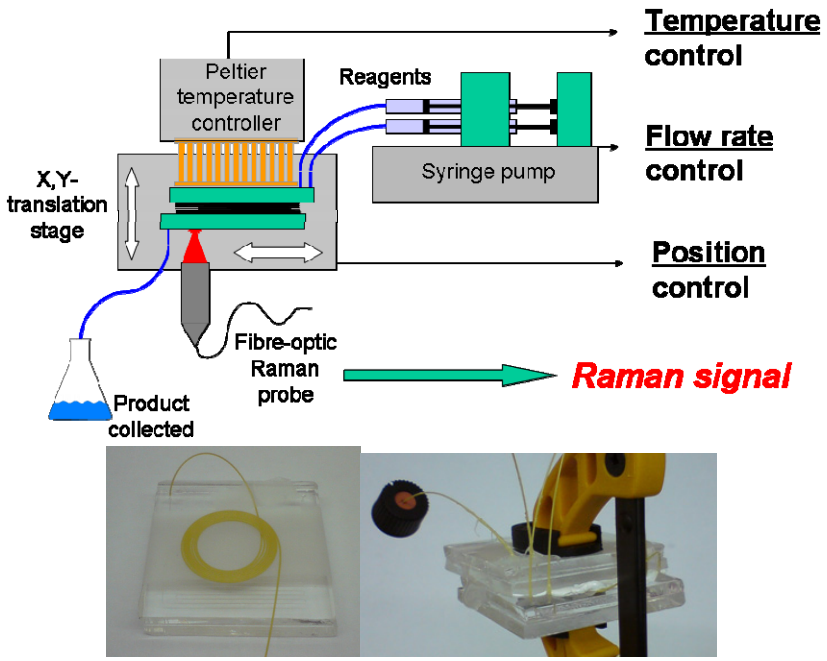

Figure 6.4. Setup schematic and the microreactor.

6.3.3. Raman spectrometry and data processing

The Raman probe used in this study has been described previously in Chapter 5. The Raman spectrometer (Rxn-1, Kaiser, USA) contained a 400 mW, 785 nm laser, the standard Kaiser spectrograph and a thermoelectrically cooled CCD camera. Care had to be taken to adjust the position of the probe to maintain focus when changing the temperature of the reaction. The microreactor channel moved out of focus by roughly 10 µm for every 10°C temperature change owing to a combination of thermal expansion effects and a change in the refractive index of the borosilicate glass used to fabricate the microreactor.

Raman spectra of the product, reagents and the catalyst obtained from a 5 mm cuvette are shown in Figure 6.5. Raman spectra of the reaction mixture collected directly from the microreactor at different times after the start of the reaction are given in Figure 6.6 for comparison. The second most intense Raman peak of the product (ethyl 2-cyano-3-phenylacrylate) located around 1600 cm^{-1} was selected for analysis and the background-corrected peak area was calculated from 1564 to 1639 cm^{-1}. The intensity of the benzaldehyde band in this region is 13 times smaller than that of the product in equimolar solutions of the compounds. At early stages of the reaction, however, benzaldehyde will make a notable contribution to the measured

signal when the product concentration is low. In order to account for this interference, separate solutions containing ethyl 2-cyano-3-phenylacrylate or benzaldehyde in methanol at different concentrations were prepared and analysed individually in the microreactor. The peak area signal from 1564 to 1639 cm^{-1} was calculated for each solution and the information was used to build response curves for each compound. These curves were combined algebraically to account for the contribution of benzaldehyde using the condition that in the reaction mixture the total concentration of the two compounds is always equal to the initial concentration of benzaldehyde.

Raman spectra were collected continuously throughout the kinetic experiments with an acquisition time of 2 seconds and 2 seconds delay time, giving 15 spectra per minute. The Holograms software (Kaiser) automatically recorded the time of each acquisition. Time conversion and data processing were performed in Matlab (Mathworks, USA). The scripts used to process spectral data are provided in Appendix 1.

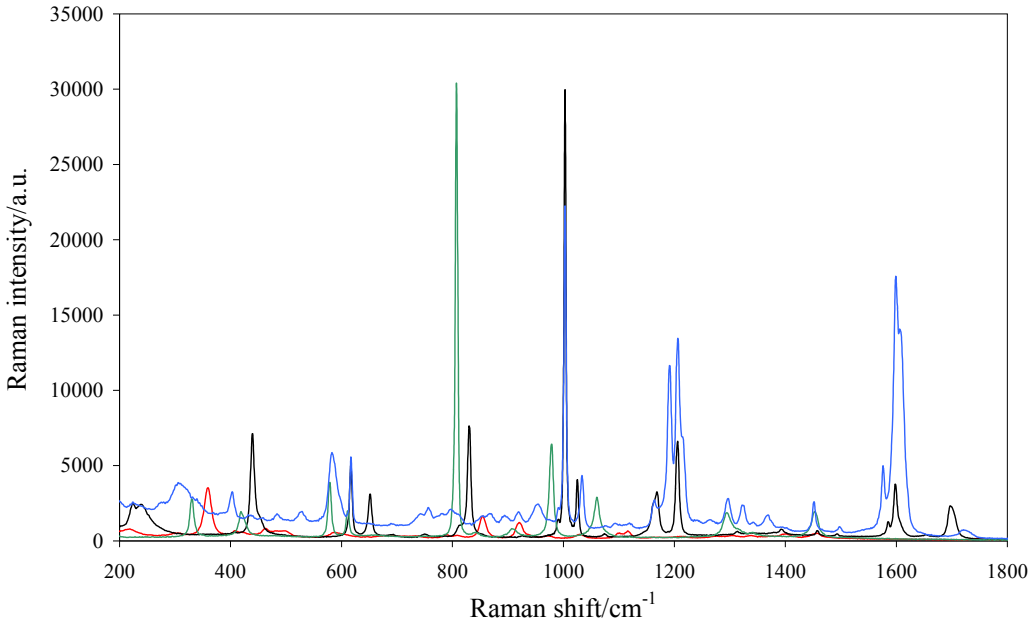

Figure 6.5. Raman spectra of the individual compounds featured in the reaction, ethyl cyanoacetate (red), benzaldehyde (black), DABCO (green) and ethyl 2-cyano-3-phenylacrylate (blue).

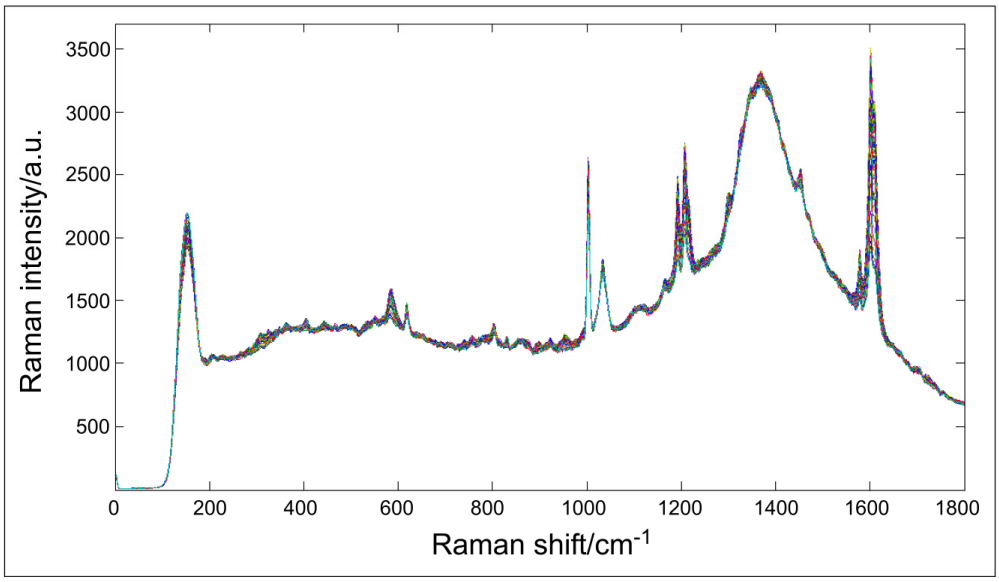

Figure 6.6. 80 overlaid Raman spectra of the reaction mixture collected from the microreactor at different times after the reaction start in the range from 5 to 80 minutes.

6.3.4. Kinetic experiments

The reaction was studied at two temperatures, 10 and 40°C. The new method (method B) was tested against a more conventional steady-state analysis (method A) where several different flow rates (0.2 - 20 μl min^{-1}) were used to create different residence times in the reactor so that the extent of the reaction was different by the time the liquid passed through the measurement zone at the end of the reactor. The analytical signal at each flow rate in method A was averaged over 10 - 60 minutes to obtain the data points for the kinetic curve. A stabilisation period, approximately 1.5 times the calculated residence time equivalent to the flow rate used, was allowed at each flow rate before measurements were initiated.

The new procedure, method B, involved initial stabilisation of the flow system at a low flow rate F_1 followed by the step increase to F_2. Seven experiments were carried out at each temperature (10 and 40°C) with different combinations of F_1 and F_2. The obtained data were processed using equation (6.12), and τ_2 values were derived graphically as described in the previous Section. Data conversion was carried out using a Matlab script, written for this methodology (see Appendix 2).

6.4. Results and discussion

6.4.1. Effects of temperature and mixing

Thermal expansion was estimated experimentally to be $3.5 \pm 0.5\%$ over the temperature change from 10 to 40 °C. Mixing of the reagent streams caused a reduction in volume by $2.5 \pm 0.5\%$. These effects were taken into account when calculating maximum concentration of the product inside the microreactor as well as reaction time in method A. The experimental procedure for these experiments is described in Appendix 3.

It transpired that both temperature and the chemical composition of the solution affected the area and shape of the Raman peak of the product. Misalignment of the Raman optical interface was observed with increasing temperature. The microreactor channel moved out of focus by roughly 10 μm for every 10 °C temperature increase owing to a combination of thermal expansion effects and a change in the refractive index of the borosilicate glass used to fabricate the microreactor although the latter is insignificant. The extent of these effects is specific to the setup used.

Having identified the optimal probe position at each of the two temperatures, the effects of temperature on the Raman peak shape and intensity were studied. Spectra of the reagent mixture left to react for 24 hours were obtained at 10 and 40 °C. The measured conversion was $100 \pm 1\%$ at both temperatures. The peak area of the product increased by 3.9% when spectra are obtained at 40°C compared to those at 10°C. In addition, a change in the product peak shape occured (Figure 6.7). In an identical experiment with a pure product solution in methanol the peak area decreased by 5% and the shape change was slightly different (Figure 6.8).

Experiments with a solution of benzaldehyde in methanol showed a similar intensity decrease. These results indicate that temperature has different effects on the Raman spectra of the product depending on the presence of the other components in the solution (DABCO, water and ethyl cyanoacetate). Similar Raman signal decrease when the product or benzaldehyde are surrounded only by methanol molecules can be linked to the combined effect of thermal expansion and refractive index increase

that reduces divergence of the optical beam and therefore makes signal collection less efficient at 40 °C. These effects were taken into account in calculations.

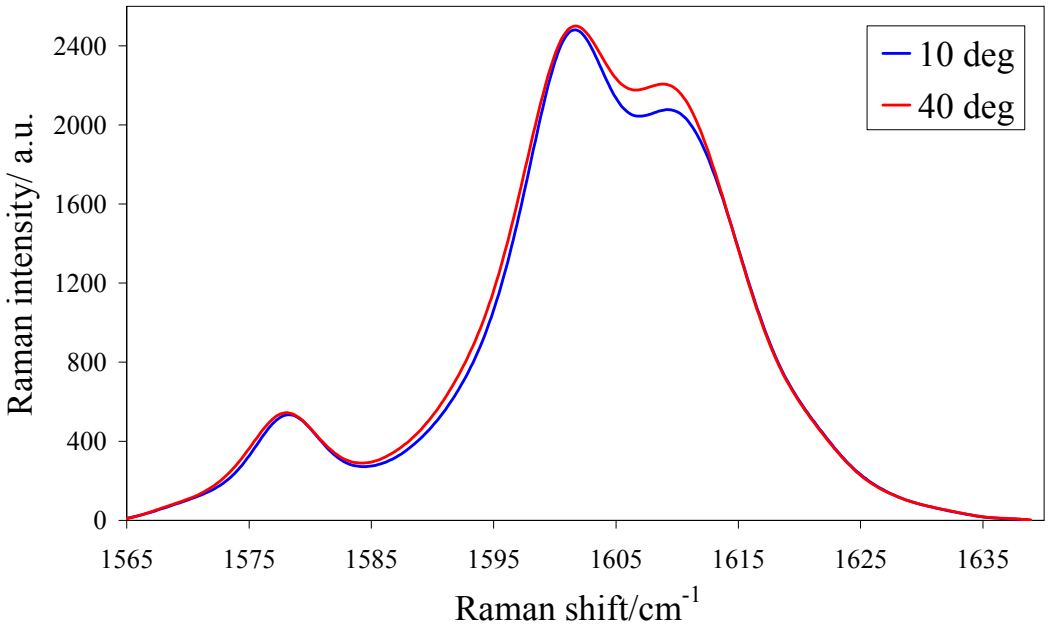

Figure 6.7. Thermal change of the Raman peak of the product. Spectra are acquired from the premixed solution of reagents allowed to react over a 24 hour period.

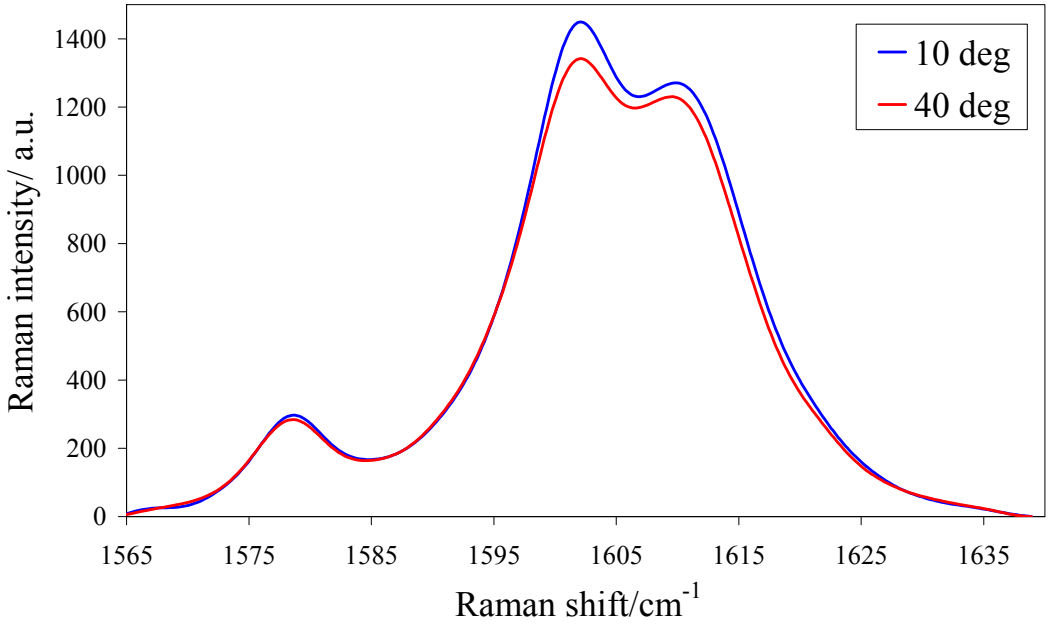

Figure 6.8. Thermal change of the Raman peak of the product. Spectra are acquired from solution of the pure product in methanol.

6.4.2. The kinetic model

The kinetics of a base-catalysed Knoevenagel condensation has been studied in several reports[238, 254-256]. The classical reaction mechanism consists of four steps:

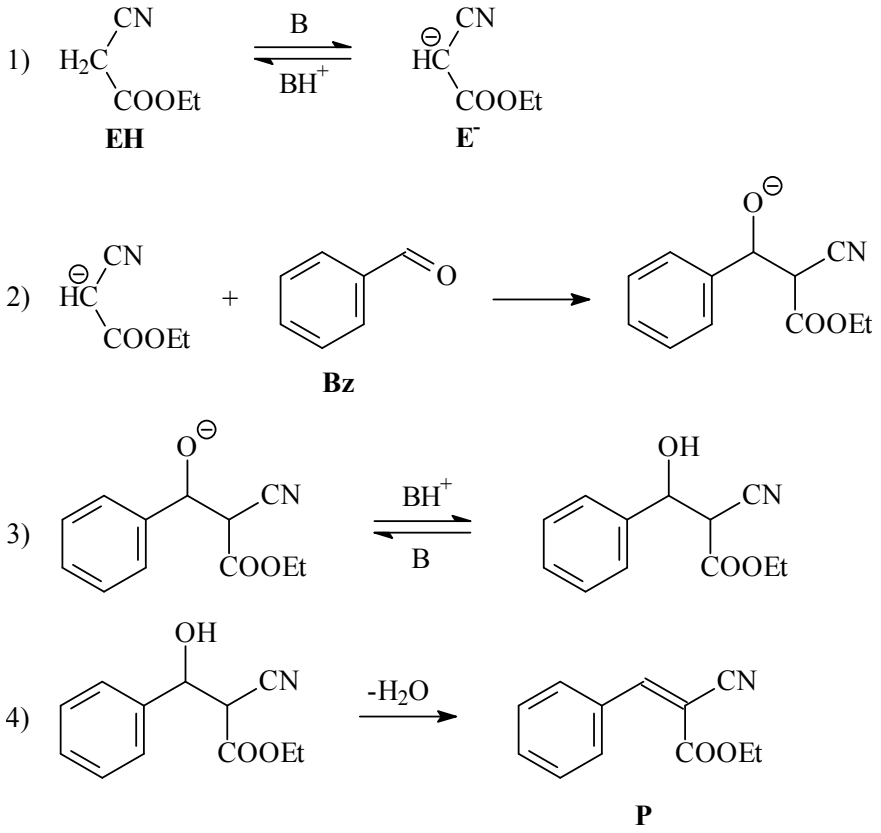

Assuming that the rate-limiting step is the nucleophilic addition (step 2), Zhang et al. [255] derived a second-order reversible kinetic rate expression for the whole process and applied it with the restriction of equal initial reagent concentrations[257].

In the present study ethyl cyanoacetate **EH** was used in excess which makes the integrated kinetic equation too complex. Therefore, a simple kinetic model was chosen to fit the experimental data, and characterise and compare the obtained results, where the rate of reaction is proportional to the concentration of benzaldehyde to the power *n*, the effective reaction order. The value of *n* can be estimated experimentally. However, it is useful to estimate it first by considering two boundary situations.

In one boundary situation, the initial concentration of ethyl cyanoacetate (**EH** + $\mathbf{E}^-$) exceeds that of **Bz** by several times, thus the total concentration of ethyl cyanoacetate

in the reaction mixture remains almost constant and the equilibrium between **EH** and $\mathbf{E}^-$ (step 1) is unaffected. Knowing that proton transfer is a much faster process than nucleophilic addition, the quasi steady-state condition can be applied to enolate ion $\mathbf{E}^-$. As it is the slowest process in the reaction chain, step 2 defines the total reaction rate resulting effectively in first-order kinetics with respect to benzaldehyde:

$$r = -\frac{d[\mathrm{P}]}{dt} = k_2[\mathrm{E}^-][\mathrm{Bz}] = k[\mathrm{Bz}] \tag{6.18}$$

Here [P], $[\mathrm{E}^-]$ and [Bz] are concentrations of the product, enolate ion and benzaldehyde, respectively. k_2 is the rate constant for step 2 and k is the effective rate constant of the product formation.

In another boundary situation, the initial concentrations of ethyl cyanoacetate and **Bz** are equal. If the rate constants of the two reversible reactions in step 1 are k_1 and k_{-1}, the concentration of $\mathbf{E}^-$ can be expressed in the following way:

$$[\mathrm{E}^-] = \frac{k_1}{k_{-1}}\frac{[\mathrm{EH}][\mathrm{B}]}{[\mathrm{BH}^+]} = \frac{k_1 K_a}{k_{-1}[\mathrm{H}^+]}[\mathrm{EH}] \tag{6.19}$$

where K_a is the acid/base dissociation constant of BH^+. Assuming that $[\mathrm{EH}] >> [\mathrm{E}^-]$, concentration of ethyl cyanoacetate in a non-dissociated form is nearly equal to concentration of benzaldehyde $[\mathrm{EH}] \approx [\mathrm{Bz}]$. If pH remains roughly constant during the process (reagents and products are much weaker acids than the solvent, and pH is defined by the base concentration which is constant), the reaction order becomes equal to 2:

$$r = -\frac{d[\mathrm{P}]}{dt} = k_2[\mathrm{E}^-][\mathrm{Bz}] = \frac{k_1 k_2 K_a}{k_{-1}[\mathrm{H}^+]}[\mathrm{Bz}]^2 \tag{6.20}$$

It is therefore reasonable to expect that in the conditions of the experiment reported here, which are within the two boundary conditions described above, the effective order with respect to benzaldehyde should be between 1 and 2.

The effective rate constant k can be found using the linearised rate equation for n-order reactions ($n \neq 1$)[257]:

$$\frac{1}{[\mathrm{Bz}]_{t_r}^{n-1}} - \frac{1}{[\mathrm{Bz}]_0^{n-1}} = (n-1)kt_r \qquad (6.21)$$

where $[\mathrm{Bz}]_{t_r}$ is the concentration of benzaldehyde at the moment when the reaction time is t_r, and $[\mathrm{Bz}]_0$ is the initial concentration of benzaldehyde in the mixture, which was 1.538 ± 0.015 mol dm^{-3} at 10 °C and 1.485 ± 0.015 mol dm^{-3} at 40 °C.

In order to find the best linear fit of the data, the optimal values of parameters *n* and *k* must be found. If *n* is not known *a priori*, it has to be determined, although as outlined above, *n* is likely to be between 1 and 2. For each experiment the value of *n* was found by plotting a series of curves (equation 6.21) using a range of *n* values from 1 to 2. The plot that had the highest value of the correlation coefficient R^2 was considered optimal and the rate constant *k* was computed for this value of *n*.

6.4.3. Kinetic analysis method A

Figure 6.9 illustrates the change in the concentration of product over time obtained at different flow rates, based on the Raman signals recorded at the end of the microreactor. Considerable variation in the Raman signals (and hence derived concentrations) was observed owing to pumping instabilities. Five other pumps and different syringes were tested and all the Raman signals demonstrated similar periodic fluctuations. Spectral noise is notably smaller than pumping-related noise.

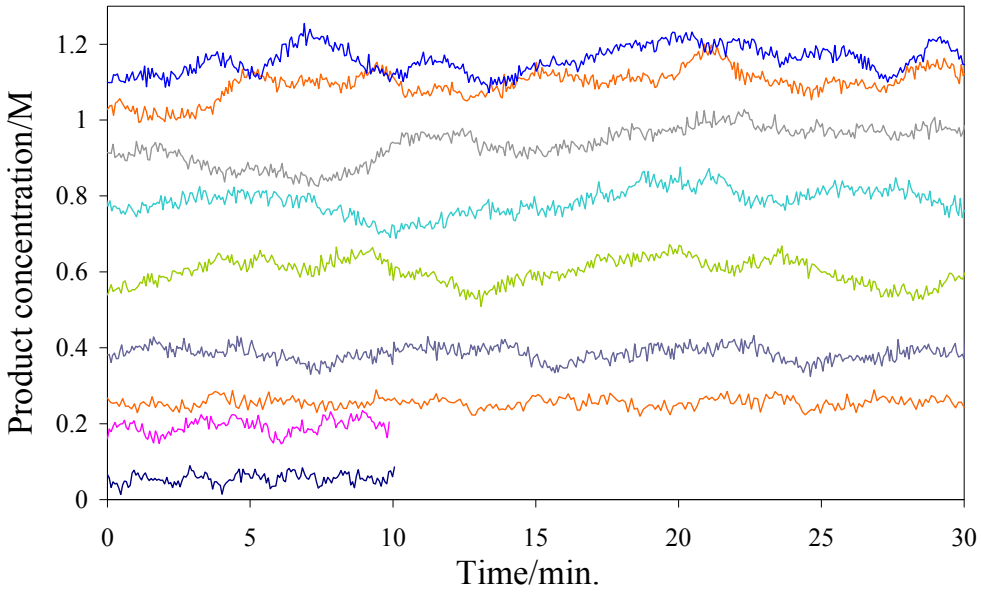

Figure 6.9. Variations in the product concentration measured in the steady state at different flow rates in method A (0.6, 0.8, 1.1, 1.6, 2.4, 4.0, 6.0, 8.0, 20 µl min^{-1} corresponding to the lines from the top to the bottom of the Figure).

To account for the pumping instability, the measured signal was averaged over 10 - 60 minutes at each flow rate, with longer times being used for the lower flow rates. By dividing the microreactor's internal volume by the flow rates used, the equivalent reaction times were calculated. The points in Figure 6.10 show the mean values of benzaldehyde conversion at the different reaction times for 10 and 40 °C. The error bars on Y-axis are standard deviations that arise owing to variations in the measured signal caused by unstable pumping. The lines in Figure 6.10 represent the optimal kinetic models found for the experimental data as outlined in the previous Section. The first 7 experimental points at each temperature were used in the calculations to avoid the influence of the increased error observed for measurements close to 100% conversion.

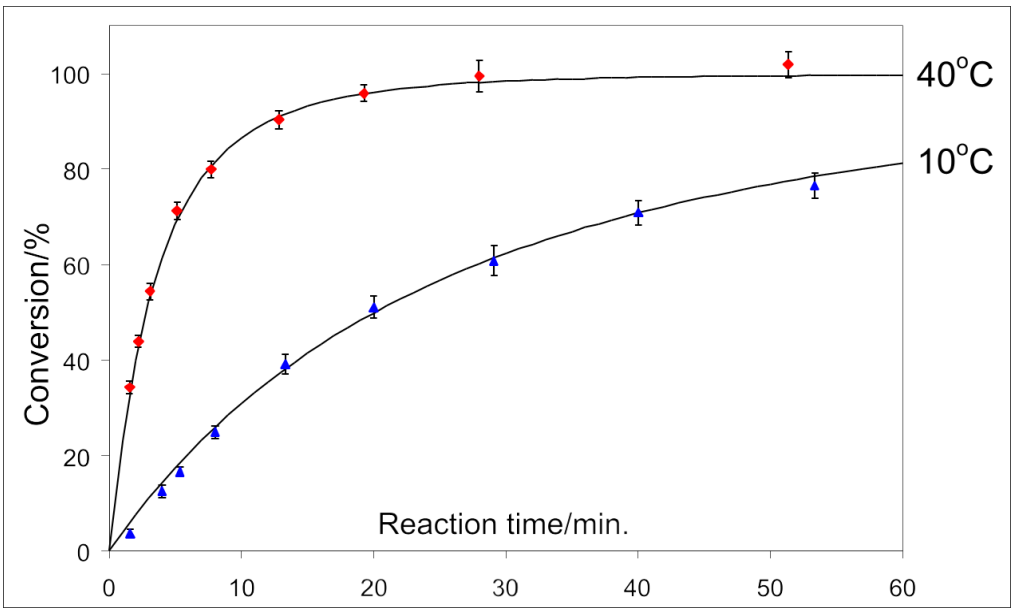

Figure 6.10. Kinetic curves obtained at 10 and 40 °C using method A based on Raman measurements of the product in the microreactor for different reaction times, calculated from flow rates (see Figure 6.9). The solid lines represent the models with the optimal reaction order on benzaldehyde (n = 1.4 at 10 °C and n = 1.3 at 40 °C).

As expected, reaction order values in the range from 1 to 2 produced the best fit at both temperatures, with $n = 1.4$ being optimal for the 10°C curve and $n = 1.3$ for the 40°C curve. Using these values of n, the rate constants derived from the data in Figure 6.10 were $(3.35 \pm 0.32) \cdot 10^{-2}$ $\text{mol}^{-0.4}\text{dm}^{3.4}\text{s}$ and $(24.4 \pm 3.2) \cdot 10^{-2}$ $\text{mol}^{-0.3}\text{dm}^{3.3}\text{s}$ for 10°C and 40°C, respectively.

6.4.4. Kinetic analysis method B

In method B, the reaction was allowed to proceed at a low flow rate for a period of time before increasing the flow to the higher rate. As the liquid exited the reactor at the higher flow rate, Raman measurements were made every 4 s to generate a reaction profile. The data were used to produce a kinetic curve, analogous to that derived with method A as illustrated in Figure 6.11 for flow rate combinations of 0.4 and 6 µl min^{-1} at 10°C and 1.1 and 20 µl min^{-1} at 40°C. This procedure was repeated for different combinations of F_1 and F_2 to investigate the influence of the choice of flow rates on the derived kinetic information.

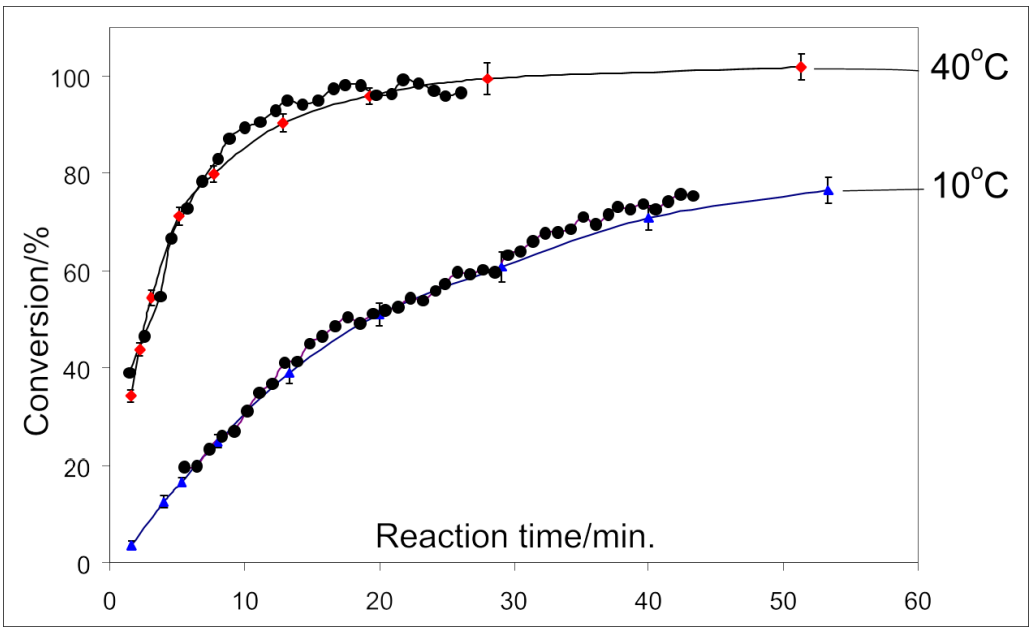

Figure 6.11. Kinetic curves (black points) computed using method B from one experiment at each temperature using flow rates (F_1 - F_2): 0.4-6 µl min^{-1} at 10°C and 1.1-20 µl min^{-1} at 40°C. The data points are overlaid with those obtained with method A (coloured points with error bars) showing that both methods produce the same result.

Optimal values of *n* and *k* of the kinetic model were calculated for each of the 14 experiments, using the same procedure as described above for method A. Different combinations of F_1 - F_2 were investigated in order to evaluate the influence that selection of flow rates could have. The results are summarised in Table 6.1.

Table 6.1. Kinetic parameters derived from method B experiments: reaction orders *n*, rate constants *k* and rate constants with *n* values forced to be equal to the values found from method A experiments.

10 °C				40 °C			
F_1-F_2 /μl min^{-1}	n	$k/10^{-2}$	$k/10^{-2}$ (n = 1.4)	F_1-F_2 /μl min^{-1}	n	$k/10^{-2}$	$k/10^{-2}$ (n = 1.3)
0.4 – 6	1.6	3.49	3.49	1.1 – 20	1.1	23.0	30.3
0.4 – 6	1.1	3.54	3.53	1.1 – 20	1.2	27.5	31.7
0.4 – 6	1.3	3.49	3.49	0.6 – 14	1.1	23.3	30.8
0.4 – 6	1.3	3.72	3.73	1.6 – 20	1.3	24.8	24.8
0.2 – 4	1.4	3.50	3.50	2.4 – 10	1.1	22.0	25.0
0.8 – 8	1.1	3.59	3.59	1.1 – 6	1.1	23.1	31.4
0.6 – 6	1.1	3.57	3.60	1.1 – 14	1.0	24.0	26.2
Average	1.27 ± 0.19	3.56 ± 0.08	3.56 ± 0.09	Average	1.13 ± 0.10	24.0 ± 1.8	28.6 ± 3.1

Although the dimensions of *k* depend on the values of *n*, the results in the Table suggest that the reaction order does not have a significant effect on the numerical value of *k* except for a few experiments at 40 °C. However, using *n* values equal to those found from method A experiments allows direct comparison of the results. In all cases average values of *n* and *k* agree well with those found with method A. The higher error observed at 40 °C is likely caused by a much greater reaction rate compared to that at 10 °C, which results in fewer experimental points in the same range of conversion as well as greater effect of any other sources of error, particularly pumping instability and error on the reaction time axis (see discussion below). Table 6.1 also shows that selection of flow rates F_1 and F_2 does not influence the results, which agrees with the theory and is useful in practice.

As discussed earlier in the Method Section, the kinetic curve computed using equation (6.12) is shifted along the X-axis (reaction time), and accurate determination of τ_2 ensures the right position of the curve. Therefore, each point on the curve is characterised with an error along the X-axis, which can be estimated as $\Delta\tau\frac{F_2}{F_1}$, where $\Delta\tau$ is the interval between consecutive measurements. This error is systematic within an experiment but random between the experiments. Therefore, faster and more frequent measurements as well as combining individual experiments into a single data set can reduce this error. It can also help compensate the influence of pumping instability when it is a subject of concern. In the present work the graphical way of estimating τ_2 proved to be sufficiently accurate to provide consistent results within the data set. However, there is another, (probably more accurate) way to find τ_2, that is applicable when the reaction order is known *a priori*. It is based on using the predicted shape of the kinetic curve to find both parameters, *k* and τ_2, from the equation derived by replacing t_r in (6.21) with (6.12):

$$\frac{1}{[\mathrm{Bz}]^{n-1}}-\frac{1}{[\mathrm{Bz}]_0^{n-1}}=-\frac{(n-1)k(F_2-F_1)}{F_1}\tau+\frac{(n-1)kF_2}{F_1}\tau_2 \qquad (6.22)$$

Plotting $\frac{1}{[\mathrm{Bz}]^{n-1}} - \frac{1}{[\mathrm{Bz}]_0^{n-1}}$ against τ gives a linear curve $y = ax + b$ where rate constant k is computed from the slope a and τ_2 – from the intercept b.

6.4.5. Comparison of the methods

Although methods A and B are two different ways of extracting essentially the same information from the microfluidic process, they differ in a few aspects which are important to highlight. Method A provides better accuracy when a specific point on the kinetic curve needs to be characterised (typically for process optimisation purposes), whereas method B is more suitable for revealing the kinetic curve shape over a range of flow rates. Another aspect is calculation of reaction time. In method A accurate values of the microreactor volume and flow rates are essential for calculating reaction time, whereas method B requires only the knowledge of the flow rate ratio F_1 / F_2 (equation 6.12), which can be useful when the exact flow rate is unknown. The third aspect concerns the time required for analysis and consumption of chemicals, which are much lower in method B. Given the reliable pumping, kinetic information can be extracted from a single experiment, while method A requires several experiments. With the conditions of the present experiments, method B is roughly 5 times faster than method A, although it depends on the number of data points used in method A.

6.4.6. Comparison with stopped-flow analysis

Method B has some similarities with what is done in stopped-flow analysis where the system initially runs at a high flow rate and is then stopped completely to allow the detector to analyse changes that take place in the still solution. Stopped-flow analysis provides similar advantages in terms of time savings and the richness of the information that can be extracted, however, the proposed method exhibits several differences that can be important in some applications. Firstly, stopped-flow analysis does not allow detection of what happens along the flow path, which could be important information when the microreactor comprises several modules, such as sections with immobilised catalysts, regions of different temperatures or additional flow entries. With the proposed method, it is possible to study where exactly on the flow path changes in composition occur, allowing the opportunity to study and

optimise the reaction. Secondly, the performance of the detection system can depend on whether the liquid moves or not. If detection is based on optical methods, photochemical effects or localised radiative heating can take place, whereas in a flowing stream these effects can usually be neglected. In the case of electrochemical detection, mass transfer issues can arise due to lack of convective mixing in the stopped flow. And finally, compared to stopped-flow analysis, the proposed method provides significant savings of equipment usage time when slow reactions are studied. By adjusting F_1 / F_2 ratio the analysis time can be reduced to no more than a few minutes after idle stabilisation, no matter how slow the reaction is.

6.5. Conclusions

The proposed method offers advantages over conventional procedures for kinetic analysis and optimisation of microfluidic reactions. The procedure makes it possible to extract location-specific information from the flow path without the need to access it directly with an optical probe. This approach enables processes to be analysed in previously difficult situations where the microreactor is not transparent, no optical access to the microchannels is possible or where optical sensing is not suitable. The developed methodology offers a way to bridge the gap between the power of in-line sensing with the convenience and flexibility of confocal spectroscopy, thus promising to advance kinetic studies and process analysis on the microfluidic platform to a new level.

Without the necessity to move the sensor along the flow path, it is possible to develop a separate unit with optimised parameters and make it compatible with standard microfluidic connectors. This approach would solve the technical difficulties encountered in this work. Firstly, sensitive Raman measurements could be made regardless of the microreactor design and material. Secondly, the measurement compartment could be kept at a constant temperature that eliminates the problem of temperature-induced distortion of Raman bands and optical or mechanical misalignments. These opportunities will be explored in the next Chapter.

In concluding this Chapter, it is worth noting that the new methodology described is not limited to Raman spectroscopy and can be successfully used with other analytical methods that can be integrated into the microchannel to rapidly extract chemical information. These alternative methods include, but are not limited to, electrochemical analysis, confocal fluorescence spectroscopy, transmission and ATR attachments for molecular absorption spectrometry, and refractive index sensors.

7. Improved optical interface between the Raman probe and the sample

The aims of this Chapter are:

1) Demonstrate the advantages of separating the measurement site from the microreactor by building an improved interface between the sample and the Raman probe;

2) Study the possibility of improving periodic flow instability using a high-volume mixer;

3) Demonstrate benefits of using principal component analysis to maximise signal to-noise-ratio obtained from Raman spectra;

4) Develop an alternative algorithm of cosmic spike removal that would not rely on acquisition of two consecutive spectra to improve the frequency of measurements.

7.1. Separation of the measurement zone from microreactors

The results of the work described in the previous Chapter have an important consequence for Raman spectroscopy with respect to its application in microfluidics-based research. The "flushed steady-state" methodology opens up an opportunity to improve the efficiency of signal collection by allowing separation of the measurement zone from the microreactor. It is possible to develop a dedicated optical interface and configure it in a specific way favourable to the requirements of Raman spectroscopy. This specialised interface can be incorporated into a separate unit compatible with various microreactors, regardless of their design and material.

The idea to optimise the optical interface in the measurement zone and separate it from the microreactor has a lot in common with optimisation of detectors for liquid-separation methods. In the last two decades some attention was devoted to using Raman spectroscopy as a detector for liquid chromatography and capillary electrophoresis. An excellent review of these attempts was published by Dijkstra et al.[258]. Their paper provides useful information that is relevant in the context of

microreactors and can be a suitable introduction to the work described in this Chapter. Indeed, capillary electrophoresis usually employs narrow capillaries with a typical diameter of 20 - 100 μm and requires frequent measurements to achieve good temporal resolution. The same requirement is necessary with the "flushed steady-state methodology".

The necessity to provide fast and frequent measurements at the end of the flow path in combination with the relatively low concentrations of analytes in typical HPLC samples present a great challenge to Raman spectroscopy. Therefore, much attention was focused on resonance Raman spectroscopy and SERS. Although resonance enhancement can significantly increase sensitivity, the limits of detection achieved with this method in HPLC were rather poor, which was mainly caused by the spectral background from eluents. In addition, resonance enhancement occurs at different wavelengths for different analytes, which makes such a detector less universal.

In this respect, capillary electrophoresis is more compatible with Raman detection due to the use of water instead of organic solvents. Water has a very low Raman cross section and does not impede analyte detection. Using conventional (unenhanced) Raman spectrometry Ruddick and co-workers[259] demonstrated limits of detection of 5 mM for nitrate and perchlorate ions in a 50 μm capillary using 1 s of acquisition time. This result was achieved owing to a special optical configuration that will be described below.

Despite the promising results achieved with a combination of resonance Raman spectrometry and capillary electrophoresis, the number of related publications is very small. An alternative to resonance enhancement is SERS. Attempts to use on-line SERS detection with immobilised nanoparticles were unsuccessful due to the difficulties with preserving the SERS substrate in a clean and active state during the measurements. When nanoparticle colloids are deliberately added to the analysed fluid, the metal is usually deposited on the inner walls of the capillary deteriorating the quality and repeatability of SERS spectra[258]. These problems prevented further development of this research direction.

These examples serve as a reminder about the type of problems that can arise when using Raman spectrometry with microreactors. It is of interest for further discussion to give some examples of the measures taken to maximise sensitivity of Raman measurements in HPLC and capillary electrophoresis.

Steinert et al. developed a Raman measurement cell for HPLC[260]. To enhance the sensitivity of the measurements, several methods were used: a high power ion-Ar laser (up to 8 W at 488 nm), a thick measurement cell (4 mm) and a spherical mirror that doubled the solid angle over which the Raman photons were collected. A detection limit of $3 \cdot 10^{-6}$ mol L^{-1} was reported for xylene isomers. However, to achieve this level of sensitivity the spectral measurement time was 150 s.

Chen and Morris[261] maximised the sensitivity of resonance Raman spectrometry in capillary electrophoresis by means of a lock-in amplification and an array of 10 collection fibres in various configurations. A 40 mW 442 nm laser beam was focused on a 75 i.d. capillary using a 5x microscope objective. The fibres were positioned at an angle of 15° to the laser beam axis. The exact optical arrangement in the region between the fibre tips and the capillary was not reported.

Ruddick and co-workers[259] used a back-scattering Raman probe with high-NA multi-element optics consisting of a 20x microscope ultra-large working distance objective and a small hypersemispherical lens. The lens increased the effective numerical aperture from 0.55 to 1.2. A 50 μm i.d. capillary was positioned on the flat side of the lens with index-matching gel being applied between the lens and the capillary to eliminate refraction of the optical beam on the glass surfaces. The laser power was 2 W at 514 nm. The combination of these improvements demonstrated that conventional Raman spectrometry can serve as a detector for capillary electrophoresis without the necessity to employ resonance enhanced Raman spectrometry.

Many examples of signal enhancement rely on increasing the laser power. However, using tightly focused high-power lasers with narrow capillaries is a risky decision that can result in the damage of both the sample and the optical interface. Marquardt et al.[262] demonstrated another approach, i.e. the use of liquid core optical fibres

(LCOF) to collect Raman spectra. They showed that liquid waveguide capillaries can serve as a detector for HPLC. This method was discussed in Section 2.3.4. A disadvantage of the LCOF approach is its sensitivity to careful alignment and gas bubbles, and a relatively large interrogated volume of the sample. The resulting reduction of the compositional resolution can be problematic when the method is applied to process analysis in microreactors.

Reaction monitoring in microreactors is probably a less demanding application than detection in chromatography or electrophoresis due to the generally higher concentrations of reagents used in chemical reactions. Therefore, with the rapidly increasing interest in fast real-time detection systems for microreactors, the experience documented in the field of chromatography can be useful. However, the similarity between the two applications has not been mentioned in the literature.

In the next stage of the research, it was necessary to demonstrate the improvements that can be achieved by using an improved optical interface between the Raman probe and the sample. In this Chapter, an example of such an interface will be given.

7.2. Experimental

7.2.1. Materials and equipment

Schematics of the experimental setup and details of some components are provided in Figure 7.1. The microreactor (University of Hull, UK) was manufactured from borosilicate glass using wet-etching technology and contained a channel with an effective diameter of 100 μm and an internal volume of 8.6 μl. The microreactor was enclosed into a water bath the temperature of which was maintained to a precision of ±0.1°C by means of a recirculating chiller (Thermotek Inc., model T255P-3CR, Carrollton, TX, USA).

Microfluidic tubing and fittings were provided by Upchurch Scientific (Oak Harbor, WA, USA). Two 1 ml plastic syringes (BD, Oxford, UK) were connected to the syringe pump (Sage Instruments, model 341A). Attached to the syringes were two identical pieces of tubing (#1532, 0.5 mm ID, length 30.5 cm) that merged in a T-junction (#P-727, swept volume 0.57 μl, through-hole 500 μm) or in a micro-mixer

(IMM GmbH, Basel, Switzerland, model SSIM, inner volume 40 µl). After mixing, the flow proceeded to the microreactor through a 5 cm tubing (#1535, 125 µm ID), a nanotight union (#P-779, swept volume 8 nl, through-hole 130 µm) and another piece of tubing (#1572, 150 µm ID, length 40 cm). The other end of the microreactor channel was connected to a 55 cm piece of tubing (#1572, 150 µm ID) that delivered the reaction mixture to a fused silica capillary (ID 100±5 µm, OD 300 µm, Polymicro Technologies, Phoenix, AZ, USA) where the Raman measurements took place. Both the internal and external cross sections of the capillary were square. The tubing was connected to the capillary using a union (#P-704, swept volume 0.28 µl, through-hole 500 µm). The capillary was firmly fixed in front of the Raman probe and its outlet on the other side was inserted into an empty flask that collected the product. The total volume occupied by the liquid between the points of reagent mixing (2 in Figure 7.1) to the detection site (6 in Figure 7.1) was estimated to be 28.7 µl for the setup with the T-junction and 73.1 µl for the setup incorporating the micro-mixer.

The probe described in Chapter 5 was modified and used for Raman measurements. The key components of the probe were dichroic beamsplitter (Laser 2000, model LPD01-785RU-25), a fibre collimator (CF-2-B, Thorlabs) in combination with a multi-element lens (effective focal length – 8 mm, 0.28 NA, Melles Griot Inc) for the laser beam collimation, and a compact aspheric lens (effective focal length 4.5 mm, 0.49 NA, working distance 2.4 m; Olympus, Japan) focusing the probing beam onto the sample. The modification involved insertion of a notch and a laser-line filter (785 nm, Kaiser, Ann Arbor, MI, USA) into the probe and replacement of the 2 m connecting fibres with a 25 m fibre cable (core diameters: 50 µm for excitation and 100 µm for collection). The other end of the fibre cable was connected to a Raman spectrometer (Kaiser Rxn-1, Ann Arbor, MI, USA) equipped with Kaiser's standard spectrograph, IDUS CCD camera and 400 mW laser operating at 785 nm.

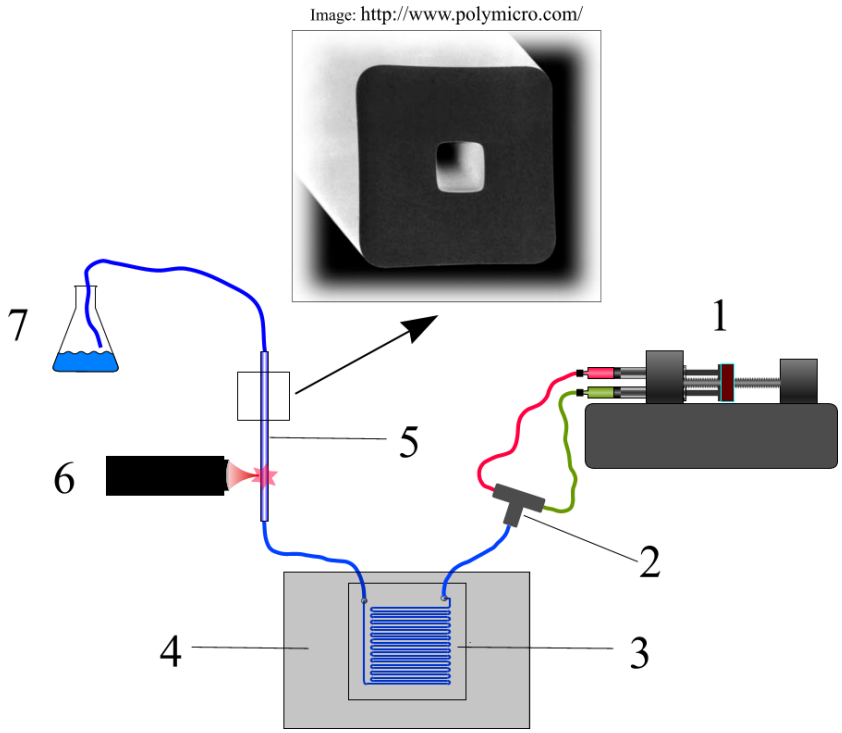

Figure 7.1. Setup schematics. 1 – syringe pump, 2 – T-junction (or micro-mixer), 3 – microreactor, 4 – water bath, 5 – square capillary, 6 – Raman probe, 7 – waste collector. The measurement site on the capillary is shown with a square.

The idea was to take Raman spectra from a fused silica capillary with superior optical properties rather than directly from the microreactor. The capillary selected for this work (Figure 7.2) has three advantages over a typical microreactor:

(i) It is made from fused silica, which is a poorer Raman scatterer than borosilicate glass and results in lower silica background;

(ii) The capillary walls are 10-30 times thinner than the walls of a typical microreactor (100 μm versus 1-3 mm) helping to reduce the silica background further;

(iii) Both internal and external cross sections of the capillary are a square. Compared to the cylindrical channel configuration, flat sides reduce beam refraction and improve signal collection efficiency.

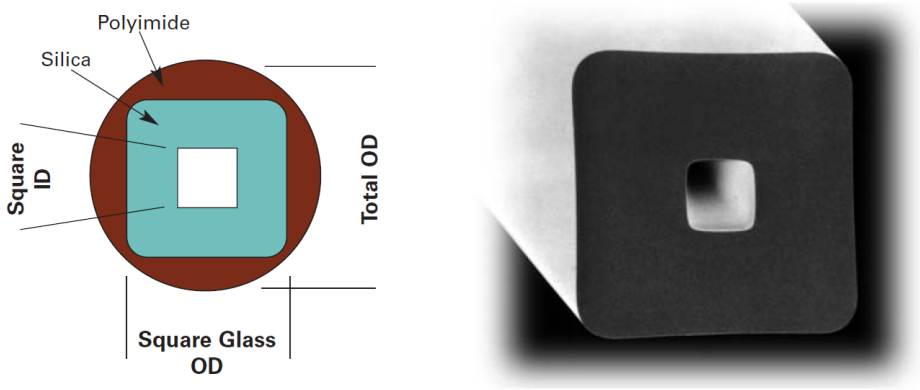

Figure 7.2. Schematics and a picture of the capillary cross section[263].

The only disadvantage of the capillary relative to a conventional microreactor is that a lot more laser light is reflected back to the probe, which is caused by the nearness of the front capillary surface to the focal point of the probe. This problem was completely solved by incorporating a notch filter into the probe.

7.2.2. Reaction monitoring

Esterification of methanol with acetic acid (catalysed by sulphuric acid) was selected as a model reaction:

$$CH_3OH + CH_3COOH = CH_3COOCH_3 + H_2O$$

Acetic (99.7% purity) and sulphuric (95-98%) acids were provided by Mallinckrodt Chemicals (Philipsburgh, NJ, USA) and methanol (99.9%) was supplied by EMD Chemicals Inc. (Gibbstown, NJ, USA).

One syringe delivered pure methanol into the flow system while the other supplied a solution of sulphuric acid in acetic acid (1.59g of H_2SO_4 in 10 ml of solution).

All experiments were carried out at a fixed temperature in the water bath. A range of flow rates was applied to the system under different conditions and Raman spectra were continuously collected using acquisition times in the range from 100 ms to 5 s and the minimum interval between the consecutive measurements.

7.2.3. Data processing

The collected spectral data were processed in Matlab (Mathworks, USA) using scripts written specifically for this work (See appendix 4).

Cosmic ray filter. The Kaiser's Holograms software used to export the spectral data to the .spc format has a built-in cosmic ray filter which required collection of two consecutive spectra. In each pair of spectra, the higher intensity at each pixel is discarded while the lower is left as the processed signal. Assuming that the chemistry of the sample does not change over the short time between the two acquisitions, this method effectively removes cosmic spikes. However, it requires extra time for collecting the second spectrum that is disadvantageous when frequent continuous analysis is needed. For the purposes of this work, a new cosmic ray filter algorithm has been developed, which did not require collecting Raman spectra in pairs. The algorithm is based on the analysis of the temporal intensity pattern recorded on each pixel of the detector. It is assumed that when spectra are acquired frequently (e.g. every few seconds), intensities recorded on each pixel in the data series change rather smoothly. A cosmic spike is distinguished as an abrupt and considerable increase in signal followed by an immediate and abrupt decrease in the next collected spectrum. Such behaviour is unique for cosmic rays. Mathematically, cosmic spikes are tracked by analysis of the differentiated intensity dependence over time (at each pixel separately) and locating a point of significantly higher intensity followed by a point of significantly lower intensity. Working with differentiated data helped locate cosmic spikes more reliably and distinguished them from genuine signal variations caused by compositional changes in the sample.

The criterion for discrimination of cosmic spikes is based on setting an intensity threshold above which any signal is considered a cosmic spike candidate. The threshold value is determined by the noise level that depends on the detector type and acquisition time. It should be sufficiently low to detect cosmic spikes, but relatively high to minimise the possibility of false positives. In this work, the optimal threshold was $5s_0$, where s_0 is the standard deviation of the differentiated signal.

This algorithm proved excellent for locating cosmic spikes virtually without errors except for some situations where variable background was observed (see Results and

Discussion) in which case nearly the whole spectrum is recognised as a cosmic spike. To prevent such misinterpretation, another threshold parameter was introduced, which specifies the maximum number of pixels recognised as cosmic spikes above which it is statistically unlikely to be true. Typically, each spectrum contains no more than a few cosmic spikes, but this number increases with acquisition time. If the number of "spiked" pixels identified by the script exceeds the threshold, the user is notified and prompted to decide whether this is caused by background variation or cosmic rays and direct the programme accordingly.

The next step after identification of the cosmic spikes is to locate their boundaries. A relatively high intensity threshold for spike intensities eliminates false positives, but does not locate the whole cosmic ray on the spectrum leaving its shoulders undetected (because their intensities are below the threshold). To extend the detected spike centres to their full widths on the spectrum and remove the cosmic spikes, the following procedures were used:

1) The maximum width of a typical cosmic spike is specified;

2) A new threshold for the intensity of a cosmic spike is selected, which is much lower than the initial threshold used for locating the cosmic spikes (e.g. $s_0/5$ compared to $5s_0$);

3) The detected cosmic spikes boundaries are extended, pixel by pixel, by means of a conditional loop, until either the maximum width of a spike is reached, or the new intensity threshold is no longer exceeded, whichever condition is met first;

4) The matrix of spiked pixels generated in this way is used to change the data matrix in such a way that unaffected pixels remain unchanged while the spiked pixels are replaced by the average value of the previous and the next experiment.

Background removal. Due to the relative simplicity of the chosen reaction, the background removal procedure was chosen to rely on the prior knowledge of the Raman spectra of the reagents and the products. The algorithm consisted of three steps: (1) specification of the boundaries of the key Raman bands; (2) approximation of the background under these Raman bands, with straight lines passing through their

boundaries; (3) subtraction of the modelled background intensity profile from the initial spectrum. The pixels beyond the specified Raman bands were assigned with zero intensity. Examples of original and processed sets of spectra of the reaction mixture are shown in Figure 7.3.

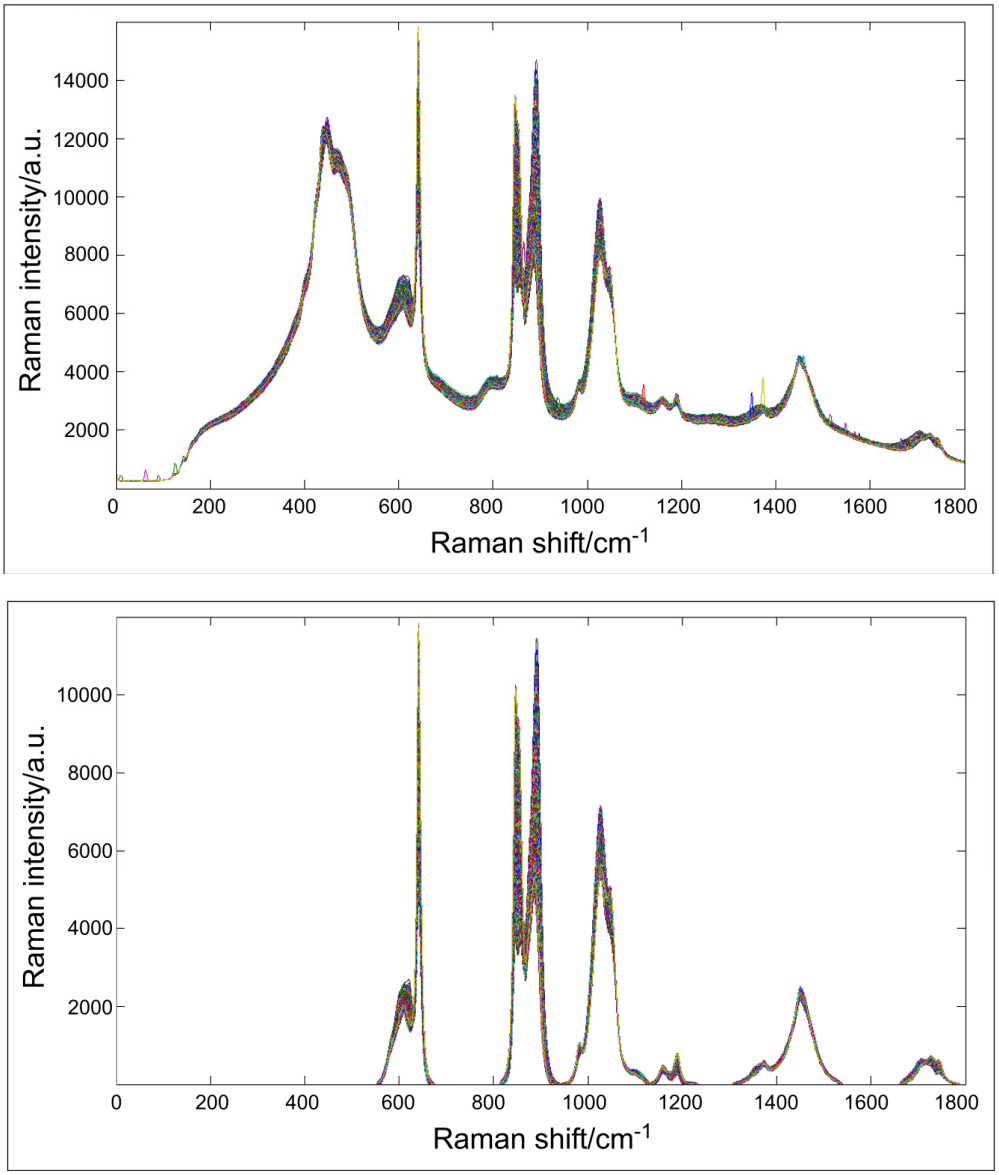

Figure 7.3. Examples of original spectra of the reaction mixture and the modified data obtained by removing cosmic spikes and the spectral regions that do not carry any useful information. Acquisition time – 5 s. 1390 overlaid spectra are shown in each plot.

Principal Component Analysis. After removal of cosmic rays and the broad silica background, the spectra were subject to Principal Component Analysis (PCA)

without mean centering or any other pre-processing procedures. The decision not to use mean centering is justified by the nature of processed data (background-corrected spectra). It was also shown that the use of mean centering resulted in a poorer ability to cope with variable background.

To build a PCA model, a group of spectra with a wide range of reaction conversions was used. The loadings for the first principal component (PC1) represented an average spectrum in the data set, whereas loadings for the second principal component (PC2) reflected the course of the reaction. The PC2 loadings curve match Raman bands of the product combined with inverse Raman bands of the reagents (Figure 7.4).

PC2 scores were found to be proportional to the acetic acid Raman band around 892 cm^{-1} over a wide range of conversions. This proportionality and the intensity of the AcOH Raman band from the pure reagent were used to calculate reaction conversions from the PC2 scores. The calibration graph is shown in Figure 7.5.

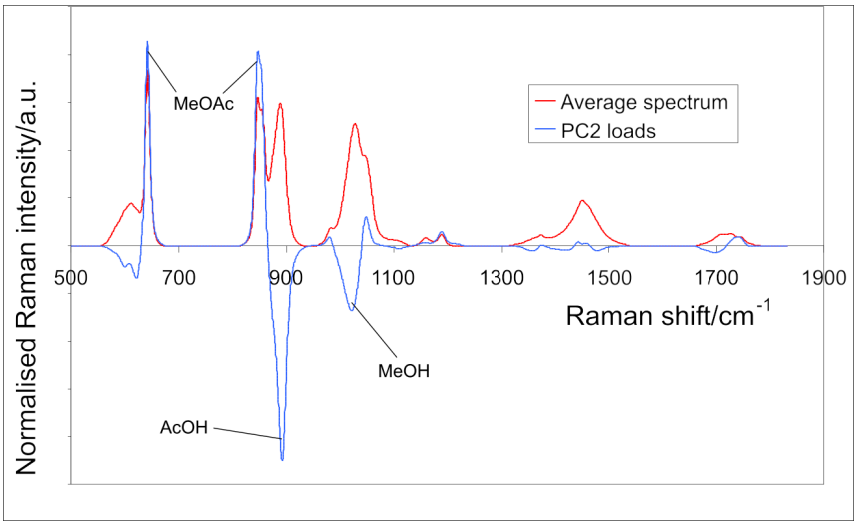

Figure 7.4. PC2 loadings compared to the normalised average spectrum of the reaction mixture.

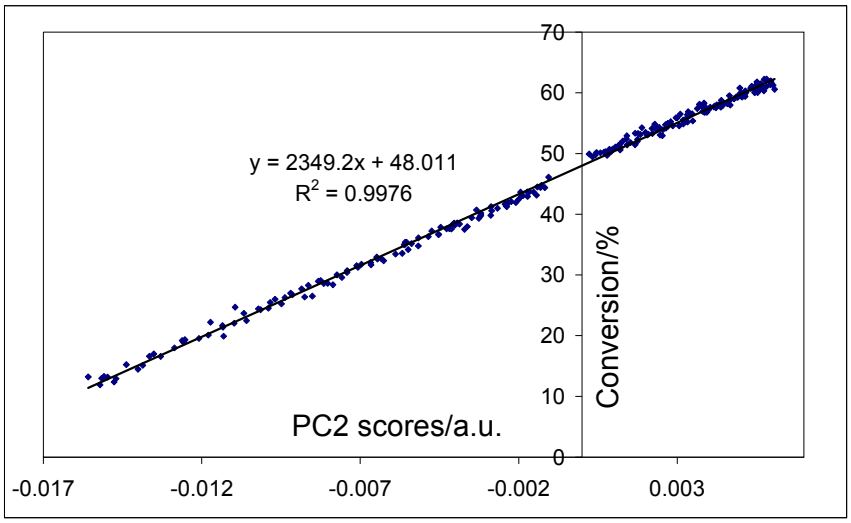

Figure 7.5. Linear correlation between the PC2 scores and reaction conversions estimated by the reduction of the acetic acid signal at 892 cm^{-1}.

7.3. Results and discussion

7.3.1. Improved optical interface

To demonstrate the advantages of the square capillary over the microreactor, Raman spectra of pure methanol collected from the capillary and directly from the microreactor are shown overlaid in Figure 7.6.

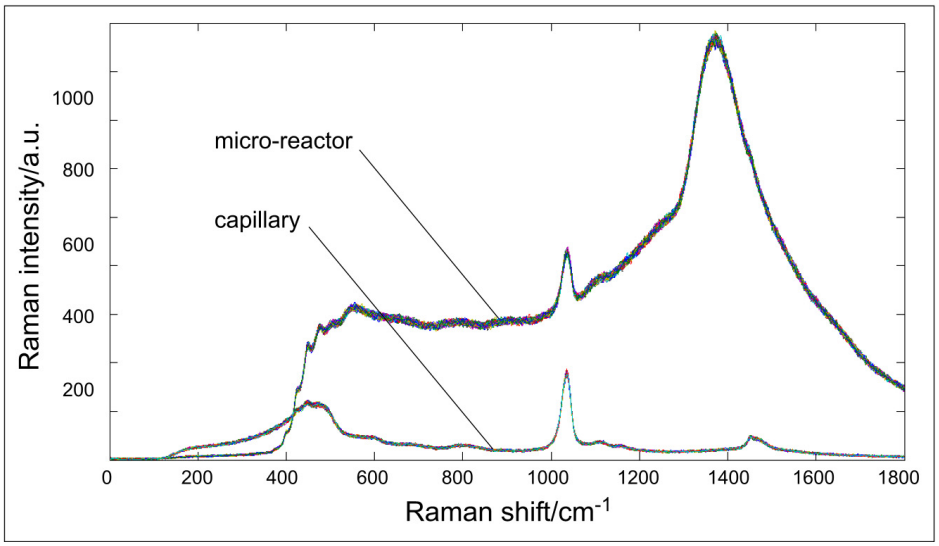

Figure 7.6. Raman spectra of pure methanol collected from the capillary and the microreactor using the same Raman instrument. 100 overlaid spectra are included in each of the two groups to demonstrate the difference in the noise level for both microchannels. Acquisition time of each spectrum is 500 ms.

Figure 7.6 shows that compared to the microreactor channel of the same diameter (100 μm), spectra obtained from the capillary have 35% higher signal intensity, reduced noise and a significantly lower background level.

7.3.2. Analysis of mixing instability

Given the difficulties with pumping stability reported previously in Chapters 5 and 6, it was appropriate to investigate the issue. An assumption was made that the two flowing streams compete for entry into the microreactor junction, and small variations in pressure can cause one stream to flow faster than the other, thus changing the composition of the resulting mixture. Previous experiments with syringe pumps showed that flow rate undulations were periodic, with the period being equal to the rotation period of the pump's driving screw. The volume corresponding to one period can be estimated from Figure 5.14 (Chapter 5). Over each pumping period in section *b* in Figure 5.14 seven Raman measurements were made with the time interval of 7.5 s. This is equivalent to a period of 52.5 s at the flow rate 18.6 μl min^{-1} or $\frac{18.6 \cdot 52.5}{60} \approx 16\,\mu l$, namely, the volume of the fluid that passes through the microreactor over one pumping period. Within a channel with a

diameter of 150 μm, it corresponds to a plug of liquid of more than 90 cm long, a length comparable with that of the whole microreactor serpentine. If the stability problem is common for many syringe pumps of the kind, the question was "Is there any way to smooth out this compositional variability along the channel?" Considering the length of the reagent plugs, they cannot mix inside the microreactor solely by diffusion within any reasonable amount of time. Only convective mixing can be helpful. A reasonable idea is to replace a Y- or T-junction prior to the microreactor by a mixing reservoir with a relatively large volume that would exceed the typical volume of the plug. The streams flowing into such a reservoir (mixer) would mix faster by means of diffusion and convective agitation inside the mixer.

The IMM micro-mixer with an internal volume of 40 μl was a suitable device to test the idea, despite the fact that this micro-mixer was designed for meso-sized flow systems with channel diameters of a few millimetres rather than tens to hundreds of micrometres as used in the present work. The micro-mixer's operation is based upon multi-lamination of the streams with subsequent geometric focusing (Figure 7.7).

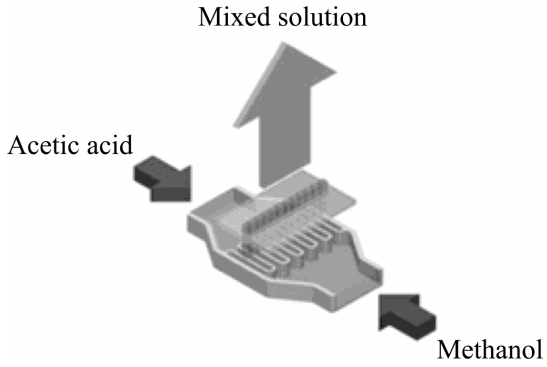

Figure 7.7. A schematic of the micro-mixer[264].

Unfortunately, the syringe pump allocated for this work produced much stabler flow than expected, and instabilities had to be generated artificially. They were achieved by intermittent pumping at a high flow rate (41.8 μl min^{-1}) where the flow was repeatedly stopped and resumed with equal time intervals (5 or 6 minutes). Two series of experiments were conducted. In the first series, pure methanol and acetic acid were pumped without the catalyst. In the second series, the catalyst was added to acetic acid as described in the experimental Section. Each experiment was carried

out in two configurations: one with the T-junction, and the other with the micro-mixer.

The spectral data collected from the experiments without the catalyst had to be processed using a different PCA model, because no chemical reaction took place in this experiment. Loadings of the first two principal components in this new model are shown in Figure 7.8. Similar to the model used to describe the reaction, PC1 loadings in the new model corresponded to the average spectrum of the data set. The PC2 loadings curve, however, matched Raman bands of pure methanol combined with inverse Raman bands of pure acetic acid, thus confirming that their ratio in the mixture varied during the experiments. The PC2 scores obtained from this series of experiments are plotted in Figure 7.9. This Figure reveals that in both setup configurations regions with different composition are generated in the flow with the period equal to the period of pumping intermissions. These regions follow the times of pumping resumptions at 10, 20 and 30 minutes, and reach the detector with the same time delay of approximately 1.25 minutes. This time corresponds to the calculated distance from the micro-mixer "centre", but is longer than the expected travel time from the T-junction (41 seconds). Taking into account the observation that the flow does not stop instantaneously after pumping is halted, the time delay of more than 41 s suggests that zones with unequal proportion of the reagents form when pumping is resumed, rather than when it is stopped.

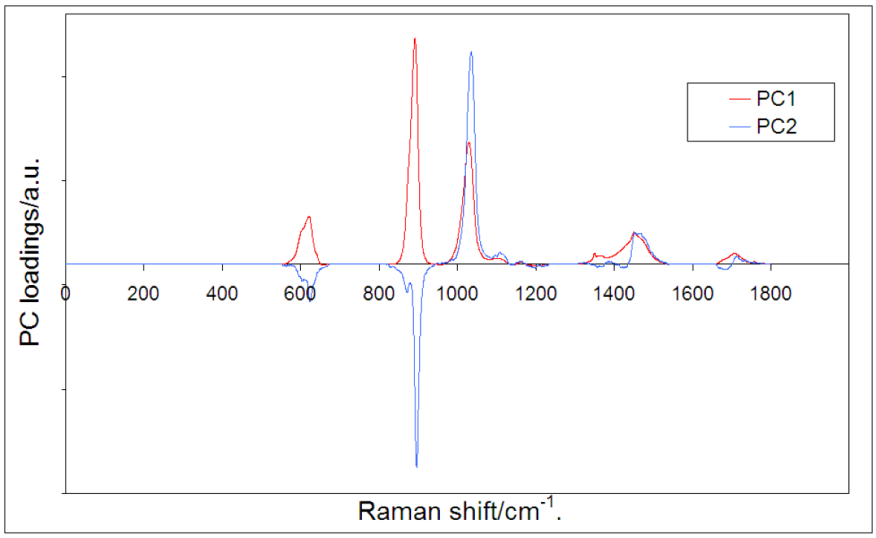

Figure 7.8. PC1 and PC2 loading curves for experiments with intermittent pumping of methanol and acetic acid and no added catalyst.

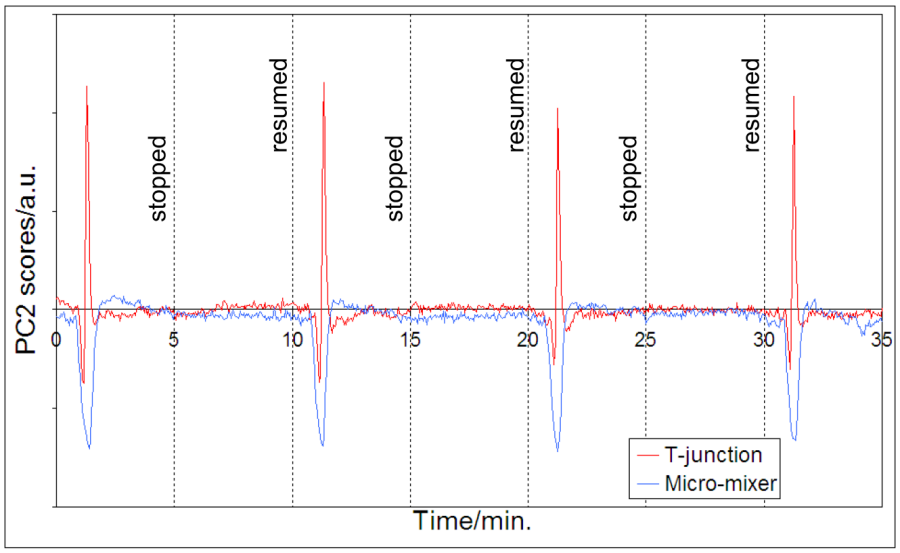

Figure 7.9. Overlaid PC2 score curves obtained from experiments with intermittent pumping of methanol and acetic acid and no added catalyst. Two different setups (with a T-junction and with a micro-mixer) were tested in identical conditions. The pump was stopped and resumed every 5 min., as indicated with vertical dotted lines. Spectral acquisition time is 500 ms.

The next step in interpretation of Figure 7.9 is analysis of the spikes' shape. In the configuration with the T-junction, the line first goes down (higher concentration of AcOH), and then up again (higher concentration of MeOH) before returning to the base line and levelling off. However, the spikes are different when the experiment is conducted with the micro-mixer. In this case, the spikes are wider, and their positive parts are completely absent. These differences are consistent with the following sequence of processes in the setup with the T-junction (Figure 7.10A):

i) When pumping is resumed, the syringe with AcOH (syringe 1) generates higher pressure than the syringe containing MeOH (syringe 2), and AcOH enters the tubing from which methanol is fed. This happens because the third exit from the T-junction, which is a microfluidic system, has much higher flow resistance than the short feed tubings, and only a small portion of AcOH can enter it.

ii) After a few seconds pressure in syringe 2 starts growing and exceeds that in syringe 1. The liquid rich with AcOH escapes towards the microreactor forming a zone that appears as a negative spike in Figure 7.9.

iii) After the AcOH-enriched zone is gone, syringe 2 continues to pump more liquid into the system (in this case the liquid is MeOH) than syringe 1 until pressures equalise. This results in a positive spike in Figure 7.9.

The same processes can take place in the micro-mixer. However, in this case the feed tubings are separated with the high volume reservoir occupied with the already mixed solution. Therefore, when syringe 1 pumps AcOH into the system, it is the premixed solution that is pushed into the MeOH feed tubing, rather than AcOH. At the same time, the excess AcOH distributes around the whole micro-mixer volume forming an extended AcOH-enriched zone. This zone forms wide negative spikes in Figure 7.9. The excessive pressure in the MeOH feed tubing pushes more methanol into the "pool" thus compensating the AcOH excess. Therefore, no zone with higher MeOH concentration (positive spike) is observed.

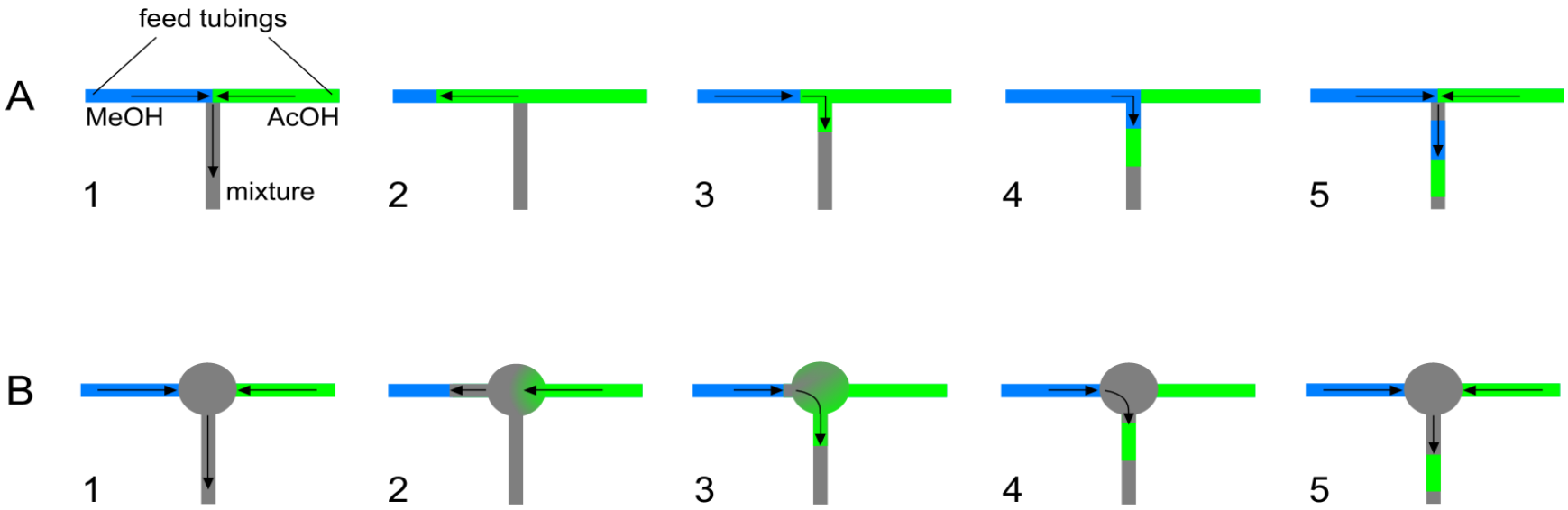

Figure 7.10. Sequence of events that follow resumption of the flow in the setup with the T-junction (A) and with the micro-mixer (B). 1 – stable pumping; 2 – pressure in the AcOH tubing is higher, MeOH tubing is filling; 3 – pressure balance changes and the liquid flows in the opposite direction filling the mixture tubing with an AcOH-rich zone; 4 – pressure in the MeOH tubing is still higher than that in the AcOH tubing, with more liquid entering the mixture tubing; 5 – pressures in the feed tubings equalise.

The same experiments were repeated with methanol and catalyst-containing acetic acid. In Figure 7.11, the computed conversion values are plotted against experimental time. The times of flow manipulations are marked in the same way as it is done in Figure 7.9. The only difference with the previous experiments was that in the experiment conducted in the setup with the micro-mixer the pumping intermission period was increased from 5 to 6 minutes to account for the observed increase in the time needed to reach a steady state.

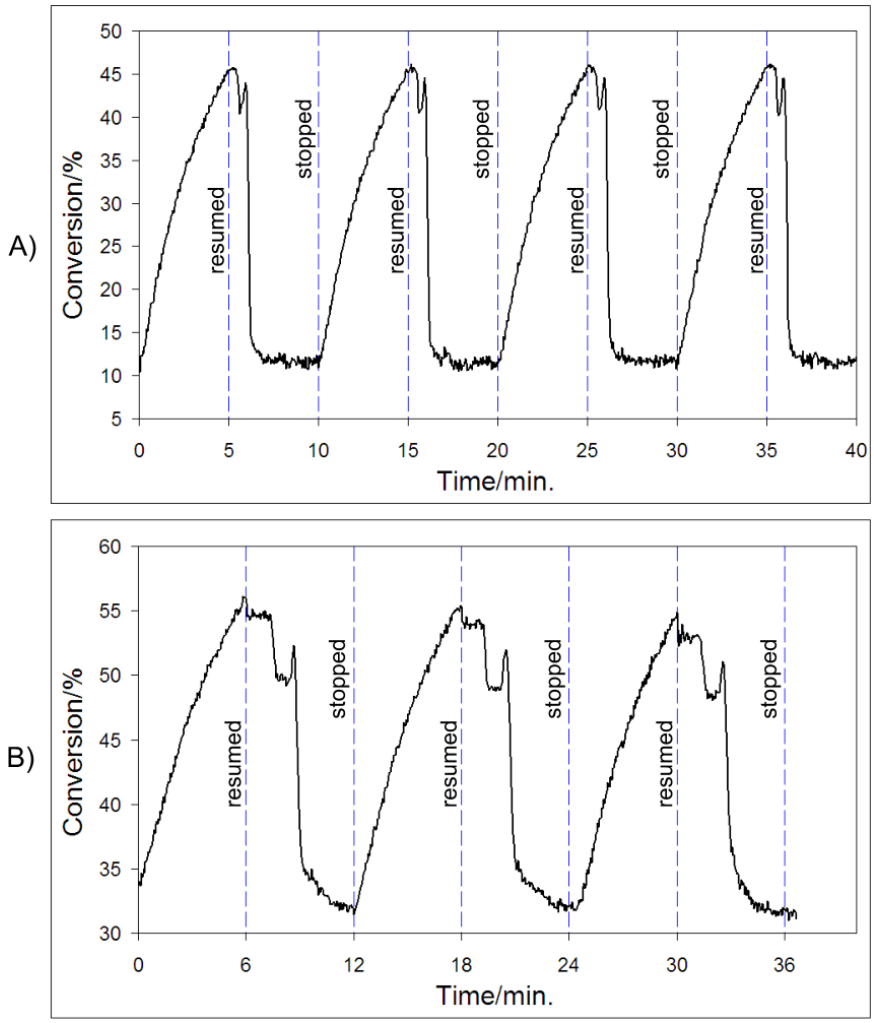

Figure 7.11. Esterification reaction in two microfluidic systems with intermittent pumping. Reagents are mixed in A) T-junction, and B) micro-mixer. The flow (41.8 µl min^{-1}) is stopped and resumed with equal intervals, A) 5 min, and B) 6 min. Acquisition time – 500 ms.

Figure 7.11 shows that the flow system responds to flow rate manipulations in an instantaneous and precise manner, which is a sign of stable and reliable pumping.

Similar to Figure 7.9, flow resumption events lead to spike-shaped compositional changes, with wider spikes being observed when the micro-mixer was used. However, the delay time is not the same in the two experiments; spikes in Figure 7.11B arrive later than those in Figure 7.11A. The cause of this difference is unknown. Another difference is that much more time is needed to reach the steady state when the micro-mixer is used. These results suggest that the use of the micro-mixer with large internal volume does not help to smooth the compositional spikes in the flow. Moreover, it results in unwanted effects such as loss of compositional resolution and an increased time for system stabilisation.

7.3.3. Fast process analysis

The ability to carry out frequent measurements is essential for process analysis and control of continuous-flow reactions. It is particularly important for "flushed steady-state analysis" described in the previous Chapter. However, Raman spectroscopy is typically used with long acquisition times, from dozens of seconds to several minutes. The goal is to acquire a spectrum within a much shorter period.

The developed Raman-microfluidic system was tested for its ability to generate high quality analytical signal using very short acquisition times. For this purpose, the reaction mixture composition was measured at different flow rates of 1.7, 3.5, 8.7, and 20.8 μl min^{-1} that resulted in different extents of reaction. At each flow rate, the system was analysed for about 20 minutes. Transitions from one flow rate to another (up and down) were also recorded. Two experiments were conducted in identical conditions, with acquisition times of 5 s and 100 ms. The results are presented in Figure 7.12.

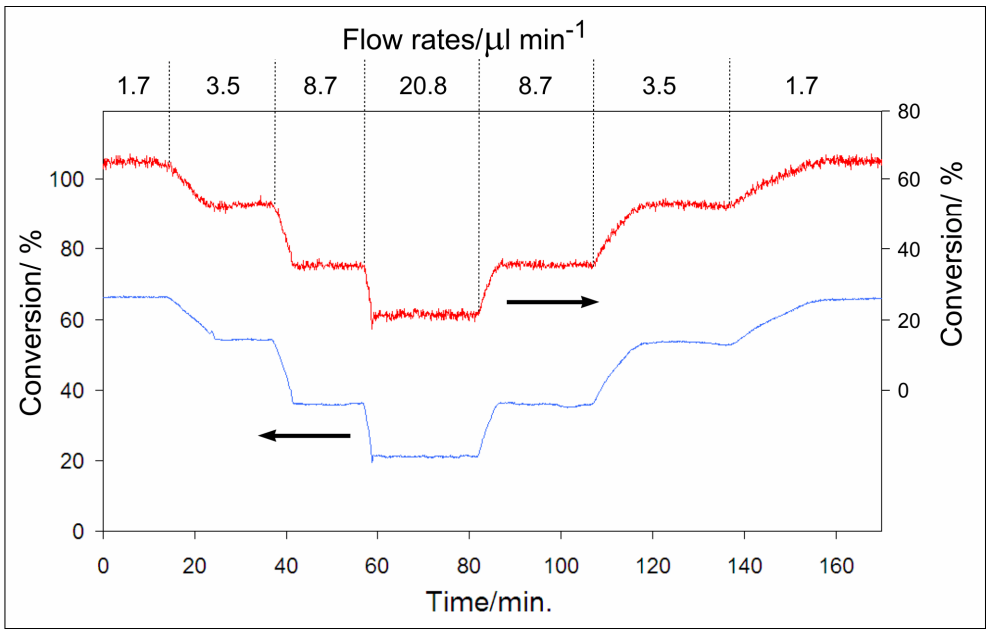

Figure 7.12. Percentage conversion of reagents at different flow rates plotted against experimental time in two identical experiments, one with an acquisition time 100 ms (red line, conversion scale on the right), and the other with an acquisition time 5s (blue line, conversion scale on the left). The curves are offset from each other to show the noise levels.

Figure 7.12 demonstrates low noise on both curves, particularly that obtained with a 5 s acquisition time. The spectral noise was calculated for both curves over the period from 60 to 80 minutes corresponding to the flow rate of 20.8 µl min^{-1}. The average conversions and standard deviations for this section were 21.04 ± 0.18 % for the experiment with 5 s acquisition time, and 21.30 ± 0.84 % for the experiment with 100 ms acquisition time. These results and the appearance of the conversion curve in Figure 7.12 demonstrate the high signal to noise ratios obtained owing to the combined benefits of the improved optical interface, the optimised probe design and a suitable signal processing protocol. Assuming perfectly stable pumping, a 50-fold reduction in acquisition time resulted in only a 4.7-fold increase in the noise level. Provided that the minimal interval between consecutive Raman measurements can be much shorter than the acquisition time, the relatively insignificant increase in the noise level resulted from the reduction in acquisition time can be compensated by the increased number of experimental points. More frequent measurements can be advantageous in certain situations with high-frequency instabilities or where the response time needs to be minimised.

7.3.4. Gas bubbles and background variation

In some experiments, considerable and abrupt background variations were observed (e.g. Figure 7.13).

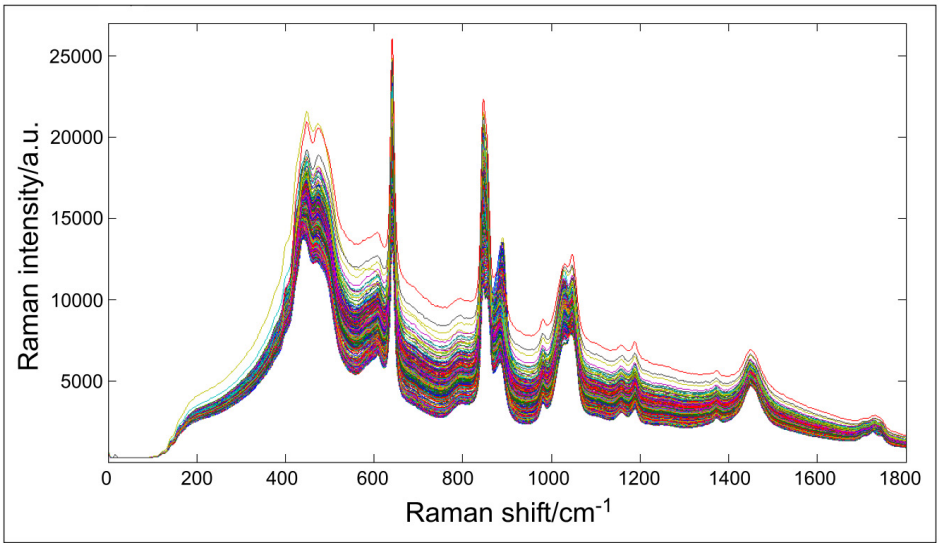

Figure 7.13. Variable background caused by the presence of bubbles in the flow. Acquisition time – 5 s. 1300 overlaid spectra are shown.

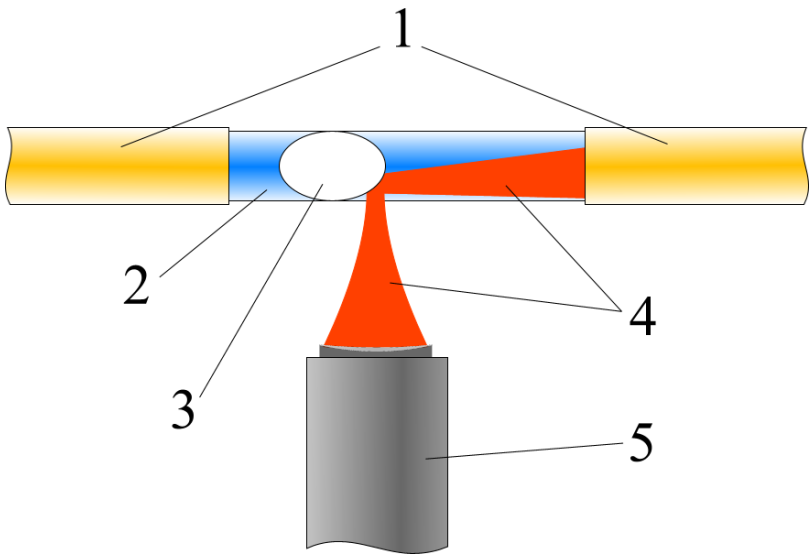

Figure 7.14. A bubble in the measurement zone causing abrupt increase of fluorescence background. 1 – polyamide-coated capillary, 2 – coating-free capillary section, 3 – air bubble, 4 – laser beam, 5 – Raman probe.

These baseline variations resemble a typical fluorescence spectrum and their temporal pattern is similar to that of cosmic rays. The cause of this phenomenon was determined. Gas bubbles passing through the focal point of the Raman probe reflected some of the laser light along the capillary axis, thus illuminating the highly fluorescent polyamide coating (located 1 cm away from the measurement point) and collecting a fluorescence signal from it (Figure 7.14). In addition to variations in the background instability, bubbles displace the liquid sample from the measurement volume resulting in an unstable Raman signal that can be misinterpreted as the consequence of variable fluid composition in the microchannel.

PCA with normalisation as the pre-processing method has been found to be exceptionally useful in these situations. Normalisation was carried out using the corresponding function in PLS toolbox (Matlab). This function computes the total area of the Raman spectrum and divides the intensity of each pixel by that value. Figure 7.15 shows two time curves of reaction conversion versus experimental time, computed from the same data set using the same experimental procedure as described in Figure 7.12. The red line represents the results obtained without using any pre-processing methods, and the blue line – using area normalisation. Two sections with significantly higher noise are clearly visible on the red line. They correspond to the periods where bubbles were present in the microchannel. In the blue line, these regions with higher noise are completely smoothed out and indistinguishable from the rest of the curve.

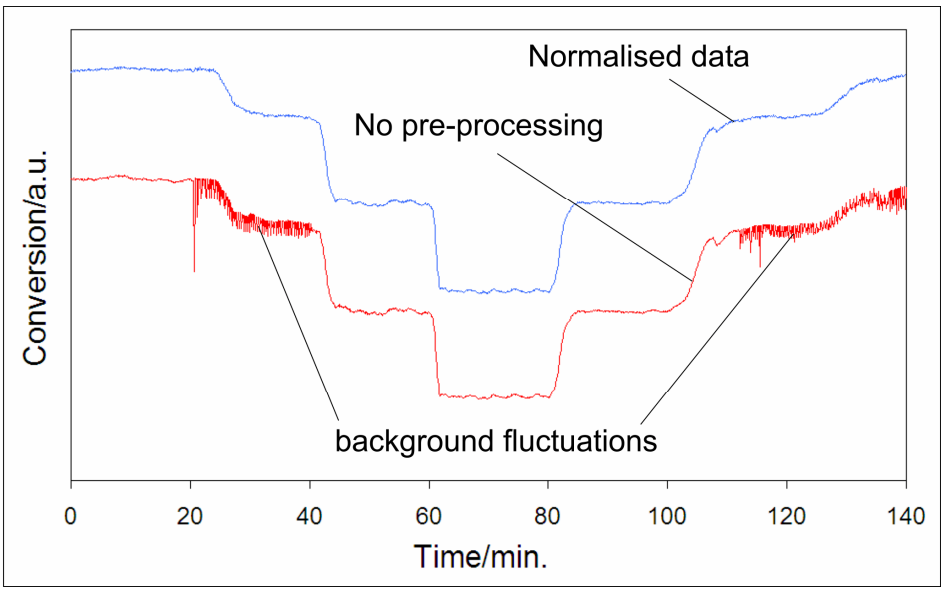

Figure 7.15. Influence of normalisation as a signal pre-processing method on smoothing background fluctuations. The experiment was conducted as described in Figure 7.12. The reagents were pumped at different flow rates of 1.7, 3.5, 8.7 and 20.8 µl min^{-1} (up and down). The two curves represent the same experiment with different data processing methods: without pre-processing (red line) and with normalisation (blue line). Acquisition time – 5 s.

Although the source of the bubbles was not determined, and their appearance was considered as a nuisance, this experiment was an example of a realistic situation. In fact, heterogeneous continuous flow processes are not rare in chemistry, hydrogenation, oxidation and reactions in droplets flowing in carrier liquid are good examples.

Provided that the intensity of the collected Raman spectra is sufficiently high, the results of this experiment have shown that the use of normalisation as a signal pre-processing method can reduce or eliminate the adverse effects that the presence of bubbles or droplets can cause. However, when the signal-to-noise ratio is not sufficiently high, normalisation can be of little or no help because the appearance of bubbles will more likely cause a reduction of the signal-to-noise ratio below the detection limit or below the noise level caused by the background variations.

7.3.5. Flow-induced shifts of acetic acid Raman bands

An interesting effect was observed when a premixed mixture of equal volumes of acetic acid and methanol was pumped into the microfluidic system at different flow

rates. Because no catalyst was present in the system and the mixture was prepared prior to loading into the syringes, the only changing factor was the flow rate. Figure 7.16 shows 809 overlaid Raman spectra of an acetic acid-methanol mixture, collected at different flow rates. Only the Raman band of acetic acid that exhibited the highest changes is shown.

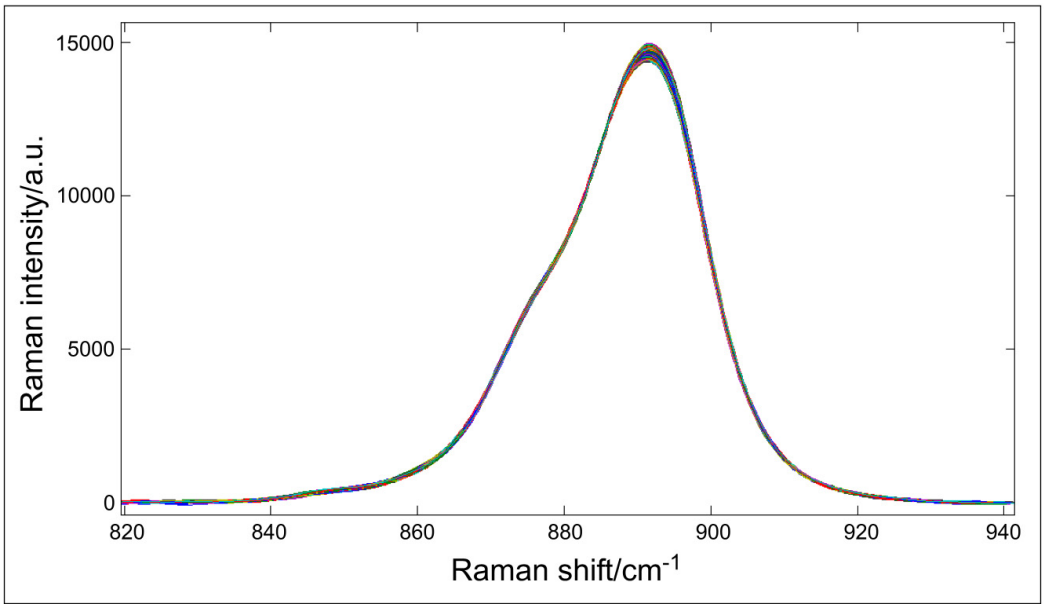

Figure 7.16. 809 overlaid Raman spectra of an acetic acid-methanol mixture, collected at different flow rates. The spectral shift is minute but is clear in the PCA model. Acquisition time – 5 s.

The spectral change is hardly visible in Figure 7.16. However, using PCA, minute differences between the spectra were detected. The nature of the spectral changes is demonstrated in Figure 7.17 where the loadings for PC1 and PC2 are plotted. It can be inferred that the primary change is a shift of the acetic acid Raman bands located around 600 and 900 cm^{-1} towards higher wavenumbers.

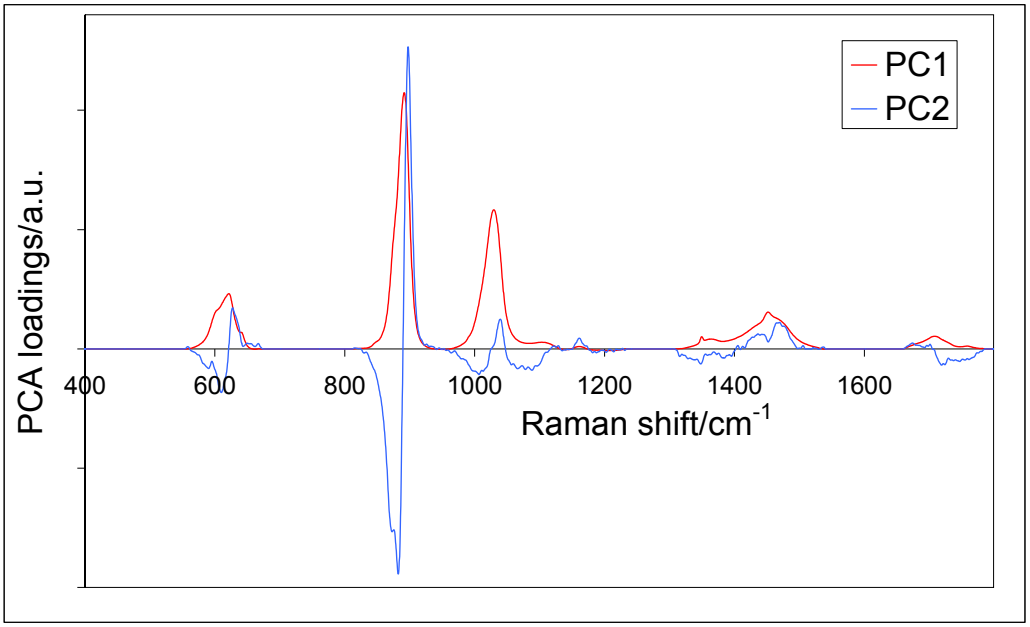

Figure 7.17. PCA scores for the first two principal components. The sample is a mixture of equal volumes of acetic acid and methanol. No catalyst was added, the acetic acid Raman bands around 600 and 900 cm^{-1} are shifted to higher wavenumbers as the flow rate increases.

PC2 scores plotted in Figure 7.18 clearly show that the observed spectral shifts occur instantaneously each time the flow regime is changed and the magnitude of the effect increases with the flow rate. In contrast to the experiments with the chemical reaction (Figure 7.12), the stabilisation time is negligibly small regardless of the flow rate value. This behaviour suggests that the spectral shifts are caused by either a pressure change or a flow rate change. The former is less likely because the pressure inside the channel is relatively small to cause such a notable effect. Flow-induced Raman shifts can be explained by the electrokinetic potential that builds up on the interface between the fluid and internal capillary walls. This potential can change the electric field around AcOH molecules causing them to either dissociate or change the distribution of other molecules around them. In fact, the acetic acid Raman band at 900 cm^{-1}, which is assigned to a C-C stretching vibration[265], is known to be sensitive to various parameters including phase state[266] and concentration[267] and its shift makes up the main contribution to the PC2 loadings in Figure 7.16.

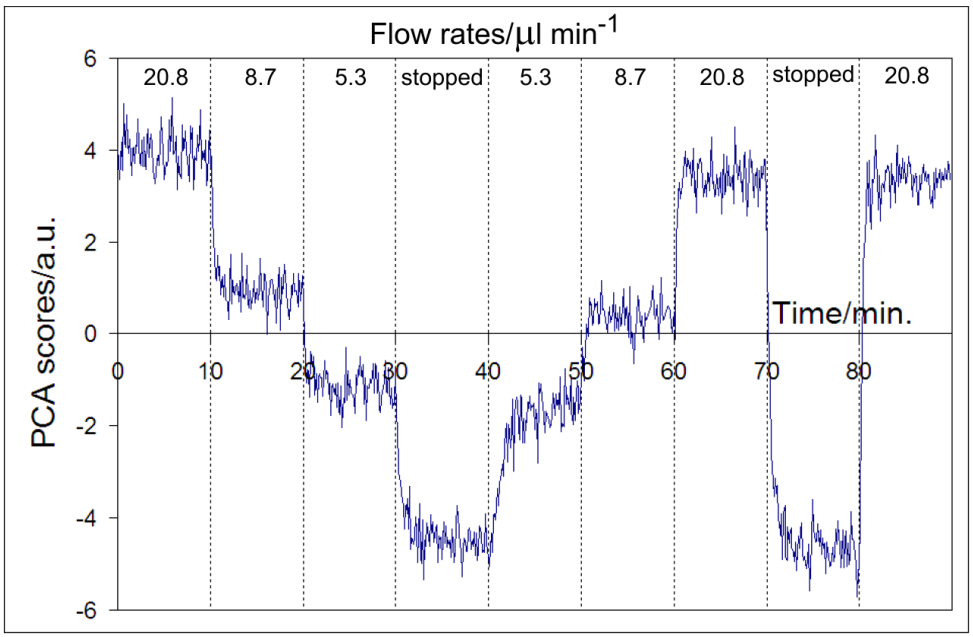

Figure 7.18. PC2 scores at different flow rates plotted against experimental time. The flow rates were changed every 10 minutes as indicated at the top of the Figure. Acquisition time – 5 s.

This experiment demonstrated that flow in microchannels could cause complex phenomena that influence chemical properties of the fluid and are likely to affect the course of chemical reactions as well. The ability of Principal Component Analysis to detect small differences in Raman spectra was demonstrated. This method can be exceptionally useful for studies of physicochemical effects inside microchannels.

7.4. Conclusions

The work described in this Chapter was the final step in achieving the central goal of the project – to understand and improve the applicability of Raman spectroscopy for studying microfluidic systems. The main result is the demonstration of the considerable effect that an optical interface between the probe and the sample has on the intensity of Raman spectra and the silica background. The factors affecting the quality of Raman spectra have also been identified.

The combination of advanced optics, an optimised Raman probe and sensitive data processing methods allow the use of Raman spectroscopy in new applications where measurements must be taken frequently in order to provide high quality process analysis and control. The findings of the last two Chapters complement each other

and can be used to design a sensitive Raman system capable of obtaining high-quality Raman spectra from any microreactor connected to it.

8. Conclusions and suggestions for future work

8.1. Conclusions

The work presented in this thesis comprised a series of inter-connected studies aimed at investigating the applicability of Raman spectrometry for process analysis in microreactors. At the initial stage of this work, various optical configurations for illumination and signal collection from a liquid sample were studied including a 90° configuration, intracavity sample illumination and a back-scattering configuration. The best setup was used to design a low-cost back-scattering fibre-optic Raman probe optimised for signal collection from 150 μm i.d. microchannels. With a spectral measurement time of 2 s, it was shown that the probe could monitor the progress of an esterification reaction in real time and quickly optimise the reagent flow rates. Although advantages of using Raman spectrometry for analysing microfluidic reactions were reported previously, the novelty of this part of the work was in demonstrating the importance of optimising the probe optics in order to maximise the intensity of the Raman signal. It was shown that satisfactory results can be achieved using fibre-optic Raman probes with compact low-cost optical elements instead of Raman microscopes with expensive objectives. In addition, it was revealed that the signal-to-background ratio of the Raman spectra can be improved by optimising core diameters of the fibres and their careful alignment in the probe.

Despite the promising results achieved, it was obvious that the lack of standards in microreactor design and materials could impede the use of Raman spectrometry as a universal method for monitoring chemical processes in microreactors. To address this issue, a new analytical methodology has been developed that allows information about a steady-state of microfluidic reactions to be quickly obtained without the necessity to move the Raman probe along the channel. The procedure was shown to be an efficient and effective way to obtain kinetic information about the reaction, and the method offers advantages over conventional experimentation for process optimisation. A further advantage of the developed method is the option to apply other non-invasive or in-line methods in a similar manner to investigate the reaction progression in microreactors. With the “flushed steady-state” methodology, a Raman

or any other probe does not have to be tailored to the geometry of microreactor channels. Instead, the measurement site can be separated from the microreactor and designed to meet the requirements of Raman spectrometry, resulting in the possibility to improve further the signal collection efficiency and signal-to-noise ratio.

An example of such an improvement was demonstrated in the last phase of the research using a fused silica capillary connected to the microchip. The capillary shape and material facilitated the Raman measurements and significantly reduced the intensity of the glass background on the spectra. Combined with suitable data processing algorithms, the improved optical interface allowed fast monitoring of a chemical reaction with a measurement time of only 100 ms. This was demonstrated for a reaction where no solvents were used and therefore the concentration of the reaction components was relatively high. Although the performance of the Raman system will be worse if it is applied to monitoring reactions in dilute solutions, the relative improvements in sensitivity demonstrated in this work can help increase the speed of measurements, reproducibility and limits of detection for each particular analyte present in the reaction mixtures monitored by Raman spectrometry.

The results obtained in this work showed that despite the relatively poor sensitivity of Raman spectrometry, it is readily applicable for process analysis in microreactors and offers unique advantages over other analytical methods. It is hoped that the reported results will revive interest in this field and contribute to the rapid developments in microfluidic technology that are observed these days.

8.2. Suggestions for future work

The value of the reported developments is not only in the demonstrated improvements in methodology and photonic aspects of Raman spectrometry, but also in opening new possibilities for future research, which can be split into two directions. The first direction concerns the potential for further improvement of the signal-to-noise ratio in Raman spectrometry. Developments in laser systems can play a significant role, but more compact and more efficient lasers are needed, especially those operating in the deep UV region (below 260 nm) due to their ability to generate

intense and fluorescence-free Raman spectra. Currently, these lasers are bulky and expensive, which prevents their wide use in routine Raman measurements. Fluorescence interference remains the main hurdle in Raman spectrometry. Therefore, creation of low-cost and reliable lasers in deep-UV would become an important milestone in the history of Raman spectrometry.

At present, single-mode UV laser radiation can be obtained by frequency tripling or quadrupling of visible and near-infrared lasers. The main issue with this approach is the low efficiency of multi-order frequency conversion. It requires the seed laser to operate at a very high power that complicates the device and increases its cost. Frequency doubling of a green or blue laser might offer a more efficient approach to obtain a deep-UV laser. Second harmonic generation is a widely used technology that can be applied to low-power lasers. For example, green laser pointers are based on second harmonic generation from a compact near-infrared semiconductor laser. A low-cost deep-UV laser can be potentially based on a similar principle. However, it would require a number of developments in photonics and material science. The problems associated with this approach include the high absorption of the common materials in the UV spectral range and the lack of suitable single-mode laser operating at wavelengths below 500 nm. Semiconductor lasers based on gallium nitride is an option[268]. However, the single-mode operation of these lasers is currently limited to a maximum power of a few milliwatts, which is far too low for generating a noticeable frequency-doubled output.

The use of pulsed or modulated excitation sources in combination with lock-in amplification presents another way to improve the signal-to-noise ratio. It would also eliminate interference from ambient light during the measurements. Lock-in amplification is widely utilised in various applications, but not in Raman spectrometry. In 1995, Bennett[269] showed that by using lock-in amplification that is simple to apply to FT-spectrometers, signal-to-noise ratio can be improved by a factor of 4 or higher. However, his work did not attract any significant attention, having been cited only three times over 15 years.

To minimize the probability of the radiative damage of microfluidic samples, it would be desirable to reduce the laser power density in the measurement point of the

microchannel. The simplest way to realise this is to decrease the laser power. However, it would results in the reduction of the Raman signal obtained. An alternative approach is to use multiplexed illumination that allows spreading of the laser power over several closely located measurement points. To do so, a high-power laser beam (e.g. from a VECSEL) can be split into several channels each fibre-coupled and projected lengthwise on the microchannel using a multiplexed optical fibre and a single lens. The Raman signal can be collected with the same fibre bundle and an appropriate beam-splitting arrangement.

The robustness and compactness of the Raman measurement interface can be improved by means of integrating miniature optical components into the microchip structure. The components that can be integrated include micro-lenses, waveguides, beamsplitters and laser diodes. This approach has been demonstrated for fluorescence[194] and potentially can also be applied to Raman spectrometry.

The second direction for future work concerns development or optimisation of other optical methods that can become part of the analytical toolbox for microreactors. These methods include refractive index sensing and MIR absorption spectrometry. An ATR-based MIR system designed for measurements in a flow cell has been demonstrated recently[270]. However, it has an enlarged measurement zone not suitable for microreactors. Recently, Kazarian reported development of a MIR-measurement cell that is suitable for high-spatial resolution measurements in microreactors[245]. It is based on an ATR sensor integrated with a microfluidic chip. The method provides a high spatial resolution on the order of tens of micrometres. This technology is a good alternative to Raman spectroscopy. MIR spectroscopy provides similar structural information and can potentially be more sensitive than Raman scattering. It would be interesting to use MIR absorption with the "flushed steady-state" methodology.

Advantages can be taken of using quantum cascade (QC) lasers as an excitation source in MIR-spectroscopy[271]. Instead of obtaining the whole MIR-spectrum, it is possible to select one or several wavelengths to probe certain absorption bands in the sample. The two beams can be easily combined and delivered to the sample directly or through a fibre. Using modulation of the laser outputs at different frequencies it is possible to discriminate absorption at the two wavelengths using a single-channel

detector and Fourier transformation of the recorded signal. This arrangement does not require a spectrometer, which can increase the frequency of measurements. Such a system could be cheaper and more compact than current instruments.

There is some potential for absorption spectrometry in the UV, visible or near-infrared ranges. The optical interface with a microchannel can be based on an ATR crystal or transmission geometry (especially for NIR). Lasers with high beam quality available in this wavelength range can help achieve high spatial resolution and high sensitivity of measurements. The use of tunable lasers with these methods would allow high-resolution spectra in the selected spectral regions to be obtained without the need to use spectrometers.

In conclusion, microfluidic technology, spectroscopy and photonics form an interdisciplinary field with great potential to revolutionise analytical and synthetic chemistry. The achievements demonstrated in this field so far have already changed traditional practices in biology, medical diagnostics and chemical sciences. We live in the era of fast technological developments, climate change and demands for increased production. Therefore, microfluidics and optofluidics will be highly relevant in the future due to the greater throughput, miniaturisation, faster analysis or synthesis, and reduced consumption of energy and resources that these technologies offer.

Appendices

Appendix 1. Matlab scripts written for processing of the spectral data

Script 1. Extracting spectral data from multiple .spc files

```
1 - Multiple_SPC_files = spcreadr;
2 - rs = Multiple_SPC_files.axisscale{2};              % Raman shifts
3 - rs = rs(:,1:6172);
4 - s = Multiple_SPC_files.data;                       % Raman signal
5 - s = s(:,1:6172);
6 - userdata = Multiple_SPC_files.userdata;
7 - clear Multiple_SPC_files;
```

Script 2. Extracting time of each spectrum

```
1 -  [b1,b2] = size(userdata);
2 -  clear b2
3 -  a = ones(b1,14);                 % preallocating for speed
4 -  for n = 1:b1
5 -      a(n,:) = userdata{n,1}(4,31:44);          % extracts time info from 'userdata'
6 -  end;
7 -  a = a – 48;                      % fixes unusual encoding of string symbols
8 -  n = (1:11);
9 -  d = a(:,n) == 10 & a(:,n+3) == 10;        % locates position of the first colon that
       will serve as reference for further manipulations with matrix a
10 - d(:,12:14) = zeros;      % makes the size of matrix d the same as that of matrix a
11 - d = d';
12 - [g,h] = find(d);           % returns indices of the first colon
13 - clear d h
14 -     filter = a == –16;          % removes spaces represented as '–16' after decoding
15 -     filter = filter == 0;
16 -     a = a.*filter;                % replaces all '–16' by zeros
17 -     clear filter
```

```
18 -        filter2 = a == 32;              % changes time format from AM/PM to 24h to
                avoid problems when experiment runs between 11:59 AM and 1:00 PM
19 -        index = sum(filter2');
20 -        index = index';
21 -        index = index*12;
22 -        n = (1:b1);
23 -        for n = 1:b1
24 -            if a(n,g(n,1) –2) == 1 && a(n,g(n,1) –1) == 2 && a(n,g(n,1) +7) == 32
                                        % if-loop prevents addition of 12h to 12:xx PM
25 -                index(n,1) = 0;
26 -            end;
27 -            a(n,g(n,1) –1) = a(n,g(n,1) –1)+index(n,1); % adds 12h where necessary
28 -        end;
29 -        clear filter2 index
30 - time = ones(n,3);                  % preallocating for speed
31 - for n = 1:b1
32 -    time(n,1) = 10*a(n,g(n,1) –2) + a(n,g(n,1) –1);          % hours column
33 -    time(n,2) = 10*a(n,g(n,1) +1) + a(n,g(n,1) +2);          % minutes column
34 -    time(n,3) = 10*a(n,g(n,1) + 4) + a(n,g(n,1) +5);         % seconds column
35 - end;
36 - clear a b1 g n
37 -    hours = time*[1;1/60;1/3600];       % absolute time in hours
38 -    min = time*[60;1;1/60];             %... minutes
39 -    sec = time*[3600;60;1];             %... seconds
40 -        hours = hours – hours(1,1);     % subtracts time of the first experiment
41 -        min = min – min(1,1);
42 -        sec = sec – sec(1,1);

% codes of the symbols in extracted userdata string:
% /          –1
% space     –16
% :          10
```

```
% A          17
% P          32
% M          29
```

Script 3. Background substraction and conversion calculations

```
clear hours sec userdata
a=size(s);              % s(samples, pixels) - initial array of spectra to be processed
% instructions 4-23 ensure the same size of data matrices, which are sometimes
  different due to unknown reasons
if a(1,1) == 6398
    s = s';
    rs = rs';
end;
if a(1,1) == 6399
    s = s';
    rs = rs';
end;
if a(1,1) == 6400
    s = s';
    rs = rs';
end;
if a(1,2) == 6400
    rs = rs(:,2:6399);
    s = s(:,2:6399);
end
if a(1,2) == 6399
    rs = rs(:,2:end);
    s = s(:,2:end);
end
clear a
b = s;
% instructions 27-51 remove pixels that do not carry useful information and
    subtract background from useful segments
```

```
27 - b(:,[1:3378 3438:3899 4167:5279 5531:end]) = zeros;
28 - n = 3379;
29 - m = 3437;
30 - step = (b(:,n)-b(:,m))/(m-n);
31 - for i = n:m
32 -     k = m-i;
33 -     b(:,i) = b(:,i) – b(:,m) – k*step;
34 - end;
35 - n = 3900;
36 - m = 4166;
37 - step=(b(:,n) –b(:,m))/(m-n);
38 - for i = n:m
39 -     k = m – i;
40 -     b(:,i) = b(:,i) – b(:,m) – k*step;
41 - end;
42 - n = 5280;
43 - m = 5530;
44 - step = (b(:,n) – b(:,m)) / (m – n);
45 - for i = n:m
46 -     k = m – i;
47 -     b(:,i) = b(:,i) – b(:,m) – k*step;
48 - end;
49 - clear step i k m n
50 - s2 = b;
51 - clear b
52 - signal = sum(s2(:,5280:5530)');        % calculating area under the product peak
53 - prod = (signal – 14031) / 116500;          % calculating product concentration
     based on prior regression analysis
54 - conv = prod / 1.5 / 1.025*100;     % Conversion calculation takes into account
     volume contraction after mixing
55 - % line 54 changes to "conv = prod / 1.5*1.01*100;" when analysis is carried out
     at 40 degrees. This is to account for thermal expansion
```

```
55 - conv = conv';
56 - prod = prod';
57 - plot(conv')
```

Appendix 2. Data processing in method B

Script 4. Calculation of reaction time from experimental time

```
1 - F1 = input('Siringe pump F1, ul/min:'); % input F1
2 - F2 = input('Siringe pump F2, ul/min:'); % input F2
3 - t0_time(1,1) = input('t0 hours:'); % input hours of flow rate change time (t0)
4 - t0_time(1,2) = input('t0 minutes:'); % input minutes of flow rate change time (t0)
5 - t0_time(1,3) = input('t0 seconds:'); % input seconds of flow rate change time (t0)
6 - t0 = t0_time*[60;1;1/60]; % Calculating absolute time in minutes
7 - min = min – t0; % offsetting time matrix to the value of t0
8 - clear t0 t0_time
9 - plot(min,conv) % plotting the kinetic curve to locate t2 value
10 - t2 = input('t2 from the plot, minutes:'); % input t2
11 - % instructions 12-19 remove unnecessary parts of kinetic curve, time and
     conversion matrices
12 - a2 = min(abs(min – t2));
13 - b2 = find(abs(min – t2) == a2);
14 - a1 = min(abs(min));
15 - b1 = find(abs(min) == a1);
16 - clear a1 a2;
17 - min = min(b1:b2,:);
18 - conv = conv(b1:b2,:);
19 - clear b1 b2
20 - tr = –(F2 – F1)/F1*min + F2 / F1*t2; % calculating reaction time (tr) from
     experiment time (min)
21 - plot(tr,conv)
```

Appendix 3. Measurements of volume change upon mixing and heating

Materials: two syringes (volume 500 µl, units 5 µl, model Gastight 1750, Hamilton, Switzerland) with needles (2), 2 ml volumetric flasks (2), 1 ml volumetric flasks (3), 5ml vials (2), chemicals (as used in the reaction monitoring), ice, water bath, glass pen.

Procedure. 1. Control experiment. To ensure that the syringes and volumetric flasks are calibrated properly all flasks are filled to the marks with methanol using the syringes. The dispensed volumes are measured and compared with the nominal volumes of the flasks.

2. Solutions of the reagents are prepared in 2 ml volumetric flasks according to the procedure described in the experimental section. The prepared solutions are transferred to 5 ml vials with wider necks to allow easy access with syringes.

3. 500 µl of each of the 2 solutions are added to a 1 ml volumetric flask (flask 1). The flask is spun and shaken gently for 5 minutes such that the solution does not wet the lid. The solution is left overnight to allow the reaction complete. Two other 1 ml volumetric flasks (flasks 2 and 3) are filled with the individual reagent solutions.

4. Flasks 1-3 are cooled to 10°C and levels of their liquid content are marked with the glass pen. Then the flasks are heated to 40°C. After thermal equilibrium has been reached, the new levels of the liquids are marked. To measure the thermal volume increase all vials are emptied and filled with methanol to the mars corresponding to 10°C. The volume of methanol necessary to fill the flasks to the 40°C marks is recorded.

5. To measure volume change upon mixing 500 µl of each of the two reagent solutions were added to a 1 ml volumetric flask and mixed as described above. Methanol is then added to the mixture dropwise and its volume necessary to fill the flask is recorded.

Results. The experiment showed that the syringes are calibrated correctly, with experimental error not exceeding 0.5%. Temperature increase from 10 to 40°C

causes considerable expansion. The values for thermal expansion found for flasks 1-3 are the same and average 3.5 ± 0.5 % of the initial volume. Reagent mixing caused reduction of the total volume by 2.5 ± 0.5 %. No change in volume due to the chemical process was noticed.

Appendix 4. Data processing in Chapter 7

Script 1 and script 2 from Appendix 1 were applied prior to the scripts given below.

Script 5. Cosmic ray filter

```
1 - a = size(s);            % s(samples, pixels) - initial array of spectra to be processed
2 - i = a(1,1);
3 – j = a(1,2);
4 - diff(1:i–1,:) = s(2:i,:) – s(1:i–1,:);            % differentiated data
5 - diff(i,:) = mean(diff(i–1,:));    % adding the edge value to equate the matrices size
6 - if i < 200            % if the number of spectra is less than 200, the threshold can be
    assigned a higher value
7 -     samp = 1:i;
8 -     std_diff_left = zeros(i,j);
9 -     std_diff_right = zeros(i,j);
10 -    for samp = 1:i
11 -        std_diff_left(samp,:) = std(diff([1:samp–1  samp+2:end],:));
          % calculating standard deviation on which the threshold will be based
12 -        std_diff_right(samp,:) = std(diff([1:samp–2  samp+1:end],:));
13 -    end;
14 -    clear samp
15 -    d5 = diff > std_diff_left*6;            % identifying abrupt increases of signal
16 -    e5 = diff < – std_diff_right*6;            % identifying abrupt decreases in signal
17 -    d2 = diff > std_diff_left / 2;            % another threshold for extending the
      matrix of spiked pixels to their shoulders
18 -    e2 = diff < – std_diff_right/2;
19 -    clear diff  std_diff_left  std_diff_right  a
20 - else
```

```
21 -    std_diff = std(diff);
22 -    d5 = diff > ones(i,1)*std_diff*5;          % identifying abrupt increases of signal
23 -    e5 = diff < – ones(i,1)*std_diff*5;        % identifying abrupt decreases in signal
24 -    d2 = diff > ones(i,1)*std_diff/2;          % another threshold for extending the
        matrix of spiked pixels to their shoulders
25 -    e2 = diff < – ones(i,1)*std_diff/2;
26 -    clear diff std_diff
27 - end;
28 - f2(2:i,:) = d2(1:i–1,:) + e2(2:i,:);    % behaviour filter - cosmic peaks rise and fall
29 - f2(1,:) = e2(1,:);           % returning the original number of samples in the matrix
30 - clear d2 e2
31 - g2 = f2 == 2;       % identifying pixels that meet typical behaviour of cosmic rays
32 - clear f2
33 - f5(2:i,:) = d5(1:i–1,:) + e5(2:i,:);
      % same manipulations with stricter selection requirements
34 - f5(1,:) = e5(1,:);
35 - clear d5 e5
36 - g5 = f5 == 2;
37 - clear f5
38 - sum_g5 = sum(g5');
39 - bad_samples = sum_g5 > 120;         % if this condition is true it is likely that the
      whole background changes, in which case the filter cannot be used
40 - indices_of_bad_samples = find(bad_samples);          % reports the numbers of
      samples where background jump is suspected
41 - clear bad_samples
42 - a = isempty(indices_of_bad_samples);
43 - if a == 1
44 -     clear indices_of_bad_samples  % removes traces if bad samples are not found
45 - else
46 -     g5(indices_of_bad_samples,:) = zeros;
        % bad samples are found, bad samples should not be corrected - the correction
        matrix for those samples is made equal to zero
```

```
47 -     g2(indices_of_bad_samples,:) = zeros;
48 - end;
49 - clear a sum_g5
50 - g = g5 + g2;
51 - clear g2 g5
52 - n = (2:j–1);
53 - k = 1;
54 - g_add = zeros(i,j);
55 - while k < 30                % extending the boundaries of the cosmic spikes matrix
       only where both g5 and g2 are non-zeros
56 -     g_add(:,n) = g(:,n+1) == 2 & g(:,n) == 1 | g(:,n–1) == 2 & g(:,n) == 1;
57 -     g = g + g_add;
58 -     k = k+1;
59 - end;
60 - clear g_add j m n k
61 - h = g == 2;              % removing redundant information from the matrix
62 - clear g
63 - p = h.*16000;            % plotting the result before the filter could be applied
      for user approval
64 - plot(p')
65 - hold on
66 - plot(s')
67 - hold off
68 - reply = input('Apply filter? y/n: ', 's');          % prompt decision
69 - if reply == 'y'
70 -     clear p
71 -     n = (2:i–1);
72 -     aver(n,:) = s(n-1,:) / 2 + s(n+1,:)/2;          % matrix of average values
73 -     clear n
74 -     aver(i,:) = 2*s(i–2,:) – s(i–1,:);        % fixes “last sample uncertainty”
75 -     aver(1,:) = 2*s(2,:) – s(3,:);           % fixes “first sample uncertainty”
76 -     clear i
```

```
77 -     aver = aver.*h;             % leaving only those averaged data that match the
         detected cosmic signals
78 -     l = h == 0;             % inverted h matrix
79 -     clear h
80 -     s = s.*l + aver;                % final correction - identified cosmic pixels are
         replaced with the averaged signals from 2 adjacent samples
81 -     clear l aver reply
82 - else
83 -     clear p h i reply indices_of_bad_samples
84 - end
```

Script 6. Background substraction

```
1 -  s = s(:,1:6172);
2 -  b = s;
3 -  b(:,[1:1906   2316:2774   4181:4419   5201:5599   6031:6172]) = zeros;
4 -  n = 1907;
5 -  m = 2315;
6 -  step = (b(:,n) – b(:,m)) / (m–n);
7 -  for i = n:m
8 -     k = m–i;
9 -     b(:,i) = b(:,i) – b(:,m) – k*step;
10 - end;
11 - n = 2775;
12 - m = 3210;
13 - step = (b(:,n) – b(:,m)) / (m–n);
14 - for i = n:m
15 -    k = m–i;
16 -    b(:,i) = b(:,i) – b(:,m) – k*step;
17 - end;
18 - n = 3211;
19 - m = 3840;
20 - step = (b(:,n) – b(:,m)) / (m-n);
```

```
21 - for i = n:m
22 -     k = m–i;
23 -     b(:,i) = b(:,i) – b(:,m) – k*step;
24 - end;
25 - n = 3841;
26 - m = 4180;
27 - step = (b(:,n) – b(:,m)) / (m–n);
28 - for i = n:m
29 -     k = m–i;
30 -     b(:,i) = b(:,i) – b(:,m) – k*step;
31 - end;
32 - n = 4420;
33 - m = 5200;
34 - step = (b(:,n) – b(:,m)) / (m–n);
35 - for i = n:m
36 -     k = m–i;
37 -     b(:,i) = b(:,i) – b(:,m) – k*step;
38 - end;
39 - n = 5600;
40 - m = 6030;
41 - step = (b(:,n) – b(:,m)) / (m–n);
42 - for i = n:m
43 -     k = m–i;
44 -     b(:,i) = b(:,i) – b(:,m) – k*step;
45 - end;
46 - clear step i k m n
47 - s2 = b;
48 - clear b
49 - plot(s2')
```

Appendix 5. The list of publications and presentations at international conferences

1. S. Mozharov, A. Nordon, D. Littlejohn, C. Wiles, P. Watts, P. Dallin and J. Girkin "Improved method for kinetic studies in microreactors using flow manipulation and non-invasive Raman spectrometry", Submitted to *Journal of the American Chemical Society* on 14.11.2010.

2. S. Mozharov, A. Nordon, J. Girkin, and D. Littlejohn "Non-invasive analysis in microreactors using Raman spectrometry with a specially designed probe", *Lab on a Chip*, 2010, **10**(16), 2101-2107.

3. S. Mozharov, A. Nordon, D. Littlejohn, J. Girkin, P. Dallin, C. Wiles, and P. Watts, "A novel approach for process optimisation in microreactors based on flow rate manipulation and real-time noninvasive measurements" (presentation at *APACT 2010*, 29.05.2010, Manchester, UK).

4. S. Mozharov, A. Nordon, D. Littlejohn, B. Marquardt, and J. Girkin, "Highly sensitive Raman measurements in a fused silica capillary for process analysis in microfluidic reactors" (poster at *APACT 2010*", 29.05.2010, Manchester, UK).

5. S. Mozharov, A. Nordon, J. Girkin, and D. Littlejohn, "A Compact Raman Probe for Rapid Reaction Monitoring in Microreactors," in *Laser Science XXV*, OSA Technical Digest (CD) (Optical Society of America, 2009), paper LSMG3.

6. S. Mozharov, A. Nordon, J. Girkin, and D. Littlejohn "Adapting Raman spectrometry for process analysis in microreactors" (poster at *IUPAC-09*, August 2009, Glasgow, UK).

References

1. J. West, M. Becker, S. Tombrink and A. Manz, *Analytical Chemistry*, 2008, **80**(12), 4403-4419.
2. T.M. Squires and S.R. Quake, *Reviews Of Modern Physics*, 2005, **77**(3), 977-1026.
3. G. Taylor, *Proceedings of the Royal Society of London, Series A: Mathematical and Physical Sciences*, 1953, **219**, 186-203.
4. S. Shuichi, *Sensors Update*, 1999, **6**(1), 3-17.
5. P.S. Dittrich, K. Tachikawa and A. Manz, *Analytical Chemistry*, 2006, **78**(12), 3887-3908.
6. V. Hessel and H. Löwe, *Chemical Engineering & Technology*, 2005, **28**(3), 267-284.
7. A. de Mello and R. Wootton, *Lab on a Chip*, 2002, **2**, 7N-13N.
8. J. Yoshida, A. Nagaki, T. Iwasaki and S. Suga, *Chemical Engineering & Technology*, 2005, **28**(3), 259-266.
9. X.Z. Zhou, R. Medhekar and M.D. Toney, *Analytical Chemistry*, 2003, **75**(15), 3681-3687.
10. T. Thorsen, R.W. Roberts, F.H. Arnold and S.R. Quake, *Physical Review Letters*, 2001, **86**(18), 4163-4166.
11. S. Sugiura, M. Nakajima, S. Iwamoto and M. Seki, *Langmuir*, 2001, **17**(18), 5562-5566.
12. G.R. Yi, S.J. Jeon, T. Thorsen, V.N. Manoharan, S.R. Quake, D.J. Pine and S.M. Yang, *Synthetic Metals*, 2003, **139**(3), 803-806.
13. H. Song, J.D. Tice and R.F. Ismagilov, *Angewandte Chemie-International Edition*, 2003, **42**(7), 768-772.
14. B. Zhao, J.S. Moore and D.J. Beebe, *Science*, 2001, **291**(5506), 1023-1026.
15. B. Zhao, J.S. Moore and D.J. Beebe, *Analytical Chemistry*, 2002, **74**(16), 4259-4268.
16. Y. Lu, W.W. Shi, L. Jiang, J.H. Qin and B.C. Lin, *Electrophoresis*, 2009, **30**(9), 1497-1500.
17. R.L. Hartman and K.F. Jensen, *Lab on a Chip*, 2009, **9**, 2495-2507.
18. K. Jahnisch, V. Hessel, H. Lowe and M. Baerns, *Angewandte Chemie-International Edition*, 2004, **43**(4), 406-446.
19. R. Knitter, D. Gohring, P. Risthaus and J. Hausselt, *Microsystem Technologies*, 2001, **7**(3), 85-90.
20. J.N. Lee, C. Park and G.M. Whitesides, *Analytical Chemistry*, 2003, **75**(23), 6544-6554.
21. J. Lee, M.J. Kim and H.H. Lee, *Langmuir*, 2006, **22**(5), 2090-2095.
22. P. Watts and S.J. Haswell, *Chemical Society Reviews*, 2005, **34**(3), 235-246.
23. A. Gavriilidis, P. Angeli, E. Cao, K.K. Yeong and Y.S.S. Wan, *Chemical Engineering Research and Design*, 2002, **80**(1), 3-30.
24. P.D.I. Fletcher, S.J. Haswell and V.N. Paunov, *Analyst*, 1999, **124**(9), 1273-1282.
25. D.C. Duffy, H.L. Gillis, J. Lin, N.F. Sheppard and G.J. Kellogg, *Analytical Chemistry*, 1999, **71**(20), 4669-4678.

26. H.C. Hunt and J.S. Wilkinson, *Microfluidics And Nanofluidics*, 2008, **4**(1-2), 53-79.
27. J. Leach, H. Mushfique, R. di Leonardo, M. Padgett and J. Cooper, *Lab on a Chip*, 2006, **6**(6), 735-739.
28. N. Paust, C. Litterst, T. Metz, M. Eck, C. Ziegler, R. Zengerle and P. Koltay, *Microfluidics And Nanofluidics*, 2009, **7**(4), 531-543.
29. A.J. deMello, *Nature*, 2006, **442**(7101), 394-402.
30. F. Sarrazin, J.B. Salmon, D. Talaga and L. Servant, *Analytical Chemistry*, 2008, **80**(5), 1689-1695.
31. R.H. Liu, M.A. Stremler, K.V. Sharp, M.G. Olsen, J.G. Santiago, R.J. Adrian, H. Aref and D.J. Beebe, *Journal Of Microelectromechanical Systems*, 2000, **9**(2), 190-197.
32. S.H. Lee, D. van Noort, J.Y. Lee, B.-T. Zhang and T.H. Park, *Lab on a Chip*, 2009, **9**(3), 479-482.
33. M. Al-Fandi, M.A.K. Jaradat, K. Fandi, J.P. Beech, J.O. Tegenfeldt and T.C. Yih, *Iet Nanobiotechnology*, 2010, **4**(3), 61-71.
34. T. Egawa, J.L. Durand, E.Y. Hayden, D.L. Rousseau and S.R. Yeh, *Analytical Chemistry*, 2009, **81**(4), 1622-1627.
35. J.B. Knight, A. Vishwanath, J.P. Brody and R.H. Austin, *Physical Review Letters*, 1988, **80**, 3863-3866.
36. M.C.R. Shastry, S.D. Luck and H. Roder, *Biophysical Journal*, 1998, **74**(5), 2714-2721.
37. C.J. Pipe and G.H. McKinley, *Mechanics Research Communications*, 2009, **36**(1), 110-120.
38. H.B. Yin, B.Z. Ji, P.S. Dobson, K. Mosbahi, A. Glidle, N. Gadegaard, A. Freer, J.M. Cooper and M. Cusack, *Analytical Chemistry*, 2009, **81**(1), 473-478.
39. P. Guillot, A. Ajdari, J. Goyon, M. Joanicot and A. Colin, *Comptes Rendus Chimie*, 2009, **12**(1-2), 247-257.
40. K. Geyer, D.C. Codée and P.H. Seeberger, *Chemistry - a Eurooean Journal*, 2006, **12**, 8434-8442.
41. B.H. Weigl, R.L. Bardell and C.R. Cabrera, *Advanced Drug Delivery Reviews*, 2003, **55**(3), 349-377.
42. J.S. Marcus, W.F. Anderson and S.R. Quake, *Analytical Chemistry*, 2006, **78**(9), 3084-3089.
43. Y. Wakamoto, I. Inoue, H. Moriguchi and K. Yasuda, *Fresenius Journal Of Analytical Chemistry*, 2001, **371**(2), 276-281.
44. Y. Takabayashi, M. Uemoto, K. Aoki, T. Odake and T. Korenaga, *Analyst*, 2006, **131**(4), 573-578.
45. D.Y. He, Z.J. Zhang, Y. Huang and Y.F. Hu, *Food Chemistry*, 2007, **101**(2), 667-672.
46. N.A. Abu-Hatab, J.F. John, J.M. Oran and M.J. Sepaniak, *Applied Spectroscopy*, 2007, **61**(10), 1116-1122.
47. I.H. Chang, J.J. Tulock, J.W. Liu, W.S. Kim, D.M. Cannon, Y. Lu, P.W. Bohn, J.V. Sweedler and D.M. Cropek, *Environmental Science & Technology*, 2005, **39**(10), 3756-3761.
48. F.B. Myers and L.P. Lee, *Lab on a Chip*, 2008, **8**(12), 2015-2031.

49. V.R. Horowitz, D.D. Awschalom and S. Pennathur, *Lab on a Chip*, 2008, **8**(11), 1856-1863.
50. E. Carrilho, A.W. Martinez and G.M. Whitesides, *Analytical Chemistry*, 2009, **81**(16), 7091-7095.
51. R. Mukhopadhyay, *Chemistry world*, 2010, **7**(11), 50-53.
52. K. Abe, K. Kotera, K. Suzuki and D. Citterio, *Analytical And Bioanalytical Chemistry*, **398**(2), 885-893.
53. S.M.Z. Hossain, R.E. Luckham, M.J. McFadden and J.D. Brennan, *Analytical Chemistry*, 2009, **81**(21), 9055-9064.
54. W. Dungchai, O. Chailapakul and C.S. Henry, *Analytical Chemistry*, 2009, **81**(14), 5821-5826.
55. A. Heller and B. Feldman, *Accounts of Chemical Research*, 2010, **43**(7), 963-973.
56. Y. Wang, et al., *Lab on a Chip*, 2009, **9**(16), 2281-2285.
57. F. Nolan-Neylan, *Chemistry world*, 2009, **6**(8), 29.
58. P. Watts and S.J. Haswell, *Chemical Engineering & Technology*, 2005, **28**(3), 290-301.
59. P. Watts and C. Wiles, *Organic & Biomolecular Chemistry*, 2007, **5**, 727-732.
60. B. Ahmed-Omer, J.C. Brandt and T. Wirth, *Organic & Biomolecular Chemistry*, 2007, **5**(5), 733-740.
61. A. Urakawa, F. Trachsel, P.R. von Rohr and A. Baiker, *Analyst*, 2008, **133**, 1352-1354.
62. H.B. Mao, T.L. Yang and P.S. Cremer, *Analytical Chemistry*, 2002, **74**(2), 379-385.
63. D.M. Roberge, L. Ducry, N. Bieler, P. Cretton and B. Zimmermann, *Chemical Engineering & Technology*, 2005, **28**(3), 318-323.
64. P. Watts and S.J. Haswell, *Chemical Society Reviews*, 2005, **34**(3), 235-246.
65. V. Hessel, P. Löb and H. Löwe, *Industrial Microreactor Process Development up to Production*. Microreactors for Organic Synthesis and Catalysis, ed. T. Wirth, Wiley-VCH, Weinheim, 2008.
66. C.C. Lee, et al., *Science*, 2005, **310**(5755), 1793-1796.
67. I.R. Baxendale, J. Deeley, C.M. Griffiths-Jones, S.V. Ley, S. Saaby and G.K. Tranmer, *Chemical Communications*, 2006, **24**, 2566-2568.
68. M. Tokeshi, T. Minagawa, K. Uchiyama, A. Hibara, K. Sato, H. Hisamoto and T. Kitamori, *Analytical Chemistry*, 2002, **74**(7), 1565-1571.
69. T. Tricotet and D.F. O'Shea, *Chemistry-A European Journal*, **16**(22), 6678-6686.
70. P. Watts, *Analytical And Bioanalytical Chemistry*, 2005, **382**, 865-867.
71. J.P. McMullen, M.T. Stone, S.L. Buchwald and K.E. Jensen, *Angewandte Chemie-International Edition*, 2010, **49**(39), 7076-7080.
72. R.S. Krishnan and R.K. Shankar, *Journal of Raman Spectroscopy*, 1981, **10**(1), 1-8.
73. B.R. Masters, *Optics & Photonics News*, 2009, **20**(2), 40-45.
74. J.L. McHale, *Molecular Spectroscopy*. 1st ed, Prentice Hall, New Jersey, 1999.
75. D.A. Long, *Raman Spectroscopy*, Mc Graw-Hill, London, 1977.

76. D.A. Long, *The Raman effect: a unified treatment of the theory of Raman scattering by molecules*, J. Wiley, Chichester; New York, 2002.
77. R.L. McCreery, *Raman spectroscopy for chemical analysis*, Wiley, New York, 2000.
78. J.R. Ferraro, K. Nakamoto and C.W. Brown, *Introductory Raman Spectroscopy*, Elsevier Science, Boston, 2003.
79. M. Kerker, *The scattering of light and other electromagnetuc radiation*, Academic press, New York, 1969.
80. *'Final Year Undegraduate Process Analysis Notes, Prof. D. Littlejohn'*, University of Strathclyde, 2008.
81. J.-X. Cheng, *Applied Spectroscopy*, 2007, **61**(9), 197-208.
82. T. Vo-Dinh, *Trends in Analytical Chemistry*, 1998, **17**(8-9), 557-582.
83. E.V. Efremov, F. Ariese and C. Gooijer, *Analytica Chimica Acta*, 2008, **606**(2), 119-134.
84. D. Zeisel, V. Deckert, R. Zenobi and T. Vo-Dinh, *Chemical Physics Letters*, 1998, **283**(5-6), 381-385.
85. S. Nie and S.R. Emory, *Science*, 1997, **275**, 1102-1106.
86. S.E.J. Bell and N.M.S. Sirimuthu, *Chemical Society Reviews*, 2008, **37**(5), 1012-1024.
87. I.R. Lewis and H.G.M. Edwards, *Handbook of Raman spectroscopy: from the research laboratory to the process line*, Marcel Dekker, New York, 2001.
88. H.W. Schrotter, H. Berger, J.P. Boquillon, B. Lavorel and G. Millot, *Journal Of Raman Spectroscopy*, 1990, **21**(12), 781-789.
89. S.C. Denson, C.J.S. Pommier and M.B. Denton, *Journal Of Chemical Education*, 2007, **84**(1), 67-74.
90. S.A. Asher, C.H. Munro and Z.H. Chi, *Laser Focus World*, 1997, **33**, 99-109.
91. E.V. Efremov, J.B. Buijs, C. Gooijer and F. Ariese, *Applied Spectroscopy*, 2007, **61**(6), 571-578.
92. N. Everall, T. Hanh, P. Matousek, A.W. Parker and M. Towrie, *Applied Spectroscopy*, 2001, **55**(12), 1701-1708.
93. G.D. Pitt, D.N. Batchelder, R. Bennett, R.W. Bormett, I.P. Hayward, B.J.E. Smith, K.P.J. Williams, Y.Y. Yang, K.J. Baldwin and S. Webster, *IEEE Proceedings-Science Measurement And Technology*, 2005, **152**(6), 241-318.
94. J.S. Yang, C.J. Lee and C.H. Wei, *Journal Of The Chinese Chemical Society*, 2002, **49**(5), 677-692.
95. I.R. Lewis and P.R. Griffiths, *Applied Spectroscopy*, 1996, **50**(10), 12A-30A.
96. T.F. Cooney, H.T. Skinner and S.M. Angel, *Applied Spectroscopy*, 1996, **50**(7), 836-848.
97. T.F. Cooney, H.T. Skinner and S.M. Angel, *Applied Spectroscopy*, 1996, **50**(7), 849-860.
98. J.Y. Ma and Y.S. Li, *Applied Optics*, 1996, **35**(15), 2527-2533.
99. X. Zheng, W. Fu, S. Albin, K.L. Wise, A. Javey and J.B. Cooper, *Applied Spectroscopy*, 2001, **55**(4), 382-388.
100. Y. Matsuura, S. Kino, E. Yokoyama, T. Katagiri, H. Sato and H. Tashiro, *Ieee Journal Of Selected Topics In Quantum Electronics*, 2007, **13**(6), 1704-1708.
101. S.O. Konorov, C.J. Addison, H.G. Schulze, R.F.B. Turner and M.W. Blades, *Optics Letters*, 2006, **31**(12), 1911-1913.

102. M.M. Carrabba and R.D. Rauh, *Apparatus for measuring Raman spectra over optical fibers*. 1992: US Patent 5112127.
103. J.B. Slater, *Compact optical measurement probe*. 2003: US Patent 2003/0147593.
104. *Semrock, Inc. Catalog Products: Notch Filters.*, http://www.semrock.com/Catalog/NotchFilter.htm.
105. *InPhotonics, Inc. Catalog Products: The Process RamanProbe.*, http://www.inphotonics.com/probeprocess.htm.
106. *Kaiser Optical Systems, Inc. MK II Filtered Probe Head.*, http://www.kosi.com/raman/probes/mkii.html.
107. H. Owen, D.J. Strachan, J.B. Slater and J.M. Tedesco, *Large-collection-area optical probe*. 2005: US Patent WO 2005/060622 A2.
108. *Kaiser Optical Systems, Inc. PhAT System.*, http://www.kosi.com/raman/analyzers/phat.html.
109. M. Kim, H. Chung, Y. Woo and M.S. Kemper, *Analytica Chimica Acta*, 2007, **587**, 200-207.
110. M. Kim, H. Chung, Y. Woo and M. Kemper, *Analytica Chimica Acta*, 2006, **579**(2), 209-216.
111. N. Everall, T. Hanh, P. Matousek, A.W. Parker and M. Towrie, *Applied Spectroscopy*, 2004, **58**(5), 591-597.
112. A.W.P. P. Matousek, *Journal of Raman Spectroscopy*, 2007, **38**(5), 563-567.
113. P. Matousek, *Applied Spectroscopy*, 2007, **61**(8), 845-854.
114. *Cobalt Light Systems products page*, http://www.cobaltlight.com/products/trs100, accessed 18.08.2010.
115. P. Matousek, I.P. Clark, E.R.C. Draper, M.D. Morris, A.E. Goodship, N. Everall, M. Towrie, W.F. Finney and A.W. Parker, *Applied Spectroscopy*, 2005, **59**(4), 393-400.
116. P. Matousek, E.R.C. Draper, A.E. Goodship, I.P. Clark, K.L. Ronayne and A.W. Parker, *Applied Spectroscopy*, 2006, **60**(7), 758-763.
117. M.V. Schulmerich, K.A. Dooley, T.M. Vanasse, S.A. Goldstein and M.D. Morris, *Applied Spectroscopy*, 2007, **61**(7), 671-678.
118. C. Eliasson, N.A. Macleod and P. Matousek, *Analytical Chemistry*, 2007, **79**(21), 8185-8189.
119. G.E. Walrafen and G. Stone, *Applied Spectroscopy*, 1972, **26**(6), 585-589.
120. M.J. Pelletier and R. Altkorn, *Applied Spectroscopy*, 2000, **54**(12), 1837-1841.
121. M.J. Pelletier and R. Altkorn, *Analytical Chemistry*, 2001, **73**(6), 1393-1397.
122. W.F. Pearman, J.C. Carter, S.M. Angel and J. Chan, *Applied Spectroscopy*, 2008, **62**(3), 285-289.
123. K.R. Kyle, T.M. Vess and S.M. Angel, *SPIE International Symposium on Optical Tools for Manufacturing and Advanced Automation*, 1993.
124. W. Xu, S. Xu, Z. Lu, L. Chen, B. Zhao and Y. Ozaki, *Applied Spectroscopy*, 2004, **58**(4), 414-419.
125. D. Meschede, *Optics, light and lasers: the practical approach to modern aspects of photonics and laser physics*, Wiley-VCH, Weinheim, 2004.
126. F. Adar, M. Delhaye and E. DaSilva, *Journal Of Chemical Education*, 2007, **84**(1), 50-60.

127. J.A. Arns, W.S. Colburn and S.C. Barden, *Proceedings of SPIE*, 1999, **3779**, 313-323.
128. H. Owen, *Journal Of Chemical Education*, 2007, **84**(1), 61-66.
129. B. Chase, *Applied Spectroscopy*, 1994, **48**(7), A14-A19.
130. M.E. Gehm, S.T. McCain, N.P. Pitsianis, D.J. Brady, P. Potuluri and M.E. Sullivan, *Applied Optics*, 2006, **45**(13), 2965-2974.
131. S.T. McCain, M.E. Gehm, Y. Wang, N.P. Pitsianis and D.J. Brady, *Applied Spectroscopy*, 2006, **60**(6), 663-671.
132. G.W. Chantry, H.A. Gebbie and C. Hilsum, *Nature*, 1964, **203**(494), 1052-1053.
133. P. Hendra, C. Jones and G. Warnes, *Fourier Transform Raman Spectroscopy: Instrumentation and Chemical Applications*, Ellis Horwood, New York, 1991.
134. B. Chase, *Applied Spectroscopy*, 1986, **40**(2), 133-137.
135. B. Chase, *Journal Of Chemical Education*, 2007, **84**(1), 75-80.
136. J. Chamberlain, *The principles of interferometric spectroscopy*, Wiley, 1979.
137. R.L. Henry and D.B. Tanner, *Infrared Physics*, 1979, **19**(2), 163-174.
138. *ARCoptix S.A. Spectrometers: ARCSpectro-NIR.*, http://www.arcoptix.com/arcspectro-nir.htm.
139. M.J. Padgett, A.R. Harvey, A.J. Duncan and W. Sibbett, *Applied Optics*, 1994, **33**(25), 6035.
140. B.A. Patterson, M. Antoni, J. Courtial, A.J. Duncan, W. Sibbett and M.J. Padgett, *Optical Communications*, 1996, **130**(1-3), 1-6.
141. D. Komisarek, K. Reichard, D. Merdes, D. Lysak, P. Lam, S. Wu and S. Yin, *Applied Optics*, 2004, **43**(20), 3983-3988.
142. J. Zhao and R.L. McCreery, *Applied Spectroscopy*, 1996, **50**(9), 1209-1214.
143. F.S. Chau, Y. Du and G. Zhou, *Journal Of Micromechanics And Microengineering*, 2008, **18**(2), 1-7.
144. H.A. Andersson, A. Manuilskiy, G. Thungstrom and H.E. Nilsson, *Measurement Science & Technology*, 2008, **19**(4), 1-10.
145. A. Manuilskiy, H.A. Andersson, G. Thungstrom and H.E. Nilsson. *New Concept of Compact Optical Fourier-Transform Spectrometer*. in *5th IEEE Conf. Sensors*. 2006.
146. T. Kamei and T. Wada, *Applied Physics Letters*, 2006, **89**(11), 114101.
147. B. Koren and M. Szawlowski, *Laser Focus World*, 1998, **34**(11), 71-+.
148. N. Quyen, E. DaSilva, N.Q. Dao and M.D. Jouan, *Applied Spectroscopy*, 2008, **62**(3), 273-278.
149. E.N. Lewis and I.W. Levin, *Applied Spectroscopy*, 1995, **49**(5), 672-678.
150. D. Stucki, G. Ribordy, A. Stefanov, H. Zbinden, J.G. Rarity and T. Wall, *Journal Of Modern Optics*, 2001, **48**(13), 1967-1981.
151. J.M.T. Pereira, *Microwave And Optical Technology Letters*, 2006, **48**(4), 712-717.
152. J.F. Brennan, M.E. Beattie, Y. Wang, M.J. Cantella, B.Y. Tsaur, R.R. Dasari and M.S. Feld, *Applied Optics*, 1996, **35**(28), 5736-5739.
153. *Hamamatsu catalogue: two-color detectors*, http://sales.hamamatsu.com/index.php?id=13183629&language=1&undefined, accessed 18.10.2010.

154. S.M. Angel, M. Carrabba and T.F. Cooney, *Spectrochimica Acta Part A-Molecular And Biomolecular Spectroscopy*, 1995, **51**(11), 1779-1799.
155. W.W. Chow, S.W. Koch and M. Sargent, *Semiconductor-Laser Physics*, Springer-Verlag, New York, 1994.
156. Y. Suematsu and A.R. Adams, *Handbook of Semiconductor Lasers and Photonic Integrated Circuits*, Chapman & Hall, Tokyo, 1994.
157. O. Svelto, *Principles of Lasers*, Springer, New York, 1998.
158. D.A. Livshits, A.Y. Egorov, I.V. Kochnev, V.A. Kapitonov, V.M. Lantratov, N.N. Ledentsov, T.A. Nalyot and I.S. Tarasov, *Semiconductors*, 2001, **35**(3), 365-369.
159. D.A. Vinokurov, et al., *Semiconductors*, 2005, **39**(3), 370-373.
160. S. Nagahama, T. Yanamoto, M. Sano and T. Mukai, *Physica Status Solidi A-Applied Research*, 2002, **190**(1), 235-246.
161. *Thorlabs LTD. Technical Data Sheet: VERTILAS single-mode VCSEL Laser Diodes*, http://www.thorlabs.com/Thorcat/12800/12800-S01.pdf.
162. K. Petermann, *IEEE Journal of Selected Topics in Quantum Electronics*, 1995, **1**(2), 480-489.
163. S. Strohmaier, C. Tilljorn, P. Olschowsky and J. Hostetler, *Optics and Photonics News*, 2010, **21**(10), 25-29.
164. R. Tkach and A. Chraplyvy, *Journal of Lightwave Technology*, 1986, **4**(11), 1655-1661.
165. D.S. Seo, J.D. Park, J.G. McInerney and M.A. Osinski, *Electronics Letters*, 1988, **24**(12), 726-728.
166. D.S. Seo, D.S. Seo, J.D. Park, J.G. McInerney and M.A.O.M. Osinski, *IEEE Journal of Quantum Electronics*, 1989, **25**(11), 2229-2238.
167. S. Dong-Sun, P. Jong-Dae, G.M. John and O. Marek, *Applied Physics Letters*, 1989, **54**(11), 990-992.
168. D. Wandt, M. Laschek, A. Tunnermann and H. Welling, *Optics Letters*, 1997, **22**(6), 390-392.
169. M. Merimaa, H. Talvitie, P. Laakkonen, M. Kuittinen, I. Tittonen and E. Ikonen, *Optical Communications*, 2000, **174**(1-4), 175-180.
170. C.J. Hawthorn, K.P. Weber and R.E. Scholten, *Review of Scientific Instruments*, 2001, **72**(12), 4477-4479.
171. L. Levin, *Optics Letters*, 2002, **27**(4), 237-239.
172. Y. Lan, R. Pan and C. Pan, *Optics Letters*, 2004, **29**(5), 510-512.
173. M. Duval, G. Fortin, M. Piché and N. McCarthy, *Applied Optics*, 2005, **44**(24), 5112-5119.
174. F.J. Duarte, *Tunable lasers handbook*, Academic Press, San Diego, 1995.
175. K.C. Harvey and C.J. Myatt, *Optics Letters*, 1991, **16**(12), 910-912.
176. W. Weyerman, B. Neyenhuis, J. Archibald, M. Washburn, D. Durfee and S. Warnick, *Proceedings Of The 2007 Ieee Conference On Control Applications, Vols 1-3*, 2007, 1239-1244.
177. E.W. Kreutz, N. Wiedmann, J. Jandeleit, D. Hoffmann, P. Loosen and R. Poprawe, *Journal of Crystal Growth*, 2000, **210**, 313-317.
178. R.G. Waters, *Progress in Quantum Electronics*, 1991, **15**(3), 153-174.
179. C.H. Henry, P.M. Petroff, R.A. Logan and F.R. Merritt, *Journal Of Applied Physics*, 1979, **50**(5), 3721-3732.
180. D.A. Shaw and P.R. Thornton, *Solid-State Electronics*, 1970, **13**(7), 919-924.

181. R. Claps, J. Sabbaghzadeh and M. Fink, *Applied Spectroscopy*, 1999, **53**(5), 491-496.
182. M.-W. Pan, G.R. Gray, L.M. Smith, R.E. Benner, C.W. Johnson and D.D. Knowlton, *Applied Optics*, 1998, **37**(24), 5755-5759.
183. M. Maiwald, G. Erbert, A. Klehr, B. Sumpf, H. Wenzel, T. Laurent, J. Wiedmann, H.D. Kronfeldt and H. Schmidt, *Reliable operation of 785 nm DFB diode lasers for rapid Raman spectroscopy - art. no. 64560W*, in *High-Power Diode Laser Technology And Applications V*, 2007.
184. *Semiconductor disk lasers*, ed. O.G. Okhotnikov, Wiley, Weinheim, 2010.
185. V.M. Baev, T. Latz and P.E. Toschek, *Applied Physics B-Lasers And Optics*, 1999, **69**(3), 171-202.
186. A. Weber, S.P.S. Porto, L.E. Cheesman and J.J. Barrett, *Journal Of The Optical Society Of America*, 1967, **57**(1), 19.
187. G.O. Neely, L.Y. Nelson and A.B. Harvey, *Applied Spectroscopy*, 1972, **26**(5), 553-555.
188. R.S. Hickman and L. Liang, *Applied Spectroscopy*, 1973, **27**(6), 425-427.
189. M. Hercher, W. Mueller, S. Klainer, R.F. Adamowicz, R.E. Meyers and S.E. Schwartz, *Applied Spectroscopy*, 1978, **32**(3), 298-302.
190. *Atmosphere Recovery Inc. Technology page*, http://www.atmrcv.com/technology.html, accessed 05.02.2010.
191. *Sigma-Aldrich Company, Ltd. FT-Raman spectra*, http://www.sigmaaldrich.com/.
192. M.A. Schwarz and P.C. Hauser, *Lab on a Chip*, 2001, **1**(1), 1-6.
193. W. Ferstl, T. Klahn, W. Schweikert, G. Billeb, M. Schwarzer and S. Loebbecke, *Chemical Engineering & Technology*, 2007, **30**(3), 370-378.
194. K.B. Mogensen, H. Klank and J.P. Kutter, *Electrophoresis*, 2004, **25**(21-22), 3498-3512.
195. E. Thrush, O. Levi, L.J. Cook, J. Deich, A. Kurtz, S.J. Smith, W.E. Moerner and J.J.S. Harris, *Sensors and Actuators B: Chemical*, 2005, **105**(2), 393-399.
196. M. Schwarz and P.C. Hauser, *Lab on a Chip*, 2001, **1**, 1-6.
197. B. Kuswandi, Nuriman, J. Huskens and W. Verboom, *Analytica Chimica Acta*, 2007, **601**(2), 141-155.
198. L. Basabe-Desmonts, F. Benito-Lopez, H. Gardeniers, R. Duwel, A. van den Berg, D.N. Reinhoudt and M. Crego-Calama, *Analytical And Bioanalytical Chemistry*, 2008, **390**(1), 307-315.
199. S. Shrinivasan, P.M. Norris, J.P. Landers and J.P. Ferrance, *Clinics in Laboratory Medicine*, 2007, **27**(1), 173-181.
200. X. Zhang, H. Yin, J. Cooper and S. Haswell, *Analytical And Bioanalytical Chemistry*, 2008, **390**(3), 833-840.
201. M. Lee, J.P. Lee, H. Rhee, J. Choo, Y.G. Chai and E.K. Lee, *Journal Of Raman Spectroscopy*, 2003, **34**(10), 737-742.
202. P.D.I. Fletcher, S.J. Haswell and X.L. Zhang, *Electrophoresis*, 2003, **24**(18), 3239-3245.
203. J.B. Salmon, A. Ajdari, P. Tabeling, L. Servant, D. Talaga and M. Joanicot, *Applied Physics Letters*, 2005, **86**(9), 094106.
204. S.E. Barnes, Z.T. Cygan, J.K. Yates, K.L. Beers and E.J. Amis, *Analyst*, 2006, **131**(9), 1027-1033.

205. S.A. Leung, R.F. Winkle, R.C.R. Wootton and A.J. deMello, *Analyst*, 2005, **130**(1), 46-51.
206. C. Shende, P. Maksymiuk, F. Inscore and S. Farquharson, *Proceedings of SPIE - Photonic Sensing Technologies*, 2006, **6371**, U45-U50.
207. L.X. Chen and J.B. Choo, *Electrophoresis*, 2008, **29**(9), 1815-1828.
208. J.C. Lingxin Chen, *Electrophoresis*, 2008, **29**(9), 1815-1828.
209. P.J. Viskari and J.P. Landers, *Electrophoresis*, 2006, **27**(9), 1797-1810.
210. B. Kuswandi, Nuriman, J. Huskens and W. Verboom, *Analytica Chimica Acta*, 2007, **601**(2), 141.
211. N.J. Everall, *Analyst*, 2010, **135**(10), 2512-2522.
212. N.J. Everall, *Applied Spectroscopy*, 2009, **63**(9), 245A-262A.
213. D. Schafer, M. Muller, M. Bonn, D.W.M. Marr, J. van Maarseveen and J. Squier, *Optics Letters*, 2009, **34**(2), 211-213.
214. D. Schafer, J.A. Squier, J. van Maarseveen, D. Bonn, M. Bonn and M. Muller, *Journal Of The American Chemical Society*, 2008, **130**(35), 11592-11593.
215. J. Dambrine, B. Geraud and J.B. Salmon, *New Journal Of Physics*, 2009, **11**, 1-22.
216. T. Park, M. Lee, J. Choo, Y.S. Kim, E.K. Lee, D.J. Kim and S.H. Lee, *Applied Spectroscopy*, 2004, **58**(10), 1172-1179.
217. D.H. Pan and R.A. Mathies, *Biochemistry*, 2001, **40**(26), 7929-7936.
218. T. Araki, K. Ueno, H. Misawa and N. Kitamura, *Analytical Sciences*, 2006, **22**(10), 1283-1289.
219. J.M. Girkin and D. Wokosin, *Practical Multiphoton Microscopy*, in *Confocal and Two-photon Microscopy: Foundations, Applications and Advances*, Ed. A. Diaspro, Wiley, New York, 2002.
220. R.M. Zuker and O. Price, *Cytometry*, 2001, **44**(4), 273-294.
221. C. Cao, G. Xia, J. Holladay, E. Jones and Y. Wang, *Applied Catalysis A: General*, 2004, **262**(1), 19-29.
222. X.Z. Zhou and M.D. Toney, *Journal Of The American Chemical Society*, 1998, **120**(50), 13282-13283.
223. H. Xue, X.W. Wu and W.P. Huskey, *Journal Of The American Chemical Society*, 1996, **118**(24), 5804-5805.
224. K. Kuwata, R. Shastry, H. Cheng, M. Hoshino, C.A. Batt, Y. Goto and H. Roder, *Nature Structural Biology*, 2001, **8**(2), 151-155.
225. S.H. Park, M.C.R. Shastry and H. Roder, *Nature Structural Biology*, 1999, **6**(10), 943-947.
226. D.L. Zechel, L. Konermann, S.G. Withers and D.J. Douglas, *Biochemistry*, 1998, **37**(21), 7664-7669.
227. T. Rob and D.J. Wilson, *Journal of the American Society for Mass Spectrometry*, 2009, **20**(1), 124-130.
228. D.A. Simmons and L. Konermann, *Biochemistry*, 2002, **41**(6), 1906-1914.
229. J. Wang, *Electrophoresis*, 2002, **23**(5), 713-718.
230. M. Miyazaki and H. Maeda, *Trends In Biotechnology*, 2006, **24**(10), 463-470.
231. P.L. Urban, D.M. Goodall and N.C. Bruce, *Biotechnology Advances*, 2006, **24**(1), 42-57.
232. A.G. Hadd, D.E. Raymond, J.W. Halliwell, S.C. Jacobson and J.M. Ramsey, *Analytical Chemistry*, 1997, **69**(17), 3407-3412.

233. T.C. Logan, D.S. Clark, T.B. Stachowiak, F. Svec and J.M.J. Frechet, *Analytical Chemistry*, 2007, **79**(17), 6592-6598.
234. G.H. Seong, J. Heo and R.M. Crooks, *Analytical Chemistry*, 2003, **75**(13), 3161-3167.
235. A. Srinivasan, H. Bach, D.H. Sherman and J.S. Dordick, *Biotechnology And Bioengineering*, 2004, **88**(4), 528-535.
236. C. de Bellefon, N. Tanchoux, S. Caravieilhes, P. Grenouillet and V. Hessel, *Angewandte Chemie-International Edition*, 2000, **39**(19), 3442-3445.
237. C. de Bellefon, N. Pestre, T. Lamouille, P. Grenouillet and V. Hessel, *Advanced Synthesis & Catalysis*, 2003, **345**(1-2), 190-193.
238. W.P. Bula, W. Verboom, D.N. Reinhoudt and H. Gardeniers, *Lab on a Chip*, 2007, **7**(12), 1717-1722.
239. Y. Ono, M. Kitajima, S. Daikoku, T. Shiroya, S. Nishihara, Y. Kanie, K. Suzuki, S. Goto and O. Kanie, *Lab on a Chip*, 2008, **8**(12), 2168-2173.
240. S. Matosevic, G.J. Lye and F. Baganz, *Biotechnology Progress*, 2009, **26**(1), 118-126.
241. S.C. Jakeway and A. deMello, *Analyst*, 2001, **126**(9), 1505-1510.
242. C. Wang, S.J. Li, Z.Q. Wu, J.J. Xu, H.Y. Chen and X.H. Xia, *Lab on a Chip*, 2010, **10**(5), 639-646.
243. A.L. Liu, T. Zhou, F.Y. He, J.J. Xu, Y. Lu, H.Y. Chen and X.H. Xia, *Lab on a Chip*, 2006, **6**(6), 811-818.
244. Y. Sarov, V. Sarova, T. Ivanov, K. Ivanova, I. Capek and I.W. Rangelow, *Chemical Engineering Journal*, 2008, **135**(Supplement 1), S284.
245. S.G. Kazarian, *Analytical And Bioanalytical Chemistry*, 2007, **388**, 529-532.
246. H. Wensink, F. Benito-Lopez, D.C. Hermes, W. Verboom, J.G.E. Gardeniers, D.N. Reinhoudt and A. van den Berg, *Lab on a Chip*, 2005, **5**, 280-284.
247. J.M. Hungerford, G.D. Christian, J. Ruzicka and J.C. Giddings, *Analytical Chemistry*, 1985, **57**(9), 1794-1798.
248. M.B. Kerby, R.S. Legge and A. Tripathi, *Analytical Chemistry*, 2006, **78**(24), 8273-8280.
249. W.D. Ristenpart, J.D. Wan and H.A. Stone, *Analytical Chemistry*, 2008, **80**(9), 3270-3276.
250. B.M. Kolakowski, D.A. Simmons and L. Konermann, *Rapid Communications in Mass Spectrometry*, 2000, **14**(9), 772-776.
251. K. Yamashita, M. Miyazaki, H. Nakamura and H. Maedatt, *Journal Of Physical Chemistry A*, 2009, **113**(1), 165-169.
252. N.J. Gleason and J.D. Carbeck, *Langmuir*, 2004, **20**(15), 6374-6381.
253. M. Graetzel and P. Inelta, *The Bases of Chemical Thermodynamics*. Vol. 1, Universal-Publishers, Parkland, Florida, 2002.
254. F.S. Prout, Beaucair.Vd, G.R. Dyrkacz, W.M. Koppes, R.E. Kuznicki, Marlewsk.Ta, Pienkows.Jj and J.M. Puda, *Journal Of Organic Chemistry*, 1973, **38**(8), 1512-1517.
255. X.F. Zhang, E.S.M. Lai, R. Martin-Aranda and K.L. Yeung, *Applied Catalysis A-General*, 2004, **261**(1), 109-118.
256. A.R. Bogdan, B.P. Mason, K.T. Sylvester and D.T. McQuade, *Angewandte Chemie-International Edition*, 2007, **46**(10), 1698-1701.
257. A.K. Coker, *Modeling of Chemical Kinetics and Reactor Design*, Butterworth-Heinemann, Boston, 2001.

258. R.J. Dijkstra, F. Ariese, C. Gooijer and U.A.T. Brinkman, *Trac-Trends In Analytical Chemistry*, 2005, **24**(4), 304-323.
259. A. Ruddick, D.N. Batchelder, K.D. Bartle, A.C. Gilby and G.D. Pitt, *Applied Spectroscopy*, 2000, **54**(12), 1857-1863.
260. R. Steinert, H. Bettermann and K. Kleinermanns, *Applied Spectroscopy*, 1997, **51**(11), 1644-1647.
261. C.Y. Chen and M.D. Morris, *Applied Spectroscopy*, 1988, **42**(3), 515-518.
262. B.J. Marquardt, P.G. Vahey, R.E. Synovec and L.W. Burgess, *Analytical Chemistry*, 1999, **71**(21), 4808-4814.
263. *Polymicro Technologies catalogue*, http://www.polymicro.com/, accessed 19.01.2010.
264. *IMM mainz catalogue*, http://www.imm-mainz.de/, accessed 05.02.2010.
265. J.E. Bertie and K.H. Michaelian, *Journal Of Chemical Physics*, 1982, **77**(11), 5263-5861.
266. T. Nakabayashi, K. Kosugi and N. Nishi, *Journal Of Physical Chemistry A*, 1999, **103**(43), 8595-8603.
267. M. Umadevi, S.A.J. Bella and V. Ramakrishnan, *Journal Of Raman Spectroscopy*, 2007, **38**(2), 231-238.
268. K. Niemax, A. Zybin and D. Eger, *Analytical Chemistry*, 2001, **73**(5), 135A-139A.
269. R. Bennett, *Spectrochimica Acta Part A: Molecular and Biomolecular Spectroscopy*, 1995, **51**(12), 2001-2009.
270. C.F. Carter, H. Lange, S.V. Ley, I.R. Baxendale, B. Wittkamp, J.G. Goode and N.L. Gaunt, *Organic Process Research & Development*, 2010, **14**(2), 393-404.
271. G. Duxbury, N. Langford, M.T. McCulloch and S. Wright, *Chemical Society Reviews*, 2005, **34**(11), 921-934.